AUTOIGNITION AND EMISSION CHARACTERISTICS OF GASEOUS FUEL DIRECT-INJECTION COMPRESSION-IGNITION COMBUSTION

by

NING WU

B.Sc., Tsinghua University, 2000
M.A.Sc., Tsinghua University, 2002

A THESIS SUBMITTED IN PARTIAL FULFILLMENT OF
THE REQUIREMENTS FOR THE DEGREE OF

DOCTOR OF PHILOSOPHY

in

THE FACULTY OF GRADUATE STUDIES

(Mechanical Engineering)

THE UNIVERSITY OF BRITISH COLUMBIA

December 2007

Abstract

Heavy-duty natural gas engines offer air pollution and energy diversity benefits. However, current homogeneous-charge lean-burn engines suffer from impaired efficiency and high unburned fuel emissions. Natural gas direct-injection engines offer the potential of diesel-like efficiencies, but require further research. To improve understanding of the autoignition and emission characteristics of natural gas direct-injection compression-ignition combustion, the effects of key operating parameters (including injection pressure, injection duration, and pre-combustion temperature) and gaseous fuel composition (including the effects of ethane, hydrogen and nitrogen addition) were studied.

An experimental investigation was carried out on a shock tube facility. Ignition delay, ignition kernel location, and NOx emissions were measured. The results indicated that the addition of ethane to the fuel resulted in a decrease in ignition delay and a significant increase in NOx emissions. The addition of hydrogen to the fuel resulted in a decrease in ignition delay and a significant decrease in NOx emissions. Diluting the fuel with nitrogen resulted in an increase in ignition delay and a significant decrease in NOx emissions. Increasing pre-combustion temperature resulted in a significant reduction in ignition delay, and a significant increase in NOx emissions. Modest increase in injection pressure reduced the ignition delay; increasing injection pressure resulted in higher NOx emissions. The effects of ethane, hydrogen, and nitrogen addition on the ignition delay of methane were also successfully predicted by FlameMaster simulation.

OH radical distribution in the flame was visualized utilizing Planar Laser Induced Fluorescence (PLIF). Single-shot OH-PLIF images revealed the stochastic nature of the autoignition process of non-premixed methane jets. Examination of the convergence of the ensemble-averaged OH-PLIF images showed that increasing the number of repeat experiments was the most effective way to achieve a more converged result.

A combustion model, which incorporated the Conditional Source-term Estimation (CSE) method for the closure of the chemical source term and the Trajectory Generated Low-Dimensional Manifold (TGLDM) method for the reduction of detailed chemistry, was applied to predict the OH distribution in a combusting non-premixed methane jet. The model failed to predict the OH distribution as indicated by the ensemble-averaged OH-PLIF images, since it cannot account for fluctuations in either turbulence or chemistry.

Table of Contents

List of Tables

List of Figures

Nomenclature and Acronyms

χ	Scalar dissipation rate
ε	Dissipation rate of turbulent kinetic energy
Γ	Penetration number
ϕ	Equivalence ratio
ρ	Density
τ	Ignition delay time or time duration
d	Injector nozzle diameter
d*	Normalized injector nozzle diameter
D	Diffusivity
E	Activation energy
h	Specific enthalpy
k	Turbulent kinetic energy
P	Pressure
P_i	Injection pressure
P_o	Pre-combustion pressure or back pressure
R	Universal gas constant
t_{d_ign}	Ignition delay time
t	Time interval from the start of injection
t_i	injection duration
T	Temperature
T_{ad}	Adiabatic flame temperature
T_f	Initial fuel temperature
T_o	Pre-combustion temperature or initial air temperature
Y	Mass fraction
$\langle Y \mid Z = \eta \rangle$	Conditional average of Y with condition $Z = \eta$
Z	Mixture fraction
Z_{st}	Stoichiometric mixture fraction
$\langle Z \rangle$	Mean of mixture fraction
$\langle Z''^2 \rangle$	Variance of mixture fraction
Z_k	Ignition kernel location

Z_k^*	Normalized ignition kernel location
Z_t	Jet length when ignition occurs
ANOVA	Analysis of variance
A.U.	Arbitrary unit
COV	Coefficient of variation (standard deviation / mean)
CMC	Conditional moment closure
CSE	Conditional source-term estimation
DISI	Direct-injection spark-ignition
DNS	Direct numerical simulation
EGR	Exhaust gas recirculation
FCT	Flux corrected transport
HCCI	Homogeneous charge compression ignition
ILDM	Intrinsical low dimensional manifold
LES	Large eddy simulation
LII	Laser induced incandescence
NOx	Oxides of nitrogen
PAH	Polycyclic aromatic hydrocarbon
PDF	Probability density function
PLIF	Planar laser induced fluorescence
PM	Particulate matter
RANS	Reynolds-averaged Navier-Stokes
SOI	Start of injection
TGLDM	Trajectory generated low-dimensional manifold

Acknowledgements

First, I would like to thank my supervisors, Dr. Martin Davy and Dr. Kendal Bushe, for their unending support, patience, and advice during my study at UBC. I also want to extend special recognition to Dr. Steve Rogak, for his support and direction during my research program.

This research would not have been possible without the help from Westport Innovations. Besides experimental hardware, the help I have got from their staff is tremendous. I want to especially acknowledge the assistance of Charlie Loo, Brian Buick, Mark Dunn, Justin Duan, Sandeep Munshi, Patric Ouellette, and Phillip Hill.

The laser experiment in this work was carried out through collaboration with the Laboratory for Advanced Spectroscopy and Imaging Research (LASIR) at the Department of Chemistry of UBC. I'd also like to say a special thank-you to Saeid Kamal, a Senior Research Associate at LASIR, for helping me set up the laser system, and providing me with lots of valuable advice and suggestions.

I also want to acknowledge all the excellent graduate students with whom I have been honoured to work; but in particular, thanks to Huang Jian, Gordon McTaggart-Cowan, Heather Jones, Bei Jin, Michael Yeung, Joey Mikawoz, Reza Kowsari, and Edward Chan.

Finally I want to thank my family, and especially my parents, for their ongoing support of my educational pursuits. Lastly, and most importantly, to my wife Xiaobing Cheng, for your unconditional love and support over the past years. I hope I can provide you with the same support that you have given me during your study in the near future.

Chapter 1
Introduction

1.1 Introduction

Traditional diesel engines offer many advantages in heavy-duty applications, but also suffer from relatively high levels of regulated and unregulated emissions. Diesel engines are reliable and robust, provide high torque at low speeds, and are as much as 25% more efficient than equivalent gasoline-fuelled engines [1]. As a result of their high efficiency, greenhouse gas emissions are low compared with other in-use transportation motive power sources. However, emissions of harmful species, including pollutants such as fine particulate matter (PM) and oxides of nitrogen (NOx), as well as air toxics such as benzene, are significantly higher.

Natural-gas-fuelled internal combustion engines have been increasingly studied because of their potential environmental and economic benefits [2-9]. Recent technological developments enable direct injection of natural gas into diesel engines [4-9]. This technology provides a practical solution for diesel engines to meet increasingly stringent emission regulations while maintaining their high thermal efficiency [5-9]. For a direct-injection natural gas engine, knowledge of the ignition and combustion processes occurring inside the combustion chamber is critical for optimizing engine design and perfecting control strategies. Although significant progress has been made recently in this regard, both experimentally [4-12] and through computer simulation studies [13-15], considerable work remains to establish fundamental relationships between operating parameters and engine performance and emissions for this class of engines.

1.2 Objectives

This research project was mainly experimentally-based using a shock tube facility to investigate various aspects of the direct-injection compression-ignition gaseous fuel jets under engine-relevant conditions, i.e., for moderate temperatures (1000 to 1350 K) and elevated pressures (16-40 bar). Meanwhile numerical simulations were also utilized to help achieve a better understanding of the experimental results. The specific objectives of the project were to:

1. Understand the influence of key operating parameters on autoignition and emissions. Variations in pre-combustion air temperature, injection duration, and injection pressure were used to investigate this effect.

2. Explore the influence of chemical composition of the fuel on autoignition and emissions. Fuels studied included methane, methane/ethane, methane/hydrogen, and methane/nitrogen.

3. Investigate the location and nature of the reaction zones of transient reacting methane jets. This was achieved by visualizing the OH distribution in the flame utilizing Planar Laser Induced Fluorescence (PLIF).

By meeting these objectives, a better understanding of the autoignition and pollutant formation of non-premixed gaseous fuel was to be achieved, specifically under engine-relevant operating conditions. From this, it may be possible to identify improved operating modes to optimize the combustion process, with the goal of maximizing engine efficiency while minimizing emissions.

1.3 Thesis Structure

One paper has been published based on methane and methane/ethane results presented in Chapters 3. Methane/hydrogen and methane/nitrogen results in Chapter 3 and OH-PLIF results in Chapter 6 are currently in preparation for submission.

The thesis content is laid out as follows. The current chapter provides a general background and the motivation for the research. Chapter 2 provides a detailed review of various experimental methods of autoignition studies, and the current state of knowledge regarding ignition studies of natural gas and detailed chemical kinetic mechanisms for natural gas combustion. The combustion structure of non-premixed gaseous combustion and NOx formation mechanisms are covered. The basic principles of laser induced fluorescence are introduced. The chapter concludes with an introduction to various closure methods for the chemical source term in turbulent combustion modelling and a mathematical model for the reduction of detailed chemistry. Chapter 3 presents experimental results of ignition measurements of jets of methane with additives. Chapter 4 presents numerical simulation results of a non-premixed counter-flow diffusion flame of methane blended with different amount of ethane, hydrogen, or nitrogen and air. Experimental results on the thermodynamic and gas dynamic effects on ignition of jets of

methane with additives from Chapter 3 is revisited and analyzed in Chapter 5. Chapter 6 presents the OH-PLIF results for transient reacting methane jets. The OH distribution in a non-premixed methane jet flame predicted by numerical simulation is presented in Chapter 7. Finally, a summary of the main conclusions from the thesis and suggestions for future work are provided in Chapter 8. References are numbered sequentially from the beginning of the thesis and are located after Chapter 8. Appendices provide further information on the experimental apparatus, procedures, and more details regarding the experimental results.

Chapter 2
Background Information

2.1 Introduction

Natural gas (commercial grade methane fuel) is the cleanest fossil energy source available in large quantities on earth [16]. On an energy basis, the combustion of natural gas releases significantly lower pollutants than fossil fuels such as coal, diesel and gasoline [16]. Because of the huge economic and environmental benefits associated with using natural gas in place of these more traditional fuels, a large number of studies have investigated the combustion of natural gas in various practical and laboratory systems. In the past decades, with the rapid development of digital computer technology, numerical simulation and analysis in conjunction with experimental investigation have been increasingly used as standard approaches in these studies.

2.2 Experimental Methods for the Study of Autoignition

Experimental studies of autoignition in well-controlled laboratory devices not only provide fundamental information regarding the characteristics of the testing fuel, but also generate valuable databases for developing and validating detailed reaction mechanisms or complex combustion models. A common feature of laboratory setups for combustion study is that the initial and boundary conditions of the reacting system are well-established, which greatly facilitates the analytical and numerical work that follows. Attributes of well-controlled reacting systems that are often measured and reported in the literature include the ignition delay time and species concentration profiles.

Studies of ignition delay time may be conducted using a variety of different experimental methods, such as jet-stirred reactors, continuous flow reactors, rapid compression machines, constant volume vessels, and shock tubes. For highly exothermic mixtures, in which ignition leads to an abrupt increase in pressure, the ignition time may be accurately measured from the pressure trace alone. However, for relatively dilute mixtures or non-premixed combustion, such as is the case in the present study, the rise in pressure at the time of ignition is very gradual, which prevents an unequivocal determination of the ignition time. To measure the ignition delay times of highly dilute test mixtures or non-premixed combustion events, the time-history of chemiluminescence (natural luminosity

from either the CH or OH radical) is often employed to identify the start of ignition. The data traces obtained by these diagnostics show a much more abrupt rise at the time ignition, relative to the pressure trace, thus allowing a more precise determination of the ignition time.

2.2.1 Jet-stirred Reactor

A schematic of a jet-stirred reactor is shown in Figure 2.1. A jet-stirred reactor is usually a ceramic cavity into which a high-speed jet of fuel and air is injected via a small nozzle. The fuel and air are typically premixed prior to entering the reactor, and liquid fuels are often vaporized with a pre-heater before premixing occurs. Jet Impingement against the reactor wall causes a vigorous mixing and recirculation of the gases that sustains the combustion process and creates a nearly homogeneous reaction zone.

The ignition time in a jet-stirred reactor is determined by increasing the reactor loading (i.e., fuel-air mass flow rate) until the flame is blown out, which may be inferred from the sudden drop in reactor temperature. The definition of the ignition time is based on the reactor residence time.

Exhaust Port →

Ceramic Reactor ←

Premixed Fuel and Air
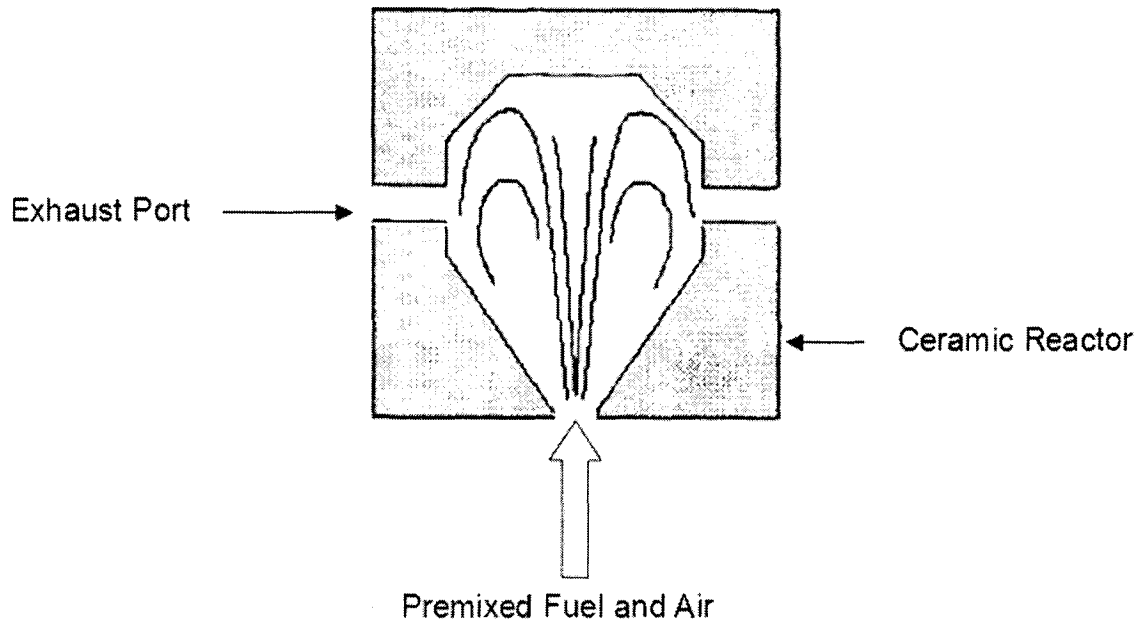
Figure 2.1 Schematic of a jet-stirred reactor [17]

2.2.2 Continuous Flow Reactor

A schematic of a continuous flow device is shown in Figure 2.2. In a continuous flow device, the air is preheated (usually by electrical heaters) to a high temperature and controlled at a constant pressure. Using a well-designed injector, gaseous fuel is injected into the flowing air stream and thus forms a homogenous combustible mixture. Liquid fuels may either be vaporized before they are injected into the air stream, or special nozzles are employed to rapidly atomize and vaporize the liquid fuel upon injection, thereby minimizing the effect of physical processes on the measured ignition delay. As the mixture flows along the tube, the mixture ignites at some distance downstream of the fuel injection location after an induction period (ignition delay time).
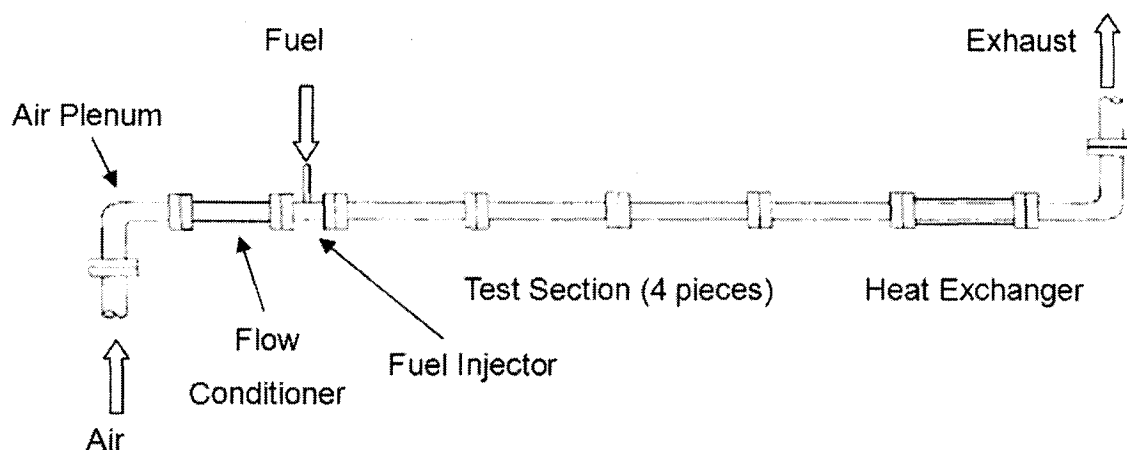
Figure 2.2 Schematic of a continuous flow reactor [17]

In a continuous flow device, the occurrence of autoignition is determined by a variety of means (e.g., UV and visible light emissions or a rapid increase in temperature at the flame front location) by a series of sensors or by adjusting the flow rate or other operational parameters of the air stream until the flame front is stabilized at the fixed sensor location. The ignition delay can be calculated from the known distance between the fuel injection point and the flame front location and the mean free-stream flow velocity.

Continuous flow reactors allow ample time for measuring and regulating many of the important variables such as temperature, pressure, flow rate (flow speed or residence time), equivalence ratio, fuel type, and fuel composition. However, the method is limited to low temperatures typically due to limitations of the heaters. Generally, the most widely used heaters in continuous flow reactor ignition delay studies are electrical residence heaters

and the upper temperature limit is at an order of 1300 K. The advantages of a continuous flow device include better simulations of gas turbine conditions, convenience of operational condition (such as temperature and pressure) control and easy integration of fuel composition simulation.

2.2.3 Rapid Compression Machine

A rapid compression machine, shown in Figure 2.3, is a single-shot, piston-cylinder compression device. The compression chamber is initially charged to a prescribed pressure with a gaseous fuel-oxygen-diluent test mixture. The composition of the diluent – which is typically a mixture of carbon dioxide, argon, and/or nitrogen – is varied to regulate the end-of-compression temperature and pressure. Compressed air actuates a high-speed air gun, which is connected to a sliding cam. When the air gun is fired, the cam is pulled forward, forcing an adjoining piston into the compression chamber. This rapid compression of the test mixture causes an abrupt rise in the temperature and pressure of the test gas.
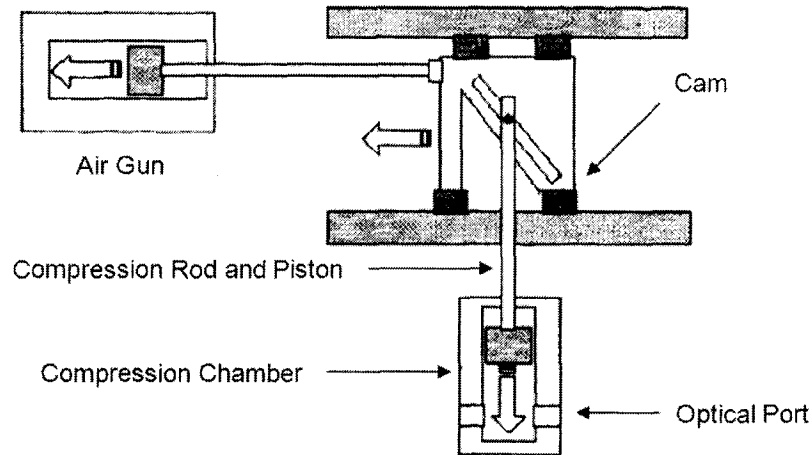
Figure 2.3 Schematic of a rapid compression machine [17]

The ignition time in a rapid compression machine is defined as the time interval between the end of the compression stroke and the time of ignition. Ignition is usually inferred from either a pressure trace, or the time-history of an intermediate species (e.g., CH, OH), which is measured via optical ports in the compression chamber. Due to the finite time required for compression (typically 20-60 μs), a rapid compression machine is usually utilized in low-temperature (<1000 K) studies, for which the ignition time is relatively long compared to the compression time.

2.2.4 Constant Volume Vessel

A constant volume vessel, shown in Figure 2.4, uses either an electrical heater, or combustion of a lean premixed mixture to create the desired temperature and pressure. A high-pressure nozzle then injects a fuel into the constant volume vessel. When testing liquid fuels, the nozzle is often designed to rapidly atomize the fuel, thereby increasing the rate of vaporization and mixing as it is injected into the constant volume vessel. However, similar to the continuous flow reactor method, these physical processes will still contribute to the overall ignition delay, and thus must be considered when interpreting ignition time data. Also, when testing liquid fuels, there may be a substantial drop in the temperature and pressure inside the vessel as the fuel vaporizes, which makes it difficult to precisely determine the conditions for the experiment.
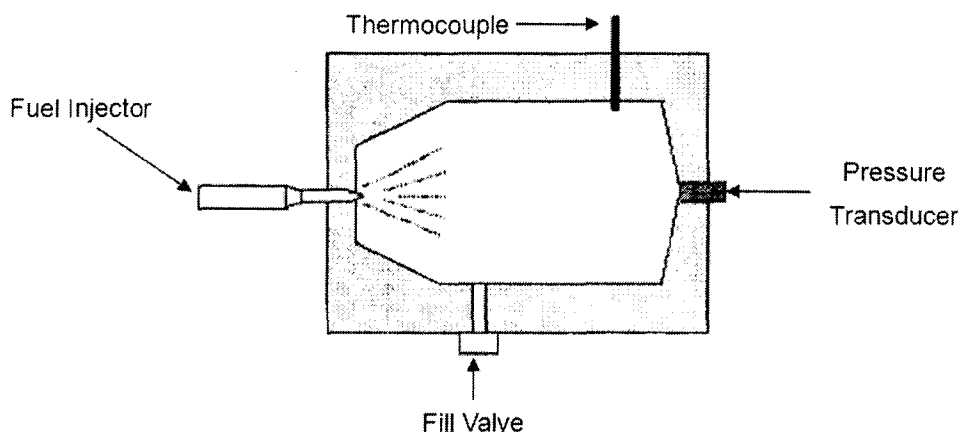
Figure 2.4 Schematic of a constant volume vessel [17]

The ignition time in a constant volume vessel is often defined as the time interval between the injection of the fuel and the initial rise in pressure that results from combustion of the fuel. Electrically-heated constant volume vessels are typically limited to low temperature (<1000 K) ignition time studies because of the limitation of electrical heating. For constant volume vessels using combustion of a lean premixed mixture, typical conditions of a diesel engine at top-dead-center can be achieved. The latter type also has very good control of the conditions at which fuel is injected, but the chemical composition of the gas in the system is limited by the method used to attain pressure and temperature. Post-combustion gases from the initial premixed event remain in the chamber and subsequently become part of the combustion process.

2.2.5 Shock Tube

A schematic of the shock tube and its working principle is shown is Figure 2.5. A shock tube is a device in which a high-pressure driver gas and a low-pressure driven gas are separated by one or two diaphragms. When the diaphragms burst, a shock wave is generated. The shock wave, which is a high-enthalpy compression wave with its local Mach number higher than one, travels downstream into the driven gas causing a pressure and temperature jump across the shock front. A contact surface that separates the driver gas from the driven gas follows the incident shock wave and travels at a lower speed. At the same time, a rarefaction fan composed of a series of expansion waves fans out into the upstream driver gas. The shock wave, upon reflection from the end wall of the shock tube, interacts with the driven gas set to move by the incident shock and brings it to a stop. The static high-temperature and high-pressure reservoir generated behind the reflected shock wave can be readily used for studies of various purposes. Under ideal conditions [18], the pressure and temperature in the experimental area can be kept constant until the arrival of the reflected rarefaction fan.

In the premixed case, ignition time is defined as the time interval between shock arrival, which is determined from a pressure trace, and the onset of combustion, which is usually inferred from either a pressure trace or the time-history of an intermediate species (e.g., CH, OH).

The advantages of a shock tube include:

1. It guarantees that surface effects will not contribute to the process since (1) the gas is not heated by hot surfaces and (2) the "event" time is too short for molecules to diffuse to or from the cold wall.

2. It is easier to construct a shock tube than a high temperature furnace and it has a much wider operating range in terms of temperatures and pressures.

On the other hand, the shortcomings of a shock tube include:

1. Measurement uncertainties: A shock tube is a single-shot instrument. For collecting data after the shock in such a short duration, it is impossible to use signal-averaging methods. It also requires fast-response instruments.

2. Run-to-run variations: Gardiner [19] pointed out that "the only recognized contributions to the run-to-run variations is in the manner of diaphragm rupture." He further suggested that the scatter caused by diaphragm-breaking variations may not be Gaussian and would therefore cause the scatter.

3. The non-idealities in shock tube behaviour caused by the formation of a boundary layer and its interactions can have serious consequences in the interpretation of experimental results. This comes down to errors in the reaction temperatures. Since rate constants in chemical reactions are usually exponentially dependent on reaction temperatures, there is the possibility of large errors.

4. Uncertainty also arises from gas dynamic effects in shock tubes. But this effect should be less than the temperature calibration factor [20]. For fixed mixture constituents, non-ideal gas dynamic effects are most sensitive to shock tube diameter, reaction pressures and the use of shock tubes.

5. Shock tube data is less accurate at lower temperatures (<1200 K). Bowman [21] estimated that inaccuracies in measured shock velocities can result in 20 K and 50 K uncertainties in temperatures behind incident and reflected waves, respectively.

6. Another fundamental problem of shock tube studies for ignition delay times is the inconsistency of the definition of the ignition delay time in experimental studies. Some investigator used the time to the initial rise in pressure of radiation as detected by the sensing device for indication of ignition, but some others used the time to peak values of pressure or light emission or to some arbitrary fraction of the peak values.

7. For premixed combustion studies, in order to get excellent mixing before putting the mixture into the shock tube, researchers usually mix the fuel and air for a long time at low temperatures. The author is unaware of any researcher who has analyzed the possible effects of pre-ignition reactions allowed by this extended mixing time on the subsequently measured ignition delay.
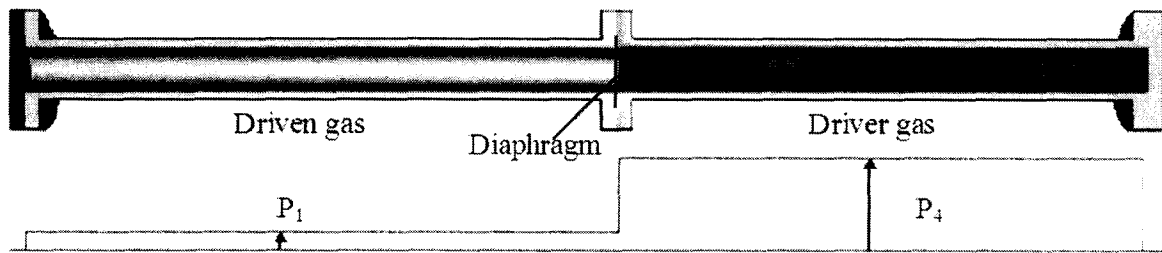
(a) Initial state: the high-pressure driver gas is separated from the low-pressure driven gas by the diaphragm
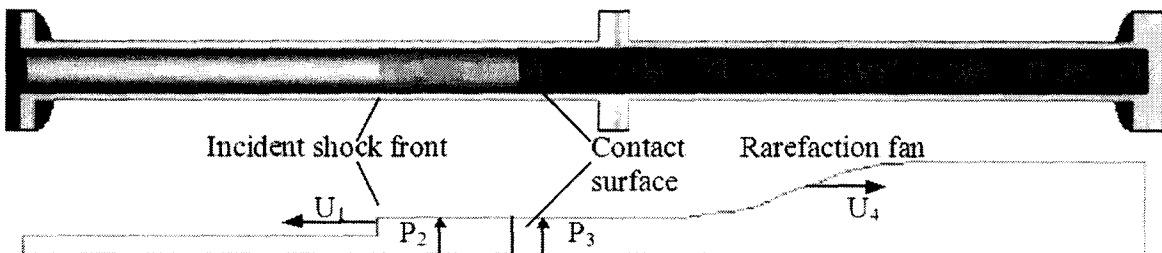
(b) An incident shock wave forms right after the bursting of the diaphragm
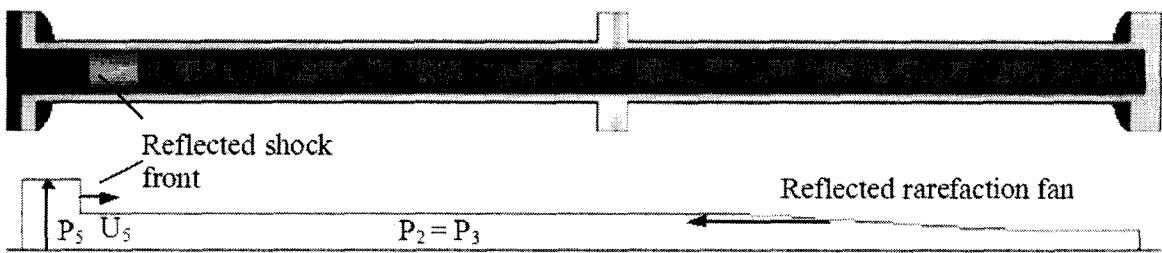
(c) The shock wave reflects from the end of the driven section
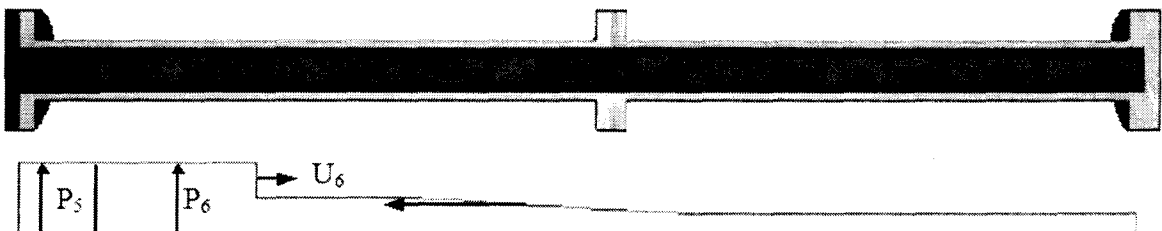
(d) The shock wave passes through the contact surface

Figure 2.5 Shock tube working principle [22]

It should be emphasized that because the autoignition is not an absolute property of the mixture or fuel, all ignition delay data must be interpreted carefully by considering how the experimental method utilized in each study may affect the measured ignition time. For example, depending on the method by which the fuel and oxidizer are mixed, physical processes (i.e., mixing, vaporization, atomization) may have a significant effect on the measured ignition time. Furthermore, because the definition of the ignition time is not unique, studies that utilize similar experimental apparatus may not necessarily employ the same definition for the ignition time. For example, in some studies the onset of ignition is inferred from a pressure trace, while in others this definition is based on the time-history of an intermediate species (e.g., CH). Thus, different values may be obtained among studies that do not utilize the same criteria to quantify the ignition time.

2.3 Natural Gas Combustion

2.3.1 Ignition Studies of Methane

Premixed Studies

For most hydrocarbon fuels, including methane, the measured ignition delay time is often correlated with initial conditions using an Arrhenius-type parametric formula given by

$$\tau = A \exp\left(\frac{E}{RT}\right)[O_2]^x[CH_4]^y \tag{2.1}$$

where τ is the ignition delay time, E is the global activation energy, R is the universal gas constant and T is temperature. The values of A, E, x, and y are obtained by fitting the experimental data using regression methods. Table 2.1 lists some of the coefficient values reported in the literature along with their experimental conditions.

The global activation energy, E, indicates the sensitivity of ignition delay with respect to changing temperature. It can be seen from Table 2.1 that at relatively high temperature, the experimentally obtained value for E is around 50 kcal/mol, while it reduces significantly to less than 20 kcal/mol at temperatures below 1300 K. The reduction in the activation energy with reducing temperature implies that the reactions which are rate-limiting in methane system are different at different temperatures. It also highlights the limitation of the above empirical coefficients, which should not be used beyond the experimental ranges within which they were obtained.

Table 2.1 Experimental conditions and empirical coefficients for methane ignition

Source	P (atm)	T (K)	x	y	A $(s(cm^3/mol)^{x+y})$	E (kcal/mol)
[23]	1.5-4	1300-1900	0.4	-1.6	7.65×10^{-18}	51.4
[24]	2-10	1500-2150	0.33	-1.03	3.62×10^{-14}	46.5
[25]	2-3	1200-2100	0.32	-1.02	2.50×10^{-15}	53.0
[26]	1-3	1600-2200	0.48	-1.94	1.19×10^{-18}	46.3
[27]	1-6	1640-2150	0.33	-1.03	4.40×10^{-15}	52.3
[28]	40-260	>1300	-0.02	-1.20	1.26×10^{-14}	32.7
[28]	40-260	<1300	-0.38	-1.31	4.99×10^{-14}	19.0
[29]	16-40	1200-1300	N/A	N/A	N/A	16
[29]	16-40	1100-1200	N/A	N/A	N/A	13
[29]	16-40	<1100	N/A	N/A	N/A	18

While most of the earlier studies focused on ignition at high temperature and low pressure, ignition delay data at elevated pressures and moderate temperatures have become more available in the literature recently [28-30]. Petersen et al. [28,30] conducted shock tube experiments on ignition of methane/air and methane/oxygen/argon mixtures at pressures from 40 to 260 atm and temperatures from 1040 to 1500 K. The objective of their study was to understand the methane ignition mechanism for ram-propulsion applications so that they covered the equivalence ratios (ϕ) in the fuel-lean ($\phi = 0.4$) and fuel-rich ($\phi > 3.0$) regions. Later, Huang et al. [29] reported shock tube ignition results for undiluted methane/air mixtures at pressures from 16 to 40 bar and temperatures from 1000 to 1350 K. The equivalence ratios ranged from slightly lean ($\phi = 0.7$) to slightly rich ($\phi = 1.3$), which is the range of great interest for internal combustion engine applications. In the above two studies, it was found that the ignition behaviour of methane is more complex at moderate temperature than that at high temperature. The measured ignition delay cannot be well correlated using a single empirical formula. The observed global activation energy decreases initially with reducing temperature, but tends to increase as the temperature drops below 1100 K. This trend is particularly prominent in the stoichiometric and rich mixtures.

Non-Premixed Studies

The autoignition process of non-premixed turbulent methane jet under Diesel-engine-environment has been studied by Sullivan et al. [31,32] in a shock tube facility. Parameters investigated included pre-combustion air temperature (1150-1400 K), fuel injector tip orifice diameter (1.1 and 0.275 mm), fuel injection pressure (60-150 bar), and

fuel injection duration (1.5-3.0 ms). Their results showed that ignition delay shot-to-shot variability at fixed operating conditions is high with coefficient of variation (COV) in the 25% to 30% range. With the small orifice ignition cannot be readily achieved below 1250 K whereas with the large orifice ignition is consistently achieved at 1150 K. They also found that ignition delay decreases significantly with increasing injection pressure ratio and is insensitive to injection duration.

2.3.2 Ignition Chemistry of Methane

Higgin and Williams [33] investigated the ignition of a lean methane/oxygen/argon mixture behind the reflected shock using a 16-step mechanism. The results from their theoretical model agreed reasonably well with their experimental data. Seery and Bowman [23] developed an 18-step reaction mechanism, which was used to study methane/oxygen/argon ignition under temperatures from 1350 to 1900 K and pressures from 1.5 to 4 atm. For mixtures with equivalence ratios between 0.5 and 2, the agreement between their experimental and numerical results is within 30%. In recent years, more complex reaction mechanisms have been developed and used in the studies of methane ignition, as summarized in Table 2.2.

Table 2.2 Mechanisms for methane combustion in the literature

Source	Number of Species	Number of Reactions
Higgin and Williams [33]	10	16
Seery and Bowman [23]	11	18
Frenklach and Bornside [34]	34	140
Li and Williams [35]	45	177
Hughes et al. [36]	37	351
Hunter et al. [37]	40	207
GRI-Mech 1.2 [38]	32	177
GRI-Mech 2.11 [39]	49	279
GRI-Mech 3.0 [40]	53	325
Huang et al. [29]	38	192

Figure 2.6 shows the main reaction paths of methane during the induction period as proposed by Huang et al. [29]. This mechanism was specifically developed for typical engine-relevant conditions, that is, for initial pressures above 16 atm, temperatures below 1400 K, and equivalence ratios from 0.7 to 1.3. Their results showed that for stoichiometric methane/air mixtures at 40 atm and 1250 K, the oxidation is mainly rate-limited by reactions consuming CH_3 radicals. For free radical species, the dots have been omitted for clarity in this thesis.

- 14 -
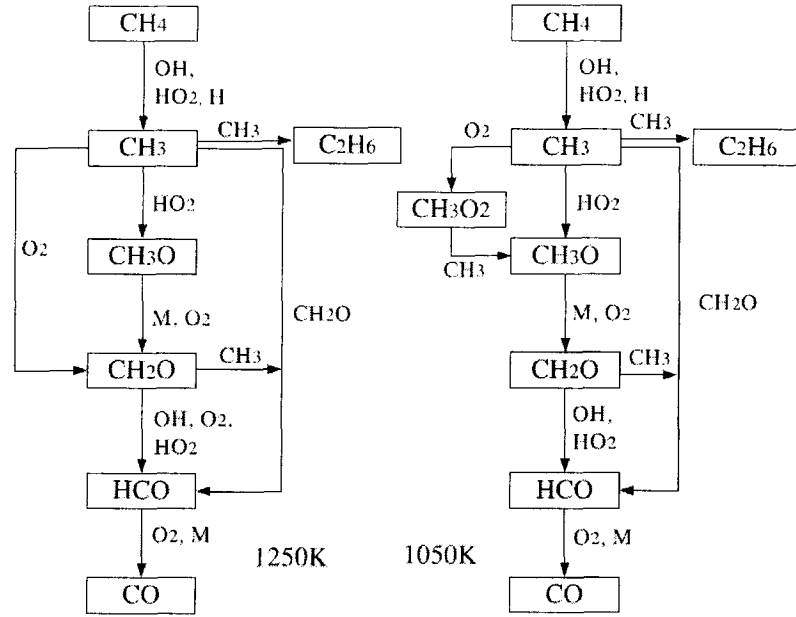
Figure 2.6 Main reaction paths during ignition in a stoichiometric methane/air mixture at 40 bar [29]

The induction period of methane can be divided into three phases [34]. In the initiation phase, methane decomposes into CH_3 and H radicals via reaction

$$CH_4 + M \Leftrightarrow CH_3 + H + M \tag{R1}$$

The H radical is rapidly consumed in the chain branching reactions

$$H + O_2 \Leftrightarrow OH + O \tag{R2}$$

$$O + CH_4 \Leftrightarrow OH + CH_3 \tag{R3}$$

The two OH radicals formed in this process accelerate the decomposition of methane through

$$OH + CH_4 \Leftrightarrow CH_3 + H_2O \tag{R4}$$

In parallel to the above path, OH radicals can be also generated through

$$HO_2 + CH_4 \Leftrightarrow CH_3 + H_2O_2 \tag{R5}$$

$$H_2O_2 + M \Leftrightarrow OH + OH + M \tag{R6}$$

Spadaccini and Colket [41] pointed out that reaction R5 is more important for ignition below 1500 K, where more HO_2 radicals are generated through the reaction between H radical and O_2. Reaction $H + O_2 \Leftrightarrow HO_2$ has a negative activation energy, thus the contribution of

- 15 -

HO_2 becomes more significant at lower temperature. Similar to the effect of H radicals, for each HO_2 radical consumed, two OH radicals are generated in the initiation phase. This makes OH a major radical in the reaction path of methane during the induction period.

The second phase of ignition is characterized by the competition between two CH_3 oxidation reactions

$$CH_3 + O_2 \Leftrightarrow CH_3O + O \tag{R7}$$

$$CH_3 + HO_2 \Leftrightarrow CH_3O + OH \tag{R8}$$

and a chain termination reaction

$$CH_3 + CH_3 \Leftrightarrow C_2H_6 \tag{R9}$$
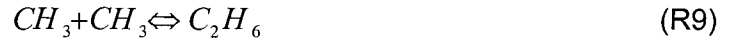
This is the longest phase in the induction period and the ignition delay time is very sensitive to the rates of key reactions in this phase [34]. It is also the phase during which the most significant differences between the high and low temperature ignition mechanisms occur. First, the rate of formation of CH_3O_2 increases for temperatures below 1300 K [28], which opens an extra oxidation path for CH_3 radicals:

$$CH_3 + O_2 \Leftrightarrow CH_3O_2 \tag{R10}$$

$$CH_3O_2 + CH_3 \Leftrightarrow 2CH_3O \tag{R11}$$

Ranzi et al. [42] pointed out that the conversion from CH_3O_2 to CH_3O can also proceed through

$$CH_3O_2 + CH_3O_2 \Leftrightarrow 2CH_3O + O_2 \tag{R12}$$

$$CH_3O_2 + HO_2 \Leftrightarrow CH_3O_2H + O_2 \tag{R13}$$

$$CH_3O_2H \Leftrightarrow CH_3O + OH \tag{R14}$$
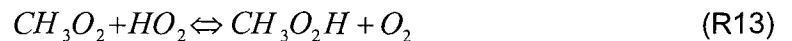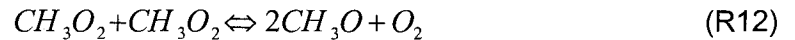
The rising significance of CH_3O_2 chemistry at relatively low temperatures is also indicated by other modelling studies [28,37]. This mechanism explains the observed reduction in the global activation energy with reducing temperature. The sensitivity of the ignition delay time to the formation of ethane in reaction R9 is higher in stoichiometric and rich mixtures compared to that in lean mixtures due to the higher methyl concentration. Consequently, the effect of CH_3O_2 chemistry is more prominent in the stoichiometric and rich regions where a greater reduction of the activation energy has been observed [28,29].

At even lower temperatures (<1100 K), the reduction in the rates of key OH generation reactions such as R6 leads to a depletion of the OH radical, which becomes a new rate-limiting mechanism [29]. The activation energy changes from decreasing to increasing with the switch in the sensitization reactions although the formation rate for CH_3O_2 remains high.

The third phase of ignition is characterized by a rapid increase of radical concentrations accompanying strong thermal feedbacks. The auto-catalytic oxidation [34] proceeds through

$$CH_3O + M \Leftrightarrow CH_2O + H + M \qquad \text{(R15)}$$

$$CH_2O + OH \Leftrightarrow HCO + H_2O \qquad \text{(R16)}$$

$$HCO + M \Leftrightarrow H + CO + M \qquad \text{(R17)}$$

$$HCO + O_2 \Leftrightarrow HO_2 + CO \qquad \text{(R18)}$$

Reactions R17 and R18 restore the concentration of active radicals (i.e., H, HO_2). These two reactions are also highly exothermic, which makes them very effective in bringing the system to ignition.

2.3.3 Ignition Studies of Natural Gas

Premixed Studies

When higher alkanes (ethane, propane, butane, etc.) are added to methane, the ignition characteristics change significantly. In most cases, a sharp reduction of ignition delay was observed with the presence of minor higher alkanes [24,33,34,43-45]. Higgin and Williams [33] observed a reduction of ignition delay by a factor of three when 1% (by volume) of n-butane was added to methane (at an equivalence ratio of 0.5, pressure between 200 and 300 torr and temperature between 1800 and 2500 K). The reduction increases to a factor of ten when 10% n-butane was added.

Spadaccini and Colket [41] reviewed results from 29 shock tube studies with simple hydrocarbon fuels, performing a series of shock tube experiments to determine the ignition delay times for mixtures of methane with ethane, propane or butane, and for a typical natural gas fuel. The experiments were designed to isolate the chemical autoignition delay time from any effects attributed to the fuel/oxidizer mixing processes. Ignition delay experiments were conducted at equivalence ratios of 0.45-1.25 for temperatures 1300-

2000 K and pressures 3-15 atm. The combined data were used to develop general correlations for predicting the ignition delays of binary methane/hydrocarbon mixtures and multicomponent natural gas mixtures in terms of temperature and the initial fuel and oxygen concentrations. For natural gas, the ignition delay was correlated by the empirical expression,

$$\tau = 1.77 \times 10^{-14} \exp(18693/T)[O_2]^{-1.05}[CH_4]^{0.66}[HC]^{-0.39} \qquad (2.2)$$

in which T is the temperature, concentrations are expressed in molecules per cubic cm and the [HC] factor represents the total molar concentration of all non-methane hydrocarbons. One of the limitations of this equation is that it is not applicable to pure methane because of the negative exponent of [HC].

Lifshitz et al. [24] studied the ignition delay of methane/oxygen/argon mixtures enriched by a small fraction of propane and hydrogen using the reflected-shock technique. They suggested that the ignition promoting effect of minor additives can be accounted for using a simple thermal theory, which treats the base fuel and additive as kinetically decoupled. They attributed the reduction in ignition delay time to the increase of temperature caused by the more rapid oxidation of the additive. Crossley et al. [43] examined the thermal theory with shock tube experiments in methane/oxygen/argon mixtures with addition of several higher alkanes (ethane, propane, iso-butane) at temperatures from 1430 to 2000 K. They found significant differences between the predicted ignition delay using the thermal theory and that from the measurements under certain experimental conditions, particularly with a relatively large fraction of higher alkanes. They concluded that the chemical coupling of the oxidation reactions between the base fuel and the additive is an important factor in explaining the reduced ignition delay time.

Zellner et al. [46] investigated the ignition of methane/air mixtures with 10% ethane, propane and n-butane additions. The results showed that these higher alkanes are similarly effective at reducing the ignition delay time of methane. A later study conducted by Eubank et al. [45] for ignition in a 1% methane/99% air mixture enriched with C2-C4 alkanes showed that the effects of the hydrocarbons are cumulative. They suggested that each alkane additive should be considered to characterize the ignition of the fuel mixture. Griffiths et al. [47] conducted a comparison study of the ignition temperature of various methane-based fuels using a spherical reactor. They found that the change of ignition temperature is most sensitive to a hydrocarbon addition below 10% by volume. Beyond this fraction, the incremental sensitivity decreases.

The effect of higher alkane on the ignition delay of methane under engine-relevant conditions has been studied by Huang et al. [48] for temperatures from 900 to 1400 K and pressures from 16 to 40 bar. The results show complex effects of ethane/propane on the ignition of methane, but a common trend observed with both hydrocarbons is an increased promotion effect for temperatures below 1100 K.

Non-Premixed Studies

To understand the bulk behaviour of transient jet combustion, Fraser et al. [49] performed experiments with fuel mixtures, including methane/ethane, injected into a pre-heated, pressurized constant-volume cylindrical vessel. The ignition delay in these experiments was determined from flame luminosity and vessel pressure measurements. Over a wide range of pressures from 5 to 55 bar and temperatures from 600 to 1700 K, they found a strong monotonic decrease in the non-premixed autoignition delay with increasing temperature and only a weak dependency on pressure. Also, the ignition delay time decreases slightly when the ethane concentration is increased.

Following that, Naber et al. [50] performed experiments in a similar, but larger, experimental facility to investigate the effects of natural gas composition on ignition delay over a temperature range of 900 to 1600 K and at a vessel pressure of 68 bar. Four fuel blends were investigated: pure methane, a capacity-weighted mean natural gas, a high-ethane-content natural gas, and a natural gas with added propane typical of peak shaving conditions. They found that the ignition delays are longer for pure methane and become progressively shorter as ethane and propane concentrations are increased. They fitted the experimental results to an empirical relation of the form,

$$\tau = \sqrt{C^2 + \left(Ae^{B/T}\right)^2}$$

(2.3)

where C corresponds to the time take to inject 2.5% of the fuel into the vessel plus the sensor delay time, T is the vessel temperature, and A and B are constants.

In a subsequent research study, Naber et al. [51] extended their observations to more realistic natural gas compositions and a wider range of thermodynamic states. Their results showed that at temperatures less than 1200 K, the ignition delay of natural gas under diesel conditions has a dependence on temperature that is Arrhenius in character and a dependence on pressure that is close to first order. Natural gas composition does not change the nature of the above dependencies but does affect the magnitude of the ignition delay. The measured ignition delays are longest for pure methane and become

progressively shorter as ethane and propane concentrations increase. At higher ambient temperatures (>1300 K), the experimental ignition delays approach a limiting value that is consistent with physical delays associated with the injection system.

2.3.4 Ignition Chemistry of Natural Gas

For methane ignition with higher alkanes, the reduction in ignition delay time is caused by the early generation of radical pools by the more active hydrocarbon additives [45,52,53]. For ignition in methane/ethane mixtures, Westbrook [53] pointed out that H abstractions of ethane and the subsequent decomposition of the resulting ethyl radicals are more efficient in producing hydrogen radicals than methane and methyl. At high temperatures, the extra hydrogen radicals lead to a quick chain initiation via reactions R2, R3 and R4, which accounts for the faster ignition. Frenklach and Bornside [34] studied the ignition delay in 9.5% methane/19% oxygen/71.5% argon mixtures enriched with 0.19 to 1.9% propane using a 140 step reaction mechanism. They attributed the ignition-promoting effectiveness of propane to its rapid decomposition as described by reactions R19 and R20,

$$C_3H_8 \Leftrightarrow CH_3 + C_2H_5 \tag{R19}$$

$$C_2H_5 \Leftrightarrow C_2H_4 + H \tag{R20}$$

An extra H radical is generated in this process that leads to buildup of radical pools in the early phase of ignition.

While the kinetic interaction between higher alkanes and methane during ignition is relatively well established for temperatures above 1400 K, it is less understood at moderate to low temperatures. As introduced above, the sensitization reactions in the pure methane system change with reducing temperature. Similarly, the low-temperature mechanism of methane/hydrocarbon systems is likely to be significantly different from that at high temperatures.

To investigate that, Huang *et al.* [48] studied methane/ethane and methane/propane oxidation at pressures from 16 to 40 bar and temperatures from 900 to 1400 K using reflected-shock technique. Figure 2.7 shows the main reaction path for the ignition process as proposed in their study. The "RO_2, RO_2H path" represents reactions related to the formation and decomposition of $C_2H_5O_2$, $C_2H_5O_2H$, $C_3H_7O_2$, and $C_3H_7O_2H$ radicals. Their analysis showed that the addition of ethane/propane does not change the main reaction path of the methane system. And the promotion of ignition is realized through accelerating the initiation phase in the induction period.

- 20 -
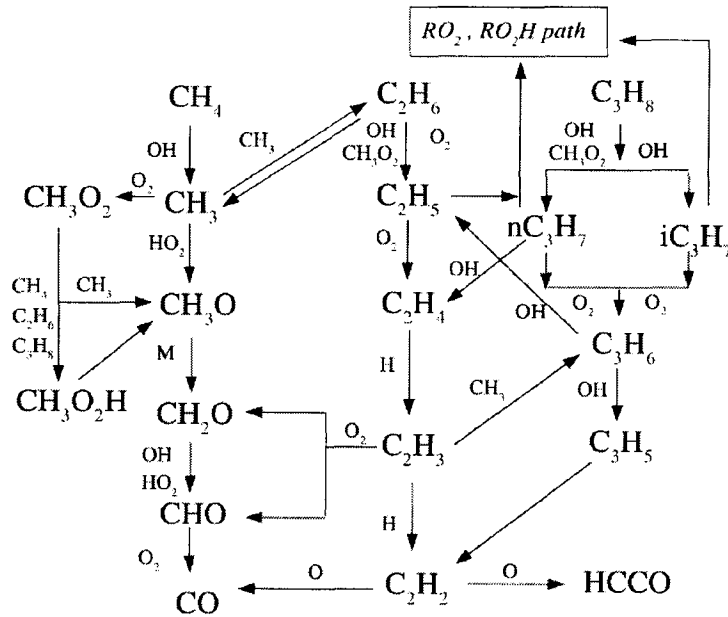
Figure 2.7 Main reaction path of methane oxidation during the induction period with the presence of minor ethane and propane additive [48]

2.3.5 Ignition Studies of Methane with Hydrogen

Premixed Studies

Shock tube studies of high-temperature ignition in methane/hydrogen/oxygen mixtures have been reported by Lifshitz *et al.* [24] as well as by Cheng and Oppenheim [54]. In both cases, the reactants were diluted with 90 percent argon. The data of Lifshitz *et al.* [24] measured at a fixed pressure of 185 torr and covered temperatures from 1600 to 1800 K. A thermal-based-promotion theory was proposed to account for the effects of hydrogen addition. Cheng and Oppenheim [54] conducted experiments for temperatures from 800 to 2000 K and pressures from 1 to 3 atm. They correlated the ignition delay of pure methane, pure hydrogen and their mixtures with the formula

$$\tau = \tau_{CH_4}^{(1-\varepsilon)} \tau_{H_2}^{\varepsilon} \tag{2.4}$$

where ε is the mole fraction of hydrogen in the total fuel and τ_{CH_4} and τ_{H_2} are the ignition delay times of pure methane and pure hydrogen under the same conditions.

Huang *et al.* [55] measured the ignition delay time of two stoichiometric methane/hydrogen/air mixtures in a shock tube facility at pressures from 16 to 40 atm and temperatures from 1000 to 1300 K. It was observed that the promoting effect of hydrogen decreases with decreasing temperature. The difference between pure methane and

- 21 -

methane/hydrogen mixtures is also more prominent at 16 atm than that at 40 atm. A low fraction of hydrogen addition shows only weak effects on the ignition delay of methane under the conditions explored.

Non-Premixed Studies

Fotache *et al.* [56] investigated the ignition delay of hydrogen-enriched methane by heated air using a counter-flow reactor. They identified three ignition regimes depending on the mole fractions of hydrogen. Methane ignition was found to benefit from hydrogen addition mainly due to the kinetic interactions between the two fuels. The modelling study showed that the promoting effect is enhanced by the spatial separation of the branching and termination steps resulting from the high diffusivity of atomic and molecular hydrogen.

The autoignition of transient turbulent hydrogen jets has been investigated by Naber *et al.* [57] in a constant-volume combustion vessel under simulated direct-injection diesel engine conditions. The results showed that the ignition delay of hydrogen has a strong Arrhenius dependence on temperature; however, the dependence on the other parameters examined is small. For gas densities typical of top-dead-centre in diesel engines, ignition delays of less than 1.0 ms are obtained for gas temperatures greater than 1120 K with oxygen concentrations as low as 5% (by volume).

2.3.6 Ignition Chemistry of Methane with Hydrogen

Huang *et al.* [55] studied the ignition of hydrogen-enriched methane under engine-relevant condition using the reflected-shock technique. The reaction process was modeled using a 195 step reaction mechanism containing 40 species. Figure 2.8 shows the main oxidation path during the induction period for the hydrogen/methane mixture as proposed in their study. Their results show that the effect of hydrogen on methane ignition is primarily related to the generation and consumption of H radicals. At high temperatures, the rapid oxidation of hydrogen molecules through

$$OH + H_2 \Leftrightarrow H + H_2O \qquad\qquad \text{(R21)}$$

$$H + O_2 \Leftrightarrow O + OH \qquad\qquad \text{(R22)}$$

are mainly responsible for the stronger ignition promoting effect. The rates of both R21 and R22 decrease rapidly with decreasing temperature. At lower temperatures, reactions between H_2 and CH_3O_2 account for a weak effect of hydrogen on methane ignition due to the production of extra H radicals.

$$H_2 \qquad\qquad CH_4$$

$$\text{OH} \bigg| CH_3 \qquad\qquad \text{OH} \bigg|$$
$$CH_3O\downarrow$$

$$\text{---}H \qquad CH_3O_2 \xleftarrow{\;O_2\;} CH_3 \xrightarrow{\;CH_3\;} C_2H_6$$

$$O_2 \bigg| \qquad\qquad\qquad HO_2 \bigg|$$

$$CH_3 \;\downarrow \qquad\qquad CH_3$$
$$\xleftarrow{\;} HO_2 \qquad CH_4 \Big|\xrightarrow{\;} CH_3O \overset{H_2}{\underset{\text{OH}}{\rightleftharpoons}} CH_3OH$$
$$HO_2 \bigg| \qquad H_2 \bigg| \qquad M \bigg| \qquad\qquad \bigg| \text{OH}$$

$$H_2O_2 \qquad CH_3O_2H \quad CH_2O \xleftarrow{\;O_2\;} CH_2OH$$
$$H_2O_2 \bigg| \qquad\qquad \text{OH} \bigg|$$
$$\qquad\qquad\qquad CH_3 \bigg|$$

$$\text{OH} \qquad\qquad\qquad \overset{H}{CHO}$$
$$CH_4 \bigg| \qquad\qquad\qquad O_2 \bigg|$$
$$H_2 \;\downarrow$$

$$H_2O \qquad\qquad\qquad CO$$
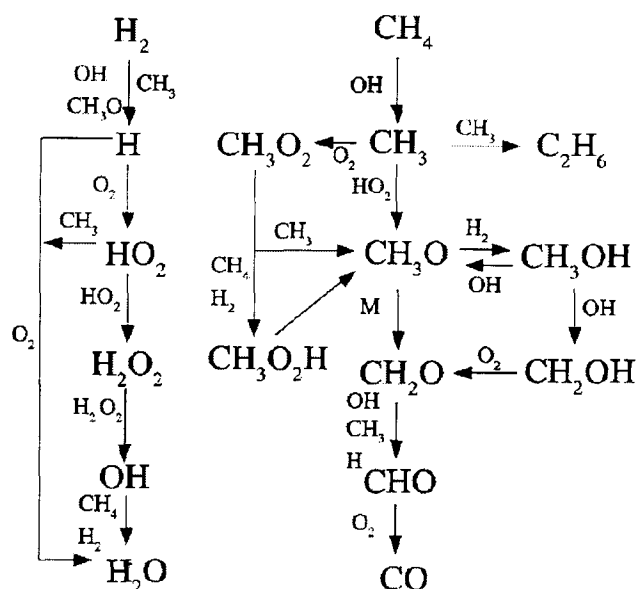
Figure 2.8 Main oxidation path during the induction period for CH$_4$/H$_2$ mixture [55]

2.4 Non-Premixed Gaseous Combustion

Compared with the autoignition of a premixed charge, the autoignition of a non-premixed flame in a turbulent flow is more complex, since it typifies the fundamental interaction between chemical reactions, molecular and thermal diffusion, and turbulent transport. Various numerical techniques have been applied to elucidate details of the non-premixed autoignition process itself, e.g. 2-D direct numerical simulation (DNS) of fuel/oxidizer slabs [58-60], conditional moment closure (CMC) and $k - \varepsilon$ modelling of a turbulent jet [61], and multiple representative interactive flamelet (RIF) modelling of a turbulent jet [62]. Some interesting common features that are observed in these studies include: (1) ignition sites are localized in zones that are characterized by a specific value of the mixture fraction (corresponding to the maximum value of reactivity in the mixture) while also having the lowest value in the domain of the scalar dissipation rate (which minimizes the heat losses); (2) the most reactive mixture fraction occurs on the lean side of the stoichiometric composition due to the beneficial effect of the higher oxidizer temperature; (3) ignition sites are typically located along the sides of a fuel jet in the slightly lean mixture between the fuel and air region; (4) autoignition delay times in the turbulent flows are longer than the ignition delay times of stagnant homogeneous mixtures. These numerical simulations have raised important questions about the local nature of the autoignition process. However, how closely these results apply to non-premixed turbulent gaseous jet remains an open question.

2.4.1 Combustion Structure

Once gaseous fuel is injected into the oxidizer, the gas jet is then carried away from the fuel injector by its own momentum. Hill and Ouellette [63] have proposed scaling laws for such type of transient axisymmetric gas jets. This development was based on dimensional analysis of the jet tip penetration length (z_t) as a function of the exit momentum flux ($\dot{M}_n$), jet density at the nozzle exit (ρ_n), ambient density (ρ_a), exit velocity (U_n), and nozzle diameter (d). Two relations were derived depending on whether the jet and ambient gas densities are equal or not, and both made use of a dimensionless constant: the penetration number, Γ. The derived relations for equal and different densities, respectively, are reproduced below:

$$\frac{z_t}{(\dot{M}_n/\rho_a)^{1/4} t^{1/2}} = \Gamma \tag{2.5}$$

$$\frac{z_t}{d\sqrt{\dfrac{\rho_n}{\rho_a}}} = \Gamma \left(\frac{\pi}{4}\right)^{1/4} \left(\frac{t U_n}{d\sqrt{\dfrac{\rho_n}{\rho_a}}}\right)^{1/2} \tag{2.6}$$

These results may be solved analytically if one assumes a transient jet of the Turner [64] variety. This model treats the transient jet as a transient vortex ball in front of a steady-state jet, and in conjunction with the well-known mass entrainment results of Ricou and Spalding [65] can be used to derive analytical equations for the vortex ball's and jet's momentum. Substituting the penetration number equations into these momentum equations yields an analytical penetration number solution [63]. Additionally, since the jet momentum, density, and penetration length in time are experimentally measurable, the penetration number may also be calculated from experimental data.

The momentum of the injected fluid provides the principal impetus for the jet propagation. Momentum transfer to the head from the jet increases the size of the head, and the corresponding diameter of the jet, as it extends. Prior to ignition, oxidizer will be mixing into the jet, with a general distribution from nearly pure fuel at the core of the jet to a steadily weaker mixture at the jet perimeter. Turbulent mixing will result in spatial and temporal non-uniformity in the mixture fraction around the jet. The total mass in the jet,

$\dot{m}(x)$, including both fuel and entrained oxidizer, at a given downstream distance x is given by [63]:

$$\dot{m}(x) = \dot{m}_o K_s \frac{x}{d} \tag{2.7}$$

where $\dot{m}_o$ is the mass rate of injected fuel, K_s is a constant (0.32) and d is the diameter of the nozzle.

Following injection, the gaseous fuel may be initiated by autoignition or by an ignition source such as a pilot flame, spark plug, or hot surface. Immediately following ignition, the premixed fuel at the jet periphery is consumed in the form of an edge flame [66]. Afterwards, the combustion process settles into the form of a diffusion flame. Fuel from the core of this combusting fuel jet diffuses to the periphery and oxidizer from the surroundings diffuses into the core; thus, the combustion process will occur in a reaction zone surrounding the jet, where the local air-fuel ratio is near-stoichiometric [67]. Note that near the nozzle exit, a high local strain rate is induced by the high relative velocity between the oxidizer and injected fuel, preventing fuel from igniting and combusting in this region. Because of this, the flame may be observed to recede from the injector nozzle [68] and appear "lifted". Immediately downstream of this lifted region, combustion occurs in the form of a triple flame (rather than a diffusion flame). A triple flame is a rich premixed flame (due to air entrainment in the lifted section) in the center of the jet that is immediately surrounded by a diffusion flame and further surrounded by a lean premixed flame on the outside [69]. Downstream of this triple flame region is where the main diffusion combustion occurs.

At the end of injection, as the injector needle closes, the rate at which fuel is added, and its corresponding momentum transfer, to the jet diminishes rapidly. Effectively, the separated jet now acts as a 'puff' jet [63]. Mixing of the tail end of the jet with oxidizer results in combustion spreading around the fuel cloud, which continues to mix and burn as its momentum carries it away from the nozzle. The combustion process will end when either there is insufficient fuel to sustain the reactions, insufficient oxidizer or when the temperature of the reactants is lowered enough (due to the arrival of the rarefaction wave at the test section in the case of shock tube) that the reactions are no longer self-sustaining.

2.4.2 NOx Emissions

NOx emissions are the main pollutant emissions from the combustion process. Severe environmental and health issues can be caused by an elevated level of NOx in the atmosphere. NOx emissions are critical components of photochemical smog. They can cause damage to the mechanisms that protect the human respiratory tract and increase a person's susceptibility to, and the severity of, respiratory infections and asthma. Long-term exposure to high levels of NOx can cause chronic lung disease. Because internal combustion engines and gas turbines are a significant source of NOx emissions, stringent regulations have been imposed by government agencies worldwide to control NOx emissions from these devices. Consequently, the formation of NOx and its reduction have become and remain to be a major focus of combustion studies by researchers from both industry and academia.

NO and NO_2 are the main nitrogen oxides generated in internal combustion engines. The mechanisms by which NOx are formed are well understood [70,71]. The primary mechanism for NO formation is the thermal (Zeldovich) mechanism [71], which is highly dependent on temperature due to the high activation energy of its rate-limiting step. The thermal mechanism is also slow, such that not only high temperatures, but a long residence time at those temperatures is required to reach equilibrium. Due to the turbulent mixing between burned gases and cool unburned charge which typically occurs in diesel engines, the thermal mechanism does not normally reach equilibrium conditions. However, it is still the dominant formation mechanism under most conditions.

Other NO formation mechanisms include the prompt and nitrous oxide routes [71]. The prompt mechanism results in the immediate formation of NO within the flame zone, unlike the thermal mechanism which, due to its low initial rate, does not contribute significantly to flame-front NO. This prompt mechanism involves the reaction of the CH radical with a nitrogen molecule to form a series of intermediate species which may eventually form NO. The controlling factor of this reaction is the CH radical, which is highly reactive and is typically found only within the flame region. The nitrous oxide (N_2O) route involves the reaction of N_2 with an oxygen radical and a third body to form N_2O ($N_2 + O + M \rightarrow N_2O + M$). The N_2O will then react with another oxygen atom to form two NO molecules. This reaction is limited by the oxygen radical concentration. Typically, it is only significant between 1000 and 2000 K, where there is a non-negligible quantity of O but where the thermal mechanism rate is very slow.

A fourth source of NO that is discussed in the literature [71] is the fuel-bound NO route. This mechanism is most significant for fuels where significant quantities of atomic nitrogen are chemically bound in the fuel, such as coal or ammonia. Although natural gas may contain significant quantities of nitrogen, it is typically as molecular nitrogen and hence participates in the NO forming reactions similarly to the nitrogen in the oxidizer.

Not all the NO produced in the combustion will be emitted, as some will decompose later in the process. One proposed mechanism for this is a reaction with the HCCO radical, which reacts with NO to form HCN and CO_2 [72]. In a non-premixed flame, the HCCO radical is present in significant quantities within the flame zone. Some of the NO in the burned gases will be removed when the burned gases pass through the reaction zone again. Another route proposed for NO decomposition in diesel engines is the reverse of the thermal and prompt mechanisms [73,74]. Independent of which mechanism is dominant, a small but significant quantity of the NO contained in the oxidizer will be decomposed in the combustion reaction when using recirculated exhaust gases [73,74]. How much of the species formed in the decomposition then recombine to form NO is unclear.

2.5 Laser Induced Fluorescence

Laser induced fluorescence (LIF) is a well-established technique for detecting the population densities of molecular or atomic species in specific quantum states. In combustion applications this information can be used to determine relevant quantities such as mole fractions, density, temperature, and velocity [75-77].

LIF is the spontaneous isotropic light emission of molecules that have been selectively driven onto an excited electronic state by tuned laser excitation (optical pumping), then relax to their ground state. The fluorescence power is then directly proportional to the excited state population through the Einstein probability coefficient A for spontaneous emission. In hot reacting media, collisions and chemical reactions can also populate excited states, but the excited populations and the subsequent emissions induced by these processes are much lower than those induced by laser pumping.

Absorption of the laser photons by molecules is directly responsible for the population of the excited state in the laser field. Besides relaxation by spontaneous emission of fluorescence at rate A, other depopulation processes such as stimulated emission, collisional quenching, energy transfers or predissociations (at global rate Q in a simplified two-level schema) are competitively involved in the interaction. The dynamics of the population transfer must be carefully examined to obtain the concentration of

investigated species in the excited state as a function of its global concentration. Then it is made possible to derive that global concentration from the measured intensity of the laser induced fluorescence emission.

Following paragraphs will emphasize the simple regimes for which the fluorescence emission is locally proportional to the laser irradiance and to the molecular population in its lower state. Different calibration procedures may be used to determine the proportionality coefficient in order to derive absolute concentration data from measured fluorescence intensity.

2.5.1 Principle of Laser Induced Fluorescence

Initial theoretical work on fluorescence was carried out by Piepmeier [78] to describe the molecular dynamics of fluorescence experiments of atomic species seeded into analyzer flames. This was achieved with a rate equation analysis of an ideal two level system by assuming that the populations of these levels reach a steady state. The following sections are a brief account of the rate equation analysis.

In the two-level model of fluorescence, one considers only two molecular quantum states that are directly populated or depopulated through interaction with the laser light. Transfer of energy resulting in the population of neighbouring quantum states is neglected. The energy transitions and the transfer mechanisms that are considered in this model are summarized in Figure 2.9.

Upper Level
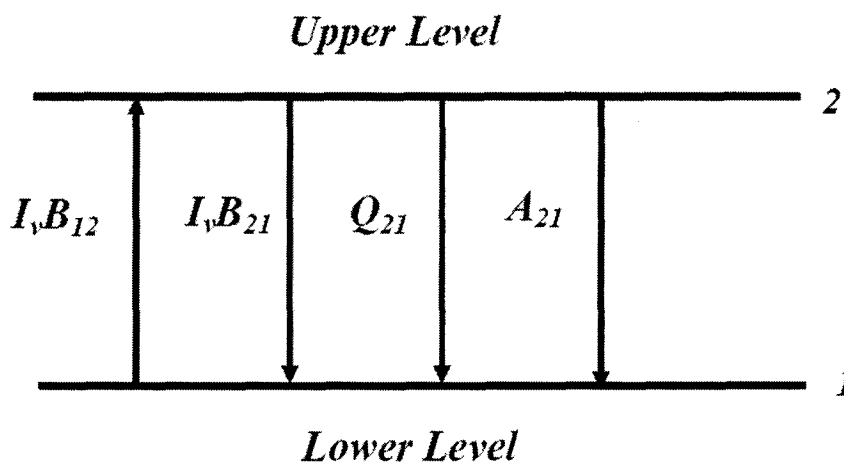
Figure 2.9 Schematic diagram of two-level model of induced fluorescence

In this model, each mechanism is represented by a rate (s^{-1}) and a direction. The rates of stimulated emission and absorption of photons resulting from laser interaction are designated by $I_\nu B_{21}$ and $I_\nu B_{12}$, respectively, where I_ν is the laser spectral intensity [J/(cm^2 s Hz)] and B_{21} and B_{12} are the Einstein B coefficients for the transition (cm^2 Hz/J). Spontaneous light emission from the upper energy level is described by the Einstein A coefficient A_{21} (s^{-1}), and the collision quenching rate from the upper level to lower level is denoted by the term Q_{21} (s^{-1}). The laser spectral bandwidth is assumed to be larger than the molecular absorption linewidth so that there is a complete overlap, rendering the details of the absorption lineshape irrelevant. In stead of resolving the temporal dynamics of the excitation process, an average intensity can be used:

$$I_\nu = \frac{1}{\tau} \int_0^\tau I_\nu(t)dt \qquad (2.8)$$

where τ is the laser pulse duration. In typical flame environments, the upper-state lifetime is on the order of 10^{-9} s whereas the laser duration is about 10^{-8} s, and in this case one can also use average population densities,

$$N_2 = \frac{1}{\tau} \int_0^\tau N_2(t)dt \qquad (2.9)$$

Stimulated emission from molecules transitioning from the upper level to the lower level possesses the same momentum and phase as the incident laser radiation. Spontaneous emission, however, has random momentum and phase and is emitted into 4π steradians (a sphere). It is portion of this radiation that is collected and constitutes the fluorescence signal. The fluorescence signal can be described by the equation:

$$S_t = \tau\eta \frac{\Omega}{4\pi} N_2 A_{21} V \qquad (2.10)$$

where η is the efficiency of the collection optics, which collect photons through a solid angle Ω; N_2 represents the number density of molecules in the upper state due to laser excitation; and V is the collection volume imaged onto one detector pixel. The collection volume is defined by the thickness of the laser sheet multiplied by the area of the sheet imaged onto a single pixel.

The rate equation describing the population in the upper state may be written as:

$$\frac{dN_2}{dt} = N_1 I_v B_{12} - N_2 (I_v B_{21} + Q_{21} + A_{21})$$

(2.11)

The first term on the right represents the rate of population transfer from the lower state to the upper state due to stimulated absorption, and the remaining terms represent depopulating mechanisms; stimulated emission, collisional quenching, and spontaneous emission, respectively. In situations where the duration of the laser pulse is long compared with the quenching time of collision, it may be assumed that the system reaches a steady state; thus Equation 2.11 becomes:

$$N_1 I_v B_{12} = N_2 (I_v B_{21} + Q_{21} + A_{21})$$

(2.12)

In flames where the temperature seldom exceeds 3000 K, the upper energy level state is initially empty. The steady state populations then satisfy the constraint:

$$N_1 + N_2 = N_1^0$$

(2.13)

where N_1^0 is the initial population in the lower state. Substituting Equation 2.12 into Equation 2.13 and introducing the result into Equation 2.10 leads to:

$$S_f = \tau \eta \frac{\Omega}{4\pi} V N_1^0 \frac{I_v B_{12} A_{21}}{I_v (B_{12} + B_{21}) + Q_{21} + A_{21}}$$

(2.14)

The initial population of the lower level is related to the total number density N_t of the species being probed by the Boltzmann fraction f_B, so that Equation 2.14 becomes:

$$S_f = \tau \eta \frac{\Omega}{4\pi} V f_B N_t \frac{I_v B_{12} A_{21}}{I_v (B_{12} + B_{21}) + Q_{21} + A_{21}}$$

(2.15)

This is the basic fluorescence equation, which may be used to relate the measured fluorescence signal to the total number density N_t. A particularly simple form is obtained for weak excitation (i.e., when $I_v (B_{12} + B_{21}) \ll Q_{21} + A_{21}$). In this limit,

$$S_f = \tau \eta \frac{\Omega}{4\pi} V f_B N_t \frac{I_v B_{12} A_{21}}{Q_{21} + A_{21}}$$

(2.16)

Since the quenching is much larger than the spontaneous emission probability ($Q_{21} >> A_{21}$)

$$S_f = \eta \frac{\Omega}{4\pi} V f_B \frac{A_{21}}{Q_{21}} B_{12} E_v N_t \qquad (2.17)$$

where τI_v is replaced by E_v, the laser spectral fluence [J(cm^2 Hz)].

The two-level model as presented above is quite appealing because it is simple; however, it does not account for many physical processes that are potentially important in laser induced fluorescence measurements. In particular, the model neglects the presence of other molecular energy levels that may play a role in the energy transfer processes. This aspect is described in refined theories that take into account energy transfer between the level being directly populated by the laser excitation and nearby rotational and vibrational energy levels. Under certain experimental conditions these additional levels must be included, especially when the laser intensity is great and the weak excitation limit is no longer valid.

2.5.2 LIF Calibration

In the regime of linear laser excitation, the quasi-steady state fluorescence signal is proportional to laser power and to the local population of investigated molecule in the laser sheet. But it is also inversely proportional to the local rate of electronic quenching which has to be known as a function of different collision partners. Thus calibrations are required to investigate the local influence of this quenching on the concentration measurement. The quenching rate can be calculated in various flames using available data for the specific quenching cross sections and weighting by the local mole fractions of these different collision partners [79,80]. Another approach is to perform direct determination of the local effective quenching rate in low pressure premixed flames by measuring the decay rate of the time resolved fluorescence signals.

However, in a more practical way, a calibration of LIF signal is usually performed under well-known conditions in well-described flames like the McKenna burner, where the absolute concentration of the investigated molecule can be calculated [81] or can be measured by another technique such as line of sight absorption spectroscopy [82].

2.6 Turbulent Reacting Flow Modelling

One fundamental issue in turbulent reacting flow modelling is to properly represent the effect of turbulent fluctuations on chemical reaction rates. For most practical turbulent flow problems, direct numerical simulations (DNS) that fully resolve the smallest turbulent scales are still beyond the reach of the current computational resources. In practice, the mean or filtered values of the flow field are often obtained by solving the Reynolds-averaged or spatially-filtered Navier-Stokes equations as in Reynolds-Averaged Navier-Stokes (RANS) models and Large Eddy Simulation (LES). The effect of unresolved fluctuations on the mean flow field is often accounted for through turbulent viscosity models. For a turbulent reacting flow, the mean value of the chemical source term is required to close the conservation equations. However, as illustrated by Warnatz [124], the averaged chemical reaction rate is strongly affected by the details of the fluctuations in the flow field, and thus cannot be computed from the mean values directly. That is, in a turbulent reacting flow

$$\bar{\omega}\left(p(x,t),T(x,t),Y(x,t)\right) \neq \omega(\bar{p},\bar{T},\bar{Y}) \tag{2.18}$$

where $\bar{\omega}$ is the mean reaction rate, p is pressure, T is temperature, Y is the mass fraction of species. One fundamental approach to address the closure problem in the chemical source term is to calculate the mean value from a statistical description of the reacting system using the probability density function (PDF). If the PDF of the turbulent flow field is known, the mean reaction rate can be integrated from the conditional reaction rates weighted by their local PDFs, i.e.:

$$\bar{\omega} = \int \dots \iiint \omega(p,T,Y)P(v,\tau,T,Y;x,t)dv_x dv_y dv_z dTdY_1 \dots dY_n \tag{2.19}$$

where τ is a characteristic time scale of turbulence, v is the velocity vector, and P is the probability density function. The probability density function is typically assumed to be a joint PDF of velocity, turbulent frequency, and thermo-chemical composition [83]. A model transport equation is solved, typically by a Lagrangian particle method, to obtain the instantaneous value of the joint PDF [83]. The merit of PDF method is that the effect of turbulent convection on non-linear chemical reaction is captured exactly. The PDF method has been successfully applied to model various turbulent combusting flows [84,85,86]. Nevertheless, as implied by Equation 2.19, the PDF-transport equation is a high-dimensional equation; numerical approaches used to solve the joint PDF, such as Monte-

Carlo methods or hybrid methods, are very time-consuming even for systems with a relatively small number of species [124].

A significant simplification of the PDF-transport equation can be achieved if the PDF is assumed to take on the form of a generic function (e.g. a β function or a clipped Gaussian), which is fully determined by a limited number of parameters, such as the mean and variance. In that case, the PDF can be constructed based on a conserved scalar whose mean and variance can be obtained by solving transport equations. Ideally, such a conserved scalar should have some physical meaning that is related to the fluctuation in the reaction rates. For non-premixed or partially premixed combustion problems, the mixture fraction (Z) is often used as such a scalar. One definition of mixture fraction is

$$Z = \frac{Y_i - Y_{i,1}}{Y_{i,2} - Y_{i,1}}$$

(2.20)

where Y_i denotes the mass fraction of element i in the mixture; $Y_{i,1}$ denotes the mass fraction of i in stream 1; $Y_{i,2}$ denotes the mass fraction of i in stream 2. Mixture fraction is a measure of the element mass fraction, which originates from the fuel (or oxidizer) stream. If all the species are assumed to have the same diffusivity, the mixing process can be characterized using the mixture fraction alone. For each mixture fraction with given density or pressure, there is a defined equilibrium state subject to the boundary conditions. If further assumptions are made that the thermal diffusivity is identical to the species diffusivity (unity Lewis number) and the chemical time scale is significantly shorter than the physical time scale (fast chemistry), all the scalar variables in a turbulent combustion problem become a known function of mixture fraction [124].

Unfortunately, due to the large separation of chemical time scales, the fast chemistry assumption is not valid in many combustion systems. Various finite-rate turbulent combustion models have been developed to address the non-equilibrium effects. In the following sections, the Laminar Flamelet model, Conditional Moment Closure, and the Conditional Source-term Estimation method are introduced. All three models are based on the two-parameter representation of the PDF of mixture fraction using its mean and the variance. Subsequently, the Trajectory Generated Low-Dimensional Manifold method for the reduction of detailed chemistry in combustion modelling will also be discussed.

2.6.1 Laminar Flamelet Model

The fundamental assumption of the laminar flamelet model is that the reacting interface of a non-premixed turbulent flame can be viewed as an ensemble of locally laminar diffusion flamelets. The model formulation was formally introduced by Peters [87], who performed a Crocco-type coordinate transformation to the conservation equations of species and enthalpy using the following rules

$$\frac{\partial}{\partial t} = \frac{\partial}{\partial \tau} + \frac{\partial Z}{\partial t}\frac{\partial}{\partial Z}$$ (2.21)

$$\frac{\partial}{\partial x_1} = \frac{\partial Z}{\partial x_1}\frac{\partial}{\partial Z}$$ (2.22)

$$\frac{\partial}{\partial x_i} = \frac{\partial}{\partial Z_i} + \frac{\partial Z}{\partial x_i}\frac{\partial}{\partial Z} \quad (i = 2,3)$$ (2.23)

where t denotes time; x_1, x_2, x_3 denote the spatial coordinates; Z denotes a new coordinate normal to the stoichiometric surface of the mixing field; Z_i $(i=2,3)$ are the two other components of the transformed spatial coordinates; τ is the transformed time coordinate given by $\tau = t$.

A schematic of the original and transformed spatial coordinates is given in Figure 2.10. The function of this transformation is to move the coordinates from an Eulerian frame to a Lagrangian frame attached to the flame front. The transformed conservation equations are written as

$$\rho\frac{\partial Y_i}{\partial \tau} = \rho D \frac{\partial Z}{\partial x_j}\frac{\partial Z}{\partial x_j}\frac{\partial^2 Y_i}{\partial Z^2} + \dot{\omega}_i - R(Y_i)$$ (2.24)

$$\rho\frac{\partial T}{\partial \tau} = \rho D \frac{\partial Z}{\partial x_j}\frac{\partial Z}{\partial x_j}\frac{\partial^2 T}{\partial Z^2} + \sum_{i=1}^{n}\frac{h_i}{c_p}\dot{\omega}_i - R(T)$$ (2.25)

where D is the mass/thermal diffusivity (assuming that all the species have the same diffusivity and the Lewis number is unity); $\dot{\omega}_i$ is the mass production rate of species i; h_i is the enthalpy of species i; and c_p is the mixture-averaged specific heat. The radiation and pressure fluctuation terms in the energy equation have been omitted. The operators $R(Y_i)$ and $R(T)$ contain the derivatives of Y_i and T with respect to Z_2 and Z_3; they are

considered as being of lower order compared with the first term on the RHS of Equation 2.24 and 2.25, and are neglected in the final form of the flamelet equations [87], giving:

$$\rho \frac{\partial Y_i}{\partial \tau} = \rho D \frac{\partial Z}{\partial x_j} \frac{\partial Z}{\partial x_j} \frac{\partial^2 Y_i}{\partial Z^2} + \dot{\omega}_i \qquad (2.26)$$

$$\rho \frac{\partial T}{\partial \tau} = \rho D \frac{\partial Z}{\partial x_j} \frac{\partial Z}{\partial x_j} \frac{\partial^2 T}{\partial Z^2} + \sum_{i=1}^{n} \frac{h_i}{c_p} \dot{\omega}_i \qquad (2.27)$$
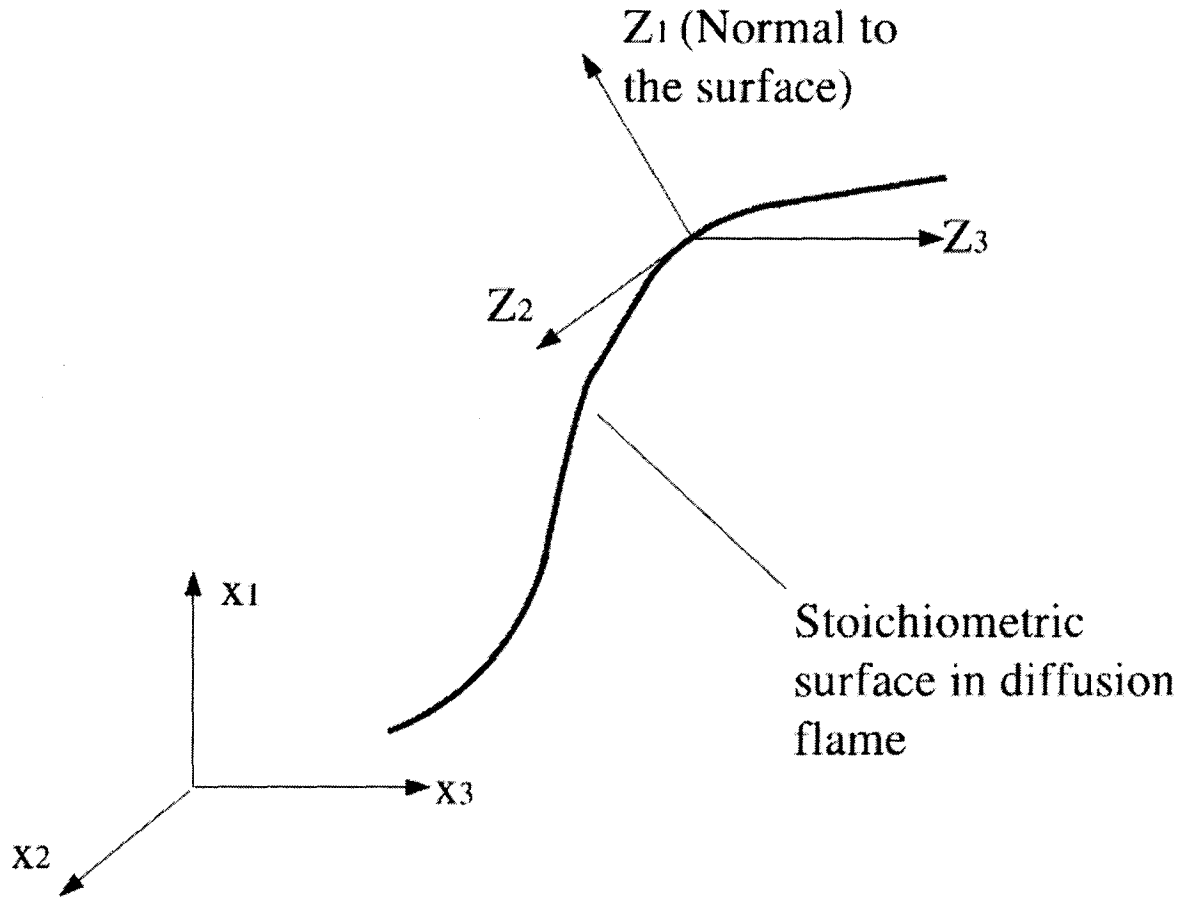
Figure 2.10 Coordinate transformation in laminar flamelet model

The above transformation and assumptions yield a one-dimensional flamelet equation which is normal to the stoichiometric surface. The instantaneous scalar dissipation rate, which is defined by

$$\chi = 2D \frac{\partial Z}{\partial x_j} \frac{\partial Z}{\partial x_j} \qquad (2.28)$$

describes the non-equilibrium effect in diffusion flames. A higher value of χ leads to a more rapid removal of species and heat from the flame; at a certain critical value, χ_q, where the chemical reaction cannot sustain the heat loss due to turbulent mixing, a quenching of the flame occurs. In turbulent flame calculations, it is preferable to represent the profile of χ with a single parameter. Following Law and Chung [88], Peters [87] proposed using the scalar dissipation at the stoichiometric surface, i.e. $\chi_{st} = \chi(Z_{st})$ as the representative parameter. Assuming flamelets of the mixing-layer type are predominant in turbulent diffusion flames, Peters chose to use the counter-flow geometry to describe the Z dependence of the χ profile. From the analytical solution, it can be shown that

$$\chi(Z) = \frac{a}{\pi} \exp\{-2[erfc^{-1}(2Z)]^2\} \qquad (2.29)$$

where $erfc^{-1}$ is the inverse of the complementary error function. The functional dependence of $\chi(Z)$ on χ_{st} can be derived from Equation 2.29

$$\chi(Z) = \chi_{st} f(Z) / f(Z_{st}), \qquad (2.30)$$

where $\chi(Z)$ is the exponential term in Equation 2.29. In RANS turbulence models, the mean value of scalar dissipation can be related to turbulent fluctuations through [87,89]

$$\tilde{\chi} = c_x \frac{\tilde{\varepsilon}}{\tilde{k}} \widetilde{Z''^2} \qquad (2.31)$$

where $\tilde{\varepsilon}$ is the Favre (or density-weighted) averaged dissipation rate of turbulent kinetic energy, defined as $\tilde{\varepsilon} \equiv \overline{\rho \varepsilon} / \overline{\rho}$; $\tilde{k}$ is the Favre averaged turbulent kinetic energy; $\widetilde{Z''^2}$ is the Favre variance of the mixture fraction where $Z'' = Z - \tilde{Z}$; c_x is a scaling coefficient with a standard value of 2.0 [89]. The representative parameter, χ_{st}, in Equation 2.30 is often

equated to its Favre-average, which can be calculated from the integral

$$\chi_{st} = \widetilde{\chi_{st}} = \frac{\bar{\chi} f(Z_{st})}{\int_0^1 f(Z) P(Z)\, dZ} \tag{2.32}$$

Once the χ profile in the flow field is solved, the mean value of a species mass fraction can be computed from the joint PDF of Z and χ

$$\widetilde{Y}_i = \int_0^\infty \int_0^1 Y_i(Z, \chi) P(Z, \chi)\, dZ d\chi \tag{2.33}$$

Further simplification can be achieved if Z and χ are assumed to be statistically independent. In that case, Equation 2.33 is reduced to

$$\widetilde{Y}_i = \int_0^\infty \int_0^1 Y_i(Z, \chi) P(Z) P(\chi)\, dZ d\chi \tag{2.34}$$

In the most direct implementation of the laminar flamelet model, the steady-state flamelet equations with various profiles of the scalar dissipation are solved numerically. The solutions are then tabulated to form a flamelet library with Z and χ as the table dimensions. The mean mass fractions can then be obtained by solving the conservation equations of various moments of Z and χ, and substituting the resulting PDF and conditional reaction rates from the pre-computed flamelet library into Equation 2.34.

The steady-state flamelet model relaxes the fast chemistry assumption significantly. However, experimental and theoretical studies have shown that the flame cannot respond instantaneously to changes in scalar dissipation [90-92]. Hence, steady-state flamelets are not suitable for modelling processes where the chemical time scale is comparable to or longer than the flow time scale. To address this issue, various unsteady flamelet models have been developed and tested with different levels of success.

Coelho and Peters [93] studied a piloted methane/air diffusion flame using an Eulerian particle flamelet model. The unsteady calculations were performed in the post-processing stage by transporting fluid particles that trace the temporal evolution of the scalar dissipation rate and solve the unsteady flamelet equation with the varying χ value. The results showed an improvement in the predicted species concentration profile compared with the steady-state model. A similar approach, called the representative interactive flamelet model (RIF) proposed by Barths et al. [94], solves the unsteady flamelet equations interactively with the solution of the flow field. This method has been

implemented in simulating combustion and pollutant formation in diesel engines [94-97] where the transient process dominates. Rao and Rutland [98] proposed a flamelet time scale model, which features lower computational cost compared with the RIF model. The model is based on a first-order expansion of the steady-state flamelet solution. A chemical time scale determined from the Jacobian matrix is used to compute the rate of change of species mass fraction from the steady-state solution.

Although the laminar flamelet model and its various derivatives are being used extensively in modelling turbulent combustion, it is important to realize their inherent limitations. The underlying assumption of flamelet models is that the turbulent flame is an ensemble of laminar flamelets. For this assumption to be valid, the structure of the flame front must remain locally laminar. In other words, the thickness of the flame must be thinner than the smallest length scale of turbulence – the Kolmogorov length scale. It is now generally accepted that the flamelet assumption is only valid in the region of large turbulent Damköhler number, D_a, which is defined by

$$D_a = \frac{\tau_p}{\tau_L} = \frac{l_p / v'}{l_L / v_L} \tag{2.35}$$

where τ_p is the macroscopic time scale of the flow field; τ_L is the characteristic time scale of the laminar flame; l_p is the largest turbulent eddy length scale; v' is the turbulence intensity ; l_L is the laminar flame thickness, and v_L is the laminar burning velocity. When the physical time scale approaches the chemical time scale, or the value of D_a is small, the suitability of the flamelet assumption becomes questionable [99,124].

2.6.2 Conditional Moment Closure

Conditional moment closure (CMC), which was proposed independently by Klimenko [100] and Bilger [101,102], is described in detail in a joint review [103]. Although the final forms of the CMC equations are unified, the mathematical methods and model assumptions adopted by Klimenko and Bilger in their derivations are quite different. Klimenko started his derivation from the transport equation of a two-dimensional joint PDF, $P(y)$:

$$\frac{\partial \langle \rho | y \rangle P}{\partial t} + div(\langle \rho v | y \rangle P) + \frac{\partial^2}{\partial y_i \partial y_j}(\langle \rho D(\nabla Y_i \cdot \nabla Y_j) | y \rangle P) \qquad (2.36)$$

$$= -\frac{\partial}{\partial y_1}(\langle W_1 \rho | y \rangle P)$$

where y is the sample space variable for Y; W_1 is the chemical source term; the expression $\langle a | c \rangle$ is short for $\langle a | b = c \rangle$ which is the conditional expectation of a conditioned on the variable b being equal to c. Equation 2.36 is multiplied by y and integrated over all y to get

$$\frac{\partial \langle \rho | \eta \rangle \langle Y | \eta \rangle P(\eta)}{\partial t} + div(\langle \rho | \eta \rangle \langle vY | \eta \rangle P(\eta)) \qquad (2.37)$$

$$= \langle \rho | \eta \rangle \langle W | \eta \rangle P(\eta) + \frac{\partial J_Y}{\partial \eta}$$

where

$$J_Y \equiv 2 \langle \rho | \eta \rangle \langle D(\nabla Y \cdot \nabla \xi) | \eta \rangle P(\eta) - \frac{\partial \langle \rho | \eta \rangle \langle \frac{\chi}{2} Y | \eta \rangle P(\eta)}{\partial \eta} \qquad (2.38)$$

Here η is the sample space variable for Z. Closure of the last term on the RHS, J_Y, which is the reaction scalar flux in conserved scalar space, was achieved through a diffusion approximation with the form

$$J_Y = A \langle Y | \eta \rangle + B \frac{\partial \langle Y | \eta \rangle}{\partial \eta} \qquad (2.39)$$

Here A and B are the drift coefficient and diffusion turbulent coefficient respectively. This closure assumption leads to the final form of the basic CMC equation which governs the evolution of the conditional values of reaction scalars;

$$\frac{\partial \langle Y | \eta \rangle}{\partial t} + \langle v | \eta \rangle \cdot \nabla \langle Y | \eta \rangle + \frac{div(\langle \rho | \eta \rangle \langle v''Y'' | \eta \rangle P(\eta))}{P(\eta) \langle \rho | \eta \rangle} \qquad (2.40)$$

$$- \langle N | \eta \rangle \frac{\partial^2 \langle Y | \eta \rangle}{\partial \eta^2} = \langle W | \eta \rangle$$

where $v'' \equiv v - \langle v | \eta \rangle$ is the velocity fluctuation about the conditional mean; similarly, Y'' is

the fluctuation of species mass fraction. The physical meaning of the second and third terms on the LHS of Equation 2.40 are the convection of the conditional value of the reaction scalar; the forth term on the LHS represents the effect of turbulent diffusion on the conditional expectation; the term on the RHS is the conditional source term.

In Bilger's derivation of the CMC equation [101,102], the conditional value of the reaction scalar is decomposed into its mean and fluctuation, which are substituted into the transport equation. After taking the conditional average, the equation becomes

$$\langle \rho \mid \eta \rangle \frac{\partial \langle Y \mid \eta \rangle}{\partial t} + \langle \rho \mid \eta \rangle \langle v \mid \eta \rangle \cdot \nabla \langle Y \mid \eta \rangle + \langle \rho \mid \eta \rangle \langle \frac{\chi}{2} \mid \eta \rangle \frac{\partial^2 \langle Y \mid \eta \rangle}{\partial \eta^2} \tag{2.41}$$

$$= \langle \rho \mid \eta \rangle \langle W \mid \eta \rangle + e_Q + e_Y$$

with

$$e_Q \equiv \langle div(\rho D \nabla \langle Y \mid \eta \rangle) + \rho D \nabla \xi \cdot \nabla \frac{\partial \langle Y \mid \eta \rangle}{\partial \eta} \mid \eta \rangle \tag{2.42}$$

$$e_Y \equiv -\langle \rho \frac{\partial Y''}{\partial t} + \rho v \cdot \nabla Y'' - div(D \rho \nabla Y'') \mid \eta \rangle \tag{2.43}$$

For large Reynolds numbers, the value of e_Q is small and can be neglected. The unconditional average of e_Y can be calculated from the integral equation

$$\int e_Y P(\eta) d\eta = -\int div(\langle \rho \mid \eta \rangle \langle v'' Y'' \mid \eta \rangle P(\eta)) d\eta \tag{2.44}$$

Closure for the unclosed term e_Y is realized through the assumption

$$e_Y P(\eta) d\eta = -div(\langle \rho \mid \eta \rangle \langle v'' Y'' \mid \eta \rangle P(\eta)) d\eta \tag{2.45}$$

which leads to the same CMC equation as Equation 2.40. The closure of the conditional source term in the CMC equation is usually achieved by neglecting the effect of the conditional fluctuations, i.e.:

$$\langle W_i(Y,h) \mid \eta \rangle \approx W_i(\langle Y \mid \eta \rangle, \langle h \mid \eta \rangle) \tag{2.46}$$

A close examination of Equation 2.40 shows that the conditional expectation of the reactive scalar is transported in a four-dimensional space: three spatial coordinates and one conditional variable (i.e. the mixture fraction). Thus the computational cost for solving the CMC equation for a complex flow is likely to be substantial.

A further simplification of Equation 2.40 can be obtained by assuming homogeneous turbulence with uniform and constant density. In that case, the basic equation reduces to

$$\frac{\partial \langle Y | \eta \rangle}{\partial t} - \langle \frac{\chi}{2} | \eta \rangle \frac{\partial^2 \langle Y | \eta \rangle}{\partial \eta^2} = \langle W | \eta \rangle \tag{2.47}$$

It is interesting to note that this form of the CMC equation closely resembles the unsteady flamelet equation discussed in the previous section; however, the subtle difference between the two models must be emphasized. The fundamental assumption of the flamelet model constrains its application in the flamelet regime, while the model assumption of CMC is more general. It is also possible to achieve closure using higher moments with CMC, thus the method has the potential to describe flames with significant conditional fluctuations (such as occur during quenching and reignition) with higher accuracy.

The CMC assumptions about conditional means are consistent with the experimental data [104]. The CMC model has been applied with considerable success in predicting reactive scalars (species mass fraction and temperature) in attached jet flames [105-108], lifted flames [109] and bluff-body flames [110,111]. It was also used in predicting soot formation in a turbulent methane/air reacting jet [112]. More recently, second-order closure methods have been developed and implemented to improve the performance of CMC in predicting jet flames [113], especially regions with significant local extinction and reignition [114].

2.6.3 Conditional Source-term Estimation

The Conditional Source-term Estimation (CSE) method [115] seeks closure of the chemical source term using the conditional average of the reaction scalars in a manner which is essentially identical to the first-order CMC. The conditional values, however, are not obtained by solving a transport equation such as that in Equation 2.40. Based on the *a priori* knowledge from DNS calculations that the conditional averages of scalars do not vary rapidly in space, Bushe and Steiner [115] proposed a method to obtain the conditional averages of the reactive scalars through inverting an integral equation using the unconditional averages of an ensemble of discrete points in a computational domain. Mathematically, the unconditional mean at any spatial location x and time t is:

$$\langle Y(x,t) \rangle = \int_0^1 P(x,t;\eta) \langle Y(x,t) | \eta \rangle d\eta \tag{2.48}$$

For a selected spatial ensemble of N points, the CSE method assumes that the conditional average is uniform within the ensemble:

$$\langle Y^n(x,t) \mid \eta \rangle = \langle Y \mid \eta \rangle_{A,t} \tag{2.49}$$

where the superscript n is the nth point in the ensemble, and the subscript A denotes the ensemble. This leads to a discrete set of N integrals:

$$\langle Y^n(x,t) \rangle = \int_0^1 P(x,t;\eta)\langle Y \mid \eta \rangle_{A,t}\, d\eta \tag{2.50}$$

Equation 2.50 can be approximated using a numerical quadrature with M quadrature points ($M < N$),

$$\langle Y^n(x,t) \rangle = \sum_{m=1}^{M} P(x,t;\eta)\langle Y \mid \eta_m \rangle_{A,t}\, \delta\eta_m \tag{2.51}$$

where $n = 1...N$. The least-squares solution of the conditional averages of interested scalars can be computed by inverting Equation 2.51.

The CSE method was initially implemented in a large eddy simulation of a piloted methane/air diffusion flame with encouraging success in predicting the experimental measurements [116]. Later, the concept of CSE was tested in conjunction with the unsteady laminar flamelet model, in which the conditional averages of reaction scalars are calculated using a linear combination of flamelet solutions [117]. The appropriate weighting factors for the flamelet solutions are determined by inverting the integral equation of the unconditional mean temperature field. The method was then used in the context of a RANS model to study turbulent methane jet ignition with some success [118,119].

In order to address the issue of ill-posedness in Equation 2.51, as well as to provide temporal continuity in the solution, Grout *et al.* [119] proposed a regularization method for the inverting process. The modified equation system for solving conditional scalars is:

$$\min\{\|\Omega\langle Y \mid \eta \rangle\|^t - \langle Y \rangle^t \| + \lambda \|\langle Y \mid \eta \rangle^t - \langle Y \mid \eta \rangle^{t-\Delta t} \|\} \tag{2.52}$$

where Ω is the original coefficient matrix for the discrete integral equations; the superscripts t and $t - \Delta t$ are the times at which the scalars are evaluated; λ is a weighting coefficient specified by the modeler. In Grout's [119] implementation, λ was chosen to add just enough *a priori* information to produce a well-behaved solution. The regularization term $\lambda \|\langle Y \mid \eta \rangle^t - \langle Y \mid \eta \rangle^{t-\Delta t} \|$ limits the change of conditional average

between two consecutive time steps and acts to stabilize the solution.

Huang *et al.* [120] further improved the regularization method by including spatial continuity for the conditional scalar field. In his implementation, the incremental limiter, $\|\langle Y | \eta \rangle^{t} - \langle Y | \eta \rangle^{t-\Delta t}\|$ in Equation 2.52 was replaced by $\|\langle Y | \eta \rangle^{t} - \langle Y^{*} | \eta \rangle^{t}\|$ where $\langle Y^{*} | \eta \rangle^{t}$ was calculated from:

$$\frac{\langle Y^{*} | \eta \rangle^{t} - \langle Y | \eta \rangle^{t-\Delta t}}{\Delta t} \approx -\frac{\partial \overline{\rho} \langle u_{i} | \eta \rangle \langle Y | \eta \rangle^{t-\Delta t}}{\partial x_{i}} \qquad (2.53)$$

Since both experiments and simulations have shown that for steady, axisymmetric jet flames, the cross-stream variations of conditional means are not significant [115,121,122], the convection of the conditional means in Equation 2.53 was only considered in the axial direction of the jet. The conditional mean velocity at the axial location x, $\langle u_{x} | \eta \rangle$, was approximated by cross-stream averaging along the isopleths:

$$\langle u_{x} | \eta \rangle \approx \frac{\int_{0}^{R} \langle u(x,r) \rangle P(\eta; x,r) dr}{\int_{0}^{R} P(\eta; x,r) dr} \qquad (2.54)$$

where R denotes the radius of the jet.

A main advantage of the CSE method is that the computational cost is substantially lower than that of CMC. Meanwhile, it does not involve constraining assumptions such as those employed by the laminar flamelet model, and is thus applicable to a wide range of turbulent non-premixed flames.

2.6.4 Reduction of Detailed Chemistry

Combustion simulations incorporating detailed chemical kinetic mechanisms are being increasingly used in studying reacting flow problems. A detailed chemical kinetic mechanism for a combustion process typically involves tens or even hundreds of reactive scalars with hundreds or thousands of chemical reactions, each with their own different time scales, which give rise to stiffness in the governing ordinary differential equations (ODEs). To solve such a stiff system of ODEs is very time-consuming since the smallest time scale must be resolved for the numerical solution to be stable [123,124]. Therefore, there is clearly a need to reduce the dimensionality and the stiffness in the detailed chemistry to reduce the computational time for combustion simulations.

Manifold methods for reducing detailed chemistry are based on the separation of chemical time scales associated with different reaction scalars. If the time scale separation

is large enough, fast processes with short time scales approach a quasi-steady state rapidly; these can be decoupled from slow processes to reduce the total dimensionality of the reacting system. The remaining low-dimensional manifold can be used to approximate the detailed chemistry with a high degree of accuracy. For a two-dimensional manifold, for example, the instantaneous rates of reaction scalars Y can be obtained from the manifold using the formula:

$$\frac{dY}{dt} = \frac{\partial Y(u,v)}{\partial u}\frac{\partial u}{\partial t} + \frac{\partial Y(u,v)}{\partial v}\frac{\partial v}{\partial t} \tag{2.55}$$

where u and v are progress variables used to parameterize the manifold. Maas and Pope [125] proposed a mathematical model for computing the Intrinsic Low-Dimensional Manifold (ILDM) by minimizing the reaction vector projected into the fast subspace, which is defined by eigenvectors associated with large negative eigenvalues of the Jacobian matrix. The manifold generated by this method is somewhat optimal globally; however, the implementation of the method is very involved.

To simplify the construction of the manifold, Pope and Maas [126] proposed the Trajectory Generated Low-Dimensional Manifold (TGLDM) method, in which the manifold is generated along reaction trajectories. The boundary formed by the initial states of the trajectories, which is called the manifold generator, can be obtained using the extreme-value-of-major-species method [126] to achieve a maximum overlap between the TGLDM and ILDM. Huang *et al.* [120] modified the TGLDM method by first suggesting that trajectories be initialized using a constrained equilibrium composition along the boundaries of the realizable space.

The parameterization of the TGLDM can be realized using the normalized trajectory length and the initial locations of the trajectory with respect to some reference. However, in locations where the reaction trajectories bunch, the projecting matrix which maps the perturbation from physical space to the manifold space becomes nearly singular. To avoid this problem, two reaction scalars, such as Y_{co_2} and Y_{H_2O}, can be used as progress variables for the manifold without parameterization. The projected TGLDM in the $Y_{co_2} - Y_{H_2O}$ plane can then be triangulated using the Delaunay method [127] to form an unstructured mesh. The interior point search and interpolation on the manifold surface can then be implemented based on the instantaneous value of Y_{co_2} and Y_{H_2O} [120].

2.7 Summary

This chapter has reviewed experimental and kinetic studies on natural gas combustion. The effect of higher alkanes and hydrogen on methane ignition has been discussed. The need for reliable experimental data on non-premixed natural gas combustion under engine-relevant conditions has been established. The main structure of non-premixed gaseous combustion and NOx formation mechanisms in hydrocarbon flames have been discussed. The basic principle of laser induced fluorescence has been introduced. Finally, three popular methods for closing the chemical source term in turbulent combustion modelling using two-parameter representation of the PDF of reactive scalar, and a mathematical model for reducing detailed chemistry have been discussed.

Chapter 3
Ignition Measurements of Jets of Methane with Additives

3.1 Introduction

Heavy-duty engine manufacturers are developing advanced in-cylinder and post-exhaust aftertreatment devices to ensure that diesel engines meet stringent new emission standards. However, reducing the in-cylinder formation of these species, as well as any attempt to reduce carbon dioxide (CO_2) emissions, is limited by the fundamental properties of the liquid diesel fuel. Replacing the fuel with natural gas offers the potential to achieve substantial pollutant emission reductions, while making use of a widely-available and competitively priced alternative fuel. Most current in-use natural gas fuelled engines use premixed charge spark-ignition technology, which suffers from reduced efficiency and high emissions of unburned methane. New technologies that retain the diesel engine's direct-injection, compression-ignition combustion process are under development. However, further understanding of the fundamentals of the high-pressure, turbulent, non-premixed natural gas combustion process is required to optimize the combustion system.

One of the barriers facing wide-spread use of natural gas in transportation applications is variations in the fuel composition. Levels of heavy hydrocarbons (ethane, propane, etc.) and of diluents vary with the fuel source, time of year, and the requirements of the gas supplier. Unconventional gases, such as synthetic natural gas, may contain substantially larger quantities of these species [128]. The addition of some species to the fuel may also be useful in enhancing ignition or reducing formation of certain pollutants.

3.2 Previous Work

3.2.1 Methane/Ethane Combustion

Ethane is a major non-methane alkane often present in natural gas. In combustion studies, ethane together with propane is often added to methane to represent typical natural gas [129]. The variation of ethane concentration in natural gas can significantly change the ignition characteristics of the base fuel, which is particularly relevant to the performance of homogeneous charge compression ignition (HCCI) engines [130,131] as well as to forced-ignition natural-gas engines and gas turbines in the sense of controlling autoignition [132,133].

Previous researchers have conducted a large number of experimental and numerical studies to understand the ignition behavior in methane/ethane mixture [24,37, 41,43,52,53,134-136]. However, most of these studies, particularly the experimental ones, were focused on premixed combustion. Our knowledge of natural gas ignition in a turbulent non-premixed flame under conditions relevant to practical combustion devices (such as internal combustion engines or gas turbines) is still insufficient.

In an effort to study the autoignition process of non-premixed turbulent gaseous jets under Diesel-engine-environment, as well as the influence of key operating parameters on emissions, Sullivan *et al.* [31,32] conducted shock tube experiments with pure methane and 90.1% methane/9.9% ethane blend at engine-relevant conditions. The autoignition and combustion process were recorded by a high speed CMOS camera. Their results showed that for pure methane, the normalized ignition kernel location relative to the equivalent orifice diameter is in the range of 25 to 65, and it is not significantly influenced by either injection pressure ratio or injection duration. The downstream location of the ignition kernel relative to the jet penetration distance is typically in the range of 0.4 to 0.8. NOx emissions are relatively insensitive to injection pressure ratio and injection duration. With 9.9% ethane addition to the methane fuel, the normalized ignition kernel location relative to the equivalent orifice diameter decreases about 20% on average, and NOx emissions increase by a factor of about 2. High run-to-run variability in autoignition and emissions was observed for both fuels.

It should be noted that the majority of the results reported by Sullivan *et al.* [31,32] refer to the autoignition of pure methane fuel. Experiments with a methane/ethane blend form only a limited subset of these results. Significantly, the methane/ethane experiments were not conducted under the same experimental conditions as was the case for the pure methane. Thus, it is not clear whether the reported differences in behavior were caused by ethane addition, or different operating conditions.

3.2.2 Hydrogen-Enriched Methane Combustion

Both natural gas and hydrogen have benefits and drawbacks as mobile vehicle fuels. In an internal combustion engine, natural gas provides excellent anti-knock properties, but suffers from low flame propagation rates and high auto-ignition temperatures. Hydrogen's low ignition energy results in a stronger tendency to knock compared to natural gas, limiting the compression ratio (and hence maximum theoretical efficiency) for homogeneous-charge hydrogen engines. When added to the air upstream of

the intake port, hydrogen's low volumetric energy density also reduces the energy content of a given volume of inducted charge [137]. However, hydrogen does have a higher flame speed than natural gas, and it is easier to ignite. This suggests that a combination of these two fuels could be a superior vehicle fuel than either individually. While hydrogen production and onboard storage are issues that have yet to be overcome, a relatively small amount of hydrogen, potentially derived from renewable sources and blended with compressed natural gas, could provide substantial benefits with little modification to an engine system developed for natural gas fuelling.

A significant amount of research has been conducted investigating methane/hydrogen blend combustion; however, few studies were identified which investigate the non-premixed combustion of methane/hydrogen blends.

Fundamental premixed studies have indicated that the preferential diffusion of hydrogen in a turbulent combustion event results in a higher flame propagation rate, even when the laminar flame speed is constant [138]. The flame's greater resistance to stretch results in fewer local extinction events, reducing CO and hydrocarbon (tHC) [139]. The presence of hydrogen in the lean premixed flame was found to increase the concentration of H, OH, and O radicals [139]. It has been suggested that the presence of more OH may contribute to the more rapid oxidation of the methane, and that using 20% hydrogen in methane can increase peak OH radical concentrations by as much as 20% [140,141].

Non-premixed combustion of methane/hydrogen blends has not been studied as extensively. In a low-pressure, low-temperature co-flow burner experiment, Karbasi and Wierzba [142] found that flame stability is enhanced by hydrogen addition to either the fuel or the oxidizer. This was attributed to higher flame speeds and improved mixing. Differences in fuel-stream density with hydrogen addition were found to be secondary [143]. The higher diffusivity of the hydrogen was found to increase flame thickness under partially-premixed conditions [144]. In industrial gas turbines and boilers, hydrogen addition was found to enhance prompt NO formation (due to high H and OH radical concentrations) while flame stability was improved [145]. In a non-premixed counter-flow methane/heated air jet experiment, the concentration of hydrogen in the methane was found to influence the ignition mechanism. At concentrations below 30% by volume, methane ignition is reported to be enhanced by the presence of H radicals, but the process is still essentially methane ignition. Above 30%, hydrogen ignition dominated the process, with ignition delays independent of the relative methane/hydrogen concentration [146].

The concept of using hydrogen as an additive to improve the combustion rate in spark-ignition engines was first suggested for conventional gasoline fuelling [147,148]. Several more recent studies have investigated the effects of blending natural gas and hydrogen for use in homogenous charge, spark-ignition engines [149-154]. These results have shown varying positive and negative results. The most important influence of hydrogen addition is under lean premixed conditions, where the lean limit is substantially extended [149,150,153]. This has been attributed to an enhanced combustion rate and shorter ignition delay [150,155]. For a given air-fuel ratio (including both stoichiometric and lean operation), NOx emissions are higher with hydrogen addition, due to the higher flame temperature, while CO and HC emissions are reduced [150,153]. These effects become more significant as the lean limit is approached. However, because of hydrogen's ability to extend the lean limit, lower NOx emissions are achieved by running at leaner air-fuel ratios with hydrogen addition [153]. Flame stability in the presence of EGR is also improved at all air-fuel ratios [152]. The effects of hydrogen addition on efficiency appear to depend on operating condition, with some studies indicating improved efficiency [156], and others reporting reduced efficiency [154].

The fraction of hydrogen in the fuel (typically reported on a per-volume percentage) varied between the different studies. Typically, values of 15-20% were found to achieve substantial improvements without impairing knock resistance [151,152]. Above 30%, substantial reductions in the charge energy density, coupled with higher potential for knock, were found to be substantial handicaps with little benefit in emissions or stability [154]. The lower energy density of the gaseous charge can be overcome through turbocharging: however, this further increases the chance of knock at high hydrogen concentrations [151].

3.2.3 Fuel Dilution with Nitrogen

Diluting the fuel with an inert species should reduce the combustion temperature, thereby reducing the formation rate of NO through the thermal (Zeldovich) mechanism. This is a technique similar to the use of exhaust gas recirculation (EGR), which has been shown to achieve very low NO emissions, at the expense of reduced efficiency and high emissions of HC, CO, and PM [157].

The effect of diluting a gaseous fuel with nitrogen has been investigated in various contexts. For a natural gas premixed charge engine, Nellen and Boulouchos [158] reported that by adding up to 14% nitrogen in the fuel, knock resistance is improved but efficiency is impaired at a constant fuel-air stoichiometry. Crookes *et al.* [159] reported similar results,

and suggest that the effects are essentially identical to increasing the EGR fraction. For the same total fuel energy content in a premixed charge system, diluting the fuel or the oxidizer has essentially the same effect of displacing oxygen from the total charge.

For non-premixed combustion, the effects of fuel dilution could vary substantially from those of oxidizer dilution. Oxidizer dilution has been studied extensively, either through the use of EGR or through nitrogen dilution of the charge [160]. Fuel dilution has not been as extensively investigated; Feese and Turns [161] reported that there is some evidence that in industrial boilers (low pressure non-premixed turbulent combustion), fuel dilution reduces NO_x emissions more effectively than does oxidizer dilution. This is attributed to enhanced mixing rates and reduced residence time in the burned gases before mixing quenches the NO_x reactions. The study suggests that the reaction-zone chemistry is insensitive to the source of the diluent. This study also indicated that, for fuel dilution levels in excess of 20%, in-flame soot formation is no longer discernable.

The use of nitrogen as a diluent in fundamental non-premixed combustion studies is relatively common, primarily as a technique to reduce fuel concentrations. For a non-premixed opposed flow diffusion flame [162], no significant effects are observed until the fuel stream contains >80% nitrogen (by volume). Above 80% nitrogen, the temperature required for ignition increases, due to the increased heat capacity of the fuel; this is generally similar to the influences of increased energy dissipation through higher turbulent strain rates. Gulder *et al.* [163] reported that in a co-flow laminar flame the soot volume fraction is reduced proportionally with the reduction in methane concentration. The authors attributed this directly to fuel dilution; they did not identify any effect of the nitrogen on soot formation or oxidation kinetics. These results indicate that the principal influence of nitrogen addition manifests itself by reducing the energy density of the fuel. There is no evidence of direct effects on the reaction kinetics, even at very high nitrogen concentrations.

One of the principal effects of nitrogen addition to the gaseous jet is reducing the energy density of the injected gas, resulting in a longer injection duration to provide the same amount of available chemical energy. For a transient jet, increasing the total injected mass significantly increases the total kinetic energy transfer to the combustion chamber gases. Changing the density of the injected fuel will also influence the penetration distance and turbulent mixing of the gaseous jet. However, no studies in the literature were found that attempt to evaluate the influence of nitrogen content on a high-pressure turbulent non-premixed jet.

- 50 -

3.3 Experimental Methods

A shock tube facility was chosen for this study in preference to a research engine in order to isolate the influence of certain operating parameters and to enable the direct measurement of run-to-run variability in ignition delays and emissions. Jet-jet, jet-wall, and jet-flow field interactions and unsteady geometry associated with actual engine operation are avoided in this setup so that key operating parameters may be isolated on a shot-by-shot basis. Extension of the shock tube results to a specific working engine requires some further testing, but the hope is that dominant features will generally be applicable to more complex working environments.

3.3.1 Shock Tube Setup

A schematic of the shock tube used in this study is shown in Figure 3.1. The stainless steel shock tube is 7.90 m long, with a 3.11 m driver section and a 4.79 m driven section, and an inside diameter of 5.9 cm. The optical section contains three 1.5 cm x 20 cm quartz optical windows. Four flush-mounted PCB Piezotronics 112B11 dynamic pressure transducers are used to measure the incident shock velocity. An AutoTran 860 vacuum sensor is used for preparing driven gas compositions and measuring initial driven gas pressure, and an Eclipse high-pressure sensor is used for measuring the driver gas pressure.
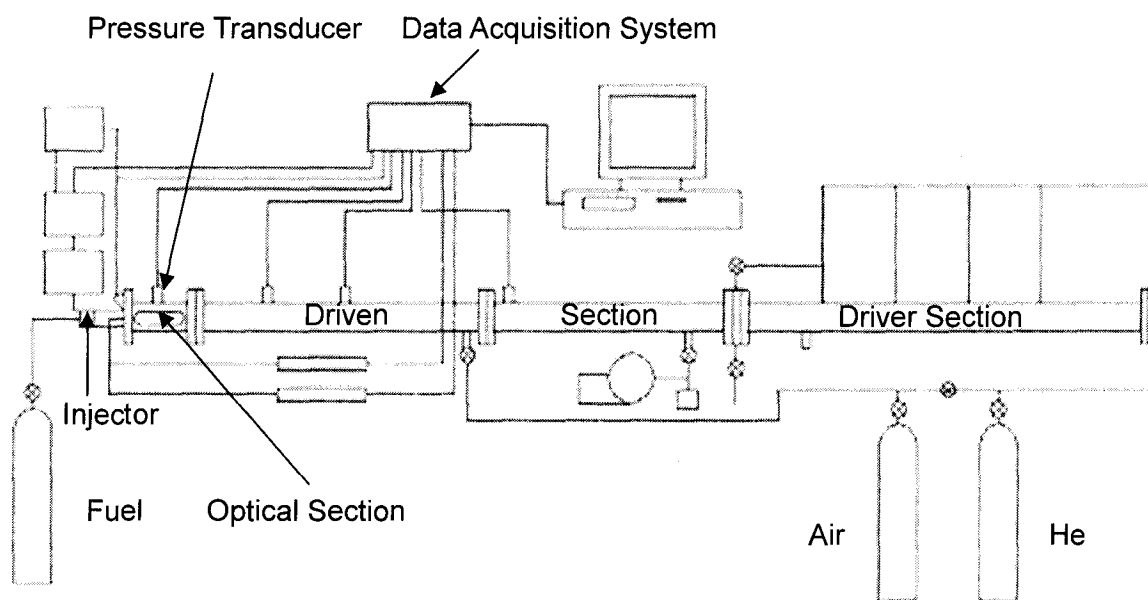
Figure 3.1 Schematics of the shock tube and attached equipment

A double-diaphragm technique was used to guarantee the rupture of diaphragms at the desired pressure ratio. Prior to each experiment, barometric pressure was recorded and the driven section gas pressure transducer was calibrated using a zero and span calibration corresponding to vacuum and atmospheric pressure. Both driven and driver sections of the shock tube were subsequently evacuated along with the tubing connecting the fuel injector, injector charging solenoid, and manual shutoff valve. The driven section was filled with air (Praxair medical grade) to the desired initial pressure and the driver section gas composition prepared manometrically with a mixture of helium (Praxair 99.9% purity) and air (Praxair medical grade). The data acquisition system (IOtech Wavebook/512) was armed, the injection delay and duration were set through Westport's WCut software and the delay between the solenoid for draining the intermediate chamber pressure in the double diaphragm system and the injector-charging solenoid was set. Finally, the intermediate chamber pressure was vented, initiating the rupture of the diaphragms, and generating the desired incident shock wave. The data acquisition system and the injector were triggered by the rising edge of the incident shock wave as it passed the piezoelectric pressure transducer closest to the shock tube endplate.

In order to ensure a quiescent, constant pressure region behind the reflected shock wave, the specific heat ratio of the driver gas was carefully tuned. This was performed by blending air and He to yield a tailored interface between the driven and driver gases upon shock reflection from the endplate. A tailored interface is one where the pressure on either side of the contact surface is equal after the reflected shock passes through the interface (from driven to driver gas), ensuring that the contact surface remains stationary and maximizing the experimental time. If the shock velocity across the interface is not equal, the driver gas pressure will be greater than the driven gas pressure, or vice versa, after the reflected shock passes through the interface, and the interface is said to be under-tailored or over-tailored, respectively. An under-tailored interface causes the test pressure to rise steadily as the contact surface encroaches into the driven section gas, while an over-tailored interface causes the experimental pressure to decrease due to the contact surface moving away from the experimental section. Both cases are undesirable, and thus by altering the composition (He fraction) of the driver gas, its specific heat ratio is tailored to tune the speed of sound across the contact surface and thus ensure that the pressure difference across the interface is zero. In this study, through careful tailoring effective run-time of 4-5 ms was achieved with nearly constant post-reflected shock pressure and temperature conditions prior to combustion.

Incident shock velocities were calculated from the pressure traces from each of the four monitored dynamic pressure transducers by measuring the time interval between rising edges as the shock passed each successive transducer location. Using the measured incident shock velocity and initial driven gas properties, the temperature and pressure immediately behind the reflected shock were determined by solving 1-D conservation equations for mass, momentum, and energy across the shock and assuming perfect gas behavior while allowing for temperature dependent heat capacities. The uncertainty in the temperature and pressure calculated in this way was estimated to be about 1-2% [29] and 3-4% [22], respectively.

Fuels studied included methane (99.97% purity), 90.0% methane/10.0% ethane, 80.3% methane/19.7% hydrogen, and 80.0% methane/20.0% nitrogen. For experiments with methane, methane/ethane, and methane/nitrogen, an electronically controlled prototype injector (J43) originally developed for a direct injection engine application by Westport Innovations was used. Since the magnetostrictive material in this injector is not compatible with hydrogen, a modified version of the injector (J43P2) with a piezoelectric actuator was used for the methane/hydrogen experiments. Both injectors share the same injector tip, with one central hole of 0.275 mm diameter. In the experiment, the injector was mounted at the center of the shock tube endplate. This enabled the injection of gaseous fuel down the centerline of the shock tube. The injection timing and duration were controlled using a customized controller. Timing was synchronized to start injection between 100 and 800 ms after shock reflection from the endplate.

3.3.2 Flame Luminosity Imaging

A high frame rate CMOS-based digital camera was used to measure natural flame luminosity and blackbody radiation from any particles in the shock tube. The trigger signal for the data acquisition system and the injector was also used to trigger the camera. The fuel jet flame was imaged through a 1.5 cm x 20 cm quartz optical access window. A Vision Research Phantom v7.1 CMOS based camera equipped with a 50mm F/1.2 Nikon lens was used to image natural flame and particle luminosity for this study. The camera was operated at a frame rate of approximately 31,000 frames/second with an effective integration time of 2 µs per frame. An aspect ratio of 80 pixels x 800 pixels was used to match the aspect ratio of the optical access window, which resulted in a nominal imaging resolution of 0.2 mm x 0.2 mm per pixel. The pixel sensitivity was approximately flat for light wavelengths from 400 nm to 700 nm with relatively sharp roll-offs at 400 and 800 nm.

Light imaged in these experiments was depth of field integrated. The lens F# used in these experiments was fixed at 2. 12-bit data was stored from each experiment in on-board camera memory and then transferred to a local PC for subsequent processing post-experiment.

In this study, an ignition kernel was defined as the emergence of a non-contiguous new flame region not generated by the propagation of an existing flame. In all experiments, small contamination from dust or tiny lexan diaphragm particles self-ignited in the camera field of view and were identified as small bright dots, readily distinguished from the spatially much broader fuel burning. Results from the present experiments are interpreted on the basis that small contamination burning did not influence ignition or burning of the fuel jet.

In this study, the autoignition delay time was defined as the time from the commencement of fuel injection until the emergence of the first ignition kernel, based on images from the CMOS camera. The injection delay (time from sending the trigger signal to the commencement of fuel injection) was determined using Schlieren imaging technique (Appendix A). The distance from the injector tip to the closest (most upstream) ignition kernel was defined as Z_k. Figure 3.2 shows an image from a typical experiment in which the ignition kernel emerges, with Z_k determined as shown. Image thresholding has been used to highlight the kernel in this image.

Figure 3.2 Typical CMOS camera image of ignition kernel

To account for the variation in fuel mass flux with injector orifice diameter, d, and pressure ratio, P_i/P_o, Z_k was normalized by:

$$Z_k{}^* = Z_k / d^*$$
(3.1)

$$d^* = d\sqrt{P_i / P_o}$$
(3.2)

as discussed by Hill and Ouellette [63] and Rubas et al. [164]. To identify the location of ignition sites relative to the jet, ignition kernel location was also normalized by Z_t, the jet length when ignition occurs. The jet length was first measured using Schlieren imaging technique, and then corrected for the operating conditions of the shock tube experiments.

3.3.3 NOx Emissions Measurement

After each experiment, the pressurized contents of the shock tube were released through an impactor-type filter into a large 400 L sampling bag constructed from electrically conducting carbon-impregnated polyolefin. The impactor filter was designed to effectively filter out particles larger than 2 microns from the flow.

An API 200E Chemiluminescent NOx analyzer was used to measure total NOx from each experiment. The API analyzer was custom modified to accommodate the helium driver gas used in the shock tube runs. Analyzer calibration was performed using a certified Praxair NOx standard. In each experiment contents from the sample bag described above were sampled by the NOx analyzer to determine the NOx concentration. Using this and knowledge of the total gas volume, the total NOx mass produced was determined.

3.3.4 Experimental Conditions

Table 3.1 summarizes the experimental conditions and main parameters in these experiments. Pre-combustion pressure, P_o, was fixed at 30 bar for all the experiments. In Series I, repeat experiments were performed at 30 bar, 1300 K to more fully examine the run-to-run variability in the experiment. In Series II, pre-combustion temperature, T_o, was varied between 1200 and 1400 K, while holding other parameters fixed. In Series III, the injection duration, t_i, was varied between 1.5 and 2.5 ms while holding other parameters constant. In Series IV, injection pressure, P_i, was varied from 60 to 150 bar with other parameters held fixed. Table 3.2 summarizes the number of experiments conducted for each fuel under each operating condition.

Table 3.1 Operating conditions for methane and methane/ethane experiments

Experiment Series	P_o (bar)	T_o (K)	P_i (bar)	t_i (ms)
I	30	1300	120	1.0
II	30	1200-1400	120	1.0
III	30	1300	120	1.5-2.5
IV	30	1300	60-150	1.0

Table 3.2 Number of experiments conducted for each fuel

Experiment Series	Methane	10% Ethane	20% Nitrogen	20% Hydrogen
I	20	20	20	20
II	16	14	13	14
III	11	11	9	0
IV	11	12	11	12

3.4 Results

Experimental results with methane fuel are used as a baseline for comparison in this chapter.

3.4.1 Methane/Ethane Results

Ignition Delay

Table 3.3 summarizes the measured ignition delay, t_{d_ign}, from Series I. Error in t_{d_ign} is approximately (+0.106 ms, -0.073 ms), attributed to uncertainty in injection delay (+0.060 ms, -0.027 ms) measured by Schlieren imaging technique and the time between CMOS camera frames (0.046 ms). No significant difference in average ignition delay is observed with the addition of 10% ethane to the methane fuel.

ANOVA analysis was applied to further investigate whether the difference in average ignition delay is statistically significant, and the results are shown in Table 3.4. In Table 3.4, "SS" is the sum of the squares of each value for each source of variation. "df" is the degrees of freedom for each source of variation (Between Groups = n-1, Within Groups = n-3). "MS" is the mean square for each source of variation, computed as: SS/df. "F" is the calculated F-statistic, computed as: $MS_{Between}/MS_{Within}$. If the two results are sampled from the same data set, "F" should be close to one since $MS_{Between}$ and MS_{Within} are both estimates of the same quantity (σ^2). If the two results are not sampled from the same data set, "F" should be larger than 1 since $MS_{Between}$ estimates something larger than σ^2. "P-value" is the probability of obtaining a calculated statistic as large or larger than the one calculated from the data.

For all the ANOVA analyses in the present study, a 5% significance level is used. ANOVA results in Table 3.4 show that ethane addition does not have a statistically significant effect on ignition delay, with a P-value of 0.085. The variability is also similar, with a coefficient of variation (COV) of 15% for methane, and 18% for methane/ethane blend.

Table 3.3 Variability in ignition delay for methane and methane/ethane

	Min (ms)	Max (ms)	Mean (ms)	Std Dev (ms)	COV
0% Ethane	0.465	0.901	0.736	0.113	15%
10% Ethane	0.438	0.903	0.671	0.119	18%

Table 3.4 ANOVA results for ignition delay ethane addition dependence

Source of Variation	SS	df	MS	F	P-value
Between Groups	0.042	1	0.042	3.125	0.085
Within Groups	0.514	38	0.014		
Total	0.556	39			

Figure 3.3 shows the variation of t_{d_ign} with T_o. The error bar in this thesis represents the absolute error at P_o=30 bar, T_o=1300 K, P_i=120 bar, and t_i=1.0 ms. The figure illustrates the expected temperature dependence, namely decreased ignition delay time with increasing air temperature for both fuels. This observation agrees with that by Sullivan *et al.* [31,32] for pure methane. There appears to be a modest reduction in ignition delay with ethane addition, particularly at lower temperatures; however, this is difficult to discern through the scatter in the data. This will be discussed in greater detail in Chapter 5 where curve fitting using a least squares approach is explored.

◊ 0% Ethane   ◆ 10% Ethane
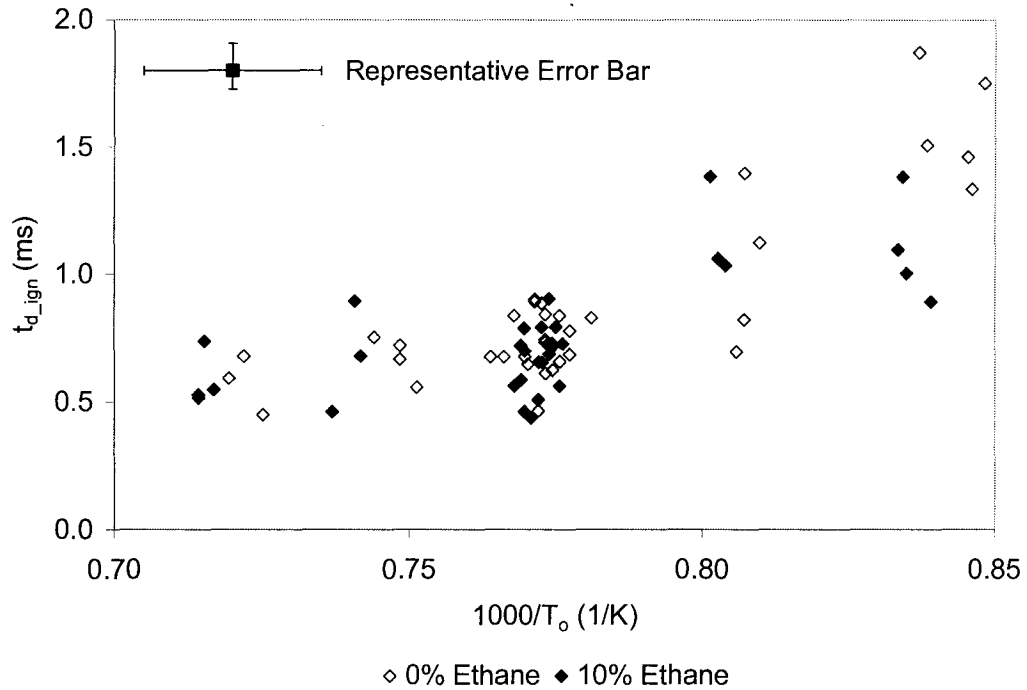
Figure 3.3 t_{d_ign} variation with T_o for methane and methane/ethane

Figure 3.4 shows the variation of t_{d_ign} with t_i. Uncertainty in t_i is approximately 0.01 ms due to the resolution of the injector controller. No significant dependence of t_{d_ign} on t_i is seen for either fuel, which agrees with the observation of Sullivan *et al.* [31,32] for pure methane.
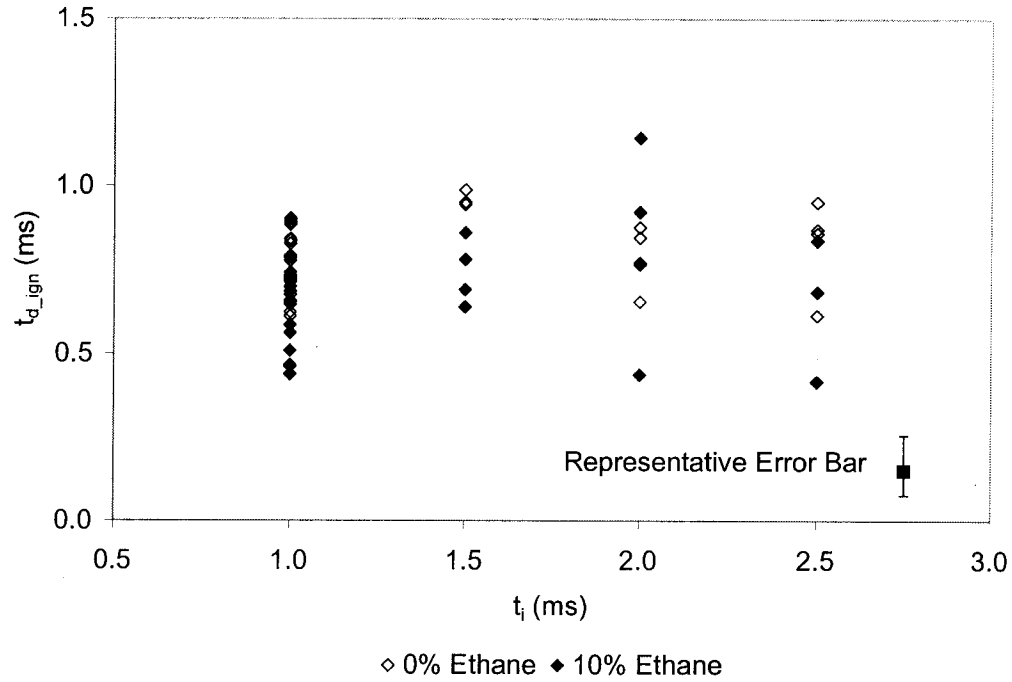
Figure 3.4 t_{d_ign} variation with t_i for methane and methane/ethane

Figure 3.5 shows the variation of t_{d_ign} with P_i/P_o. Uncertainty in P_i/P_o is estimated to be approximately 3-4%. There is a clear trend toward decreasing t_{d_ign} with modestly increasing P_i/P_o, which agrees with the earlier observation by Sullivan *et al.* [31,32] for pure methane. Ignition delay appears to start to increase at higher values of P_i/P_o. There are also some physical reasons suggesting such a trend between the ignition delay and injection pressure ration does exist. These will be discussed in greater detail in Chapter 5.
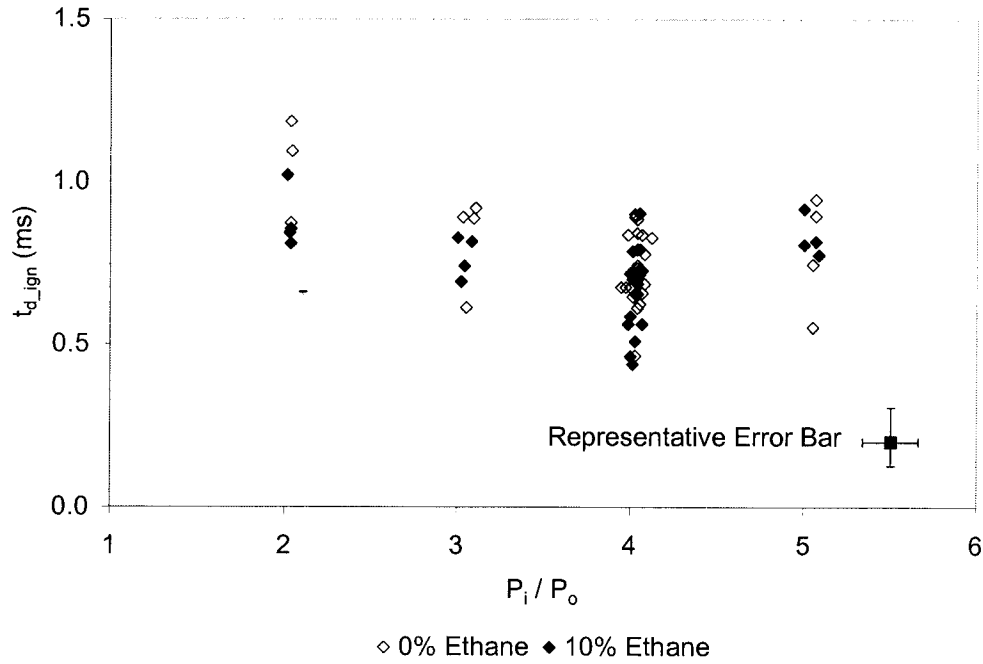
Figure 3.5 t_{d_ign} variation with P_i/P_o for methane and methane/ethane

Ignition Kernel Location

Table 3.5 summarizes Z_k/Z_t, the downstream ignition kernel location normalized by the jet length, from Series I. Uncertainty in Z_k/Z_t is estimated to be approximately 1%, mainly due to P_o and T_o used when estimating Z_t. With ethane addition, the average Z_k/Z_t increases 30%, while COV almost keeps unchanged. ANOVA results in Table 3.6 also suggest the effect of ethane addition on Z_k/Z_t is significant, with a P-value of 0.00017.

Table 3.5 Variability in Z_k/Z_t for methane and methane/ethane

	Min	Max	Mean	Std Dev	COV
0% Ethane	0.25	0.75	0.50	0.11	23%
10% Ethane	0.30	0.84	0.65	0.14	22%

Table 3.6 ANOVA results for Z_k/Z_t ethane addition dependence

Source of Variation	SS	df	MS	F	P-value
Between Groups	0.211	1	0.211	17.55	0.00017
Within Groups	0.432	36	0.012		
Total	0.643	37			

Table 3.7 summarizes Z_k^*, the ignition kernel location relative to the equivalent orifice diameter, from Series I. Uncertainty in Z_k is estimated to be approximately 1 mm (5 pixel widths) due to camera spatial and temporal resolution. After normalization, uncertainty

in Z_k^* is approximately 2%. With ethane addition, the ignition kernel moves further downstream with a 28% increase in mean Z_k^*. Note that this result contradicts that previously presented by Sullivan *et al.* [31,32], in which the methane/ethane experiments were not conducted under the same operating conditions as was the case for the pure methane. ANOVA analysis in Table 3.8 also suggests that the difference between these two sets of data is significant with a P-value of 0.003. Ethane addition does not affect the variability of Z_k^*, with COV=26% for both fuels.

Table 3.7 Variability in Z_k^* for methane and methane/ethane

	Min	Max	Mean	Std Dev	COV
0% Ethane	18	54	32	8	26%
10% Ethane	19	55	41	11	26%

Table 3.8 ANOVA results for Z_k^* ethane addition dependence

Source of Variation	SS	df	MS	F	P-value
Between Groups	766.6	1	766.7	10.0	0.003
Within Groups	2759.7	36	76.7		
Total	3526.3	37			

Figures 3.6 and 3.7 show the variation of Z_k/Z_t and Z_k^* with T_o, respectively. Neither Z_k/Z_t nor Z_k^* shows obvious dependence on T_o.

◇ 0% Ethane ◆ 10% Ethane
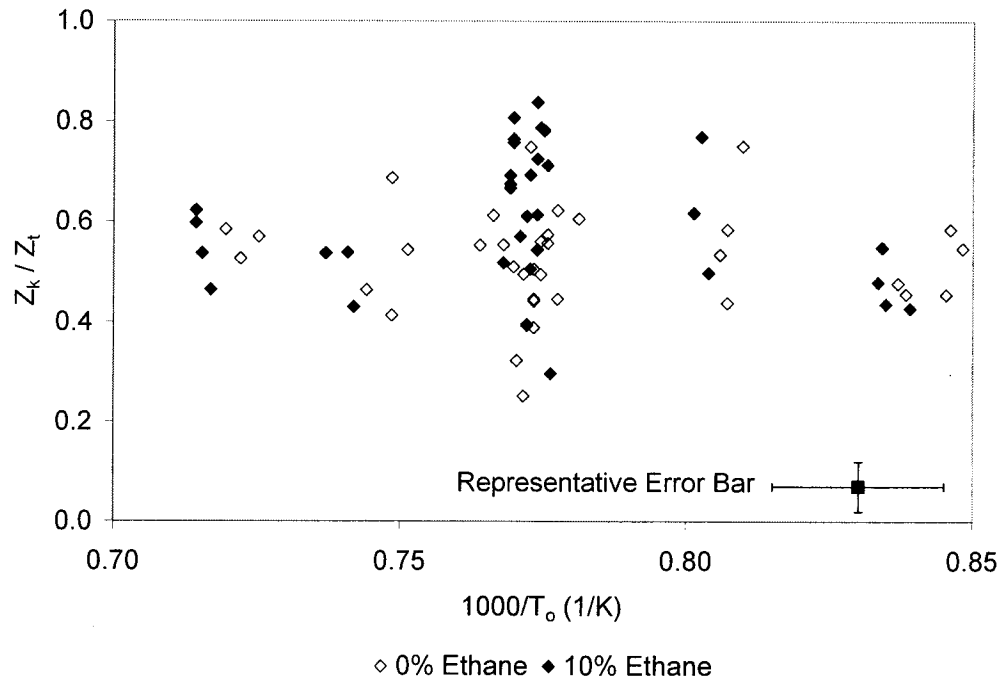
Figure 3.6 Z_k/Z_t variation with T_o for methane and methane/ethane
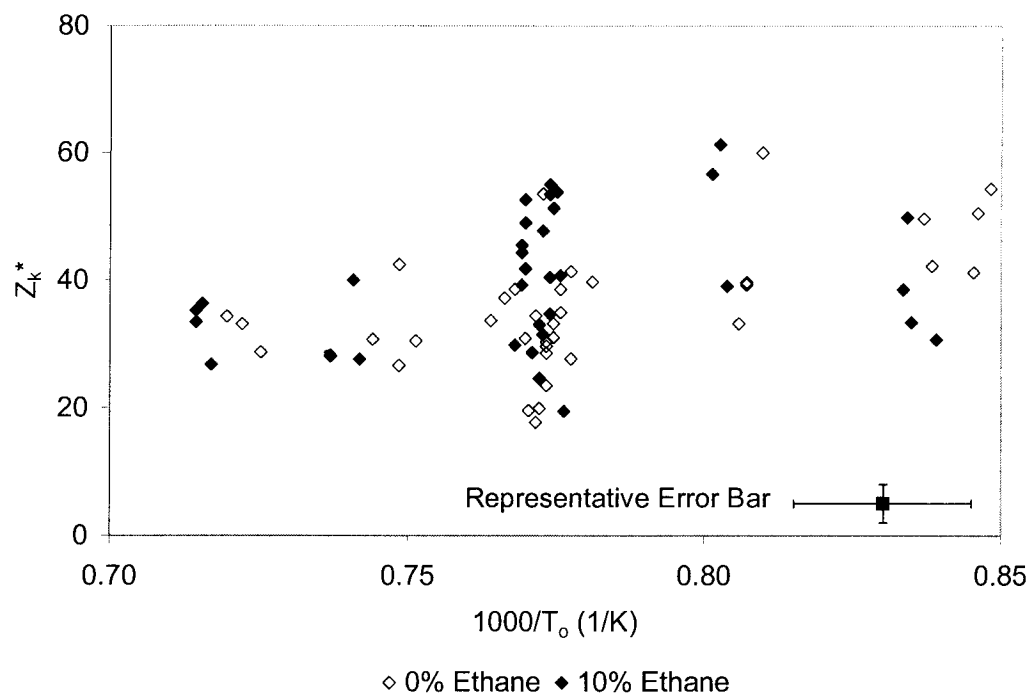
Figure 3.7 Z_k^* variation with T_o for methane and methane/ethane

Figures 3.8 and 3.9 show the variation of Z_k/Z_t and Z_k^* with t_i, respectively. No clear dependence of Z_k/Z_t or Z_k^* on t_i is observed, in agreement with the earlier observations of Sullivan *et al.* [31,32] for pure methane.
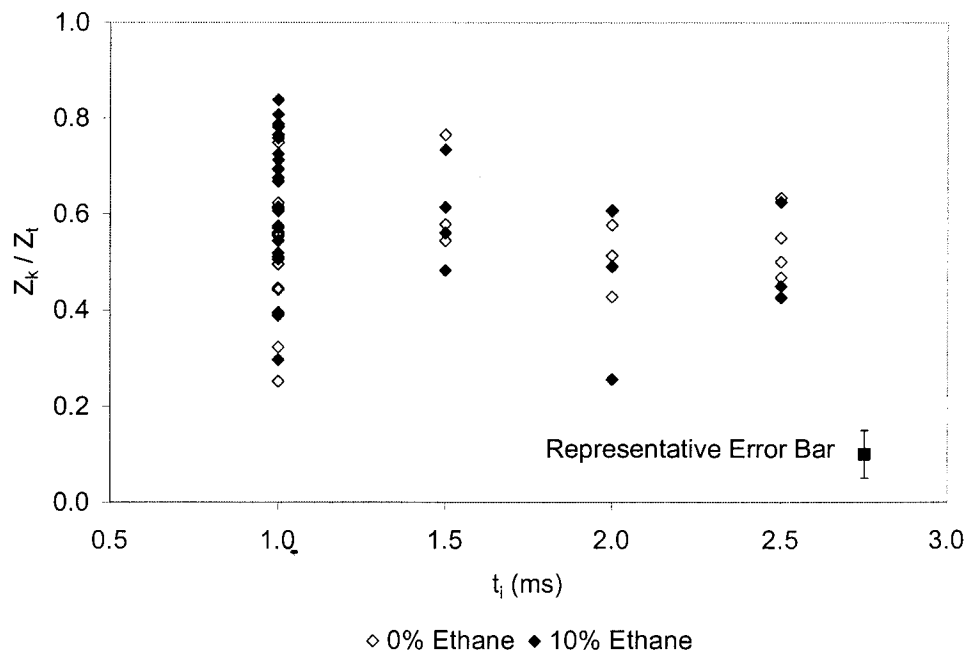
Figure 3.8 Z_k/Z_t variation with t_i for methane and methane/ethane

Figure 3.9 Z_k^* variation with t_i for methane and methane/ethane

Figures 3.10 and 3.11 show the variation of Z_k/Z_t and Z_k^* with P_i/P_o, respectively. Given the natural variability in Z_k/Z_t, no apparent dependence of Z_k/Z_t on P_i/P_o is observed. Z_k^* does not show dependence on P_i/P_o, either, which again agrees with the results of Sullivan et al. [31,32] for pure methane.

Figure 3.10 Z_k/Z_t variation with P_i/P_o for methane and methane/ethane
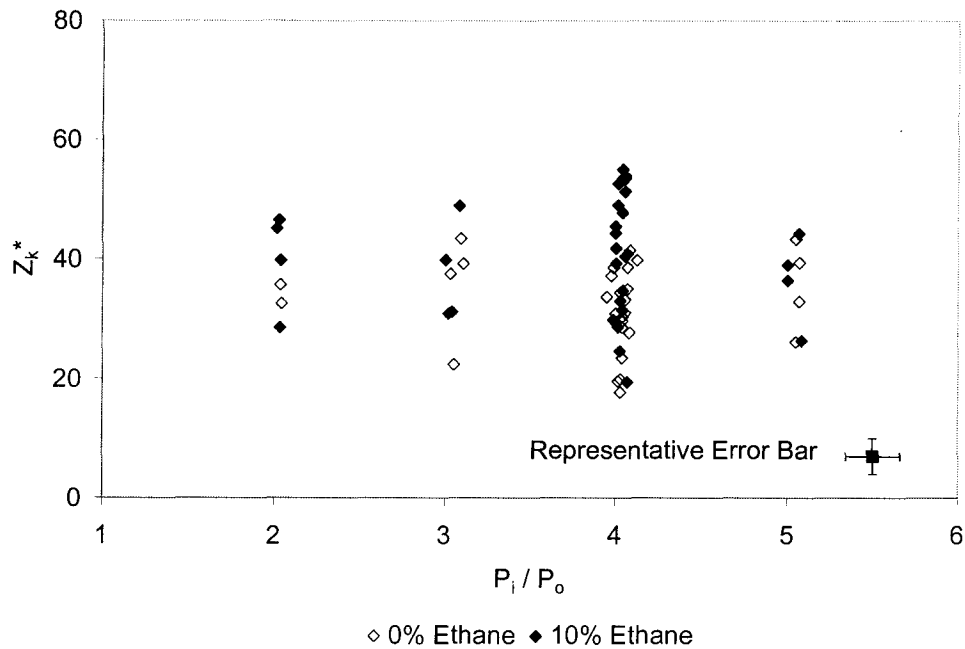
Figure 3.11 Z_k^* variation with P_i/P_o for methane and methane/ethane

NOx Emissions

To facilitate comparison between experiments with different fuel injection masses all of the results below for NOx mass emissions are normalized by the fuel injection mass. Error in normalized NOx emissions is estimated to be around 5%, mainly due to the uncertainty in the amount of fuel injected per shot.

It should be noted that the NOx levels in the present study are generally higher than those reported by Sullivan *et al.* [31,32]. This discrepancy is explained by the different measurement procedures. In Sullivan *et al.* [31,32], NOx emissions were measured after a 20-60 min settling period. Recent measurements have shown that NOx levels may decrease substantially during this period because of ongoing reactions. To minimize the uncertainty associated with this error, NOx emissions in the present study were measured immediately after each experiment and are thus higher than those reported previously.

Ethane addition causes a significant increase in NOx emissions, with a 36% increase in the mean value from the baseline methane case, as shown in Table 3.9. This difference is also evidenced by the P-value of 6.5×10^{-7} from ANOVA analysis in Table 3.10. An increased flame temperature of the methane/ethane fuel under lean conditions might contribute to increased NOx emissions, as suggested by Sullivan *et al.* [31,32].

Table 3.9 Variability in normalized NOx emissions for methane and methane/ethane

	Min	Max	Mean	Std Dev	COV
0% Ethane	2.35%	5.88%	4.55%	0.96%	21%
10% Ethane	4.54%	7.28%	6.22%	0.82%	13%

Table 3.10 ANOVA results for normalized NOx emissions ethane addition dependence

Source of Variation	SS	df	MS	F	P-value
Between Groups	0.0028	1	0.0028	35.5	6.5×10^{-7}
Within Groups	0.0030	38	7.9×10^{-5}		
Total	0.0058	39			

Figure 3.12 shows normalized NOx emissions variation with T_o. As expected NOx emissions increase with increasing temperature for both fuels, which can be attributed to the dominance of the thermal mechanism for NO formation.
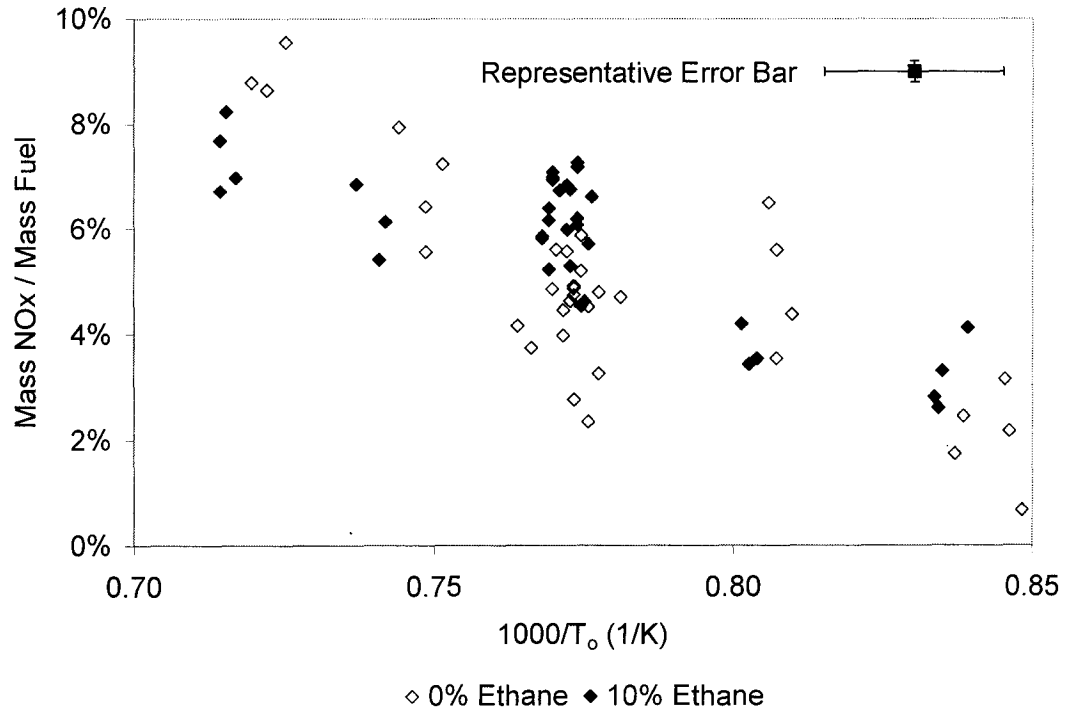
Figure 3.12 Normalized NOx emissions variation with T_o for methane and methane/ethane

Figure 3.13 shows normalized NOx emissions variation with t_i. For methane, a longer injection duration results in higher NOx production. This trend is not observed for methane/ethane blend. However, these results are complicated by the finite run-time of the shock tube. In the case of long injection duration, the rarefaction wave arrives at the test section area before combustion is fully completed. Because of this, it is difficult to draw conclusions from this figure.
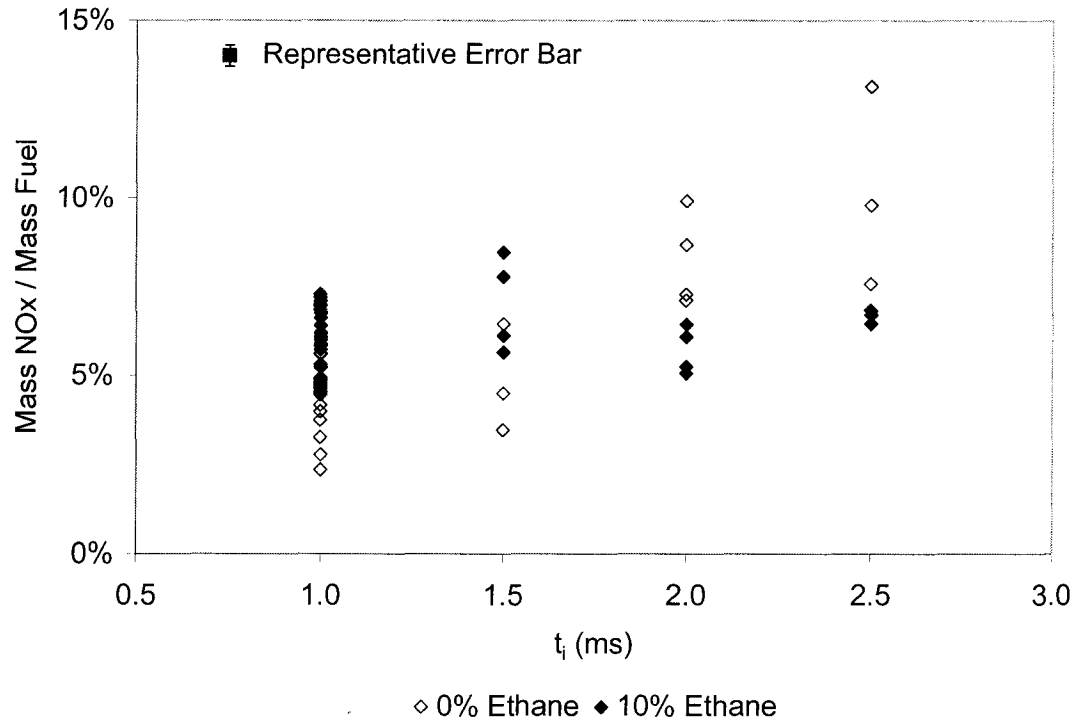
Figure 3.13 Normalized NOx emissions variation with t_i for methane and methane/ethane

Figure 3.14 shows the variation of normalized NOx emissions with pressure ratio P_i/P_o. NOx emissions appear to increase with increasing P_i/P_o. This trend agrees with the observation by Dumitrescu et al. [10]. It should be noted that this result again differs from that reported previously by Sullivan et al. [31,32] for pure methane, although it should also be noted that Sullivan and co-workers suggested that the influence of P_i/P_o on NOx emissions might have been masked by the run-to-run variability in their experiments.

◇ 0% Ethane ◆ 10% Ethane
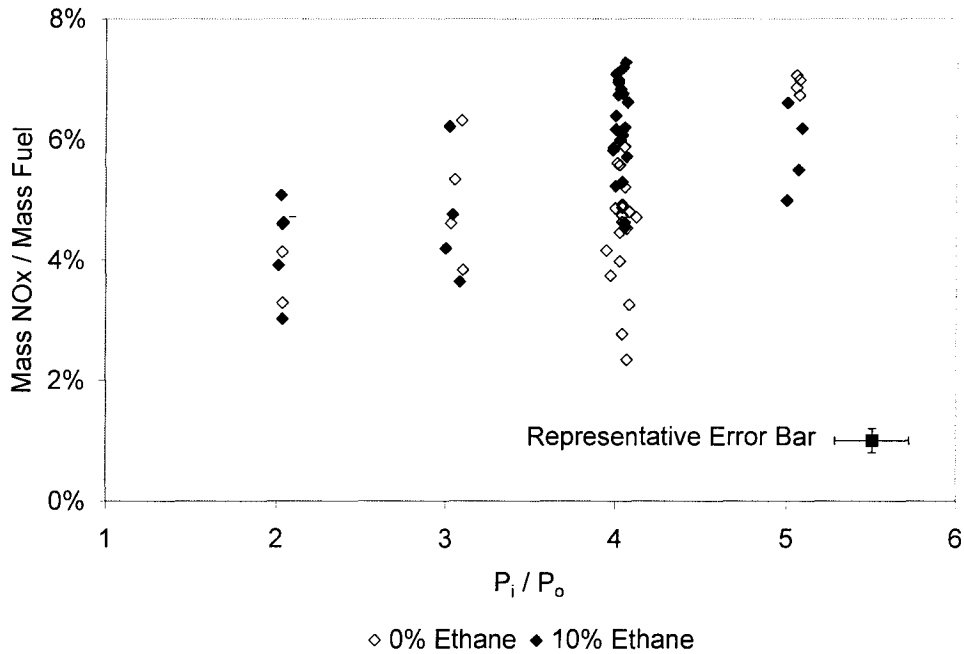
Figure 3.14 Normalized NOx emissions variation with P_i/P_o for methane and methane/ethane

3.4.2 Methane/Hydrogen Results

Ignition Delay

No statistically significant difference in ignition delay is observed with the addition of 20% hydrogen to the methane fuel, as shown in Table 3.11. The minimum and maximum ignition delay times are similar. The average ignition delay time shows a decrease of 7%. ANOVA results show that this decrease is insignificant, with a P-value of 0.172. The variability is also similar, with COV=15% for methane, and COV=16% for methane/hydrogen blend.

Table 3.11 Variability in ignition delay for methane and methane/hydrogen

	Min (ms)	Max (ms)	Mean (ms)	Std Dev (ms)	COV
0% Hydrogen	0.465	0.901	0.736	0.113	15%
20% Hydrogen	0.471	0.887	0.687	0.110	16%

Table 3.12 ANOVA results for ignition delay hydrogen addition dependence

Source of Variation	SS	df	MS	F	P-value
Between Groups	0.024	1	0.024	1.940	0.172
Within Groups	0.475	38	0.013		
Total	0.499	39			

Figure 3.15 shows the variation of t_{d_ign} with T_o. The ignition delay decreases significantly with increasing air temperature. It is interesting to note that the ignition delay times of the pure methane and the methane/hydrogen blend are quite close when the pre-combustion temperature is above 1250 K; however, the ignition delay decreases significantly with 20% hydrogen addition at lower temperatures.
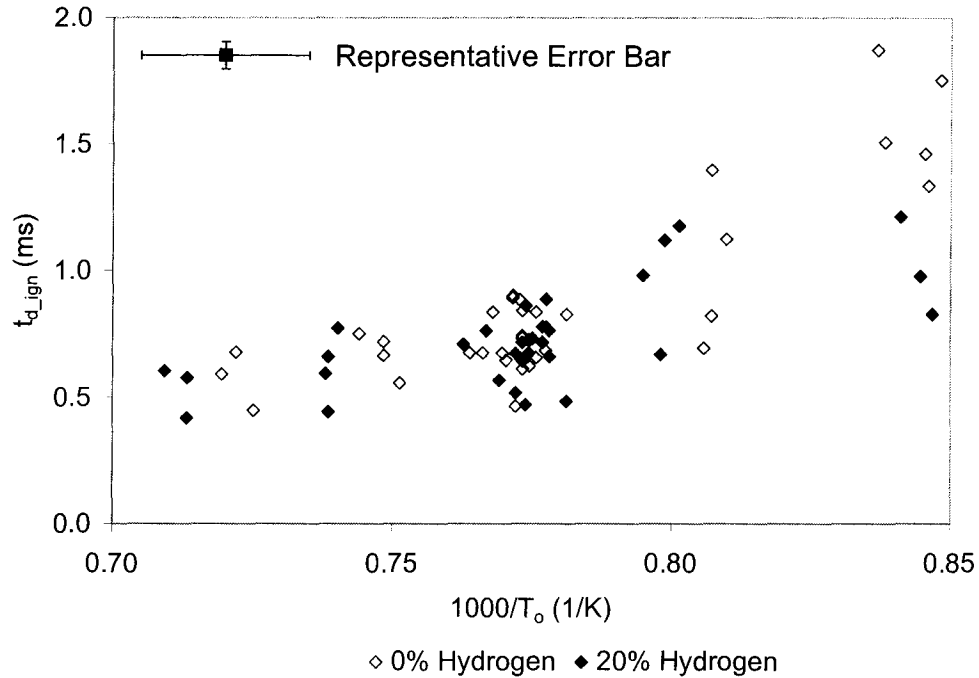
Figure 3.15 t_{d_ign} variation with T_o for methane and methane/hydrogen

Figure 3.16 shows the effect of injection pressure on the ignition delay time of both the pure methane case and the 20% hydrogen blend. The trend between t_{d_ign} and P_i/P_o for hydrogen addition is similar to that observed in §3.4.1 with ethane addition. t_{d_ign} decreases with modestly increasing P_i/P_o, and increases slightly at higher values of P_i/P_o.
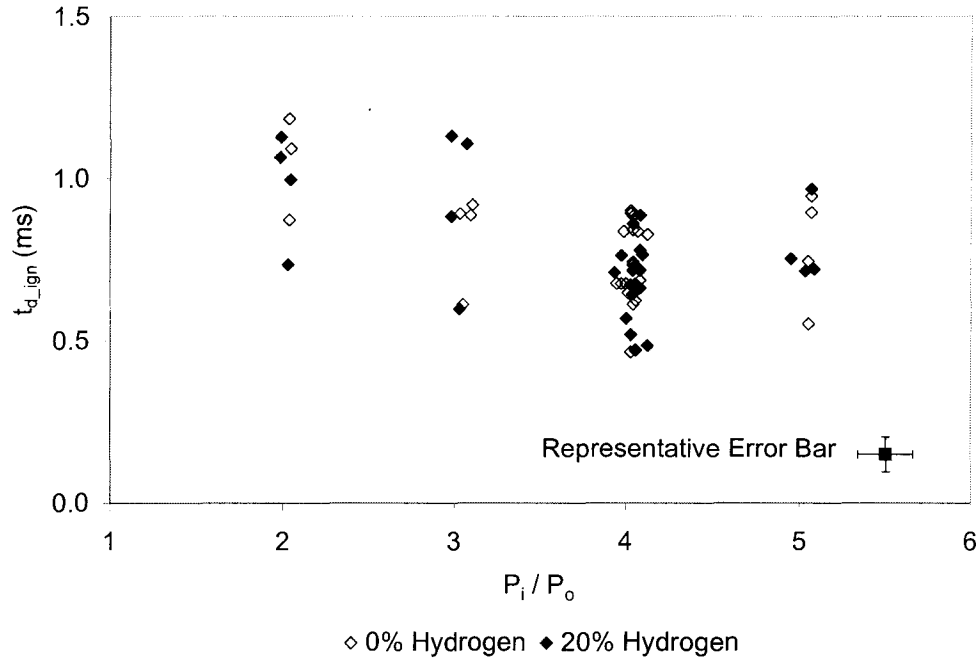
Figure 3.16 t_{d_ign} variation with P_i/P_o for methane and methane/hydrogen

Ignition Kernel Location

With hydrogen addition, the average Z_k/Z_t is almost unchanged, while the COV increases from 23% to 31%, as shown in Table 3.13. ANOVA results in Table 3.14 also suggest the effect of hydrogen addition on Z_k/Z_t is not statistically significant, with a P-value of 0.747.

Table 3.13 Variability in Z_k/Z_t for methane and methane/hydrogen

	Min	Max	Mean	Std Dev	COV
0% Hydrogen	0.25	0.75	0.50	0.11	23%
20% Hydrogen	0.32	0.83	0.52	0.16	31%

Table 3.14 ANOVA results for Z_k/Z_t hydrogen addition dependence

Source of Variation	SS	df	MS	F	P-value
Between Groups	0.002	1	0.002	0.106	0.747
Within Groups	0.733	38	0.019		
Total	0.735	39			

The addition of 20% hydrogen to the methane fuel does not show significant effect on the Z_k^*, either, as shown in Table 3.15. The results of the ANOVA analysis presented in Table 3.16 also suggest that the difference is insignificant. However, it is notable that COV of Z_k^* increases from 26% to 35% with the addition of 20% hydrogen to the fuel.

Table 3.15 Variability in $Z_k{}^*$ for methane and methane/hydrogen

	Min	Max	Mean	Std Dev	COV
0% Hydrogen	18	54	32	8	26%
20% Hydrogen	16	53	31	11	35%

Table 3.16 ANOVA results for $Z_k{}^*$ hydrogen addition dependence

Source of Variation	SS	df	MS	F	P-value
Between Groups	15.24	1	15.24	0.161	0.690
Within Groups	3591.86	38	94.52		
Total	3607.10	39			

Figures 3.17 and 3.18 show the variation of Z_k/Z_t and $Z_k{}^*$ with T_o, respectively. No strong relation between either Z_k/Z_t and T_o, or $Z_k{}^*$ and T_o, is observed.
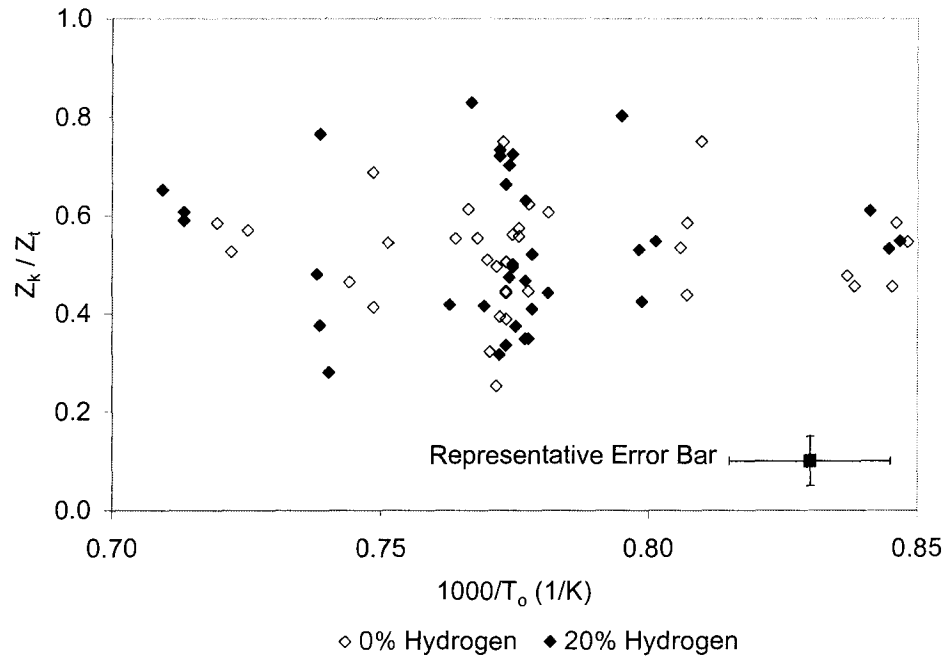
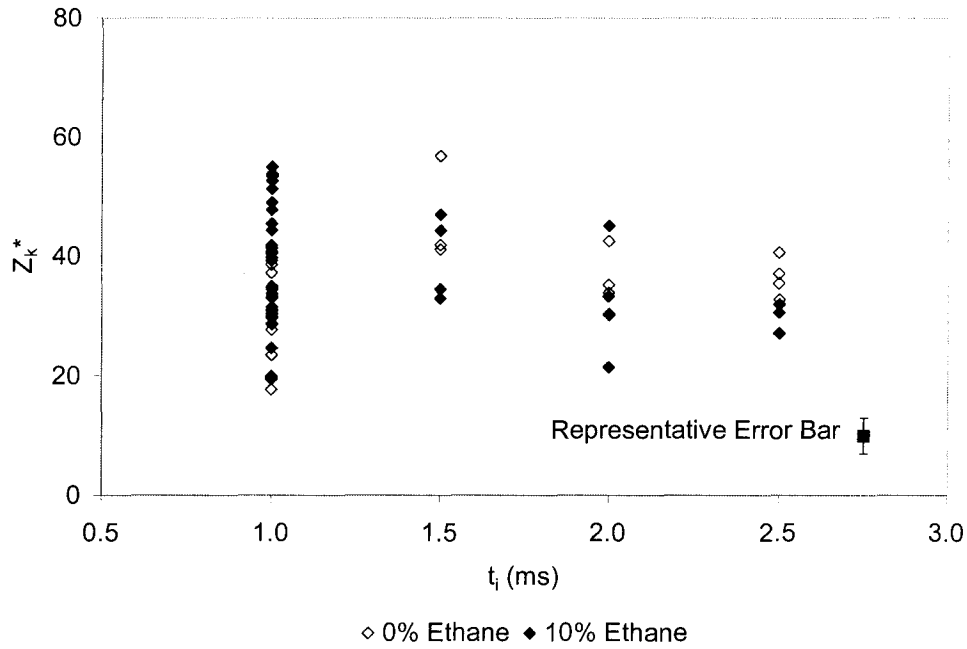Figure 3.17 Z_k/Z_t variation with T_o for methane and methane/hydrogen

Figure 3.18 Z_k^* variation with T_o for methane and methane/hydrogen

Figures 3.19 and 3.20 show the variation of Z_k/Z_t and Z_k^* with P_i/P_o, respectively. No clear dependence of Z_k/Z_t or Z_k^* on P_i/P_o is observed.
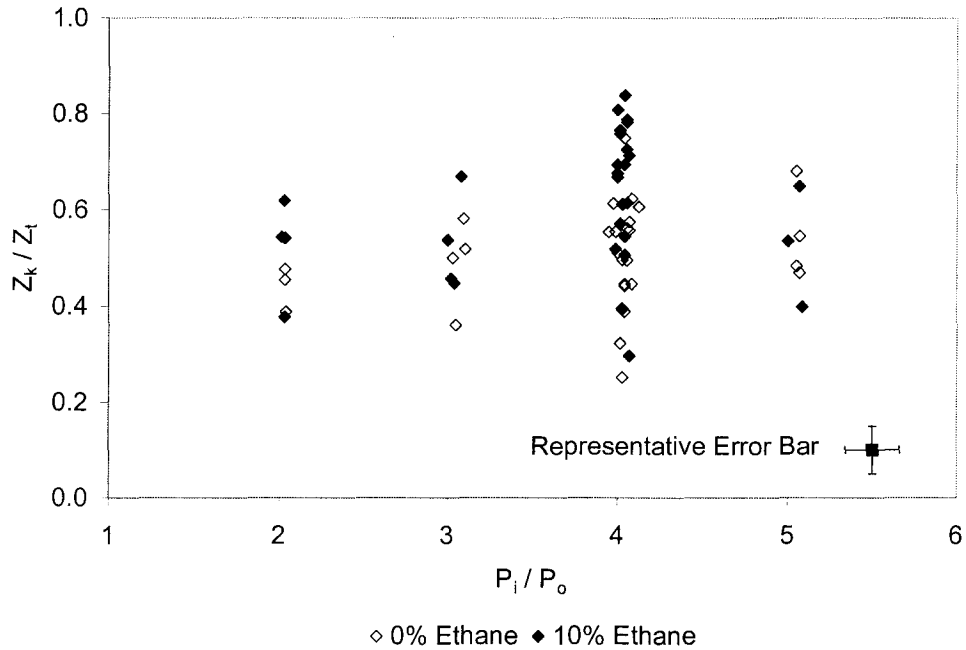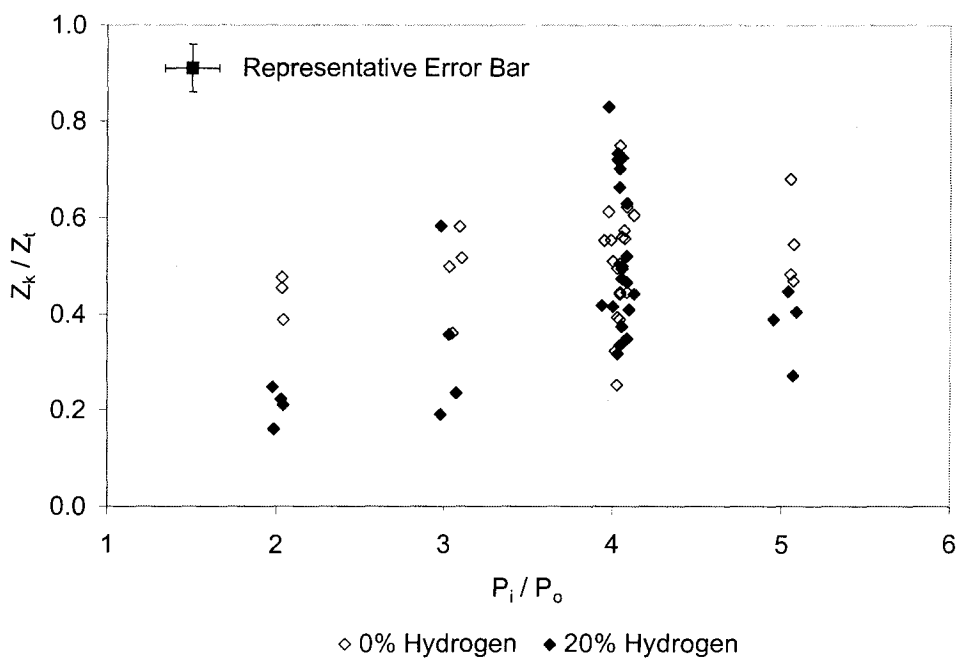

Figure 3.19 Z_k/Z_t variation with P_i/P_o for methane and methane/hydrogen
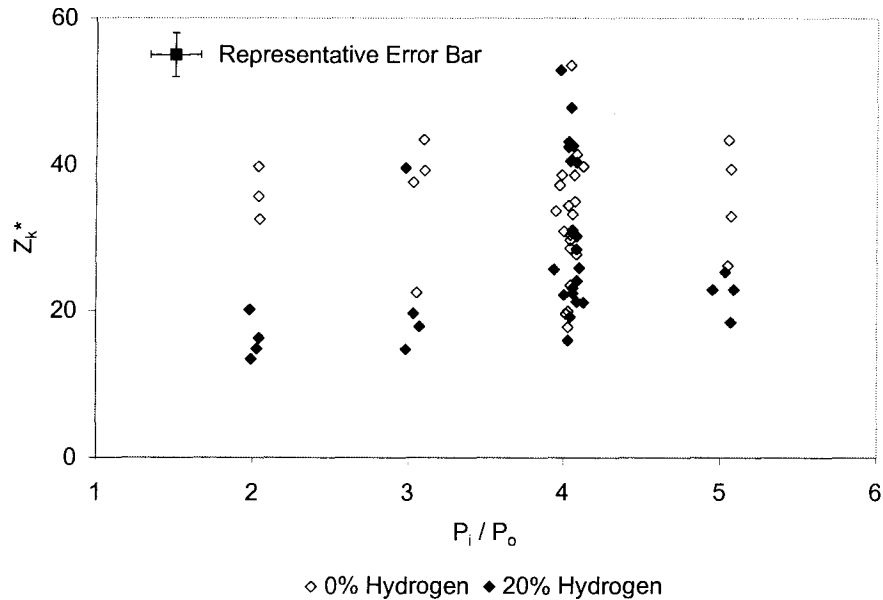
Figure 3.20 $Z_k{}^*$ variation with P_i/P_o for methane and methane/hydrogen

NOx Emissions

Hydrogen addition causes a significant decrease in NOx emissions, with a 46% decrease in the mean value from the baseline methane case, as shown in Table 3.17. This difference is also evidenced by ANOVA analysis, as shown in Table 3.18. Similarly to the ethane addition case reported in §3.4.1, a substantial decrease (33%) in NOx emissions variability is also observed with the addition of 20% hydrogen to the methane.

Table 3.17 Variability in normalized NOx emissions for methane and methane/hydrogen

	Min	Max	Mean	Std Dev	COV
0% Hydrogen	2.35%	5.88%	4.55%	0.96%	21%
20% Hydrogen	1.85%	3.19%	2.46%	0.35%	14%

Table 3.18 ANOVA results for normalized NOx emissions hydrogen addition dependence

Source of Variation	SS	df	MS	F	P-value
Between Groups	0.0044	1	0.004	84.00	3.64×10^{-11}
Within Groups	0.0020	38	5.189×10^{-5}		
Total	0.0063	39			

Figure 3.21 shows the variation of normalized NOx emissions with the pre-combustion temperature, T_o, for the baseline fuel and the 20% hydrogen blend. As expected, NOx emissions increase with increasing T_o for both fuels. Notably, the addition of 20% hydrogen results in lower average NOx emissions at all the five temperatures studied.

- 71 -

Figure 3.21 Normalized NOx emissions variation with T_o for methane and
methane/hydrogen

Figure 3.22 shows normalized NOx emissions variation with P_i/P_o. Similarly to the
ethane case reported previously, NOx emissions appear to increase with increasing P_i/P_o.
Hydrogen addition reduced average NOx emissions at all the four injection pressure ratios
studied.
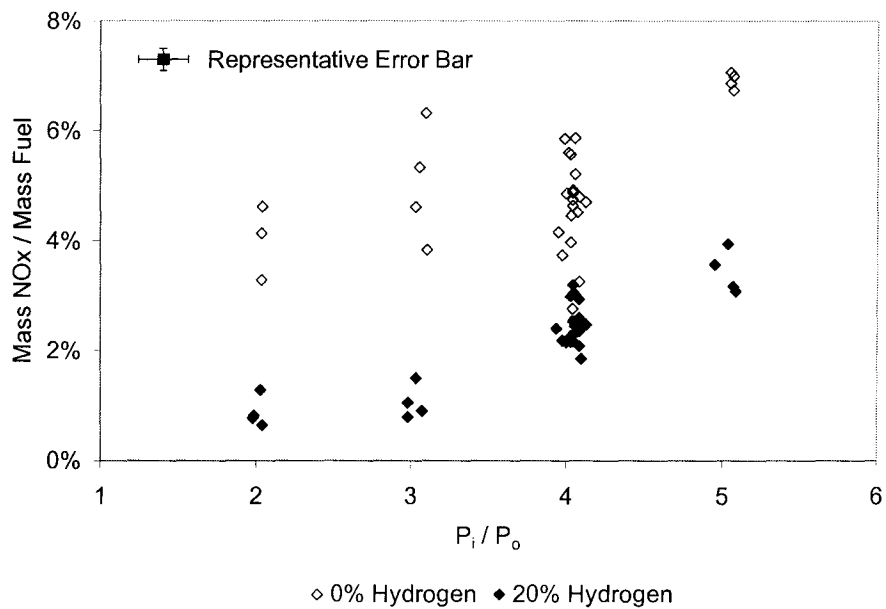
Figure 3.22 Normalized NOx emissions variation with P_i/P_o for methane and
methane/hydrogen

3.4.3 Methane/Nitrogen Results

Ignition Delay

As shown in Table 3.19 below, the average ignition delay increases 13% with the addition of 20% nitrogen, to the baseline methane fuel. However, due to the high run-to-run variability, ANOVA results presented in Table 3.20 indicates a relatively high P-value of 0.073. Adding nitrogen to the methane results in wider range of ignition delays. It is interesting to note that the minimum ignition delay times are almost unchanged, but that the longest observed ignition delay increases 30%. The higher variability is represented by an increase in the COV of the ignition delay from 15% for pure methane to 25% for methane/nitrogen blend.

Table 3.19 Variability in ignition delay for methane and methane/nitrogen

	Min (ms)	Max (ms)	Mean (ms)	Std Dev (ms)	COV
0% Nitrogen	0.465	0.901	0.736	0.113	15%
20% Nitrogen	0.453	1.172	0.833	0.204	25%

Table 3.20 ANOVA results for ignition delay nitrogen addition dependence

Source of Variation	SS	df	MS	F	P-value
Between Groups	0.093	1	0.093	3.401	0.073
Within Groups	1.038	38	0.027		
Total	1.131	39			

Figure 3.23 shows the variation of ignition delay with pre-combustion temperature. Nitrogen dilution does not change the relation between ignition delay and pre-combustion temperature. As pre-combustion temperature increases, a steady decrease in ignition delay is observed.
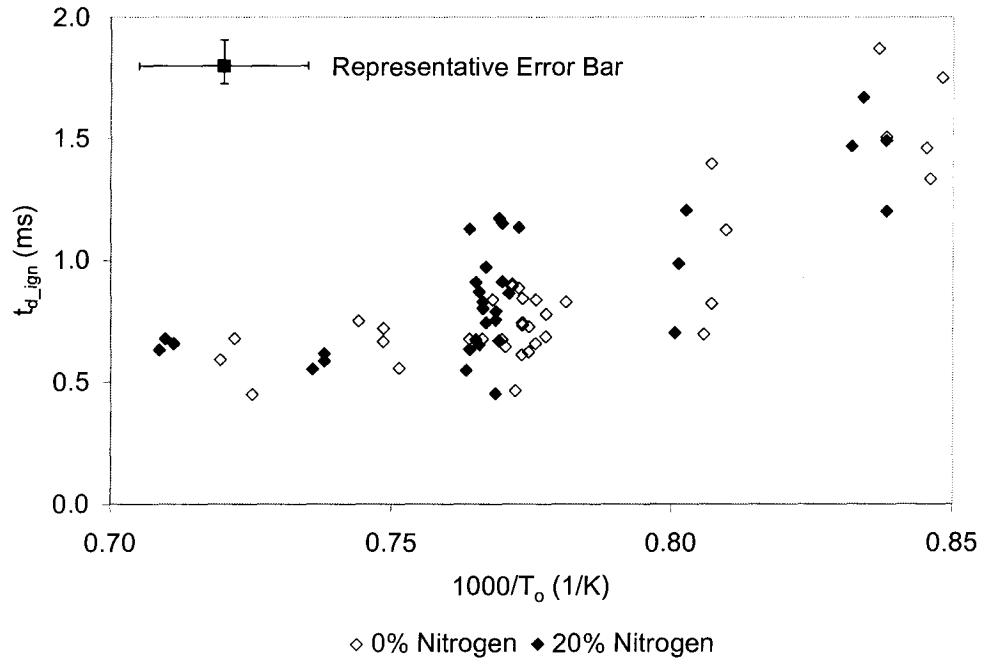
Figure 3.23 t_{d_ign} variation with T_o for methane and methane/nitrogen

Figure 3.24 shows the variation of t_{d_ign} with t_i. Similarly to the results with ethane or hydrogen addition, no relation between t_{d_ign} and t_i is observed.
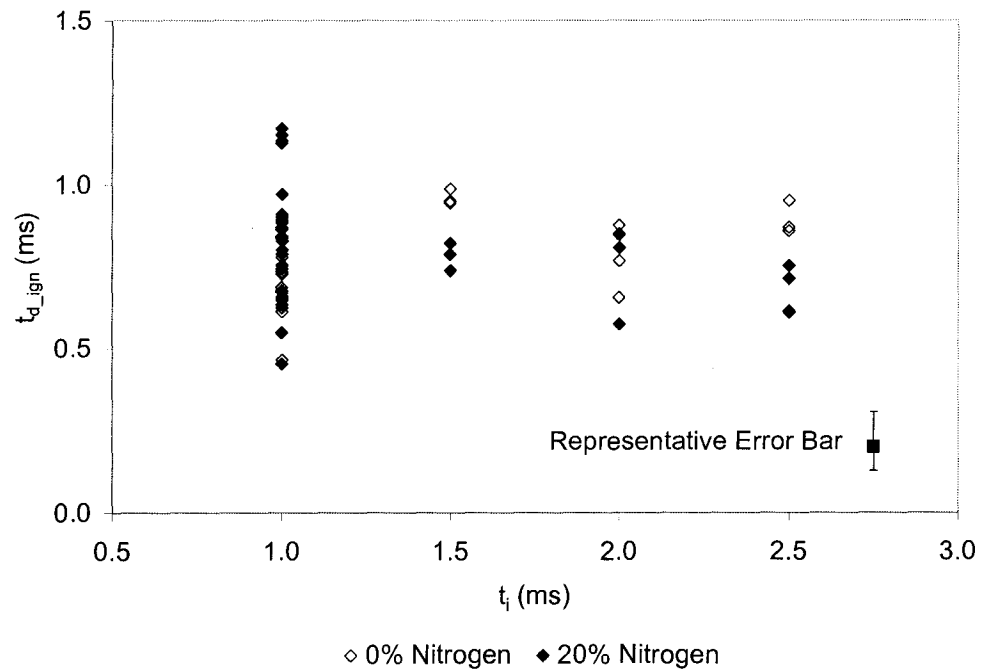
Figure 3.24 t_{d_ign} variation with t_i for methane and methane/nitrogen

Figure 3.25 shows the variation of t_{d_ign} with P_i/P_o. The trend between t_{d_ign} and P_i/P_o with nitrogen dilution is also similar to that seen with ethane or hydrogen addition to the base fuel, i.e., minimum t_{d_ign} is reached at modest P_i/P_o. With nitrogen addition, much longer ignition delay is observed at lower injection pressure ratios in some cases.

◇ 0% Nitrogen   ◆ 20% Nitrogen
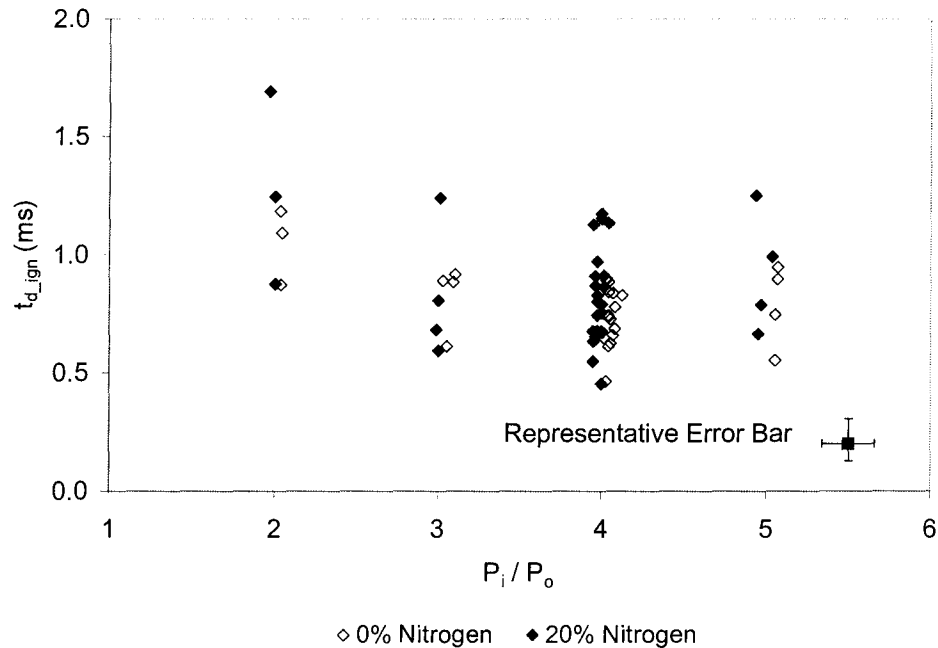
Figure 3.25 t_{d_ign} variation with P_i/P_o for methane and methane/nitrogen

Ignition Kernel Location

With nitrogen addition, the average Z_k/Z_t increases by 16%, while the COV increases by 30%, as shown in Table 3.21. However, ANOVA results in Table 3.22 suggest that the correlation between nitrogen addition and the increase in Z_k/Z_t is not strong, with a P-value of 0.095.

Table 3.21 Variability in Z_k/Z_t for methane and methane/nitrogen

	Min	Max	Mean	Std Dev	COV
0% Nitrogen	0.25	0.75	0.50	0.11	23%
20% Nitrogen	0.26	0.90	0.58	0.17	30%

Table 3.22 ANOVA results for Z_k/Z_t nitrogen addition dependence

Source of Variation	SS	df	MS	F	P-value
Between Groups	0.062	1	0.062	2.932	0.095
Within Groups	0.809	38	0.021		
Total	0.872	39			

With fuel dilution, the ignition kernel moves further downstream; the mean Z_k^* increases 28%. ANOVA results indicate that the difference is statistically significant with a P-value of 0.011. This result is similar to that seen in the case of ethane addition, but no change was seen in the case of hydrogen addition. That the nitrogen addition increases the variability of the ignition process is also seen in Z_k^*, with the COV increasing from 26% for pure methane to 31% for the methane/nitrogen blend.

Table 3.23 Variability in Z_k^* for methane and methane/nitrogen

	Min	Max	Mean	Std Dev	COV
0% Nitrogen	18	54	32	8	26%
20% Nitrogen	17	69	41	13	31%

Table 3.24 ANOVA results for Z_k^* nitrogen addition dependence

Source of Variation	SS	df	MS	F	P-value
Between Groups	839.074	1	839.074	7.093	0.011
Within Groups	4495.241	38	118.296		
Total	5334.315	39			

The ignition kernel location relative to the jet length does not change with increasing T_o, as shown in Figure 3.26. No strong relation between Z_k^* and T_o is observed, either, as shown in Figure 3.27.
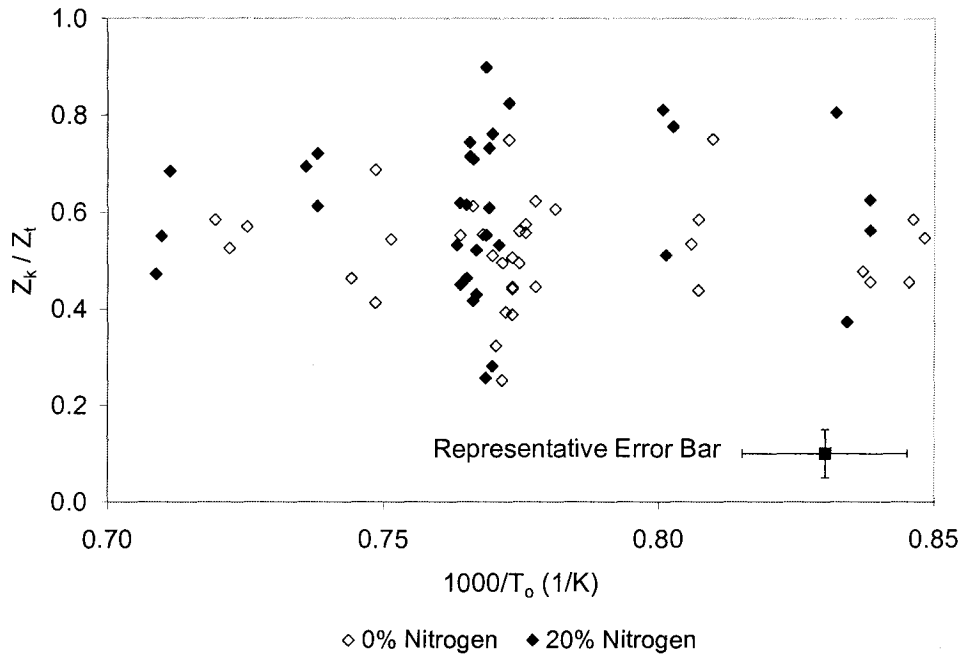
Figure 3.26 Z_k/Z_t variation with T_o for methane and methane/nitrogen
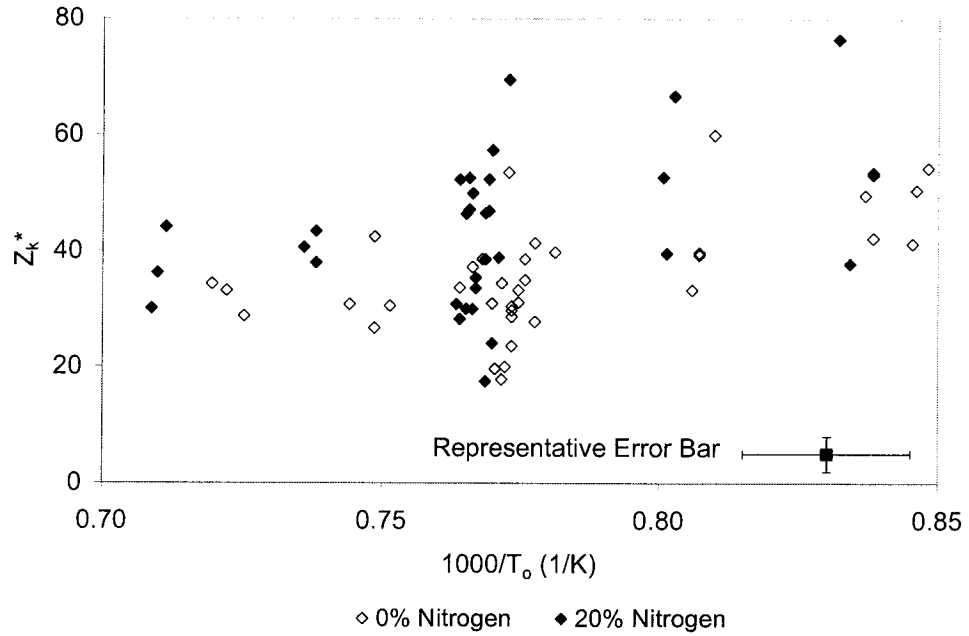
Figure 3.27 Z_k^* variation with T_o for methane and methane/nitrogen

Results in Figures 3.28 and 3.29 suggest that the normalized ignition kernel location is not affected by injection duration.
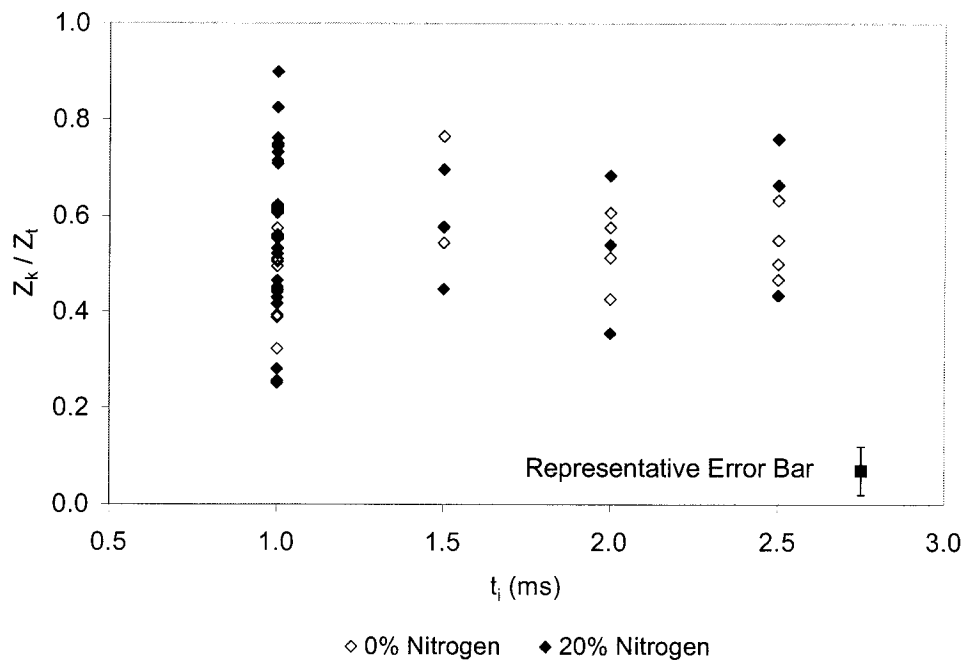
Figure 3.28 Z_k/Z_t variation with t_i for methane and methane/nitrogen
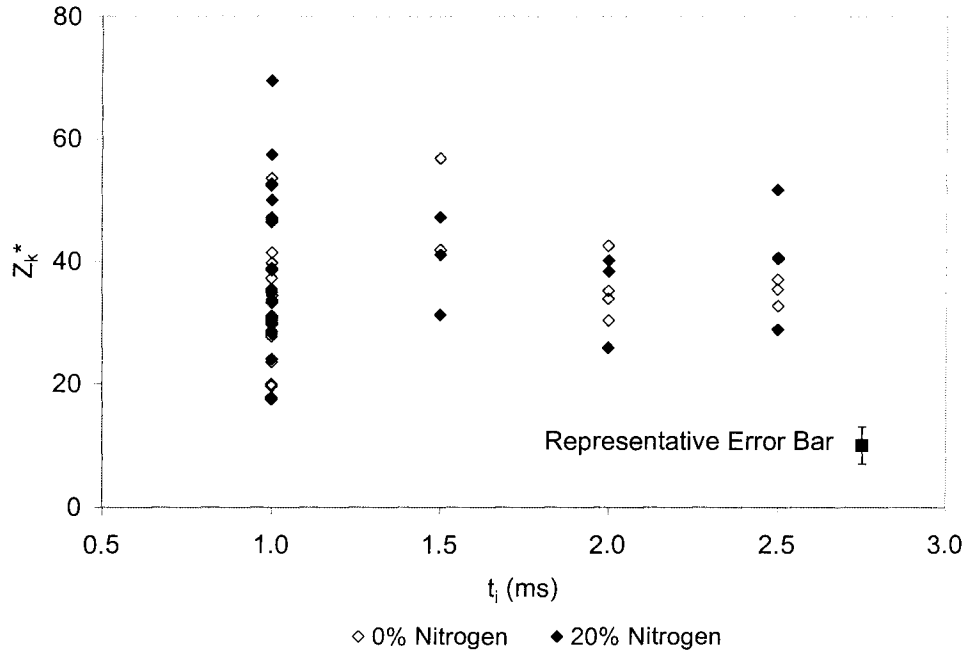
Figure 3.29 Z_k^* variation with t_i for methane and methane/nitrogen

Figures 3.30 and 3.31 show the variation of Z_k/Z_t and Z_k^* with P_i/P_o, respectively. Similarly to the ethane case, the normalized ignition kernel location does not show strong dependence on injection pressure ratio.
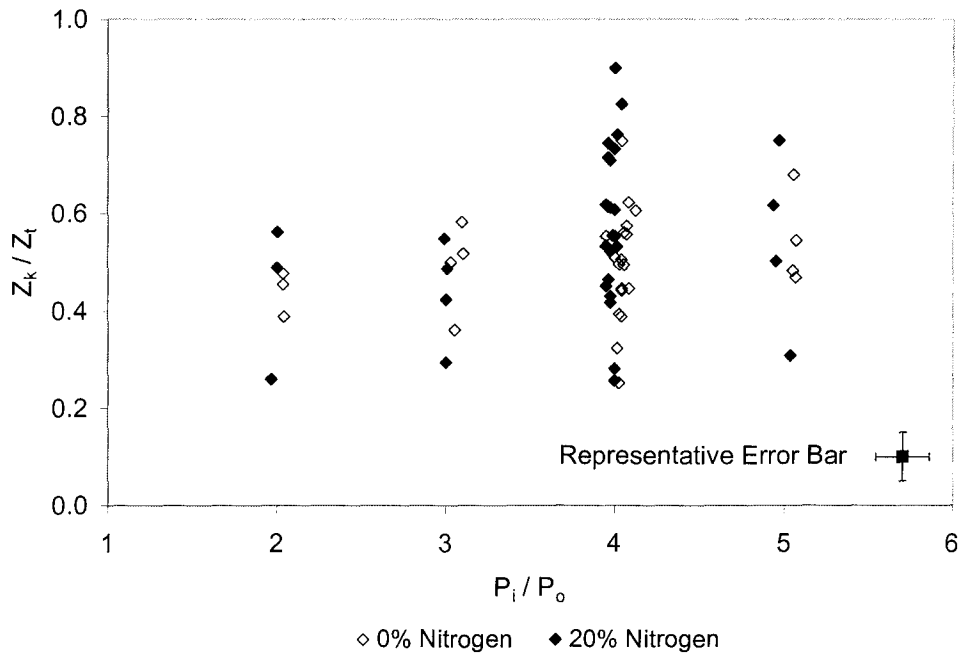
Figure 3.30 Z_k/Z_t variation with P_i/P_o for methane and methane/nitrogen

○ 0% Nitrogen   ◆ 20% Nitrogen
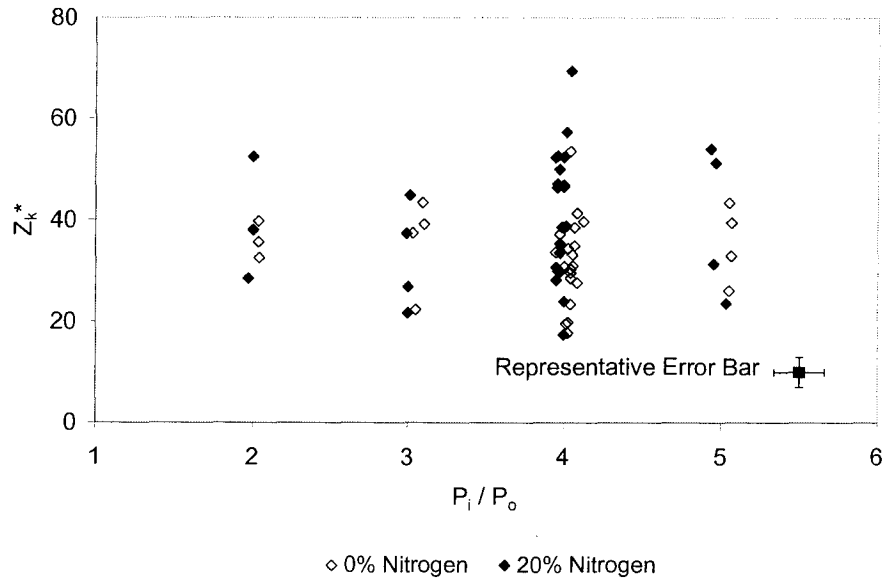
Figure 3.31 $Z_k{}^*$ variation with P_i/P_o for methane and methane/nitrogen

NOx Emissions

Table 3.25 summarizes the measured NOx emissions from Series I. Both sets of data are normalized by the mass of methane injected. Nitrogen addition results in a significant decrease in NOx emissions, with a 64% decrease in the mean value. This difference is statistically significant as shown by the ANOVA results in Table 3.26.

Table 3.25 Variability in normalized NOx emissions for methane and methane/nitrogen

	Min	Max	Mean	Std Dev	COV
0% Nitrogen	2.35%	5.88%	4.55%	0.96%	21%
20% Nitrogen	0.44%	3.09%	1.63%	0.81%	50%

Table 3.26 ANOVA results for normalized NOx emissions nitrogen addition dependence

Source of Variation	SS	df	MS	F	P-value
Between Groups	0.009	1	0.009	108.618	1.07×10^{-12}
Within Groups	0.003	38	7.847×10^{-5}		
Total	0.012	39			

Further insight into the effects of temperature and injection pressure ratio on NOx emissions are shown in Figures 3.32 and 3.33, where the normalized NOx emissions are plotted against the temperature and the injection pressure ratio, respectively. As expected, NOx emissions increase with increasing temperature. The NOx emissions are also higher at higher injection pressure ratios. Nitrogen addition results in lower average NOx emissions for all the temperatures and injector pressure ratios studied.

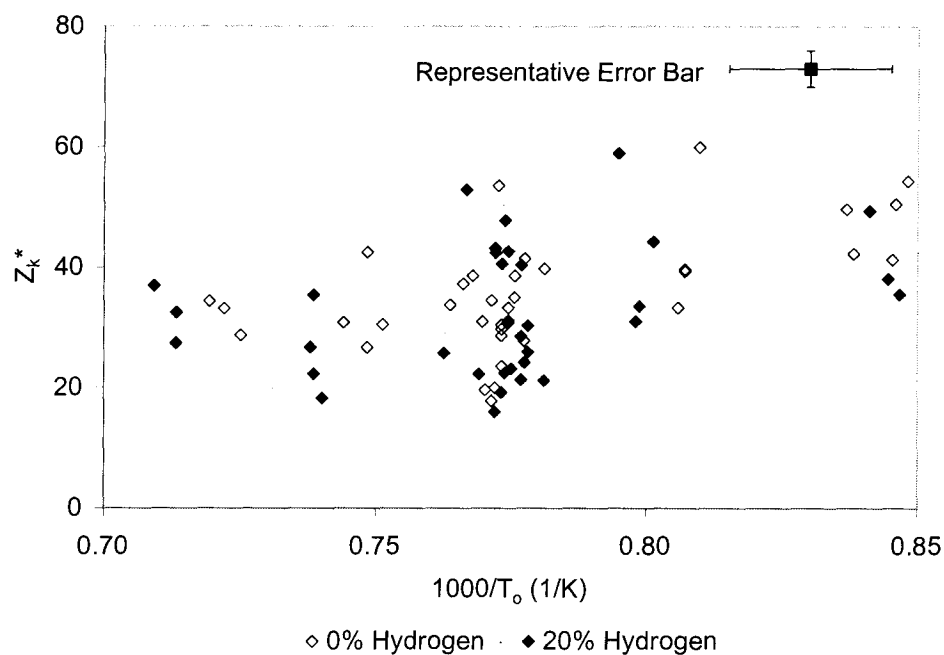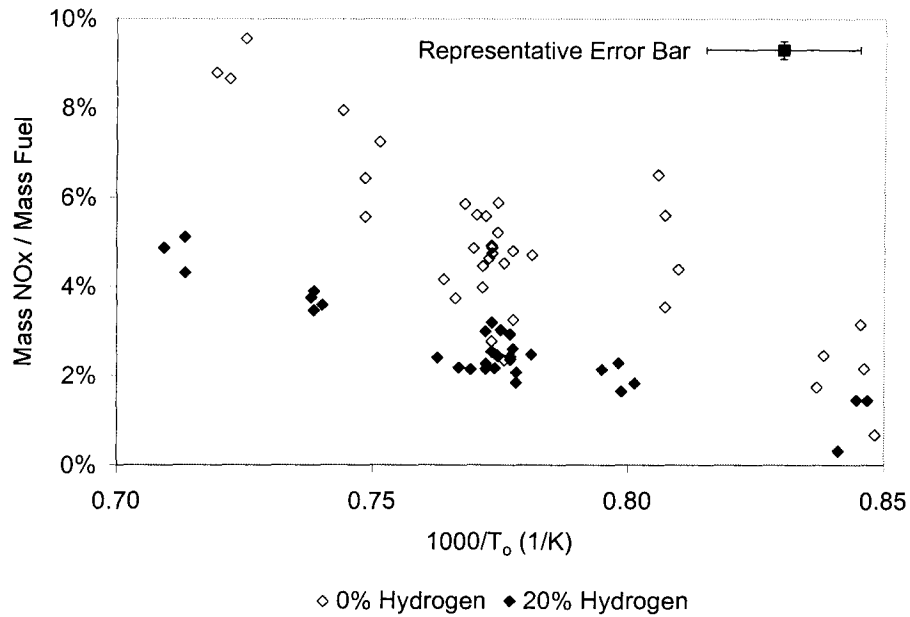- 79 -
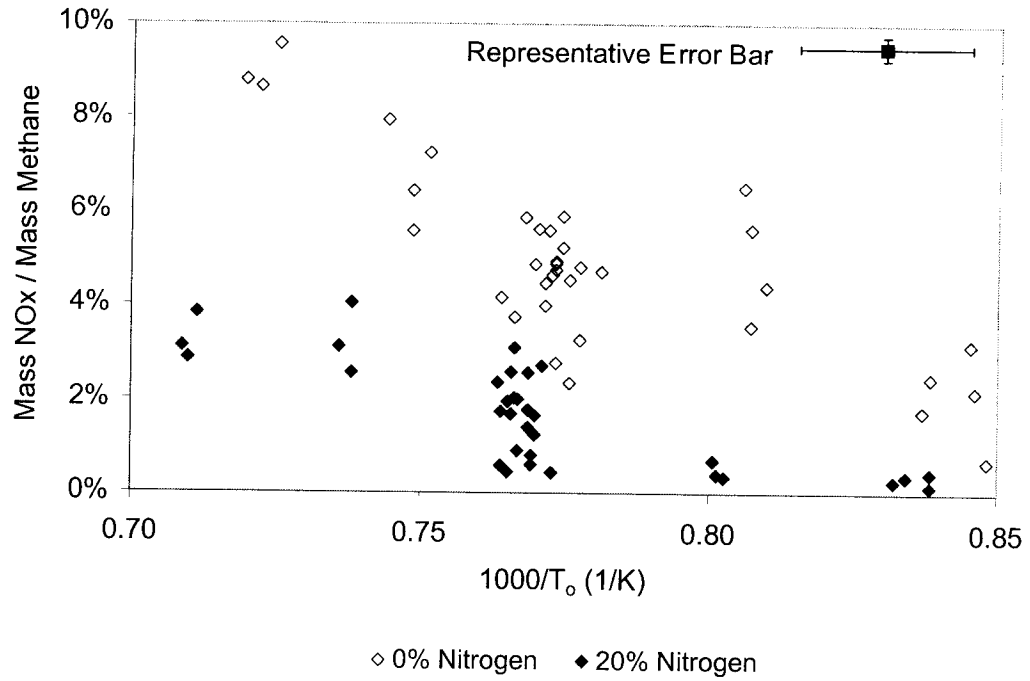
Figure 3.32 Normalized NOx emissions variation with T_o for methane and methane/nitrogen
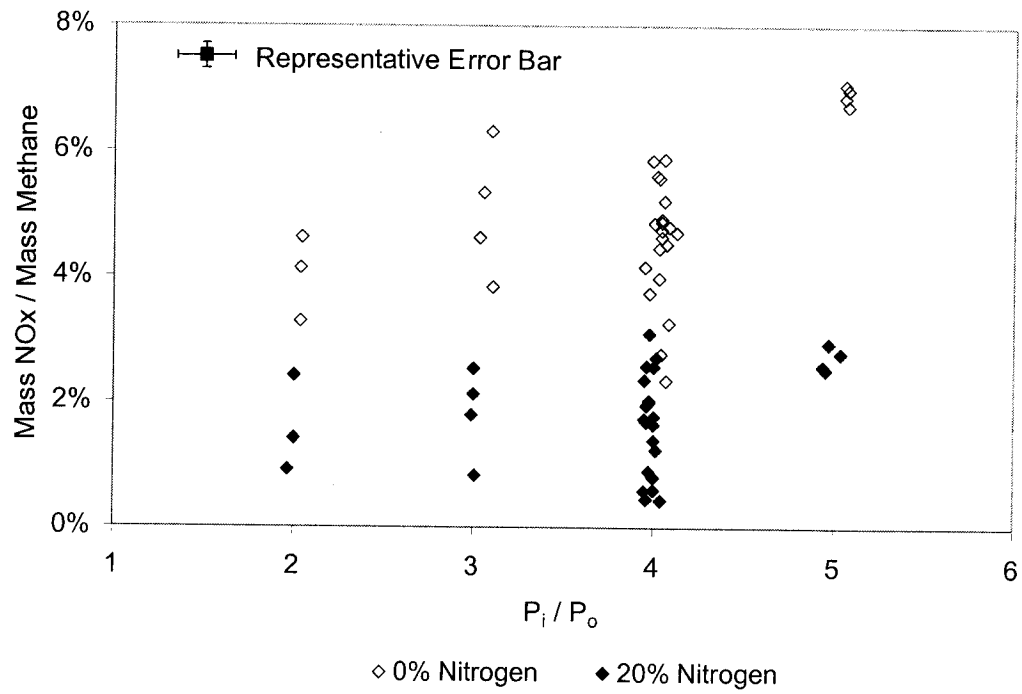
Figure 3.33 Normalized NOx emissions variation with P_i/P_o for methane and methane/nitrogen

Figure 3.34 shows normalized NOx emissions variation with t_i. Similarly to the ethane case, no obvious relation between NOx emissions and t_i is observed.
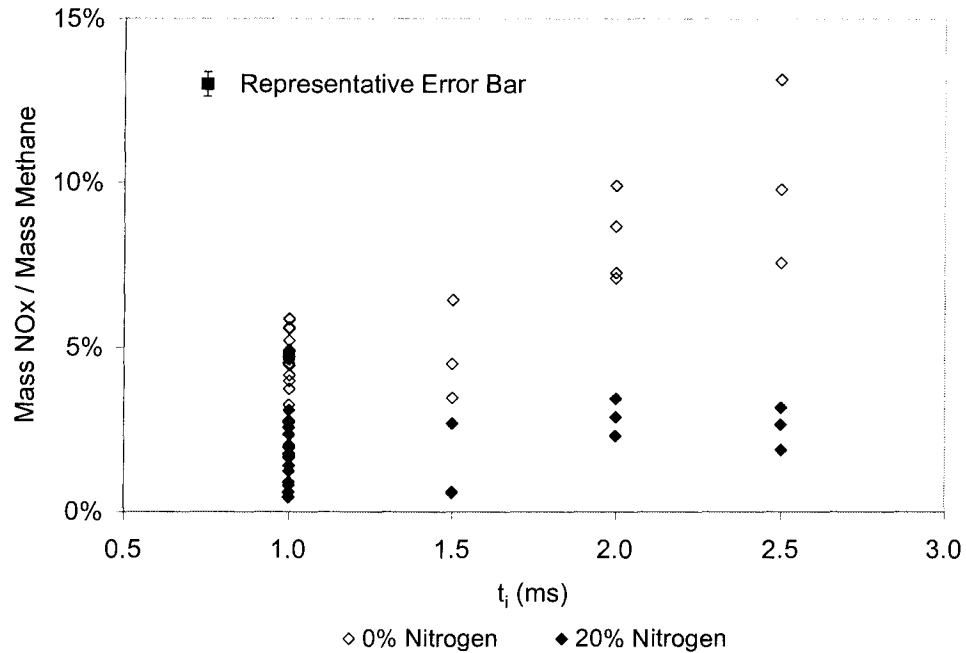
Figure 3.34 Normalized NOx emissions variation with t_i for methane and methane/nitrogen

3.5 Conclusions

Based on the results of 20 repeat shock tube experiments conducted at nominally identical conditions for each fuel, the effects of fuel additives on the autoignition process of methane jets are summarized as following:

1. Within the bounds of a 95% confidence interval, the experimentally determined ignition delay of the baseline methane fuel is unaffected by the addition of 10% ethane or 20% hydrogen or 20% nitrogen.

2. With ethane or nitrogen addition, the ignition kernel moves further downstream both relative to the injector tip and relative to the jet length. The addition of hydrogen does not show significant influence on the ignition kernel location.

3. NOx emissions increase significantly with ethane addition, and decrease significantly with hydrogen or nitrogen addition.

The addition of 10% ethane, 20% hydrogen or 20% nitrogen to the baseline fuel changes the variability of the autoignition and combustion process in the following manner:

1. The variability in ignition delay increases for all fuels, albeit by a small amount for the ethane and hydrogen cases. Diluting the fuel with nitrogen results in higher variability in ignition delay.

2. The variability in ignition kernel location is almost unchanged by the addition of ethane to the baseline fuel. The addition of hydrogen or nitrogen results in increased variability in the ignition kernel location.

3. The variability in NOx emissions is substantially decreased by the addition of 10% ethane or 20% hydrogen to the baseline fuel. The variability in the measured NOx emissions is increased by the addition of nitrogen.

As a final note to this chapter, the interested reader will have observed a significant degree of scatter in the experimental results of tests designed to elucidate the effects of pre-combustion temperature, injection duration, and injection pressure. At this stage, it is believed that that the random nature of the developing turbulent jet is mainly responsible for the significant run-to-run variability. Various realizations of the jet starting and penetration process yield different strain histories and mixture fraction histories, some of which provide more favorable conditions for kernel formation than others. Influences from the initial temperature field may also play a role; in the current series of experiments, however, the temperature field is not measured. This influence remains topics for further study. Since only a limited number of tests were performed in each case, it is considered inappropriate to draw conclusions concerning the role of these variables on the autoignition and combustion of any fuel at this point. These results will be revisited and further analyzed in Chapter 5.

Chapter 4
Chemical Kinetic Effects on Ignition of Jets of Methane with Additives

4.1 Introduction

The shock tube results presented in Chapter 3 show that the ignition delay of the baseline methane fuel is unaffected by the addition of either 10% ethane, 20% hydrogen, or 20% nitrogen within the bounds of a 95% confidence interval. However, small changes to the mean ignition delays are observed – the addition of 10% ethane or 20% hydrogen to the methane fuel is seen to decrease the mean ignition delay, while the addition of 20% nitrogen results in an increase in the mean ignition delay. Given the high level of uncertainty associated with these experimental observations, a non-premixed counter-flow diffusion flame of methane blended with different amount of ethane, nitrogen, or hydrogen and air was simulated in an effort to better understand the chemical kinetic effects on ignition of jets of methane with additives. The simulation was performed using the FlameMaster software package developed by Pitch [165].

This combustion configuration of the simulation is clearly different from that of the shock tube experiments, in which turbulent gaseous fuel is injected in heated and compressed air. However, the hope is that results from this simple configuration can provide some insight about what may happen in the more complicated flow. FlameMaster solves the flamelet equation, which is effectively the same as a first-moment closure CMC approach for a homogenous, isotropic flow. The far-field of a jet resembles a homogeneous, isotropic flow. So the simulation and the experiments are not totally unrelated.

Main parameters in the simulation included fuel composition, initial fuel temperature, T_f, initial air temperature, T_a, pressure, P, and scalar dissipation rate, χ. The mechanisms adopted in the simulation for methane, methane/ethane, and methane/hydrogen oxidization were proposed by Huang *et al.* [29,48,55], as has been discussed in Chapter 2. The mechanism adopted for methane/nitrogen is the same as that for methane, considering nitrogen to be an inert gas. Ignition delay was defined as the time from the start of the simulation until the first abrupt increase in the normalized temperature field:

$$T_{Normal} = \frac{T - T_{\min}}{T_{\max} - T_{\min}}$$ (4.1)

in which $T_{\min}$ is the minimum temperature at each mixture fraction, and $T_{\max}$ is the maximum temperature at each mixture fraction.

4.2 Results

4.2.1 Fuel Composition

Effect of Ethane Addition

The ignition-promoting effect of ethane is more prominent in the simulation than is indicated by the experiments in §3.4.1, as shown in Figure 4.1. The ignition delay decreases 38% and 58% respectively with 10% and 20% ethane addition.
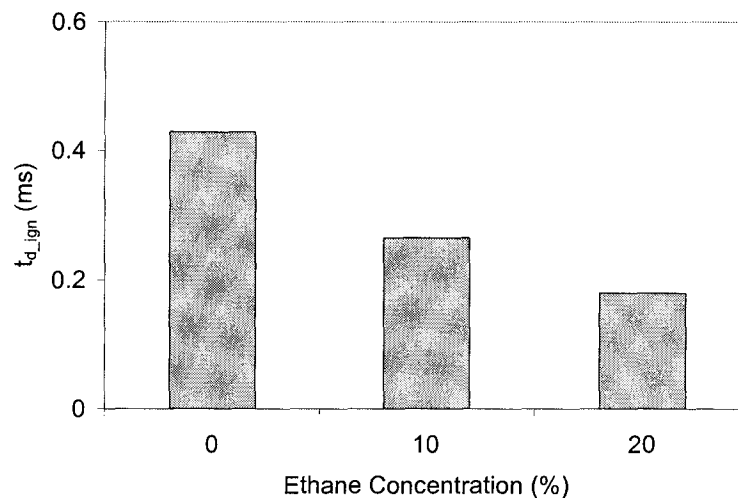
Figure 4.1 The effect of ethane addition on t_{d_ign} (T_f=300 K, T_o=1300 K, P=30 bar, χ=1)

As has been discussed in Chapter 2, the addition of ethane does not change the main reaction path of the methane system; the promotion of ignition is realized through accelerating the initiation phase in the induction period. CH_3, H, OH, and HO_2 are important intermediate species for methane oxidation. Figure 4.2 shows the mass fraction history for these species at stoichiometric mixture fraction, Z_{st}, for different methane/ethane blends (Table 4.1). With the addition of ethane, the peaks of CH_3, H, OH, and HO_2 mass fraction all shift to earlier times. When the ethane concentration increases, a more rapid rise in mass fraction right after the start of the reaction for all of these species is observed.

Ethane addition at the beginning of reaction shifts the equilibrium of R9 ($CH_3 + CH_3 \Leftrightarrow C_2H_6$), which is a main chain termination step at high temperature, so that less methyl is consumed. The H-atom abstraction of ethane is very efficient in producing H radicals, causing the rapid rise in H mass fraction right after the start of the reaction. OH and HO_2 are two of the most important active radicals for methane oxidation. All of these effects contribute to accelerate the methane oxidation, resulting in a shorter ignition delay.

Table 4.1 Z_{st} for different methane/ethane blends

	0% Ethane	10% Ethane	20% Ethane
Z_{st}	0.0552	0.0558	0.0670
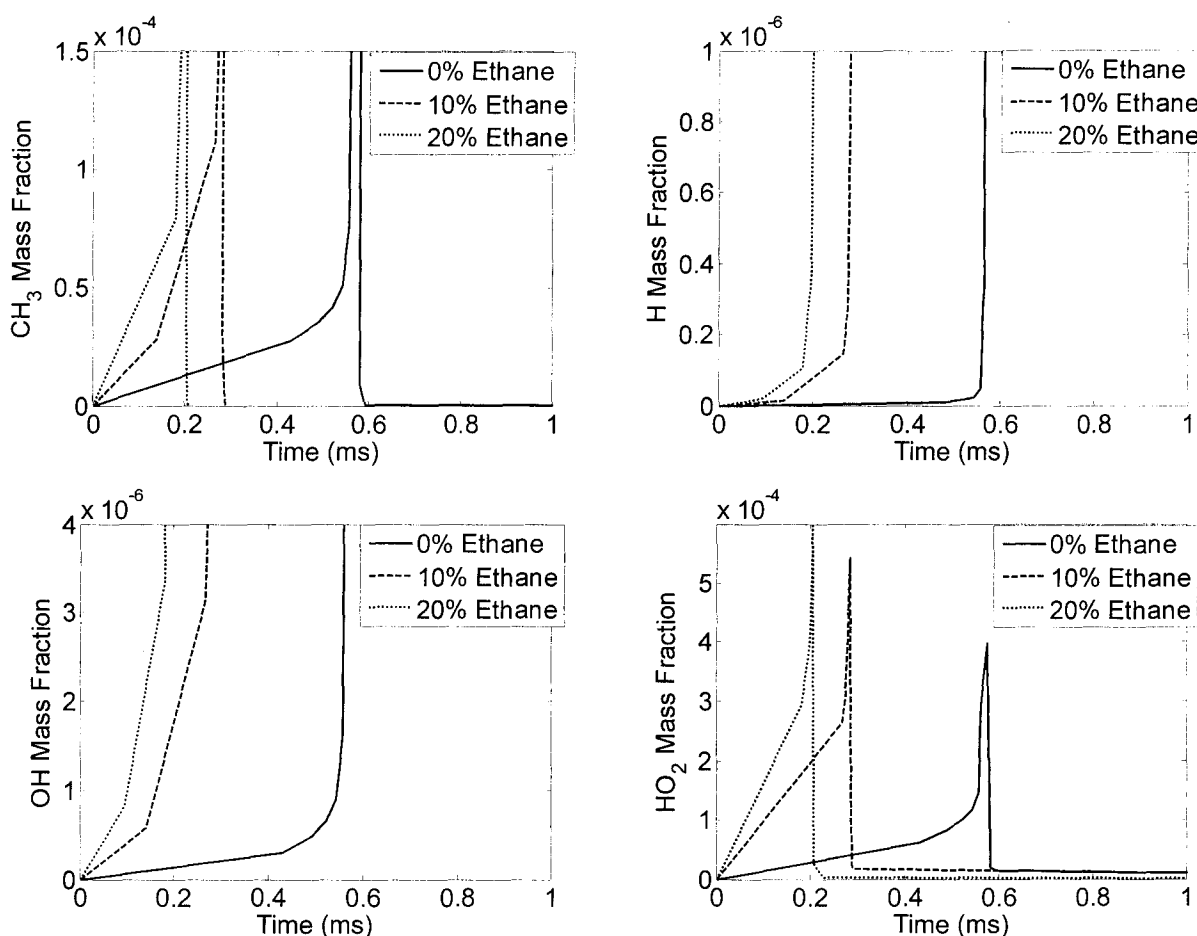
Figure 4.2 CH_3, H, OH, and HO_2 mass fraction history at Z_{st} for methane/ethane blends

(T_f=300 K, T_o=1300 K, P=30 bar, χ=1)

Effect of Hydrogen Addition

Similarly to the case of ethane addition, the FlameMaster results presented in Figure 4.3 predict that the ignition delay of the baseline fuel is reduced with hydrogen addition, even though the reduction is not predicted to be as significant as that with ethane addition. When 10% and 20% hydrogen is added to the fuel, the ignition delay decreases 13% and 32%, respectively.
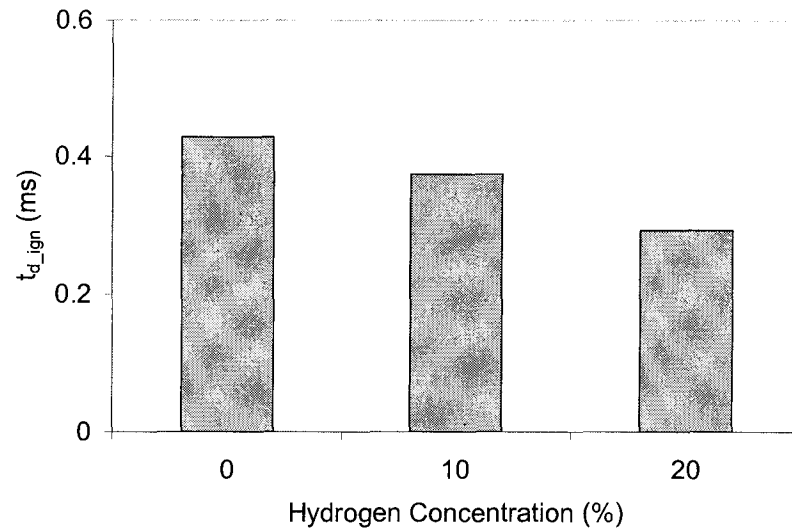
Figure 4.3 The effect of hydrogen addition on t_{d_ign} (T_f=300 K, T_o=1300 K, P=30 bar, χ=1)

Again, the addition of hydrogen does not change the main reaction path of the methane system. The effect of hydrogen on methane ignition is primarily related to the generation and consumption of H radicals. Figure 4.4 shows mass fraction profiles of CH_3, H, OH, and HO_2 at Z_{st} for different methane/hydrogen blends (Table 4.2). The addition of hydrogen is predicted to cause the peaks of CH_3, H, OH, and HO_2 mass fraction to move earlier in time. When the hydrogen concentration increases, a more rapid rise in mass fraction right after the start of the reaction for all these species is observed. All of these effects contribute to accelerate the methane oxidation, which results in a shorter ignition delay.

Table 4.2 Z_{st} for different methane/nitrogen blends

	0% Hydrogen	10% Hydrogen	20% Hydrogen
Z_{st}	0.0552	0.0545	0.0536
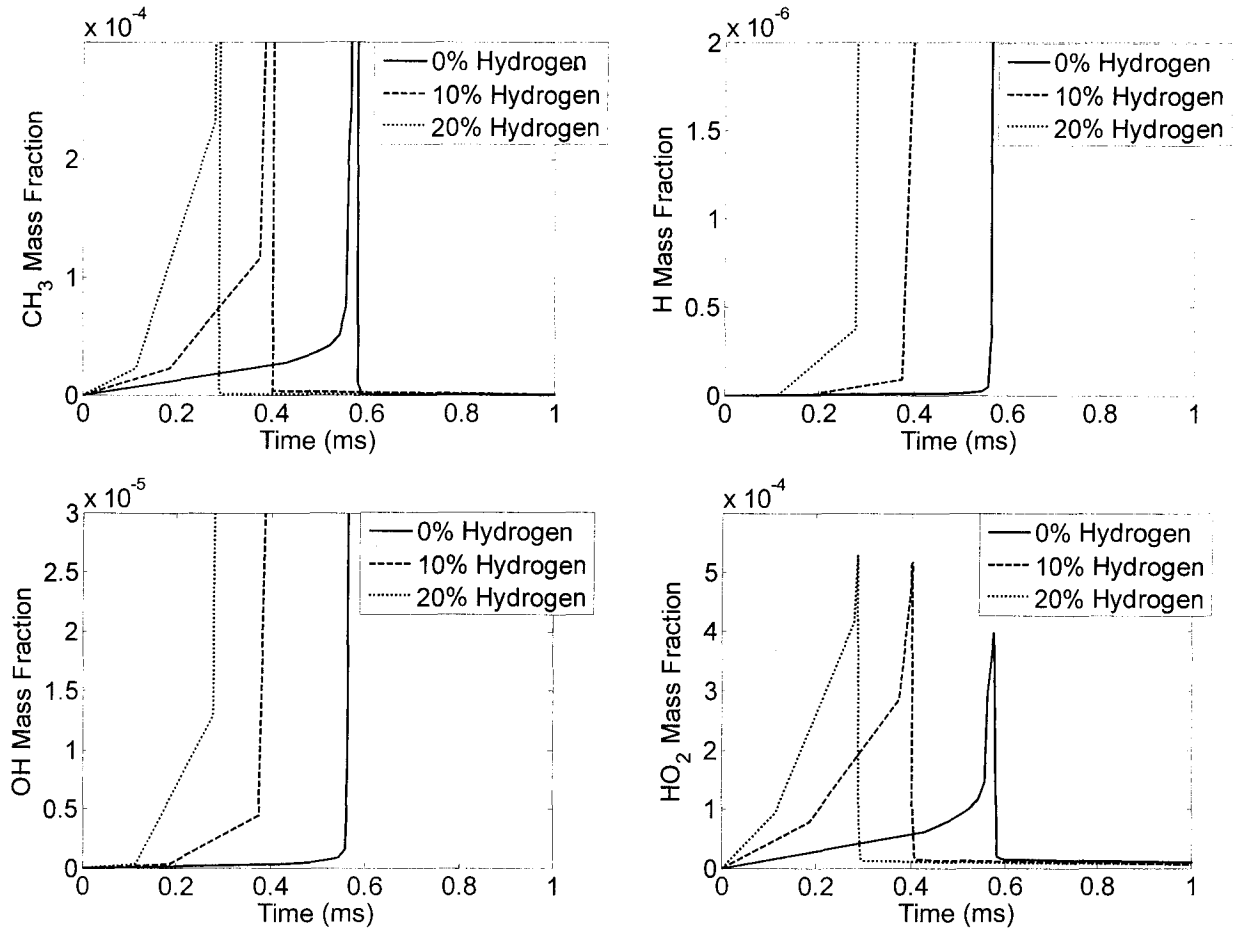
Figure 4.4 CH_3, H, OH, and HO_2 mass fraction history at Z_{st} for methane/hydrogen blends

$(T_f=300$ K, $T_o=1300$ K, P=30 bar, $\chi=1)$

Effect of Nitrogen Addition

Figure 4.5 shows the FlameMaster results for nitrogen addition. These results predict that the presence of nitrogen in the fuel will result in longer ignition delays than for the baseline methane fuel. Interestingly, the increase in the ignition delay is not proportional to the nitrogen concentration. The ignition delay increases by 11% when 10% nitrogen is added to methane, and remains unchanged with 20% nitrogen addition.

Figure 4.6 shows the species mass fraction history for CH_3, H, OH, and HO_2 at Z_{st} for different methane/nitrogen blends (Table 4.3). The addition of nitrogen shows the opposite effect to ethane addition. With nitrogen dilution, the peaks of CH_3, H, OH, and HO_2 mass fraction are all retarded in time. When the nitrogen concentration increases, a less rapid rise in mass fraction right after the start of the reaction for all these species is observed. All of these effects contribute to inhibit the methane oxidation and result in a longer ignition delay.
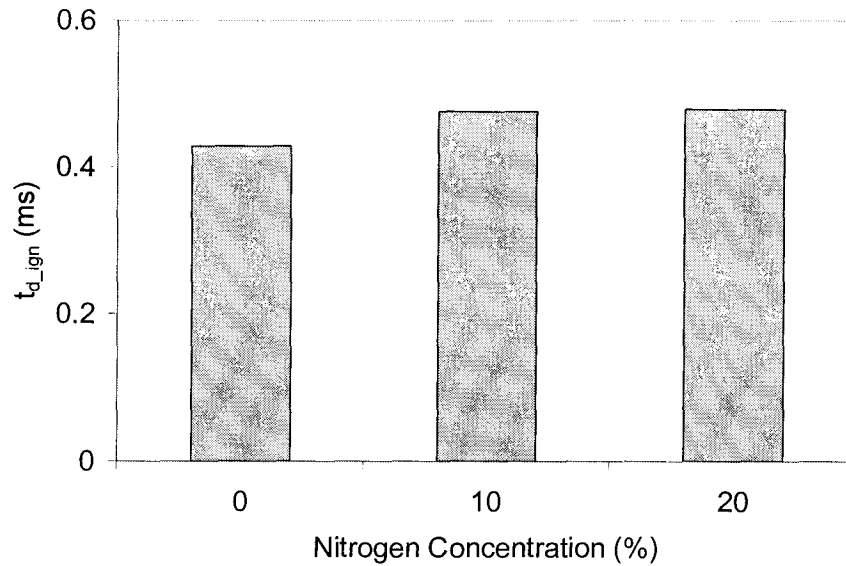
Figure 4.5 The effect of nitrogen addition on t_{d_ign} (T_f=300 K, T_o=1300 K, P=30 bar, χ=1)

Comparison of Effects of Different Fuels

In appearance, the CH_3, H, OH, and HO_2 mass fraction history at Z_{st} for methane/ethane blends in Figure 4.2 is very similar to that for methane/hydrogen blends in Figure 4.4. Significantly, they are markedly different from the results for the methane/nitrogen blends shown in Figure 4.6. To more clearly show the differences and the similarities between the behaviour of the three different fuel additives, the time axes of the CH_3, H, OH, and HO_2 mass fraction profiles in Figures 4.2, 4.4, and 4.6 are normalized by the time when the peak is reached for each fuel blend and the results are summarized in Figures 4.7 and 4.8.

With ethane or hydrogen addition, the CH_3, H, OH, and HO_2 mass fraction evolves differently in time. While with nitrogen addition, the normalized curves almost overlap each other. This is evidence that the presence of ethane or hydrogen changes the ignition chemistry of methane, while nitrogen appears to only add thermal mass to the fuel and is not involved in chemical reactions generating reactive radicals.

Table 4.3 Z_{st} for different methane/nitrogen blends

	0% Nitrogen	10% Nitrogen	20% Nitrogen
Z_{st}	0.0552	0.0652	0.0774
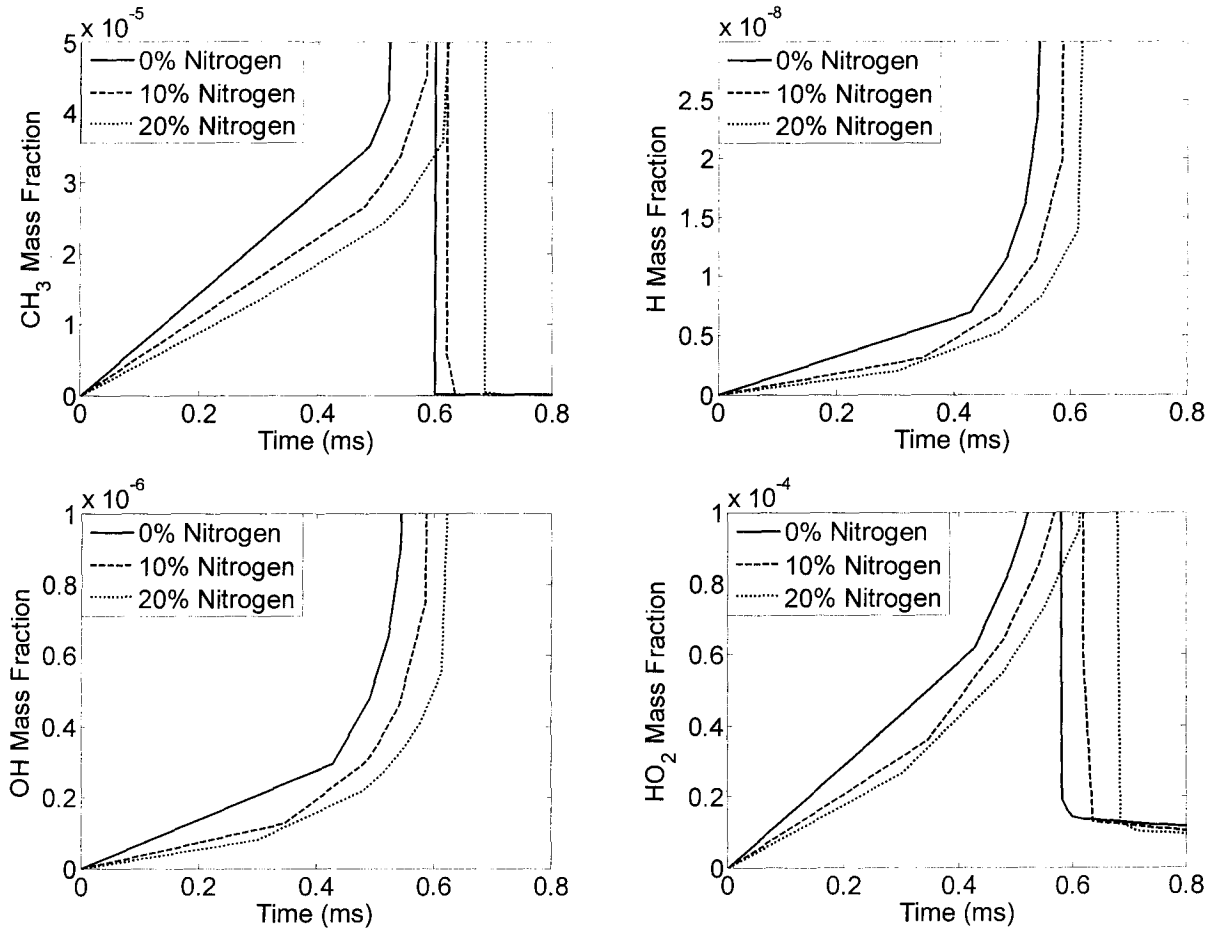
Figure 4.6 CH_3, H, OH, and HO_2 mass fraction history at Z_{st} for methane/nitrogen blends

(T_f=300 K, T_o=1300 K, P=30 bar, χ=1)
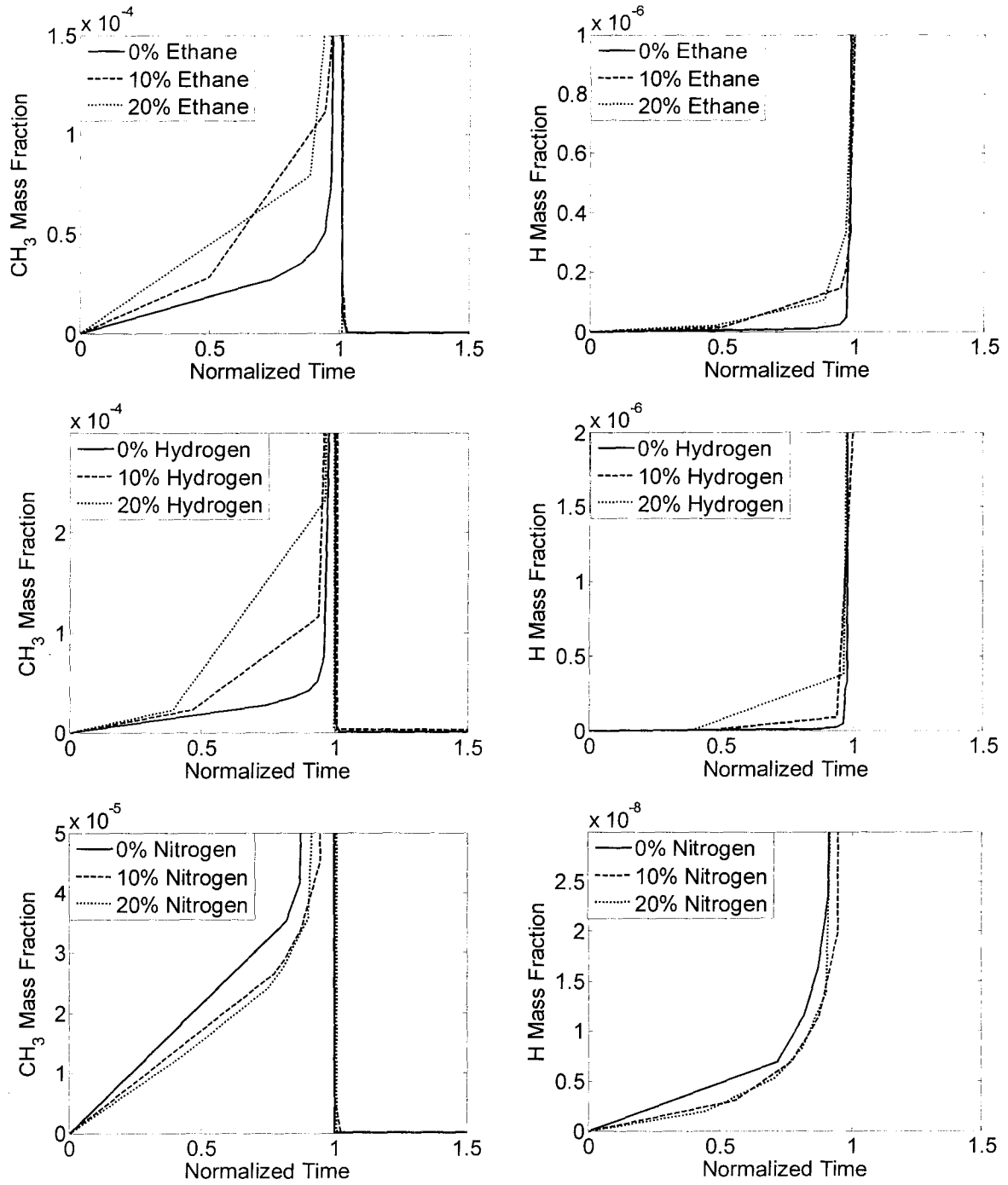
Figure 4.7 Normalized CH_3 and H mass fraction history at Z_{st} for different fuels

$(T_f=300$ K, $T_o=1300$ K, P=30 bar, $\chi=1)$
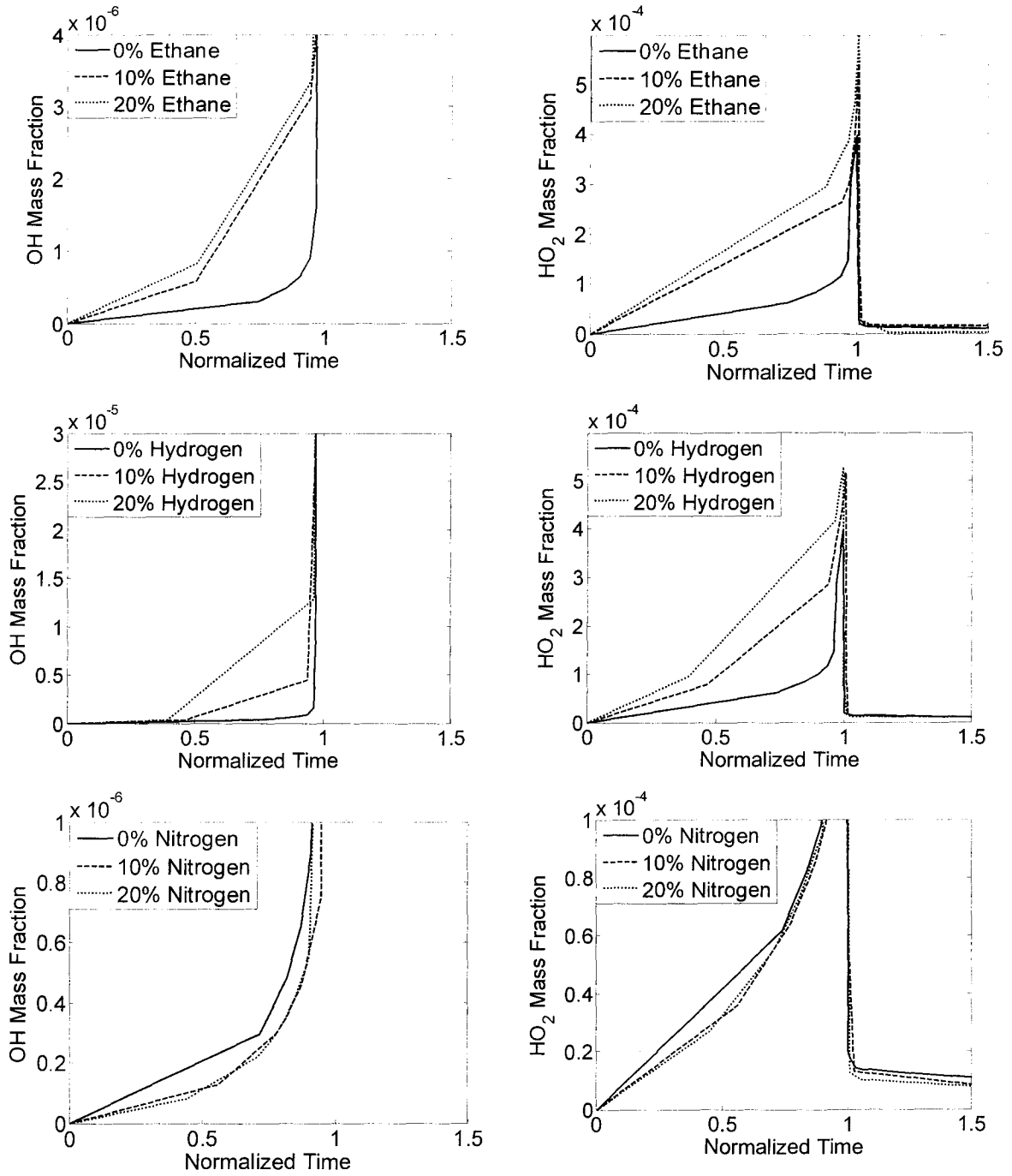
Figure 4.8 Normalized OH and HO_2 mass fraction history at Z_{st} for different fuels

(T_f=300 K, T_o=1300 K, P=30 bar, χ=1)

4.2.2 Initial Air Temperature

Figure 4.9 shows the effect of initial air temperature on ignition delay as predicted by FlameMaster. For all the four fuels there is a steady decrease in ignition delay when temperature increases from 1200 to 1400 K. The ignition delay increases with nitrogen addition, and decreases with ethane or hydrogen addition for all the five temperatures studied. The difference in the ignition delay for different fuels is more prominent at lower temperatures.

···· Methane --- 10% Ethane --- 20% Hydrogen —— 20% Nitrogen
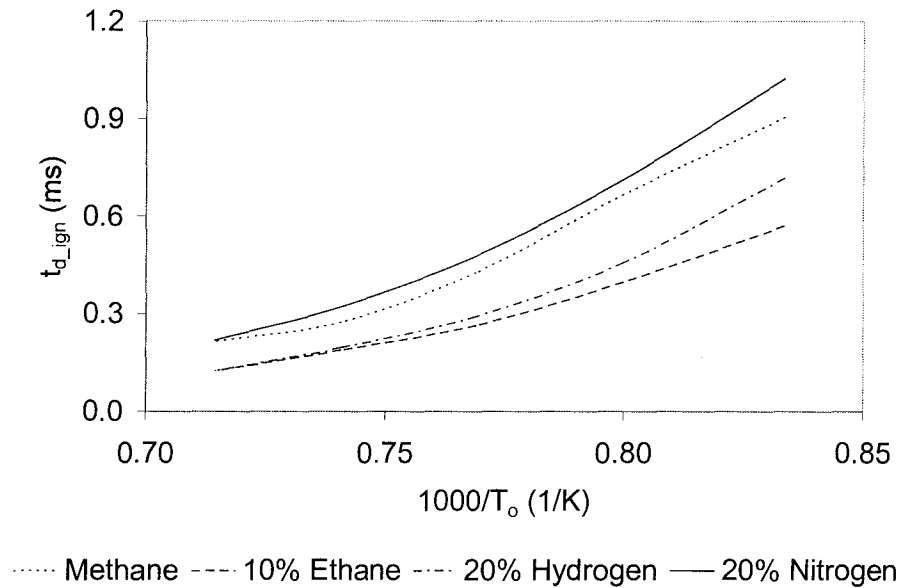
Figure 4.9 t_{d_ign} variation with T_o (T_f=300 K, P=30 bar, χ=1)

4.2.3 Scalar Dissipation Rate

In turbulent flows, the scalar dissipation is seen as a scalar energy dissipation and its role is to destroy (dissipate) scalar variance (scalar energy) analogous to the dissipation of the turbulent kinetic energy. The scalar dissipation is indirectly a function of injection pressure ratio, in that a high injection pressure ratio will lead to a higher jet momentum, in turn leading to a higher jet Reynolds number and hence to increased mean and peak scalar dissipation and increased fluctuations in scalar dissipation. If the dissipation rate is too high, autoignition will be inhibited since the heat released in the combustion process is dissipated too quickly. Extinction might even occur at high enough scalar dissipation rate.

Figure 4.10 shows the effect of scalar dissipation rate on ignition delay for different fuels. For all the four fuels, the ignition delay increases with increasing scalar dissipation rate. This suggests that the ignition-promoting effect of scalar dissipation is not prominent under the conditions studied. The ignition delay increases with nitrogen addition, and decreases with ethane or hydrogen addition for all the five scalar dissipation rates studied. At χ=100, ignition could not be achieved for all the four fuels.

····· Methane ─ ─ ─ 10% Ethane ─··─ 20% Hydrogen ─── 20% Nitrogen
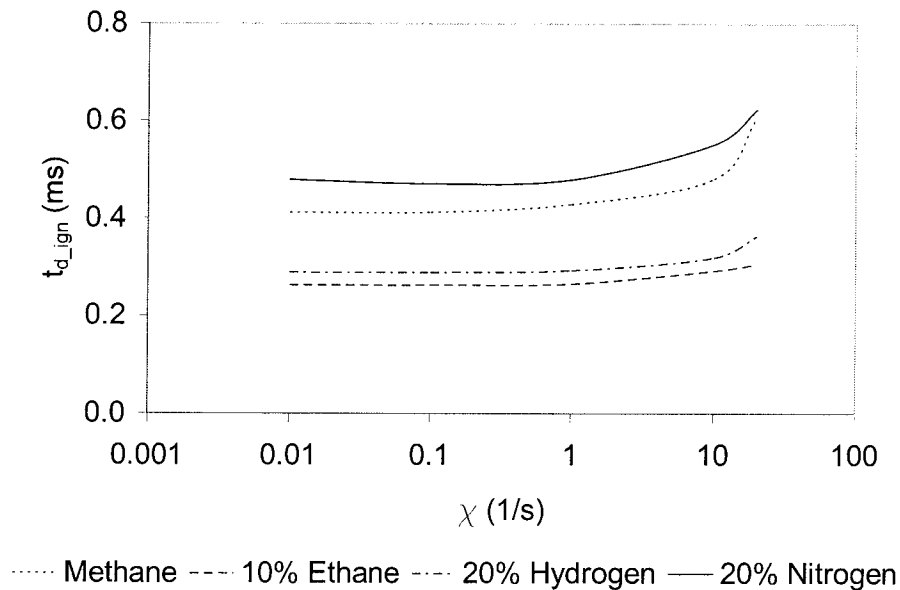
Figure 4.10 t_{d_ign} variation with scalar dissipation rate (T_f=300 K, T_o=1300 K, P=30 bar)

4.3 Conclusions

A non-premixed counter-flow diffusion flame of methane blended with different amount of ethane, hydrogen, or nitrogen and air was simulated using FlameMaster. The simulation results show that:

1. The ignition delay of the baseline fuel is reduced by the addition of ethane or hydrogen. The decrease in ignition time with ethane or hydrogen addition is shown to be caused by changes in the chemical kinetics – the addition of ethane or hydrogen accelerating the generation of reactive radicals.

2. The addition of nitrogen increases the ignition delay of the baseline fuel as a result of increased thermal mass. No changes in chemical kinetics are seen.

3. The ignition delay decreases with increasing initial air temperature. The difference in the ignition delay time for different fuels is more prominent at lower temperatures.

4. The ignition delay increases with increasing scalar dissipation rate to a limiting value beyond which combustion can not be sustained due to extinction.

Chapter 5
Thermodynamic and Gas Dynamic Effects on Ignition of Jets of Methane with Additives

5.1 Introduction

Chapter 3 of this work concluded with the observation that the significant scatter in the experimental results precluded the author from drawing conclusions regarding the effects of pre-combustion temperature, injection duration, and injection pressure on autoignition and combustion based upon the data from individual additives. However, when the results for all fuels are considered as a whole some clear trends emerge.

To demonstrate these trends, the present chapter represents results from Chapter 3 such that experiments with same operating conditions but different fuel compositions are summarized in a single plot. Furthermore, the experimental data are fitted to regression curves based on a least-squares analysis to help better identify the thermodynamic and gas dynamic effects on the ignition process. Typically, a simple linear regression is used to show an increasing or deceasing trend. Where applicable, the physical significance of a fitted trendline is discussed within the text.

5.2 Results

5.2.1 Ignition Delay

Figure 5.1 shows the variation of t_{d_ign} with T_o. The experimental data for all fuels shows, in agreement with the modelling results presented in the previous chapter, a clear trend of decreasing t_{d_ign} with increasing T_o. Assuming the autoignition process to be similar to that of a premixed homogeneous system in which a single-step reaction occurs, the experimental data in this figure are fitted to:

$$t_{d\_ign} = A \exp\left(\frac{E}{RT_o}\right) \tag{5.1}$$

where E is the global activation energy, R is the universal gas constant. The coefficients and R^2 values for the fitting are summarized in Table 5.1.
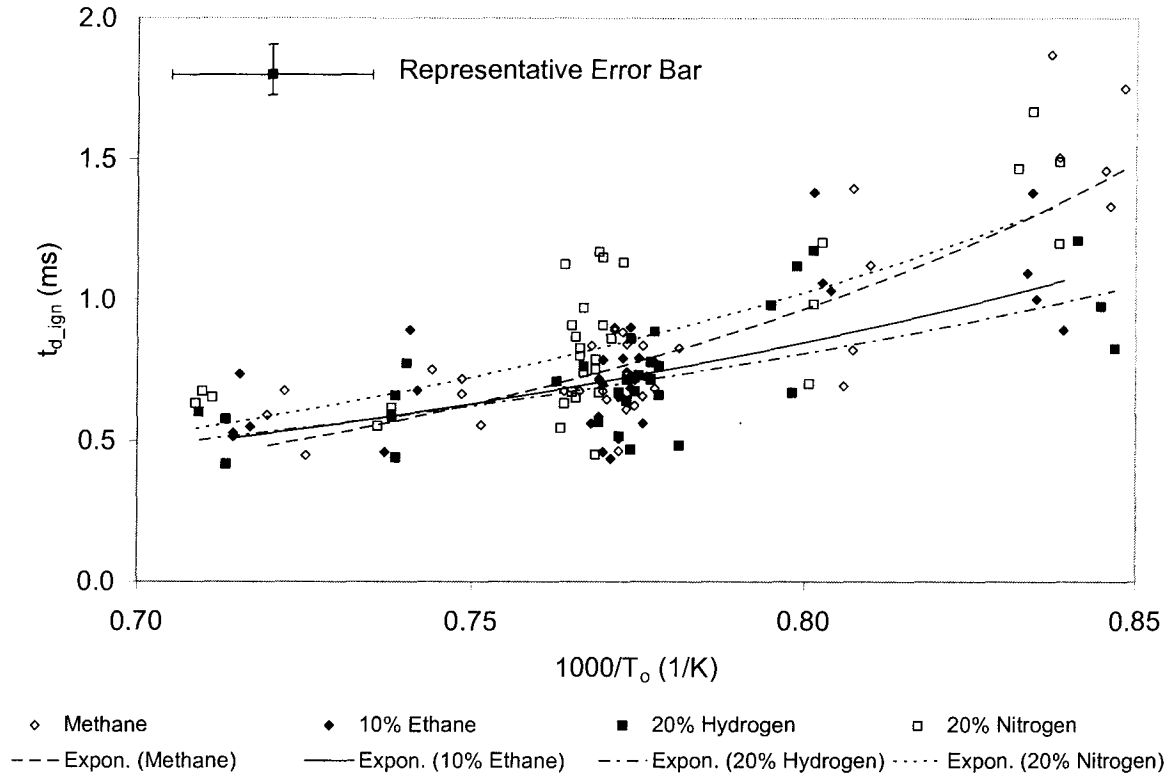
Figure 5.1 t_{d_ign} variation with T_o

Table 5.1 Least-squares fitting results for t_{d_ign} and T_o

	A (ms)	E (kcal/mol)	R^2
Methane	0.0010	17.1	0.6924
10% Ethane	0.0073	11.8	0.4372
20% Hydrogen	0.0124	10.4	0.4232
20% Nitrogen	0.0039	13.8	0.5097

R^2 values in Table 5.1 are calculated as:

$$R^2 = 1 - \frac{\sigma_{y,x}^2}{\sigma_y^2} \tag{5.2}$$

where

$$\sigma_y^2 = \sum_{i=1}^n \frac{(y_i - y_m)^2}{n-1} \tag{5.3}$$

$$\sigma_{y,x}^2 = \sum_{i=1}^n \frac{(y_i - y_{ic})^2}{n-2} \tag{5.4}$$

$$y_m = \frac{\sum_{i=1}^n y_i}{n} \tag{5.5}$$

The y_i are the actual values of y, and the y_{ic} are the values computed from the correlation equation for the same value of x.

For a perfect fit $\sigma_{y,x} = 0$ because there are no deviations between the data and the correlation. In this case $R^2 = 1$. If $\sigma_{y,x} = \sigma_y$, then $R^2 = 0$, indicating a poor fit or substantial scatter around the fitting curve. In the present study, because the significant scatter in the experimental data, it is not surprising to find that R^2 values are relatively low in general. However, R^2 values are expected to stabilize to a value less than 1 as the number of data points approach infinity, suggesting enough data points have been collected and converged results have been achieved.

The strong dependence on temperature seen in the results is attributed to the importance of chemical kinetic processes during the autoignition process under diesel engine conditions [21]. Numerical simulations by Bi and Agrawal [166] similarly concluded that the kinetic delay decreases as temperatures are increased. They proposed the notion of a "kinetic" and "physical" component to ignition delay time, and defined a kinetic delay as the ignition delay time component attributable to the chemical reaction and a physical delay as the portion attributable to the time necessary for the fuel and oxidant to mix and create a locally combustible mixture with a sufficiently favourable strain rate to facilitate autoignition.

It is interesting to note that there is reduced scatter in the measured ignition delay at higher temperatures for all fuels. The developing turbulent jet is stochastic in nature. Various realizations of the jet starting and penetration process yield different strain histories and mixture fraction histories, some of which provide more favourable conditions for kernel formation than others. However, at higher temperatures when the chemical kinetics are expected to be dominant, the physical mixing processes contribute less to the autoignition process and the scatter in the results should be expected to decrease.

Although the experimental results are characterized by significant scatter – particularly at lower pre-combustion temperatures – it is interesting to note that the global activation energy value for methane reported in Table 5.1 is very close to the value reported by Huang et al. [29] for premixed methane ignition under similar experimental conditions.

The results shown in Table 5.1 suggest that the global activation energy of the fuel decreases with either ethane or hydrogen addition. This is not surprising since both ethane and hydrogen promote the autoignition of methane through changes to the chemical kinetics as indicated by the FlameMaster results shown in the previous chapter. However,

the results shown in Table 5.1 also suggest that the global activation energy decreases with nitrogen dilution. This is unexpected since the FlameMaster results suggest that the presence of nitrogen simply increases the thermal mass of the fuel. It is most likely that this unusual result is the result of the scatter in the data. However, this is not confirmed at this time.

Injection duration has a potential influence on autoignition behaviour by virtue of its fuel metering properties, control of overall mixture equivalence ratio, and cooling effects. Additionally, the transient nature of short-duration impulsive jets produces a direct flow field dependence on injection duration, which dictates the temporal evolution of temperature, species, and velocity gradients in the flow, which in turn influence the thermodynamic, kinetic, and transport processes necessary for autoignition. Employing the ignition delay model of Bi and Agrawal [166], infinitesimally short injection durations will be expected to nearly instantly produce a combustible mixture (negligible mixing time scales) and the autoignition time will approach the kinetically-limited premixed autoignition delay time. At the opposite extreme, long injection durations reach a steady state after a fixed period of time and only produce a combustible mixture once the physical delay is exceeded.

Figure 5.2 shows the variation of t_{d_ign} with t_i. Interestingly, given the above discussion, no strong relation between t_{d_ign} and t_i is observed from the experimental data. Data in this figure are fitted to:

$$t_{d\_ign} = a + bt_i \tag{5.6}$$

The coefficients and R^2 values for the fitting are summarized in Table 5.2. The standard error of the slope estimate b, SE(b), is also shown in the table, which is calculated as:

$$SE(b) = \frac{SE(y)}{\sigma(x)\sqrt{n}} \tag{5.7}$$

where SE(y) is the standard error of the estimate of y for a given x:

$$SE(y) = \sqrt{\frac{1}{n-2}\left[\sum y_i^2 - \frac{1}{n}\left(\sum y_i\right)^2 - \frac{\left[\sum x_i y_i - \frac{1}{n}\sum x_i \sum y_i\right]^2}{\sum x_i^2 - \frac{1}{n}\left(\sum x_i\right)^2}\right]} \tag{5.8}$$

$\sigma(x)$ is the biased standard deviation of a:

$$\sigma(x) = \sqrt{\frac{\sum x_i^2}{n} - \frac{\left(\sum x_i\right)^2}{n^2}} \qquad (5.9)$$

and n is the number of data points.

The fitting results also show that there is no consistent trend between t_{d_ign} and t_i, as evidenced by the 2 positive and 1 negative slopes. For ethane addition case, the lower limit and upper limit of the slope is -0.0130 and 0.0976, respectively, suggesting there is no obvious dependence of t_{d_ign} on t_i
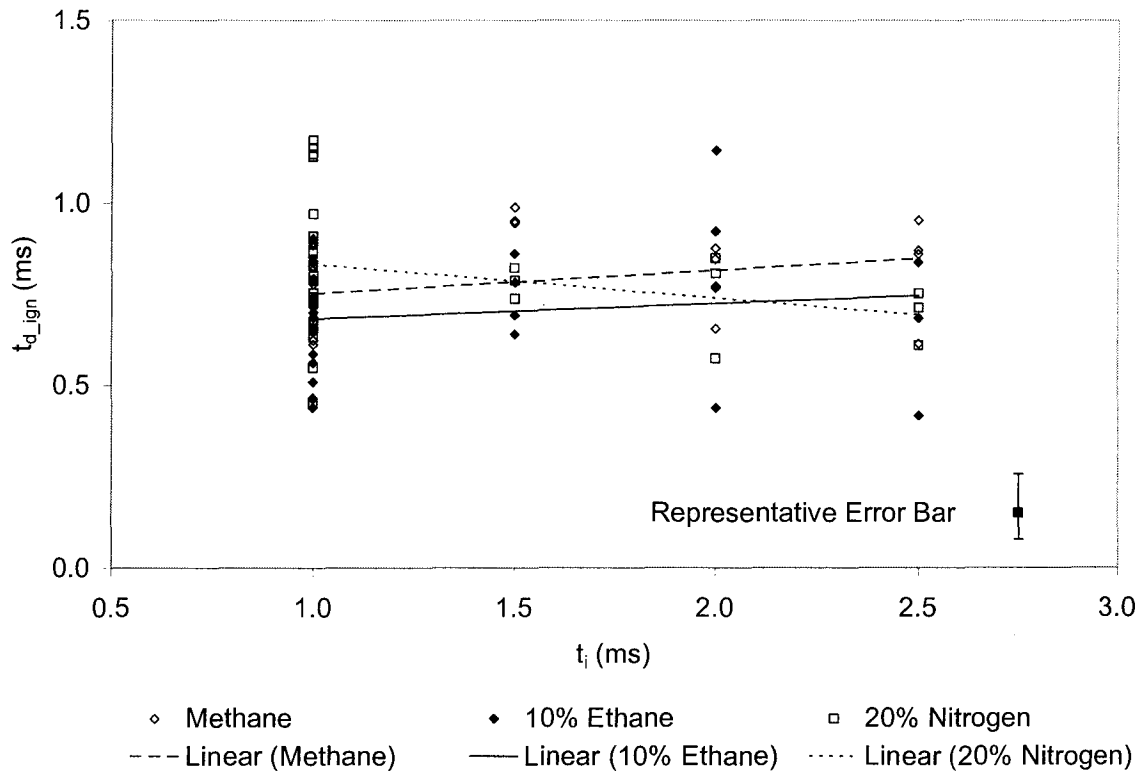
Figure 5.2 t_{d_ign} variation with t_i

Table 5.2 Least-squares fitting results for t_{d_ign} and t_i

	a (ms)	b	SE(b)	R^2
Methane	0.6878	0.0641	0.0402	0.0807
10% Ethane	0.6404	0.0423	0.0553	0.0198
20% Nitrogen	0.9254	-0.0929	0.0640	0.0724

On further consideration, the independence between t_{d_ign} and t_i observed in Figure 5.2 is not surprising. With the small gas hole used in this study, the choke point is moved from the needle/nozzle interface within the injector to the gas hole, making the injector quite insensitive to the lift of the needle. When the needle closes, there remains a high pressure trapped in the sac. This suggests that the injector is injecting for an additional period after the needle closes, thus extending the perceived injection time, which leads to the insensitivity of t_{d_ign} on t_i observed here.

Figure 5.3 shows the variation of t_{d_ign} with P_i/P_o for all fuel blends considered in this study. A consistent trend is seen in the data whereby t_{d_ign} appears to decrease with increasing P_i/P_o, and starts to increase at higher values of P_i/P_o. To capture this feature, data in this figure are fitted to second-order polynomial curves:

$$t_{d\_ign} = a + b(P_i / P_o) + c(P_i / P_o)^2 \qquad (5.10)$$

The coefficients and R^2 values for this fitting are summarized in Table 5.3. It can be seen from the figure that the second-order polynomial curves achieve a reasonable fit to the experimental results, with a lowest R^2 value of 0.2362 among the 4 sets of data. The fitting results also suggest that minimum t_{d_ign} is reached at modest values of P_i/P_o.

The dependence of ignition delay on injection pressure is explicable if one again adopts the notion of a "kinetic" and "physical" component to ignition delay time as proposed by Bi and Agrawal [166]. Increasing the injection pressure ratio will yield a higher Reynolds number and certainly improves mixing between fuel and oxidant. This will reduce the physical delay. Also, at higher injection pressure ratios more fuel is injected in the same time interval, increasing the likelihood of collisions between fuel molecules and oxygen molecules in the surrounding air. However, as described in §4.2.3 if the injection pressure is increased excessively, the scalar dissipation rate may become so large as to dissipate any heat released in the combustion process so rapidly that any small flame kernels that are formed are immediately extinguished.
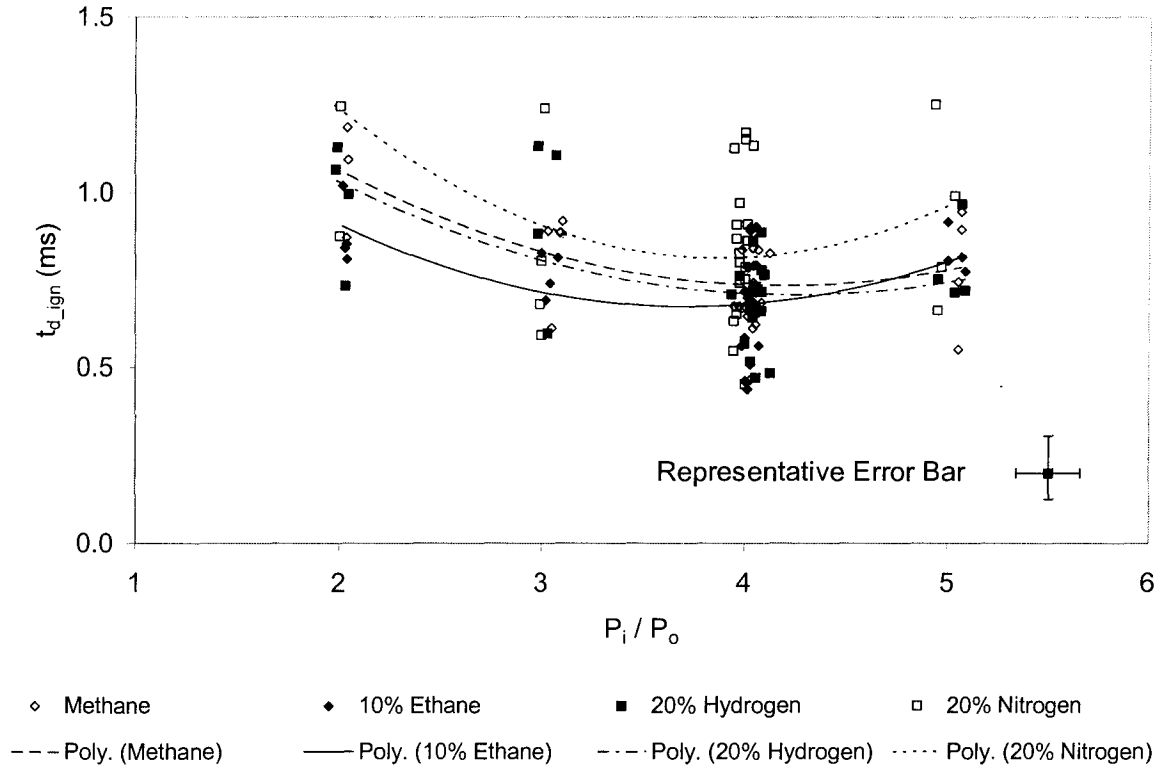
Figure 5.3 t_{d_ign}-variation with P_i/P_o

Table 5.3 Least-squares fitting results for t_{d_ign} and P_i/P_o

	a (ms)	b (ms)	c (ms)	R^2
Methane	1.9319	-0.5712	0.0682	0.3681
10% Ethane	1.7640	- 0.5858	0.0788	0.3601
20% Hydrogen	1.8529	- 0.5393	0.0636	0.3487
20% Nitrogen	2.6010	- 0.9208	0.1186	0.2362

5.2.2 Ignition Kernel Location

Figures 5.4 and 5.5 show the variation of Z_k/Z_t and Z_k^* with T_o, respectively for all fuels under consideration. A linear regression was used to fit the data in these two figures with the form:

$$Z_k / Z_t = a + b(1000 / T_o) \tag{5.11}$$

$$Z_k^* = a + b(1000 / T_o) \tag{5.12}$$

The fitting results are summarized in Tables 5.4 and 5.5.

The significant scatter in the data results in low R^2 values in all cases. The results of the line fit do not indicate any trend between Z_k/Z_t and T_o, as evidenced by the low absolute value and high standard error of the slope. There does appear to be a common trend toward decreasing Z_k^* with increasing T_o however, as evidenced by the high absolute value and relatively low standard error of the slope.
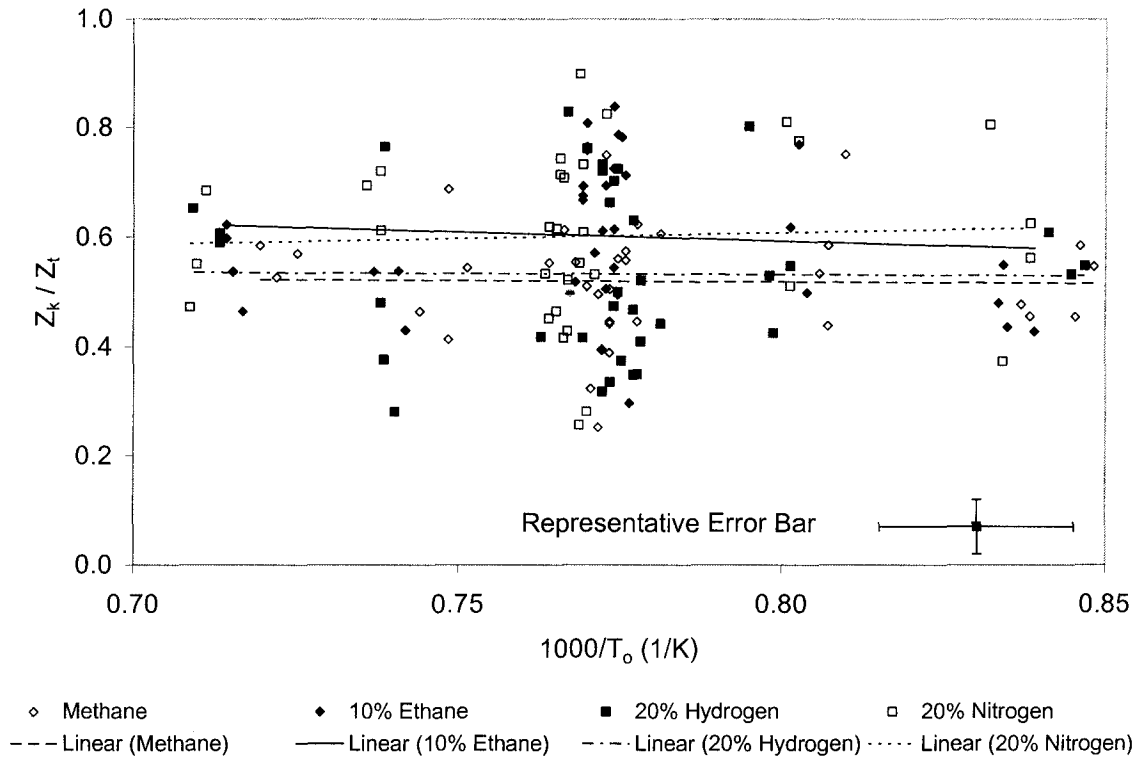
Figure 5.4 Z_k/Z_t variation with T_o

Table 5.4 Least-squares fitting results for Z_k/Z_t and T_o

	A	b (K)	SE(b) (K)	R^2
Methane	0.5616	-0.0539	0.5392	0.0003
10% Ethane	0.8572	-0.3303	0.7315	0.0063
20% Hydrogen	0.5672	-0.0443	0.8307	9×10^{-5}
20% Nitrogen	0.4368	0.2143	0.8627	0.0020
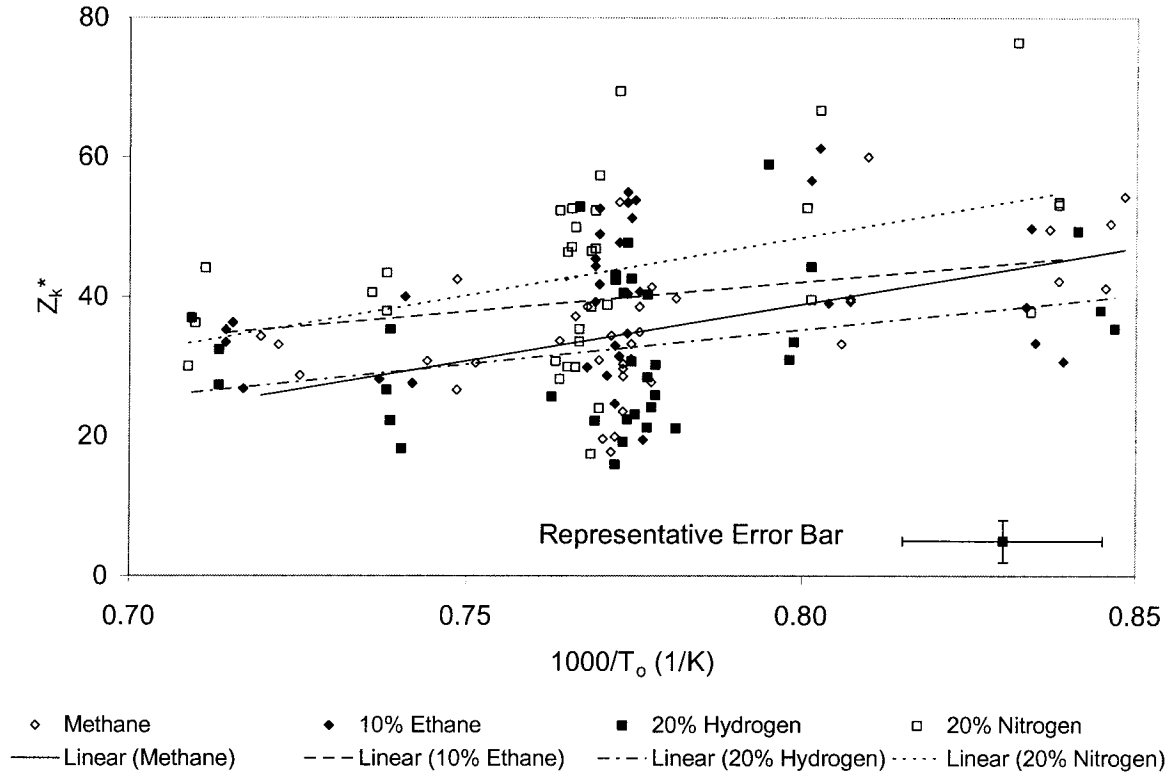
Figure 5.5 Z_k^* variation with T_o

Table 5.5 Least-squares fitting results for Z_k^* and T_o

	A	b (K)	SE(b) (K)	R^2
Methane	- 91.261	162.74	41.83	0.3080
10% Ethane	- 25.934	85.10	54.85	0.0699
20% Hydrogen	- 44.471	99.69	56.76	0.0879
20% Nitrogen	- 84.572	166.35	64.82	0.1752

To get further insight into the relation between ignition kernel location and pre-combustion temperature, Figures 5.6 and 5.7 show the variation of Z_t and Z_k with T_o, respectively. Both Z_t and Z_k appear to decrease with increasing T_o. Linear regression is used to fit the data in these two figures with the form:

$$Z_t = a + b(1000 / T_o)$$
(5.13)

$$Z_k = a + b(1000 / T_o)$$
(5.14)

The fitting results are summarized in Tables 5.6 and 5.7.

All the slopes in Tables 5.6 and 5.7 are positive and the standard errors of the slopes are relatively low, suggesting there is a trend of decreasing Z_k and Z_t with increasing T_o. Shorter ignition delay at higher temperature results in shorter jet length when ignition occurs, as shown in Figure 5.6. Since Z_k/Z_t is almost unchanged with increasing temperature as shown in Figure 5.4, it is reasonable that both Z_k and $Z_k{}^*$ decrease with increasing temperature, as shown in Figures 5.7 and 5.5, respectively.
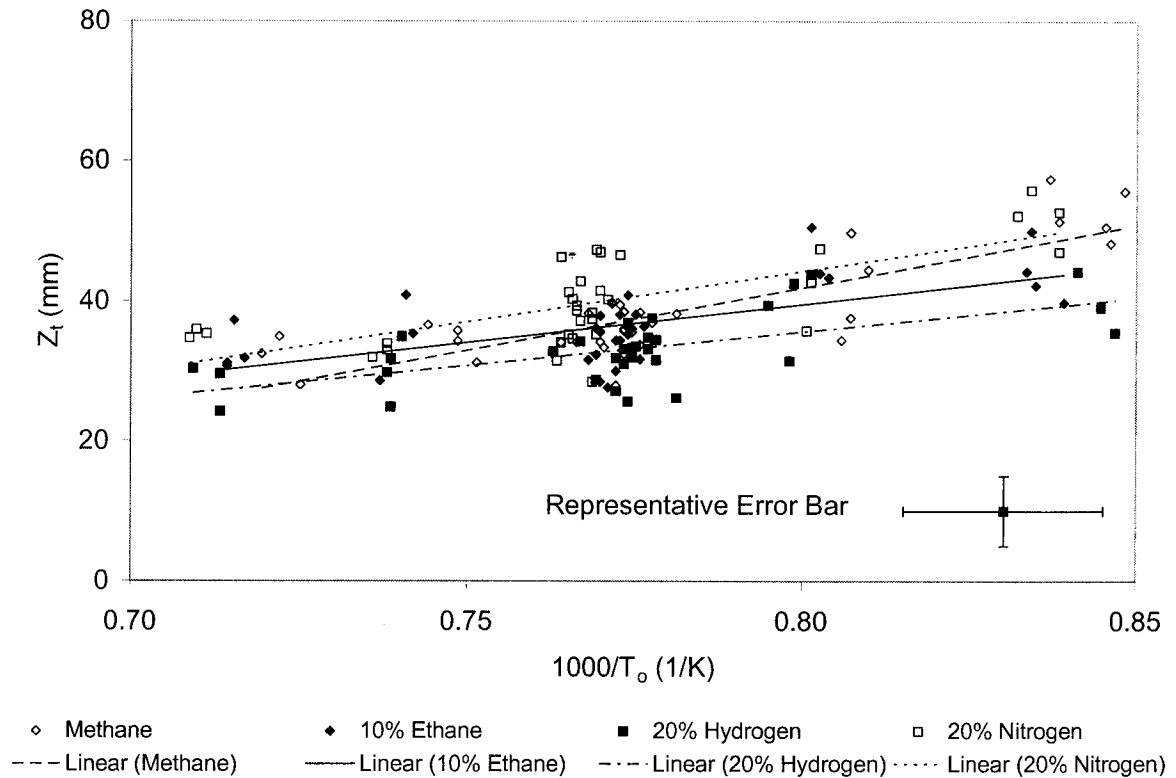
Figure 5.6 Z_t variation with T_o

Table 5.6 Least-squares fitting results for Z_t and T_o

	a (mm)	b (mm/K)	SE(b) (mm/K)	R^2
Methane	- 100.56	178.08	21.13	0.6762
10% Ethane	- 47.525	108.84	23.48	0.4017
20% Hydrogen	- 41.498	96.43	21.10	0.3948
20% Nitrogen	- 70.812	143.84	25.82	0.5002
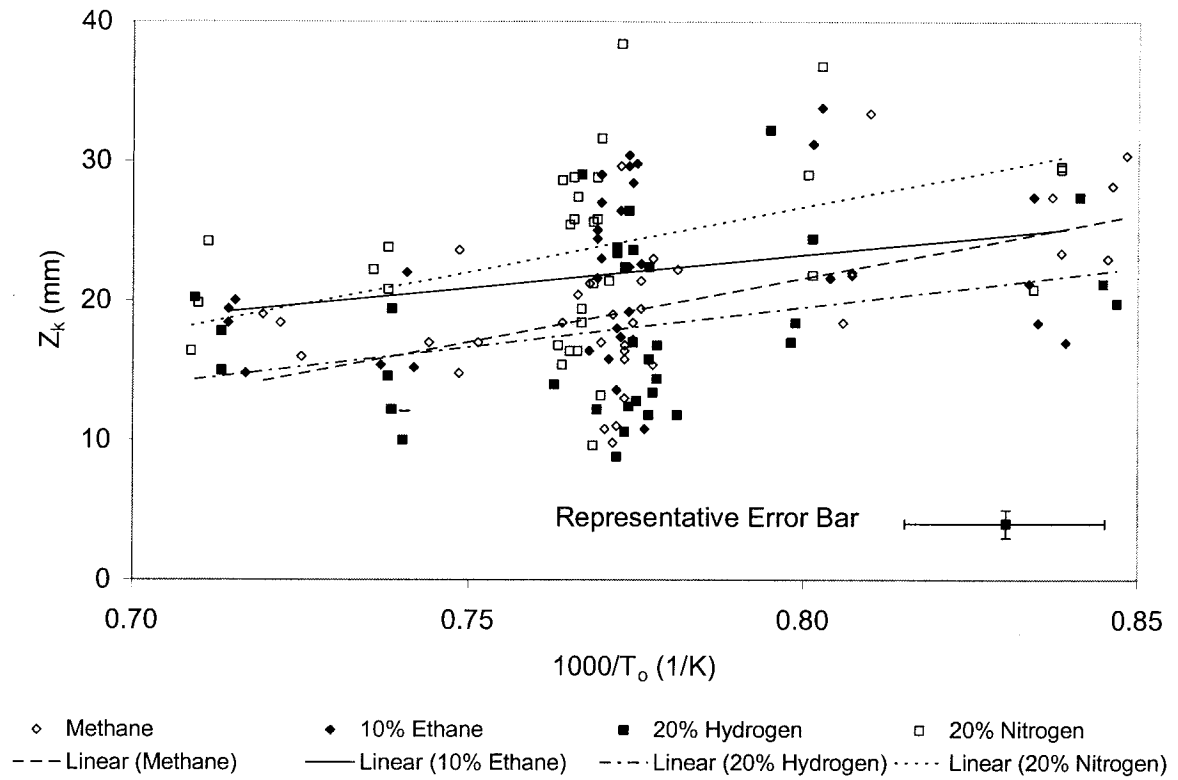
Figure 5.7 Z_k variation with T_o

Table 5.7 Least-squares fitting results for Z_k and T_o

	a (mm)	b (mm/K)	SE(b) (mm/K)	R^2
Methane	- 51.444	91.302	23.312	0.3109
10% Ethane	- 14.590	47.297	30.334	0.0706
20% Hydrogen	- 26.133	57.074	31.068	0.0954
20% Nitrogen	- 47.824	93.146	34.714	0.1799

Figures 5.8 and 5.9 show the variation of Z_k/Z_t and Z_k^* with t_i, respectively. Linear regression is used to fit the data in these two figures with the form:

$$Z_k / Z_t = a + bt_i \qquad (5.15)$$

$$Z_k^* = a + bt_i \qquad (5.16)$$

The fitting results in Tables 5.8 and 5.9 do not indicate any consistent trend between either Z_k/Z_t and t_i, or Z_k^* and t_i.
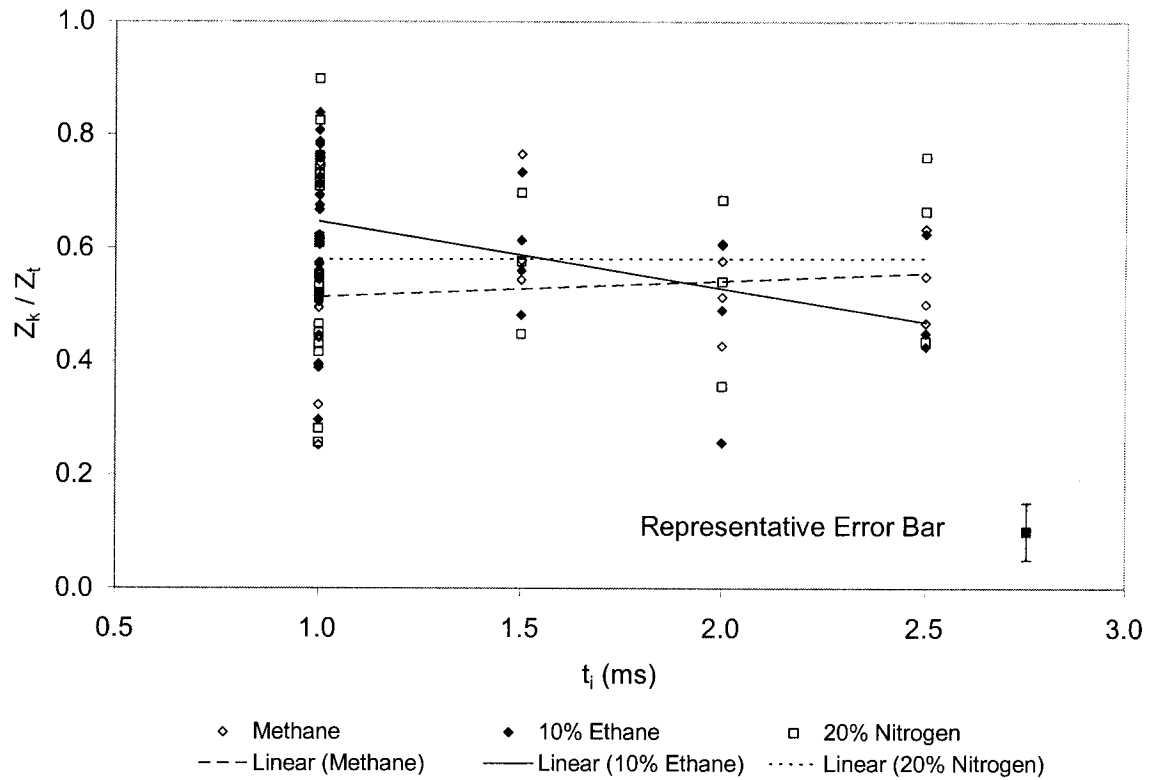
Figure 5.8 Z_k/Z_t variation with t_i

Table 5.8 Least-squares fitting results for Z_k/Z_t and t_i

	a	b (1/ms)	SE(b) (1/ms)	R^2
Methane	0.4856	0.0282	0.0353	0.0216
10% Ethane	0.7649	-0.1181	0.3163	0.1769
20% Nitrogen	0.4856	0.0282	0.0628	0.0216
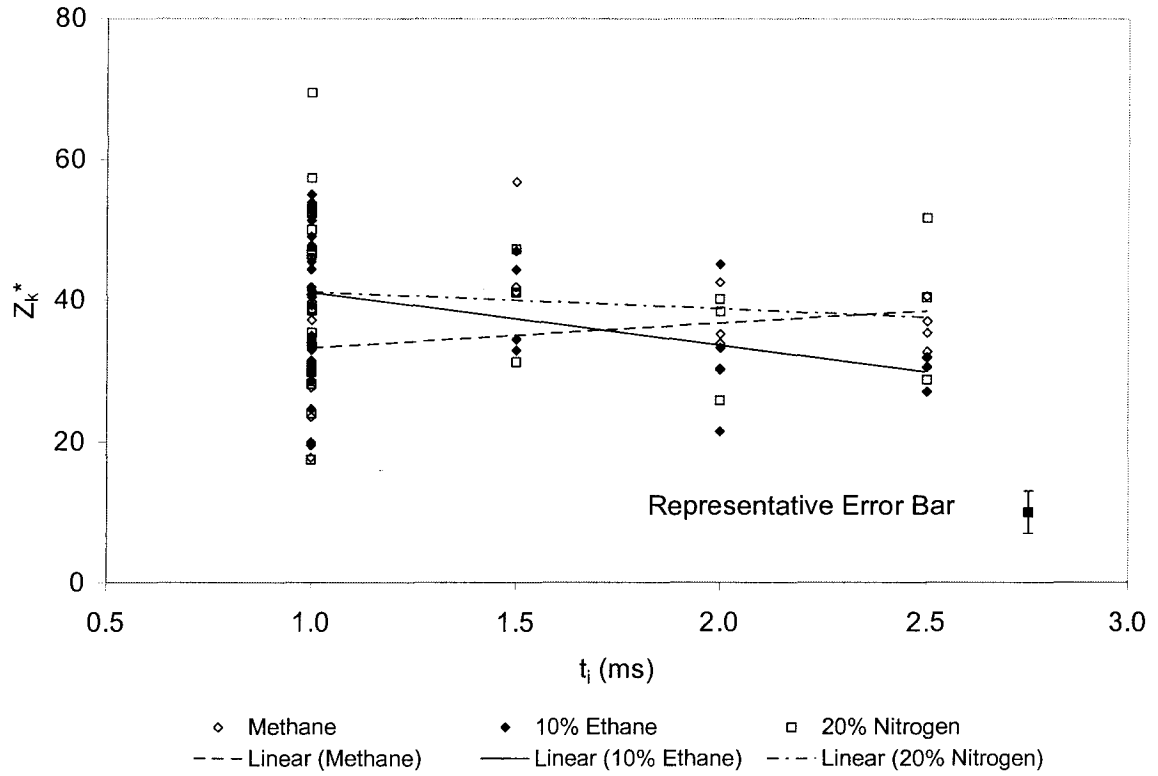
Figure 5.9 Z_k^* variation with t_i

Table 5.9 Least-squares fitting results for Z_k^* and t_i

	a	b (1/ms)	SE(b) (1/ms)	R^2
Methane	29.823	3.477	2.746	0.0524
10% Ethane	48.526	-7.446	3.292	0.1500
20% Nitrogen	43.542	-2.367	4.228	0.0115

Figure 5.10 shows the variation of Z_k/Z_t with P_i/P_o. Data in this figure are fitted to:

$$Z_k / Z_t = a + b(P_i / P_o) \tag{5.17}$$

The fitting results in Table 5.10 indicate a common trend of increasing Z_k/Z_t with increasing pressure ratio, P_i/P_o, for all fuels.
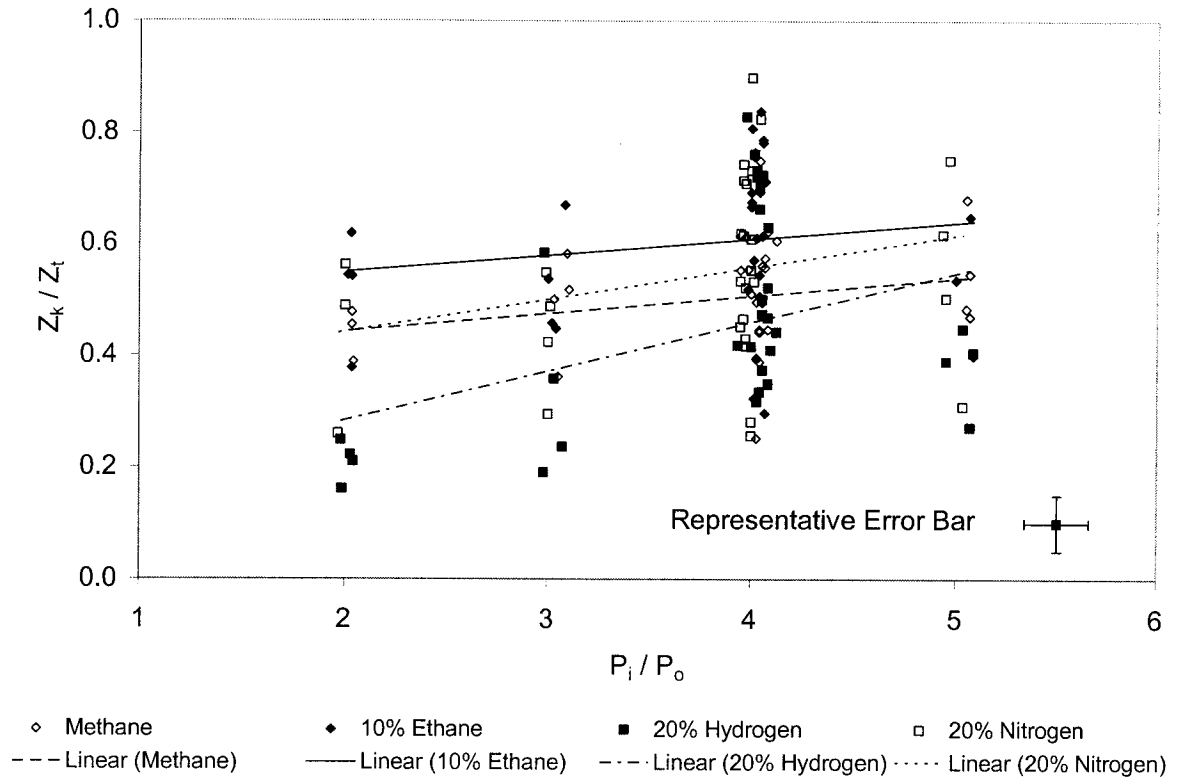
Figure 5.10 Z_k/Z_t variation with P_i/P_o

Table 5.10 Least-squares fitting results for Z_k/Z_t and P_i/P_o

	a	b	SE(b)	R^2
Methane	0.3788	0.0319	0.0235	0.0595
10% Ethane	0.4904	0.0296	0.0293	0.0328
20% Hydrogen	0.1076	0.0879	0.0364	0.1769
20% Nitrogen	0.3264	0.0578	0.0411	0.0718

The relationships between jet length, Z_t, ignition kernel location, Z_k, and injection pressure ratio, P_i/P_o, are considered further in Figures 5.11 and 5.12, respectively. Linear regression is used to fit the data in these two figures with the form:

$$Z_t = a + b(P_i / P_o) \tag{5.18}$$

$$Z_k = a + b(P_i / P_o) \tag{5.19}$$

The fitting results are summarized in Tables 5.11 and 5.12. All the slopes in Tables 5.11 and 5.12 are positive and the standard errors of the slopes are relatively low, indicating that there is a common trend of increasing Z_t and Z_k with increasing P_i/P_o.
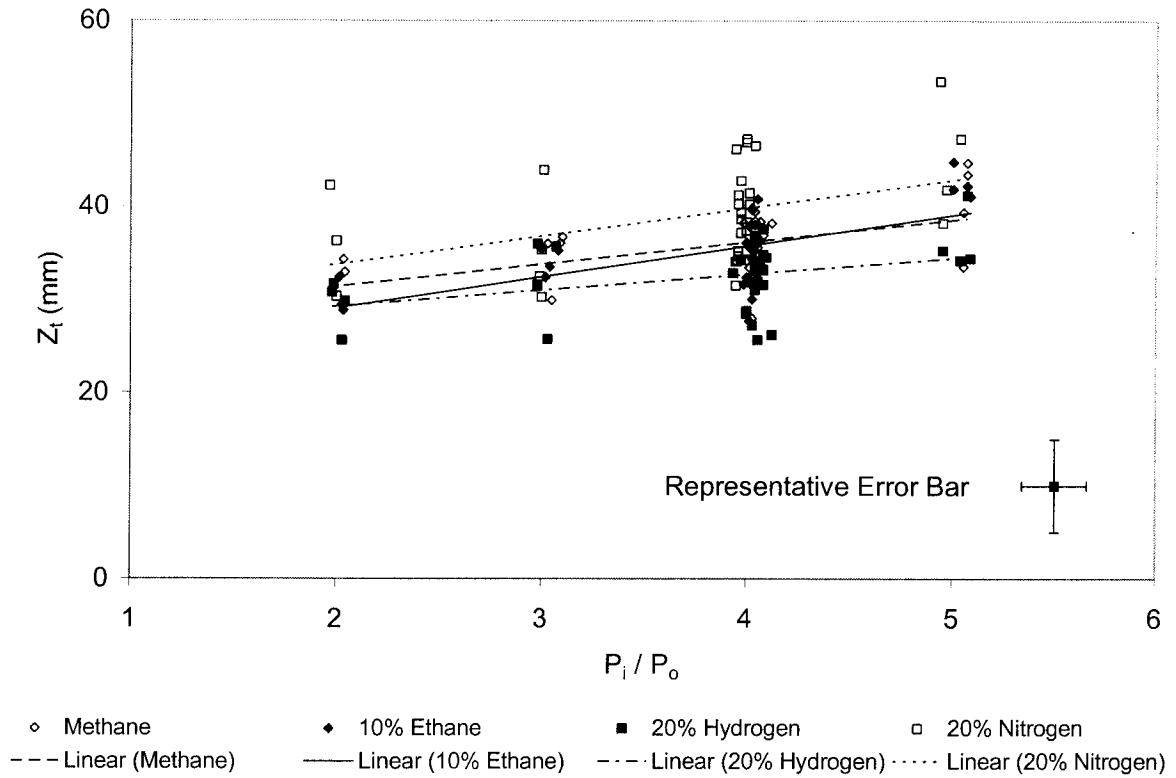
Figure 5.11 Z_t variation with P_i/P_o

Table 5.11 Least-squares fitting results for Z_t and P_i/P_o

	a (mm)	b (mm)	SE(b) (mm)	R^2
Methane	26.621	2.3895	0.7525	0.2580
10% Ethane	22.359	3.3492	0.6968	0.4350
20% Hydrogen	25.769	1.7376	0.7101	0.1664
20% Nitrogen	27.688	3.0360	1.2789	0.1627

There are two competing effects of injection pressure ratio present. Increasing P_i/P_o will act to increase jet length at a fixed time after injection. Meanwhile, modestly increasing P_i/P_o also acts to reduce ignition delay through improved mixing as discussed in §5.2.2. In turn, reduced ignition delay results in a shorter jet length when ignition occurs. In Figure 5.11, Z_t increases with increasing P_i/P_o, suggesting that the effect of P_i/P_o on jet length is more prominent than its effect on ignition delay for all of the fuels considered. Since Z_k/Z_t appears to increase slightly with increasing P_i/P_o, it is reasonable that Z_k also increases with increasing P_i/P_o, as shown in Figure 5.12.
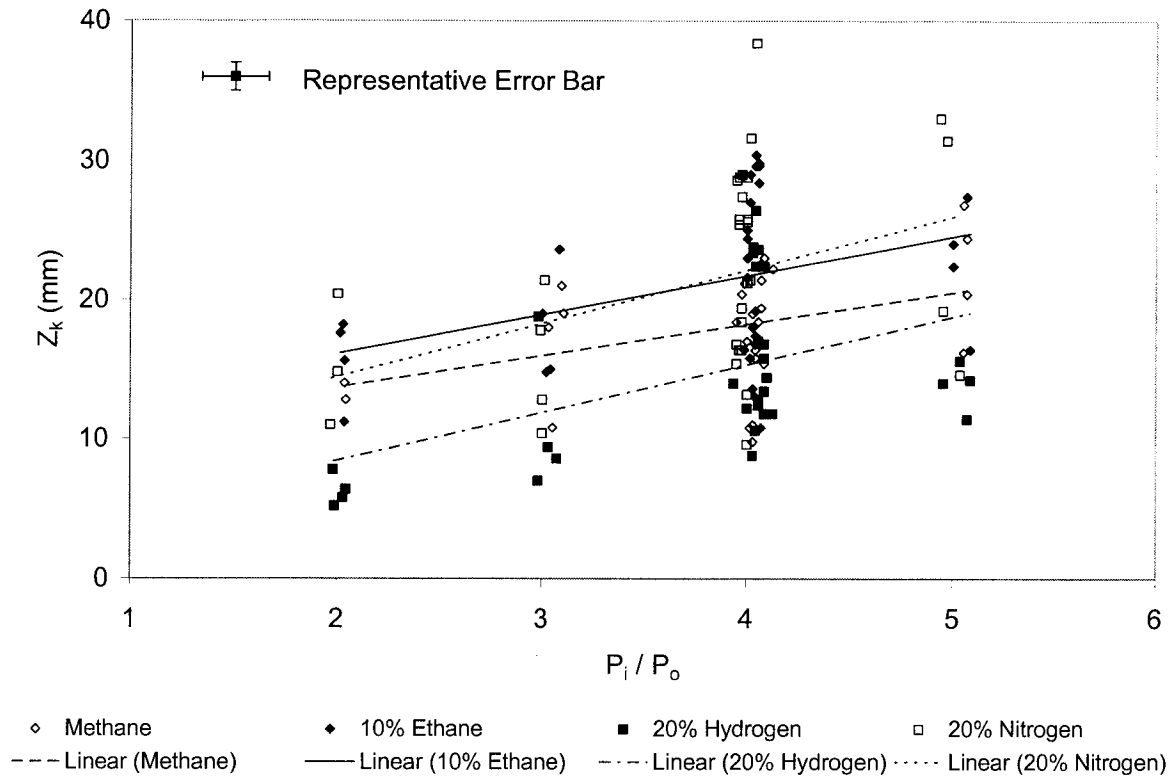
Figure 5.12 Z_k variation with P_i/P_o

Table 5.12 Least-squares fitting results for Z_k and P_i/P_o

	a (mm)	b (mm)	SE(b) (mm)	R^2
Methane	9.1855	2.2659	1.0104	0.1478
10% Ethane	10.548	2.7973	1.1131	0.1739
20% Hydrogen	1.5650	3.4403	1.1917	0.2174
20% Nitrogen	6.7979	3.8338	1.5908	0.1669

To conclude this discussion of jet penetration and ignition kernel location, it should be noted that Z_t will be dependant to some extent on the density of the injected fuel. The addition of ethane or nitrogen to methane increases the density of the fuel blend, increasing the penetration of the jet, while the addition of hydrogen reduces the density and decreasing the jet penetration. However, the changes in penetration distance due to the density changes of the fuels are small. Figure 5.13 shows the predicted jet penetration for the four fuels under consideration in this work calculated using the scaling model of Hill and Ouellette [63].
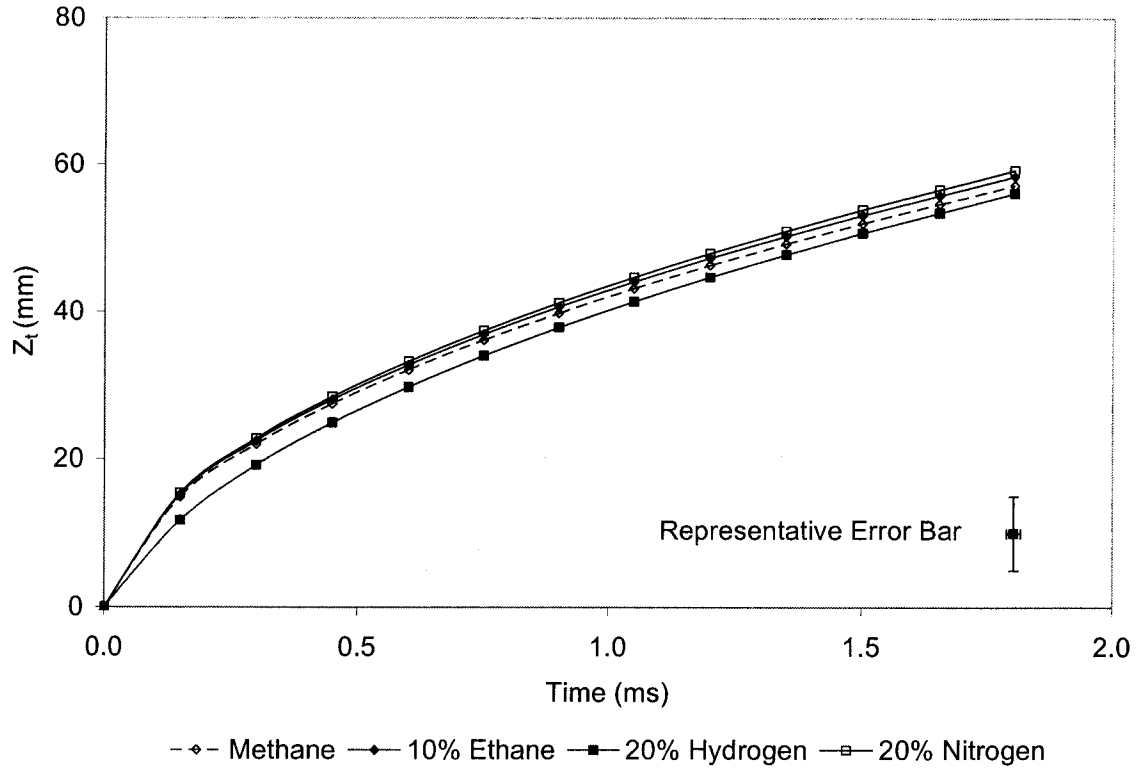
Figure 5.13 Estimated Z_t as function of time based on scaling model

$(T_f=300 \text{ K}, T_o=1300 \text{ K}, P_i/P_o=4)$

5.2.3 NOx Emissions

Figure 5.14 shows normalized NOx emissions variation with T_o. Data in this figure are fitted to:

$$Normalized\ NOx\ Emissions = a + b(1000/T_o) \qquad (5.20)$$

The fitting results are summarized in Table 5.13.

All the slopes reported in Table 5.13 are negative and the standard errors of the slopes are relatively low, indicating that there is a common trend of increasing NOx emissions with increasing T_o regardless of fuel composition.
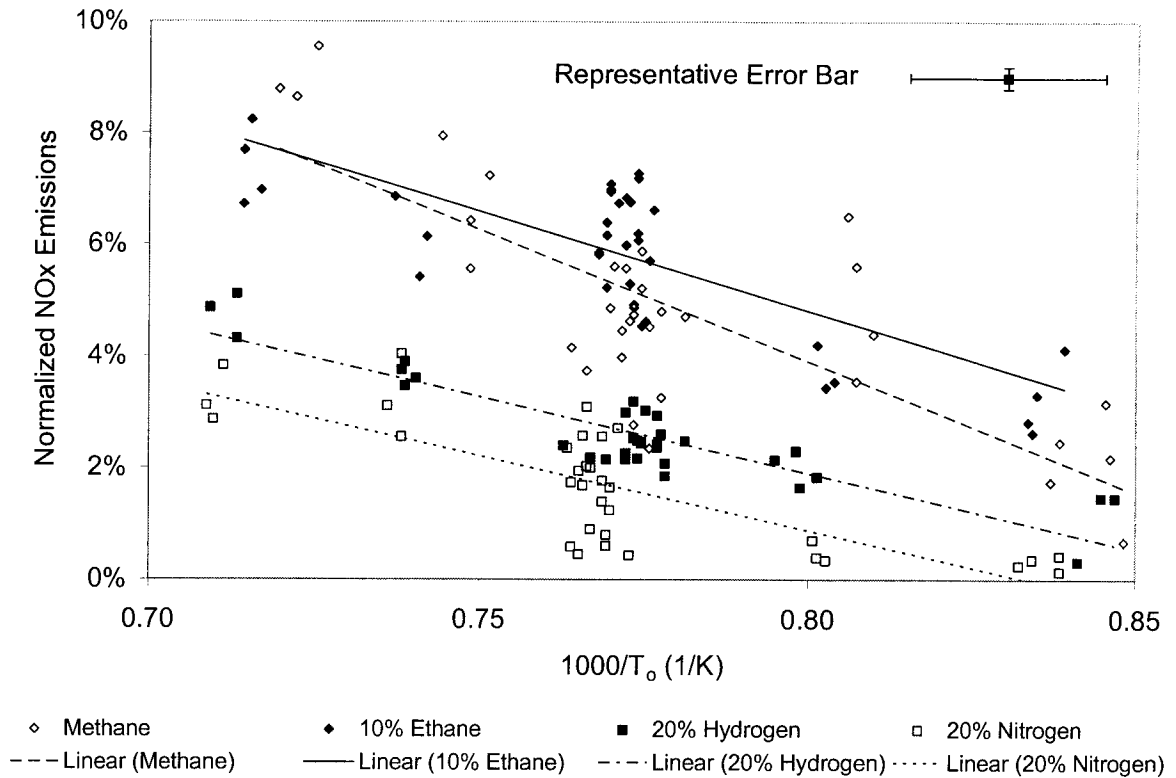
Figure 5.14 Normalized NOx emissions variation with T_o

Table 5.13 Least-squares fitting results for normalized NOx emissions and T_o

	a	b (K)	SE(b) (K)	R^2
Methane	0.4160	-0.4713	0.0635	0.6185
10% Ethane	0.3332	-0.3564	0.0485	0.6275
20% Hydrogen	0.2382	-0.2740	0.0233	0.8120
20% Nitrogen	0.2218	-0.2662	0.0393	0.5964

Figure 5.15 shows the variation of normalized NOx emissions with injection pressure ratio, P_i/P_o, for all of the fuel blends under consideration. Linear regression is used to fit the data in this figure with the form:

$$Normalized\ NOx\ Emissions = a + b(P_i / P_o)$$ (5.21)

The fitting results are summarized in Table 5.14. All the slopes in the table are positive and the standard errors of the slopes are relatively low, suggesting there is a common trend of increasing NOx emissions with increasing pressure ratio; this may be due to enhancement of the jet turbulence at higher pressure ratios which, in turn, promotes a more effective heat release.
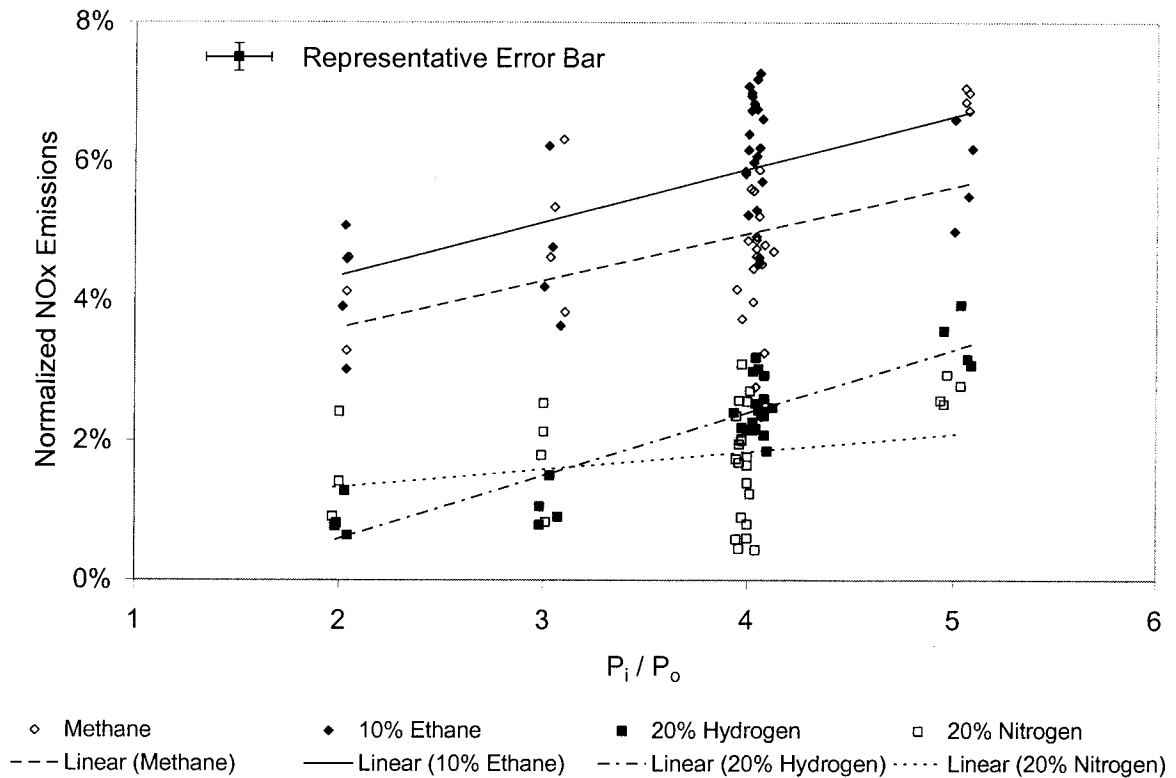
Figure 5.15 Normalized NOx emissions variation with P_i/P_o

Table 5.14 Least-squares fitting results for normalized NOx emissions and P_i/P_o

	a	b	SE(b)	R^2
Methane	0.0226	0.0067	0.0025	0.2008
10% Ethane	0.0283	0.0077	0.0020	0.3279
20% Hydrogen	- 0.012	0.0090	0.0008	0.8028
20% Nitrogen	0.0083	0.0025	0.0018	0.0609

A notable feature of the results presented in Figures 5.14 and 5.15 that, as reported previously in Chapter 3, the addition of ethane to the methane fuel increases the emission of NOx, while conversely, the addition of hydrogen or nitrogen is seen to reduce NOx emissions. A simple thermodynamic analysis suggests that changes in flame temperature with fuel additions under lean conditions may be the primary cause.

As shown in Table 5.15, under lean conditions at a molecular air-to-fuel ratio of 20 by moles the adiabatic flame temperature (T_{ad}) of the methane/ethane blend is 107 K higher than that for pure methane fuel. By contrast, under the same conditions the adiabatic flame temperature of the methane/hydrogen blend is 148 K lower than that for pure methane fuel. Nitrogen dilution not only directly reduces the adiabatic flame temperature, but also tends to reduce the concentration of methane on the fuel side of the

non-premixed flame, resulting in a leaner mixture for an equivalent amount of mixing. This combination results in a significant reduction in adiabatic flame temperature, as shown in Table 5.15.

Table 5.15 Adiabatic flame temperatures for different fuels
$(T_f=300$ K, $T_o=1300$ K, P=30 bar)

	Air/Fuel=10 (mol/mol)		Air/Fuel=20 (mol/mol)	
	ϕ	T_{ad} (K)	ϕ	T_{ad} (K)
Methane	0.95	2800	0.48	2243
10% Ethane	1.02	2797	0.51	2350
20% Hydrogen	0.81	2642	0.41	2095
20% Nitrogen	0.76	2554	0.38	2025

Finally in this section, the variability in the NOx results is considered. In an earlier study, Sullivan et al. [31,32] reported that the variability in NOx emissions was well correlated with ignition delay variability for pure methane, with lower t_{d_ign} resulting in higher NOx emissions. Figures 5.16, 5.17, and 5.18 show normalized NOx emissions variation with t_{d_ign}, Z_k/Z_t and Z_k^* for all of the fuel blends under consideration. Linear regression is used to fit the data in these figures with the form:

$$Normalized\ NOx\ Emissions = a + b(t_{d\_ign}) \qquad (5.22)$$

$$Normalized\ NOx\ Emissions = a + b(Z_k / Z_t) \qquad (5.23)$$

$$Normalized\ NOx\ Emissions = a + b(Z_k^*) \qquad (5.24)$$

The fitting results are summarized in Tables 5.16, 5.17, and 5.18.

Even though all the slopes in these three tables are negative, the standard errors of the slopes are, in some cases, relatively large. The relationship between ignition delay and NOx emissions reported by Sullivan et al. [31,32] is not obvious in the present study. NOx emissions does not show strong dependence on ignition kernel location either, which does agree with the earlier observation of Sullivan et al. [31,32] in the case of pure methane fuel.
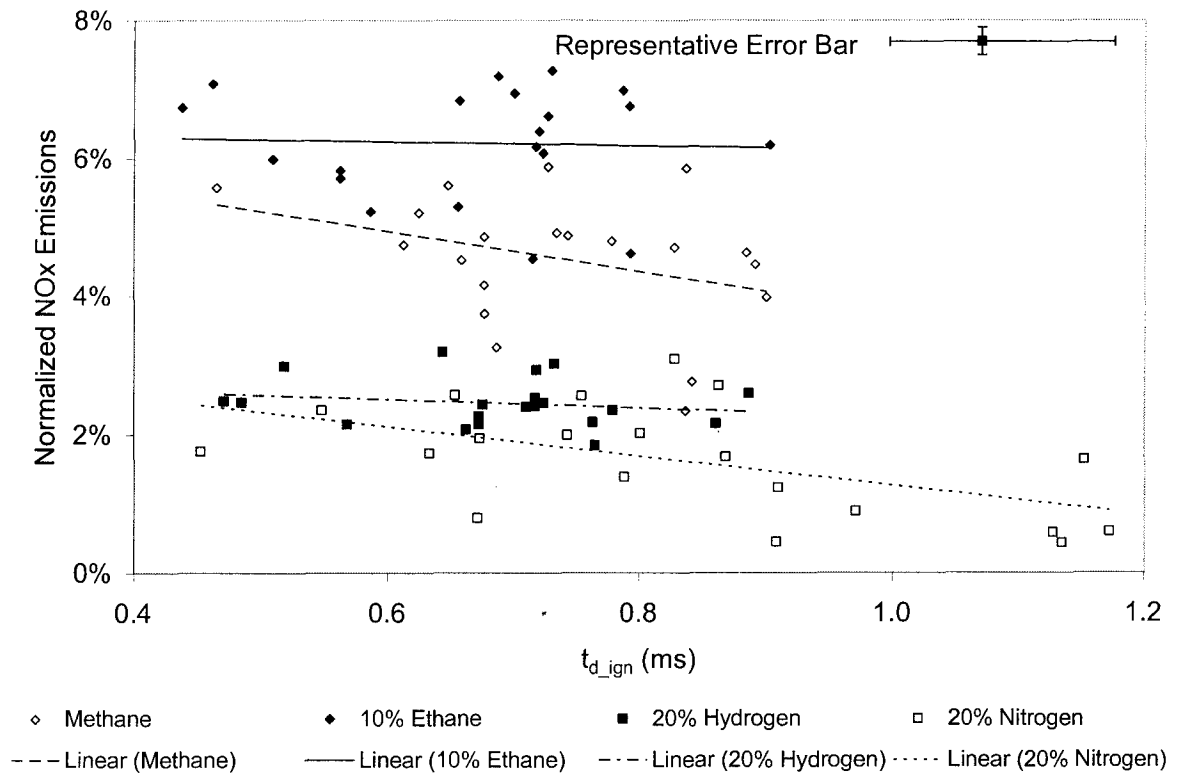
Figure 5.16 Normalized NOx emissions variation with t_{d_ign}

Table 5.16 Least-squares fitting results for normalized NOx emissions and t_{d_ign}

	a	b (1/ms)	SE(b) (1/ms)	R^2
Methane	0.0669	-0.0291	0.0187	0.1191
10% Ethane	0.0642	-0.0029	0.0162	0.0017
20% Hydrogen	0.0287	-0.0060	0.0073	0.0364
20% Nitrogen	0.0339	-0.0211	0.0079	0.2862
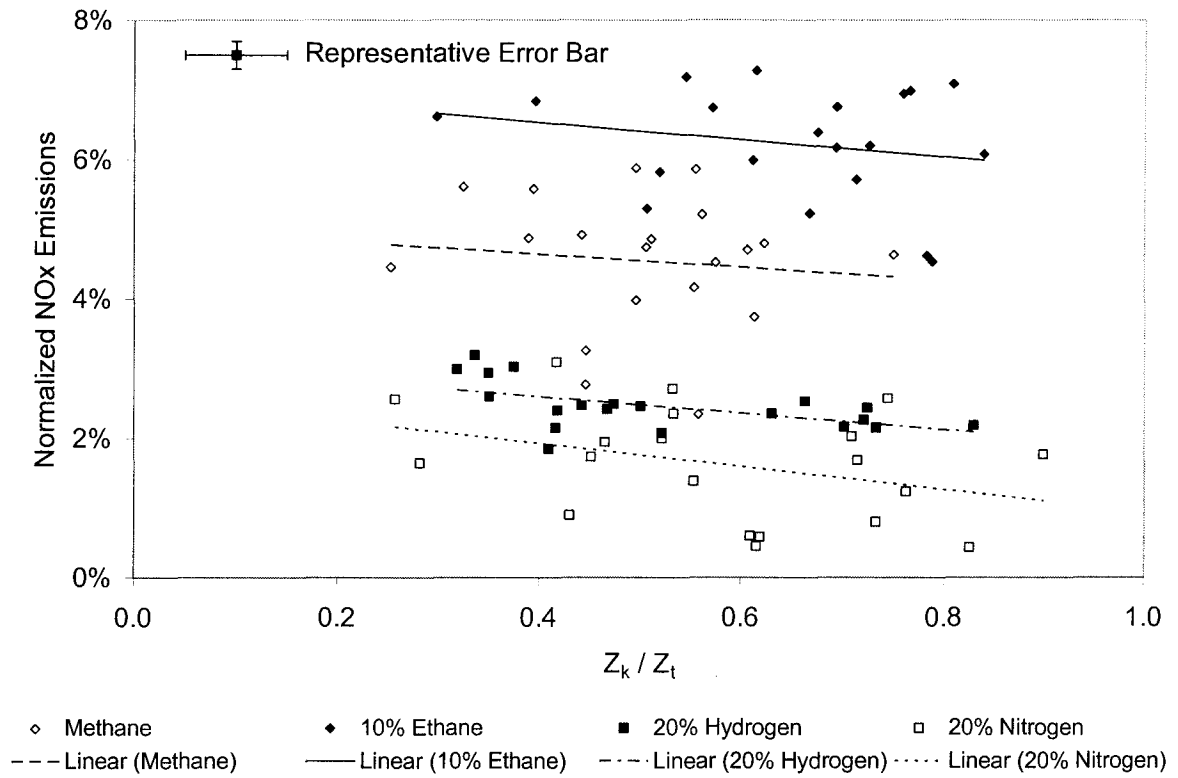
Figure 5.17 Normalized NOx emissions variation with Z_k/Z_t

Table 5.17 Least-squares fitting results for normalized NOx emissions and Z_k/Z_t

	a	b	SE(b)	R^2
Methane	0.0501	-0.0092	0.0197	0.0120
10% Ethane	0.0703	-0.0124	0.0133	0.0462
20% Hydrogen	0.0307	-0.0118	0.0043	0.2930
20% Nitrogen	0.0259	-0.0165	0.0103	0.1237
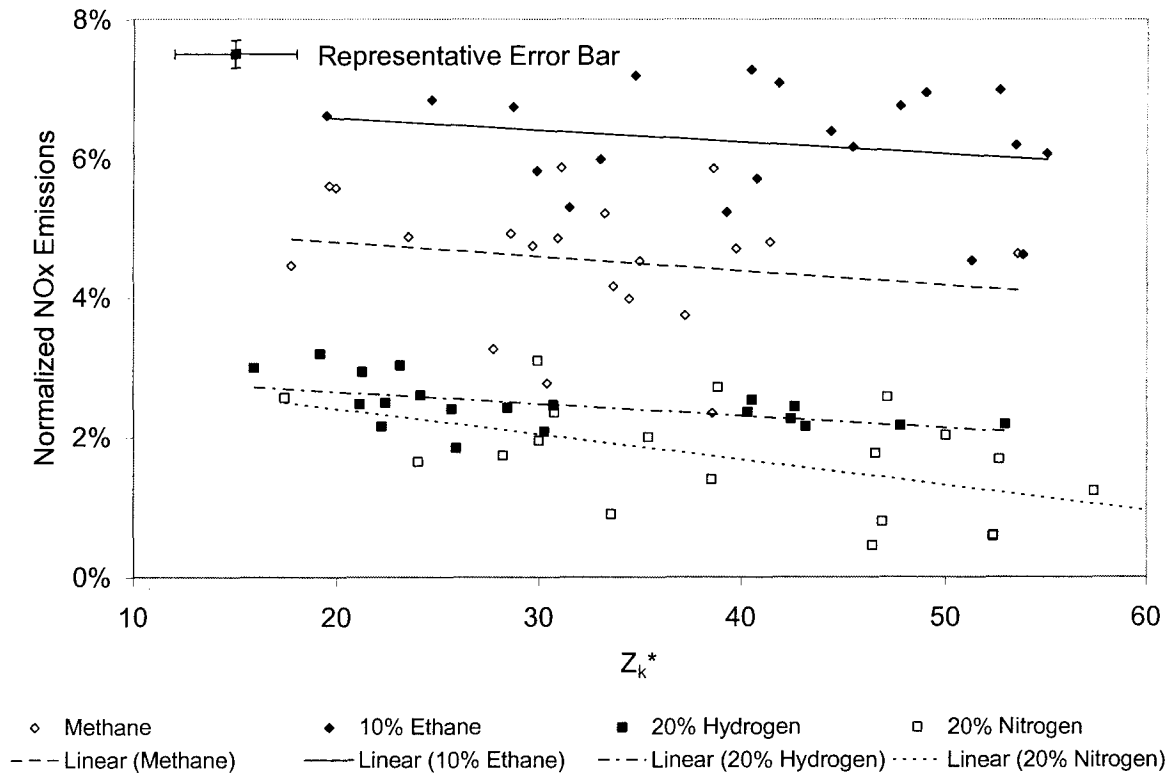
Figure 5.18 Normalized NOx emissions variation with Z_k^*

Table 5.18 Least-squares fitting results for normalized NOx emissions and Z_k^*

	a	b	SE(b)	R^2
Methane	0.0521	-0.0002	0.0003	0.0329
10% Ethane	0.0691	-0.0002	0.0002	0.0468
20% Hydrogen	0.0299	-0.0002	0.0001	0.2800
20% Nitrogen	0.0312	-0.0004	0.0001	0.3313

5.3 Conclusions

Experimental results on thermodynamic and gas dynamic effects on ignition of jets of methane with additives are analyzed using least-squares fitting. The curve fits confirm the existence of some common trends between fuels. However, because of the large amount of scatter in the experimental data, only relatively low R^2 values are achieved for most fits. With respect to the results presented in this chapter the following conclusions can be made:

1. Increasing pre-combustion temperature; significantly decreases the ignition delay for all fuels, causes the ignition kernel to move closer to the injector tip – although the kernel location relative to the jet length is unchanged, increases NOx emissions.

2. Increasing injection pressure ratio; initially decreases the injection delay before increasing the delay again as the associated increase in scalar dissipation rate promotes flame extinction at higher values of P_i/P_o, moves the ignition kernel further downstream both relative to the injector tip and relative to the jet length, increases NOx emissions due to enhancement in the fuel-air mixing which promotes the heat release.

3. Injection duration does not show significant influence on ignition delay or ignition kernel location.

4. Variability in NOx emissions does not correlate with the variability in ignition delay or the ignition kernel location.

5. The increase in NOx emissions observed with the addition of ethane to the base methane fuel is likely due to the associated increase in adiabatic flame temperature. Conversely, the reduction in NOx emissions observed with the addition of hydrogen or nitrogen to the base methane fuel is likely due to the associated reduction in adiabatic flame temperature

Chapter 6
OH Distribution in Igniting Turbulent Methane Jets

6.1 Introduction

The location of the reaction zones is among the most fundamental aspects of combustion. Knowledge of these reaction zones is central to improving our understanding of combustion, and the associated production of emissions. This information is critical for the development of truly predictive computer models and for guiding the design of future engines that must have both higher efficiencies and lower emissions.

Planar laser induced fluorescence (PLIF) imaging of the combustion radicals provides a means of studying the combustion reaction zones. Both the CH [167-171] and OH [82,167-169,172,173] radicals have been used in burner experiments to visualize the reaction zones in hydrocarbon flames. Although the CH radical is generally a better marker of the reaction zone [167-171], PLIF of CH can be difficult due to weak signals and the required laser characteristics (wavelength and pulse duration) [171]. In contrast, OH-PLIF typically has a much stronger signal, the laser system is straightforward, and although polycyclic aromatic hydrocarbon (PAH) and laser induced incandescence (LII) interferences are still a concern, they can be adequately removed by spectral filtering.

Because of these advantages, OH-PLIF has been widely applied to the study of both premixed [167] and diffusion [168,169,173] flames in burners. These and other burner studies (using both absorption and point laser induced fluorescence) have shown that the OH radical distribution is initiated in the flame front and almost immediately rises to high (super-equilibrium) concentrations that are on the order of 3 to 5 times flame-zone equilibrium levels [81]. In the post-combustion gases, the OH concentration gradually drops off to the local equilibrium value by a three-body recombination reaction [174] whose rate is strongly dependent on pressure. This rate is slow at atmospheric pressure, and OH often persists well away from the flame front making it a less useful marker of the reaction zone [174]. However, as ambient pressure is increased, the super-equilibrium OH concentrations in the flame zone are more rapidly reduced to the equilibrium levels outside the flame zone [175]. Furthermore, for diffusion flames, the equilibrium level itself falls rapidly outside of the flame zone [174]. The combination of these two effects causes the OH concentration (and hence OH PLIF signal) to closely mark the reaction zone in high-

pressure diffusion flames, with a large signal differential from the flame zone to the surrounding gas.

Another effect that would cause the OH distribution to be more localized about the flame zone is the removal of OH by soot oxidation. Burner studies have shown that OH is important in soot oxidation, and conversely indicated that the presence of soot and soot precursors can decrease OH concentrations. Puri *et al.* [176] demonstrated this effect by measuring the OH concentrations in a simple diffusion flame for three different fuels that produced increasing amounts of soot and related hydrocarbons. For the lowest sooting fuel (methane), they found OH persisting far from the flame zone on the fuel side of the diffusion flame. As other species (butane and butene) were added to the methane, progressively more soot was produced, and the OH concentration fell off at progressively higher rates on the fuel side of the diffusion flame.

Finally, the burner studies indicate the PLIF of OH will provide a good image of the diffusion flame but may not be capable of detecting the premixed combustion in diesel engines, which measurements have shown occurs at equivalence ratios in the range of 2 to 4 [177] for the typical operating condition examined. OH concentration in diffusion flames and in lean and near-stoichiometric premixed flame are relatively high with peak concentrations ranging from about 0.6×10^{16} to $2.0 \times 10^{16}/cm^3$ [176]. These concentrations give strong PLIF signals and are easily imaged. However, for fuel-rich premixed flames Lucht *et al.* [178] found both peak and near-equilibrium OH concentrations to be much lower. Also, as they increased the equivalence ratio in the rich flame, OH concentrations continued to drop, with both peak and post-combustion gas values being about 100 times less for an equivalence ratio of 2.02 than those for an equivalence ration of 0.78. Thus, the fuel-rich premixed combustion in a diesel engine (equivalence ratios of 2 to 4) will likely have OH concentrations that are below the detectability limits of OH PLIF.

OH-PLIF has also been demonstrated as a technique for studying flames in internal combustion engines. At beginning most parts of these works have involved using OH-PLIF to visualize the flame fronts in spark-ignition engines [179-182]. Later extensive research of applying OH-PLIF in diesel engines has been carried out at Sandia National Laboratories in the U.S. Such things as the turbulent diffusion flame structure of reacting diesel fuel jets [183], the effects of injection timing and diluent addition on the late-combustion soot burnout [184], interactions between the combusting fuel jet and the piston-bowl wall [185], the diffusion flame lift-off length of diesel jets [186] were investigated. More recently the application of OH-PLIF has been extended to direct-injection spark-ignition (DISI) engines

to investigate the structure and flame propagation characteristics of stratified and homogeneous combustion [187,188], and to homogeneous charge, compression ignition (HCCI) engines to investigate the in-cylinder mixture distribution and combustion process [189-191].

In the present study, OH-PLIF was applied to study the non-premixed turbulent methane jet flame. The application of OH-PLIF in a shock tube has several challenges. Because of the high run-to-run variability resulting from the stochastic nature of developing turbulent jet, repeat experiments are needed to achieve a converged result. However unlike an engine, in which ensemble-averaged images can be relatively easily obtained over hundreds of cycles, shock tube experiments have a very limited run-time and only single-shot images can be obtained from each experiment. Considering the relatively long time it takes to prepare for each experiment, it is impractical to conduct hundreds of repeat experiments for each operating condition. Thus, one area of significant interest in the present work was to investigate how the number of repeat experiments and variability in the ignition delay will affect the convergence of the mean radical field.

6.2 Experimental Methods

6.2.1 OH-PLIF Setup

Figure 6.1 shows the OH-PLIF experiment setup. A 400 mJ pulse from a Nd:YAG laser (Big Sky Ultra PIV 200) at a wavelength of 532 nm was used to pump a tuneable dye laser (Sirah Cobra-Stretch) which contained a solution of Rhodamine 590 dye. The dye laser output at 567.85 nm was then frequency doubled by a harmonic unit (Sirah THU-205) to give a wavelength of 283.92 nm.

Before forming the laser sheet, the laser beam passed through an Ophir beam splitter and the reflected laser beam was monitored by an Ophir power meter (PE25BB-DIF-SH-V2) for shot-to-shot variation. The collimated laser beam was formed into a sheet using a 750 mm focal length spherical lens and a 25.4 mm focal length cylindrical lens. The laser sheet was then reflected by a UV mirror and entered the shock tube through a quartz window, and traversed the shock tube across the centerline. The sheet was approximately 80 mm wide and 200 μm thick in the test section, and due to the 750 mm focal length spherical lens changed little over the field of view. The laser energy was about 13 mJ prior to forming the laser sheet. Further losses due to the combination of optical components resulted in an estimated laser energy within the shock tube of about 10 mJ.

The fluorescence signal was captured by a 12-bit image intensified CCD camera (LaVision NanoStar S-20, 1280 pixels x 1024 pixels) equipped with a UV lens (Nikkor f/4.5, 105 mm focal length). A 100 ns gate-width was used for all OH-PLIF images, which, combined with the filters described below, eliminates any detectable natural flame emission signal. All the OH-PLIF images were acquired with a single intensifier gain, so relative intensities may be quantitatively compared. The autoignition and combustion process was also recorded by the Phantom high speed camera.
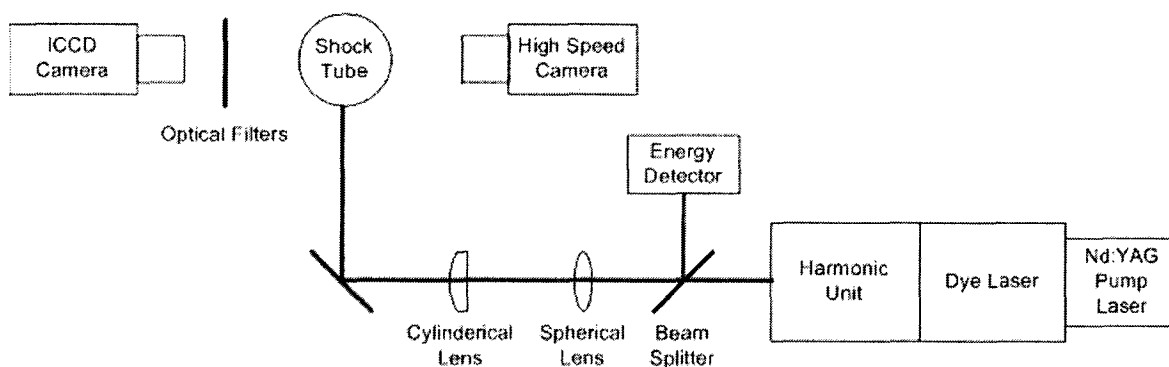
Figure 6.1 OH-PLIF experiment setup

In order to isolate the OH fluorescence signal from interference caused predominantly by laser elastic scattering, PAH fluorescence and soot particle incandescence [192], a combination of optical filters were placed into the optical path of the camera which consisted of a band pass filter (total bandwidth of 16 nm) centred on 312 nm and a 358 nm low pass filter. To confirm whether the fluorescence signals detected were indeed solely due to the presence of OH and not other fluorescing species, images were acquired at a non-resonant wavelength of 282.80 nm. Because simultaneous online and offline images could not be acquired from a single test, typical online and offline images from 2 different runs were compared to evaluate the veracity of the OH fluorescence.

Figure 6.2 shows typical single-shot OH-PLIF images obtained at the non-resonant and resonant wavelengths which confirms that the LIF signal was indeed due to the detection of the OH radical and in addition, that the optical filters used were effective in minimizing signal interference due to elastic laser scattering and other species which might fluoresce at the same excitation wavelength.
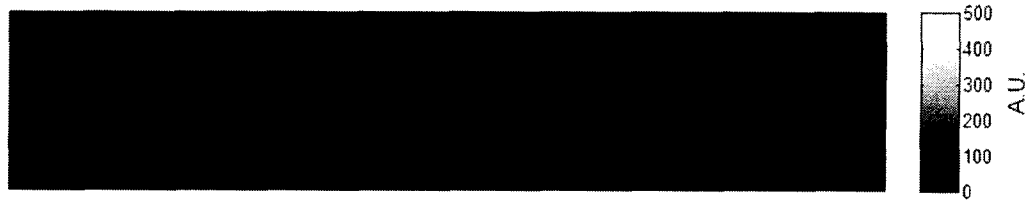
(a) Laser Offline
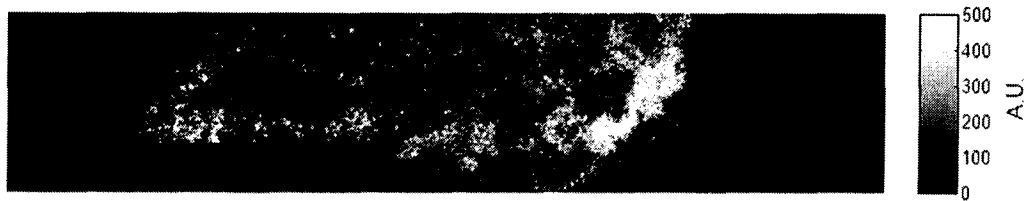
(b) Laser Online

Figure 6.2 Single-shot OH-PLIF images obtained at an offline wavelength of 282.80 nm and online wavelength of 283.92 nm

6.2.2 Image Post-processing Procedures

In the present study, the OH-PLIF images had several corrections performed on them to correct for dark signal, background signal, shot-to-shot and spatial variations in the laser sheet intensity, but were not intended for quantitative measurements.

An ensemble-averaged background image acquired under shock tube non-firing conditions (with no fuel or combustion products present) was subtracted from each OH-PLIF image thus simultaneously correcting for background and dark signal. Spatial variations in the laser sheet intensity were also taken into account by acquiring a sequence of on-site 'calibration images' of 3-pentanone fluorescence at the same excitation wavelength of 283.92 nm.

To achieve that, A UV tube filled with 3-pentanone water solution was put into the test section along the centerline of the shock tube. Firing the laser across the 3-pentanone water solution allowed the acquisition of a LIF image cross section. However when the laser sheet passed through the 3-pentanone water solution from bottom to top, the attenuation of the laser intensity was not negligible, as shown in Figure 6.3.

- 123 -
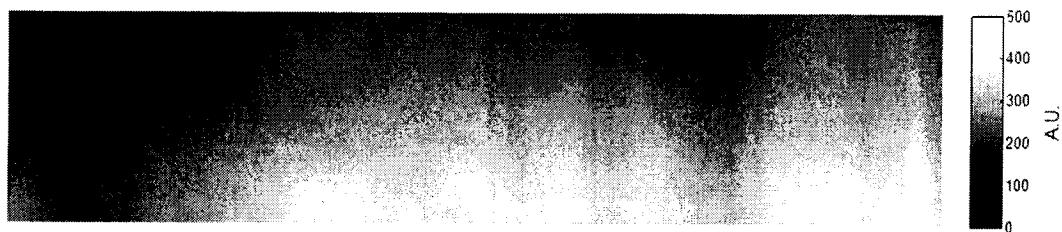
Figure 6.3 Background-corrected 3-pentanone fluorescence image

Because of the inhomogeneity of the calibration image, it is invalid to perform a pixel-by-pixel ratio of the background-corrected OH-PLIF image to the background-corrected 'calibration image'. For weak excitation in this study, the 3-pentanone fluorescence signal is proportional to the number density of 3-pentanone molecules. Since the thinnest part of the laser sheet is focused along the centerline of the shock tube, the laser sheet is more converged near the centerline. The number of 3-pentanone molecules in the passage of the laser sheet will not change much near the centerline when the laser sheet passes the solution from bottom to top. For that reason, the central section of the image was selected for calibration.

Figure 6.4 shows the average laser intensity profiles over 3 selected central sections of 10, 30, and 50 pixels width respectively. No obvious difference in the average laser intensity profiles is observed. In the present study, the average laser intensity profile over the central section of 10 pixels width was used to correct OH-PLIF images for variations in the direction perpendicular to the passage of the laser sheet.
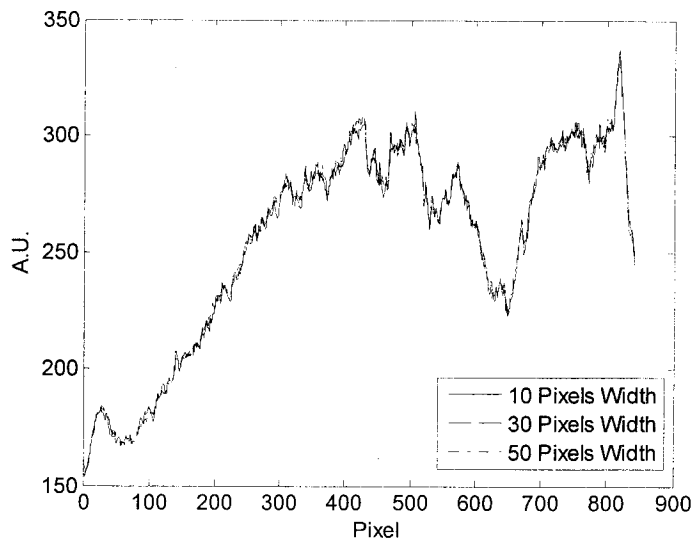
Figure 6.4 Average laser intensity profiles over different central sections

Finally, the image post-processing routine also accounted for variations in shot-to-shot laser intensity permitting a semi-quantitative analysis of the LIF data acquired.

6.2.3 Experimental Conditions

Table 6.1 summarizes the experimental conditions and main parameters in the OH-PLIF experiments. Methane (99.97% purity) and the J43P2 injector were used for all the OH-PLIF experiments. For each experiment, one single-shot OH-PLIF image was obtained. The autoignition and combustion process was also recorded by the Phantom high speed camera to determine the ignition delay.

Table 6.1 Operating conditions for OH-PLIF experiments

Number of experiments	OH-PLIF Timing (ms after SOI)	P_o (bar)	T_o (K)	P_i (bar)	t_i (ms)
20	0.989	30	1300	120	1.0
20	1.189	30	1300	120	1.0
100	1.389	30	1300	120	1.0

6.3 Results and Discussion

6.3.1 OH Field Evolution

Figures 6.5, 6.6, and 6.7 show selected single-shot OH-PLIF images from the shock tube experiments at different stages of combustion. It should be noted that PLIF is a planar technique and each image is a slice through the centerline of the jet. The size of the image is 15 mm x 75 mm, with the width of the image exactly matching that of the optical window. It is immediately obvious that, even though the 5 images in each figure were taken at the same time relative to the start of injection under nominally identical operating conditions, the OH distributions shown in the individual images are totally different from each other, not only in the location and the shape of the reaction zone, but also in the areas it occupies. This is to be expected as a result of the high run-to-run variability in ignition delay and ignition kernel location reported in previous chapters. In images taken shortly after the ignition (Figure 6.5), only a small reaction zone is observed. In images taken relatively longer after ignition (Figures 6.6 and 6.7), the flame has propagated further downstream and occupies a larger area. In some cases, e.g. the lower image of Figure 6.6, a clearly defined diffusion flame is observed. The flame recedes from the nozzle and appears lifted. Combustion is extinguished in the near nozzle region due to the high local strain rate induced by the high relative velocity between the oxidizer and injected fuel.
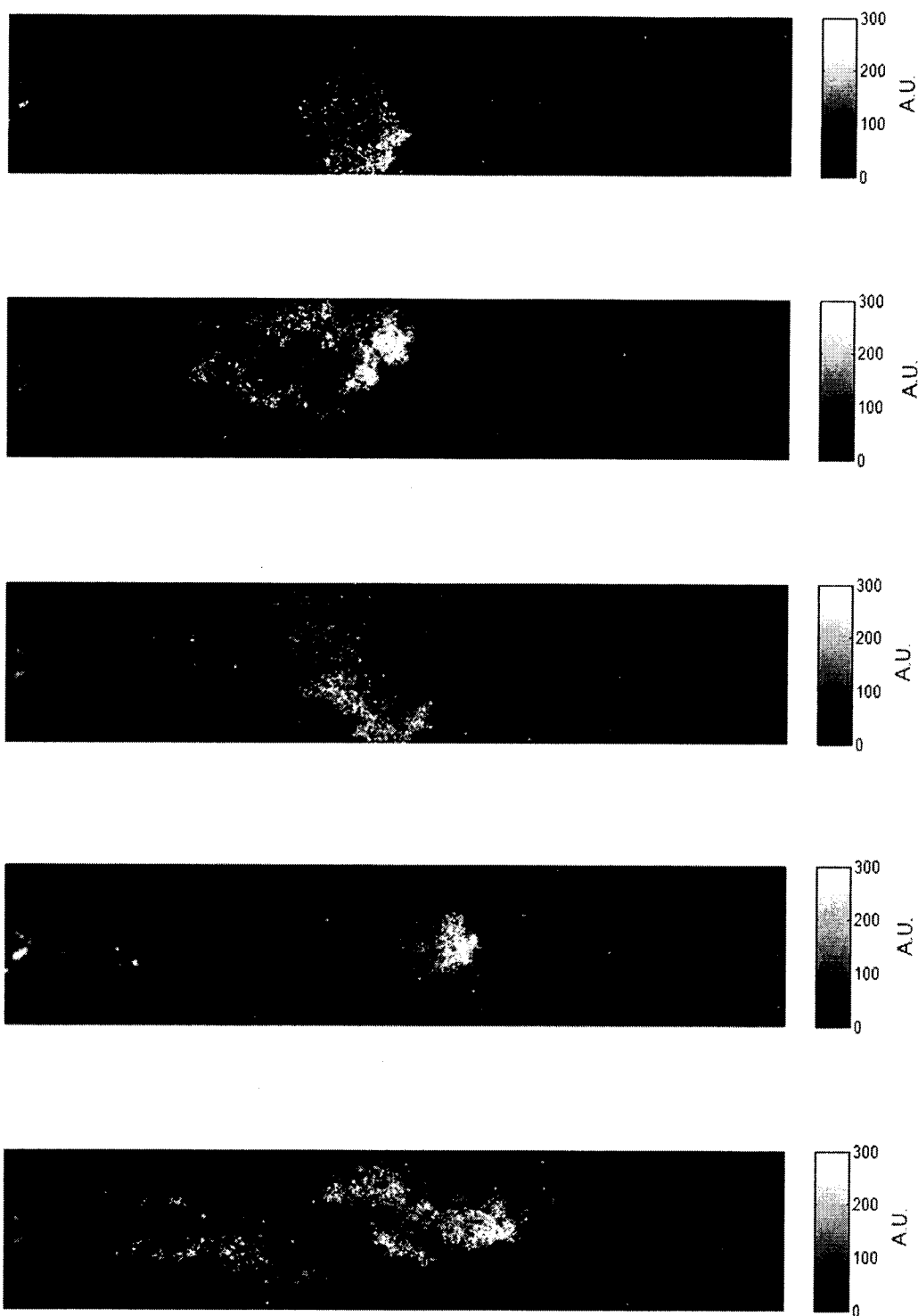
Figure 6.5 Single-shot OH-PLIF images (t=0.989 ms)
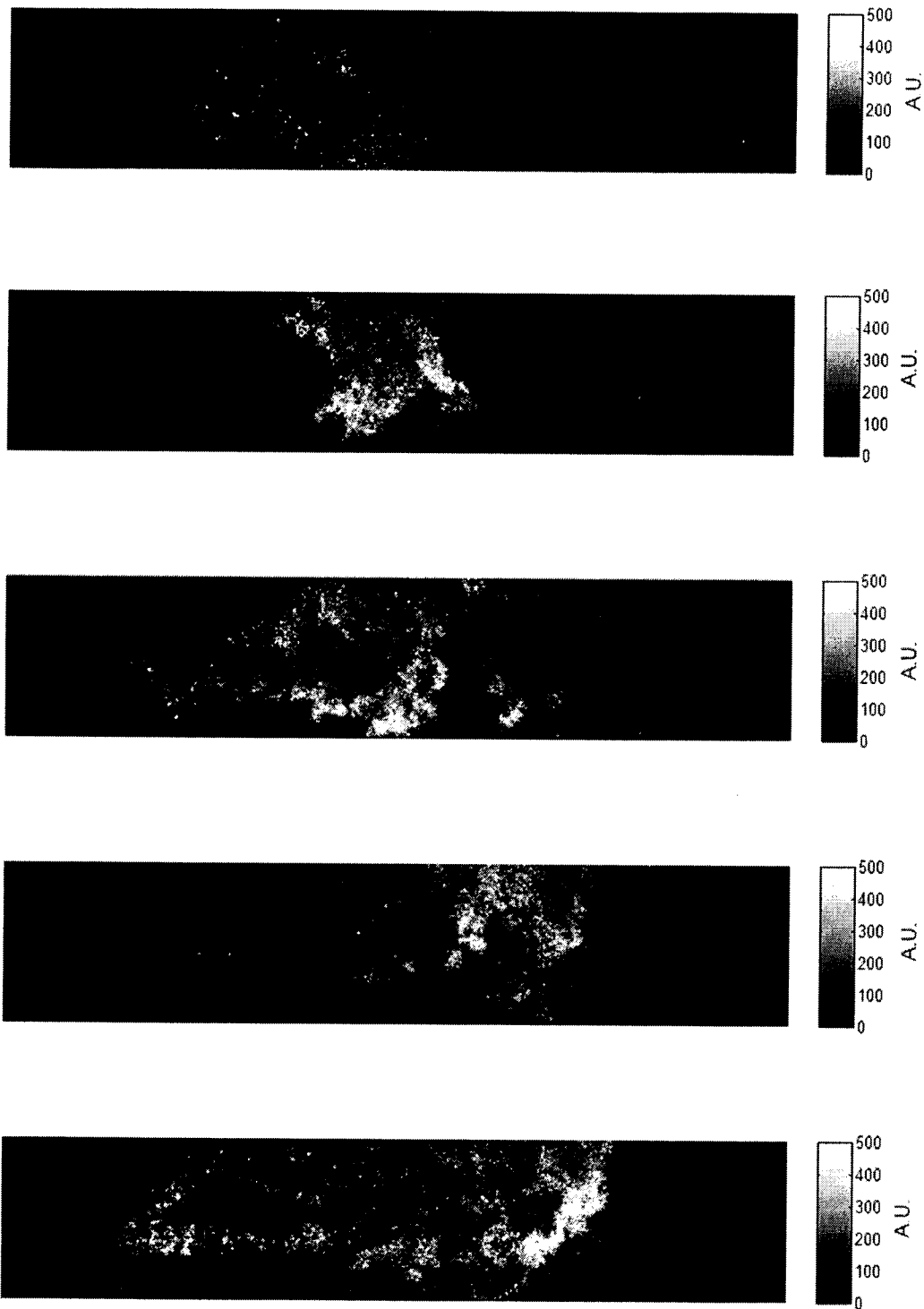
Figure 6.6 Single-shot OH-PLIF images (t=1.189 ms)
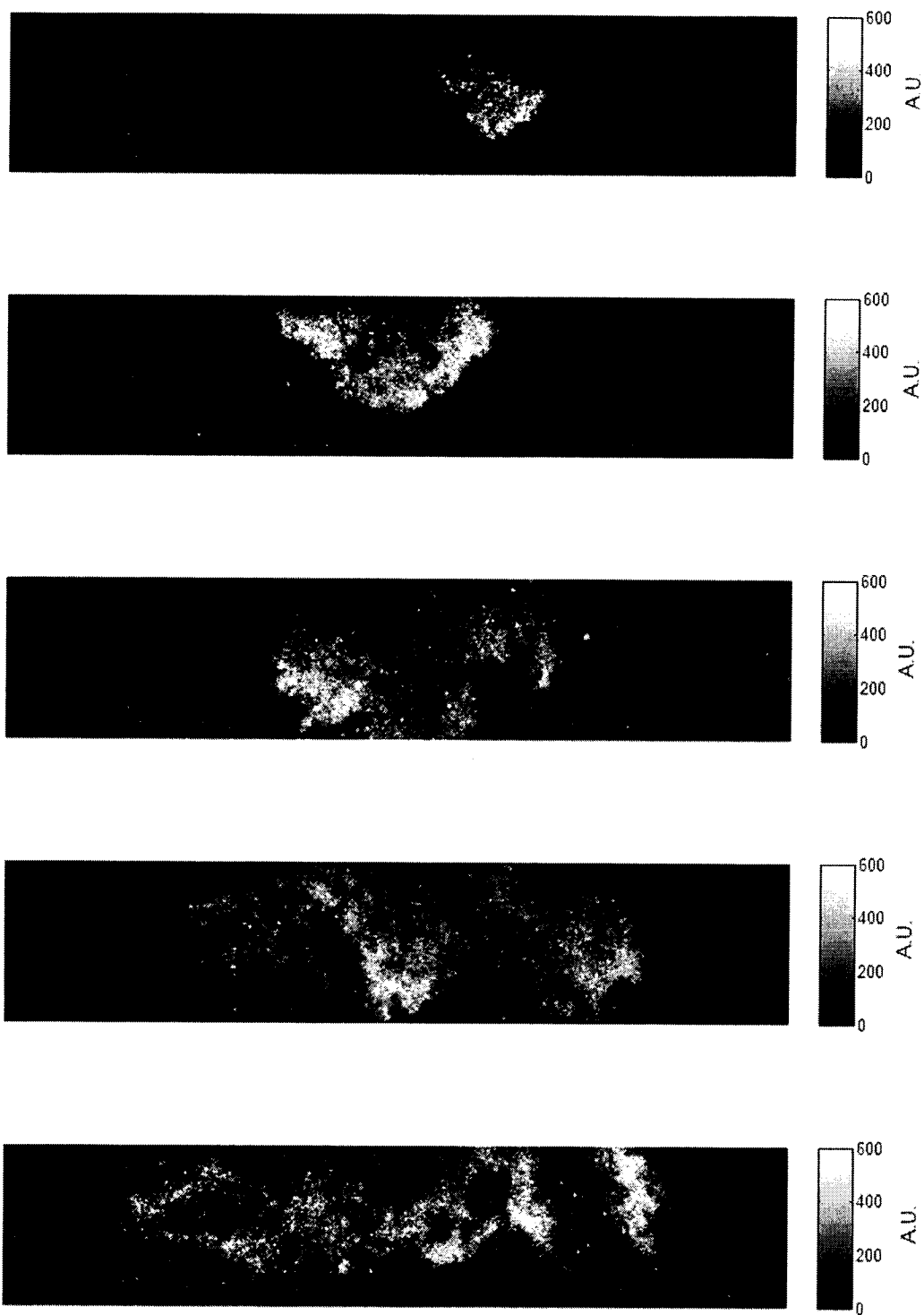
Figure 6.7 Single-shot OH-PLIF images (t=1.389 ms)

Ensemble-averaged OH-PLIF images were obtained based on those single-shot images, as shown in Figure 6.8. By taking advantage of the axisymmetry of the jet, these images were also mirrored along the centerline of the jet. Thus, the ensemble averaged images shown in Figures 6.8(a) and 6.8(b) are constructed from 40 individual realizations of the OH field whereas the ensemble average shown in Figure 6.8(c) represents 200 realizations of the radical distribution. On inspection, the reader will immediately note that the OH distribution in the ensemble-averaged images, shown in Figures 6.8(a), 6.8(b), and 6.8(c), is totally different from that shown in the corresponding single-shot images (Figures 6.5, 6.6, and 6.7, respectively). The flame occupies a much larger area in the ensemble-averaged images than it does in any individual realization of the OH field and the ensemble-averaged image resembles the shape of a developing turbulent jet. The significance of this result will be discussed later in the thesis.

6.3.2 OH Presence Probability Imaging

An imaging methodology which has been used successfully to evaluate the macroscopic pulse-to-pulse spray variations [193,194] is adopted in the present study to evaluate the macroscopic run-to-run OH field variations. The procedure of applying this image processing technique to quantify the OH field variation is as following.

1. The region of the OH presence in each single-shot OH-PLIF image is identified using a user-defined threshold value. The individual images are then binarized based on the threshold selection. The OH region is displayed as white pixels with a grayscale value of 1, and the remaining area as black pixels with a value of 0.

2. The grayscale value for every pixel location is then summed on pixel-by-pixel for all images.

3. The resulting image is then scaled so that the pixels with a grayscale value of 100 on the presence probability image correspond to the locations of 100% probability of OH presence, and the pixels with a value of 0 represent no OH presence and a 0 probability. In this final, scaled image, each pixel intensity corresponds to the probability of finding OH presence locations.

4. Taking advantage of the axisymmetry of the jet, the presence probability image is also mirrored along the centerline of the jet.
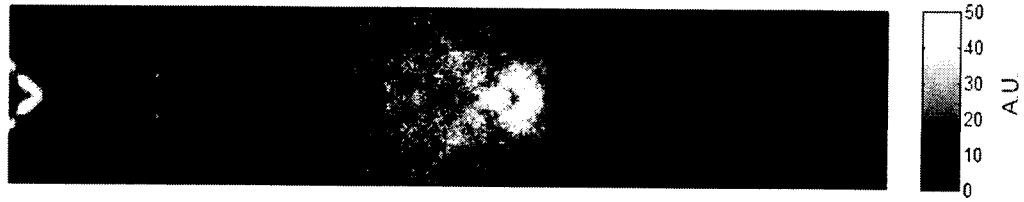
(a) t=0.989 ms
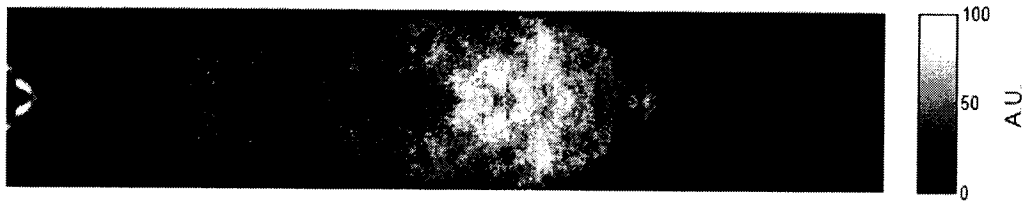
(b) t=1.189 ms
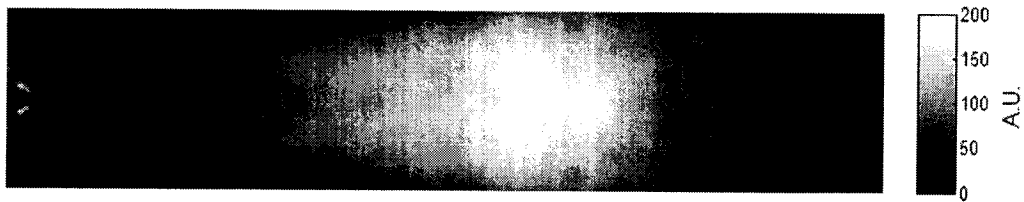
(c) t=1.389 ms

Figure 6.8 Ensemble-averaged OH-PLIF images at different stages of combustion

Figure 6.9 shows the presence probability images at different stages of combustion. In appearance, these images are very similar to the ensemble-averaged OH-PLIF images in Figure 6.8. Presence probability values in these images get progressively larger from t=0.989 ms to 1.189 ms, both due to larger sample size and larger areas occupied by the flame at later stages of combustion. These images also show that the run-to-run variation can be found mostly around the boundary. The variation keeps decreasing from the boundary to the core of the jet.
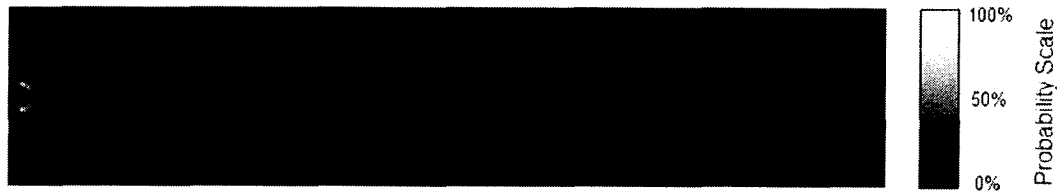
(a) t=0.989 ms
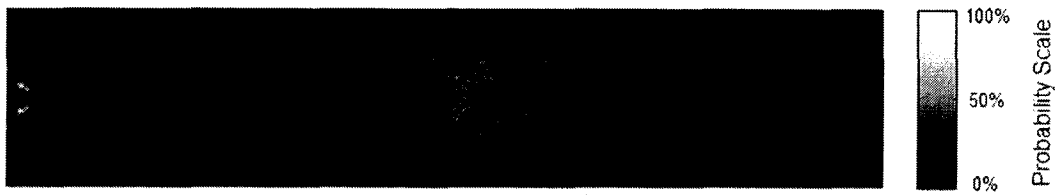
(b) t=1.189 ms
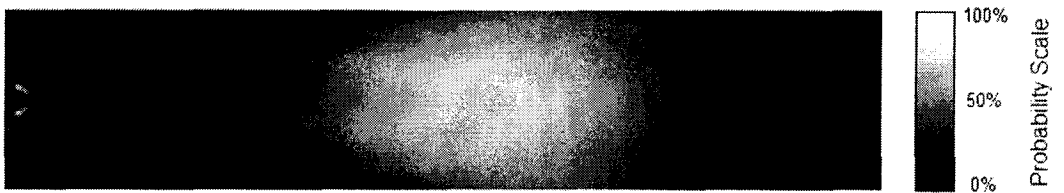
(c) t=1.389 ms

Figure 6.9 Presence probability images at different stages of combustion

In essence, the presence probability image is an ensemble image of OH radical presence, consisting of a set of binarized OH-PLIF images. It provides a new way to examine the OH field variation in terms of a probability defined for the presence of the flame region. However, since the image is binarized, there is no account for the different amount of OH radical present within a flame. It is simply a measure of whether OH radical is present or not at the location. In addition, the presence probability image combines the variations of the OH field from all the images considered, and therefore it does not necessarily resemble the shape or the appearance of the individual OH field.

6.3.3 Convergence of Ensemble-averaged OH-PLIF Images

The randomness in the location and the shape of the OH field in the single-shot OH-PLIF images shown earlier in this chapter raises the question about the convergence of the ensemble-averaged images. To examine the issue of convergence, the following procedure was adopted.

1. A new ensemble-averaged image is obtained by removing one image from the total sample.

2. The average pixel intensity (I_{avg}) over the flame region (based on the presence probability images in §6.3.2) for both the original and the new ensemble-averaged images were calculated and then compared.

3. Pixel-by-pixel intensity over the flame region of these two ensemble-averaged images were compared.

4. Steps 1-3 were then repeated for all the single-shot OH-PLIF images collected.

Figure 6.10 shows the minimum, average, and maximum absolute changes in I_{avg} when a single image is removed from the total sample for each operating condition. For the ensemble-averaged image at t=1.389 ms, only minor change (0.50% in average) in I_{avg} is observed, suggesting that a converged result has been obtained for the mean OH field. The images at t=0.989 ms and 1.189 ms are less converged, mainly due to a much smaller sample size (20 versus 100). With the same sample size, the ensemble-averaged image at t=1.189 ms is more converged than that at t=0.989 ms, mainly due to the larger volume occupied by the more fully-developed flame.

To further examine this claim, the absolute change of pixel intensity for each pixel over the flame region when a single image is removed is calculated and compared to different threshold values (5%, 10%, 20%, 30%, and 40%). Pixels whose absolute change in pixel intensity is greater than a certain threshold value are categorized together. The number of pixels in each category is counted. In the following, P(threshold value) is used to represent the percentage of the pixels over the flame region whose absolute changes in pixel intensity are greater than the threshold value.

Figure 6.11 summarizes the minimum, average, and maximum P values for different threshold values under each operating condition. Similarly to the results in Figure

6.10, it shows that the ensemble-averaged image at t=1.389 ms is the most converged. On average, when a single image is removed from the total 100 images, less than 10% of the pixels over the entire flame region see an absolute change greater than 5% in pixel intensity. Moreover, these pixels are mainly on the boundary of the flame region as shown by the presence probability image presented in §6.3.2.
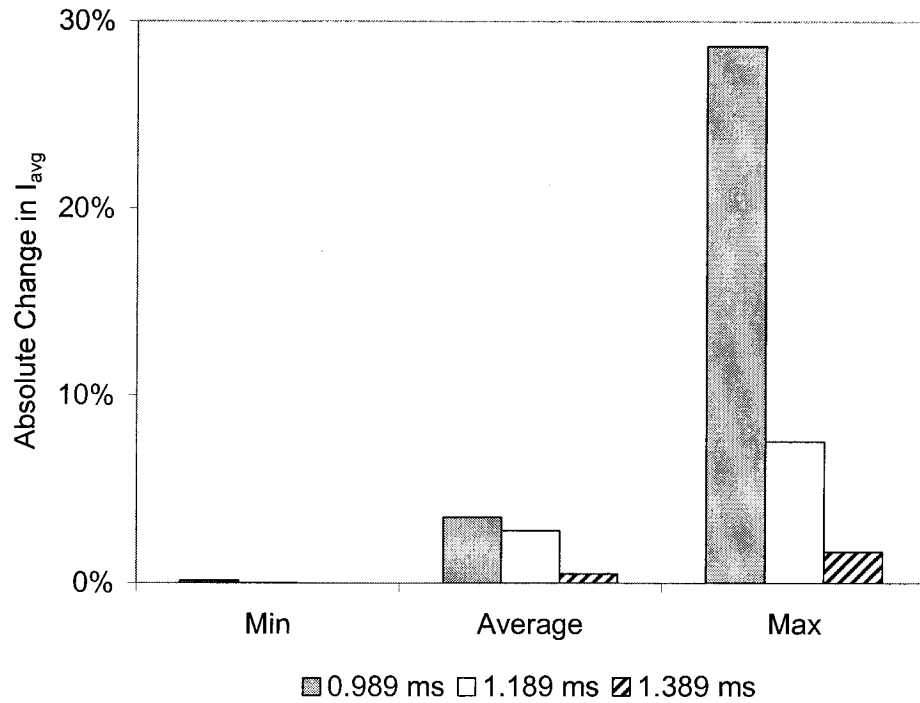
Figure 6.10 Minimum, average, and maximum absolute changes in I_{avg}
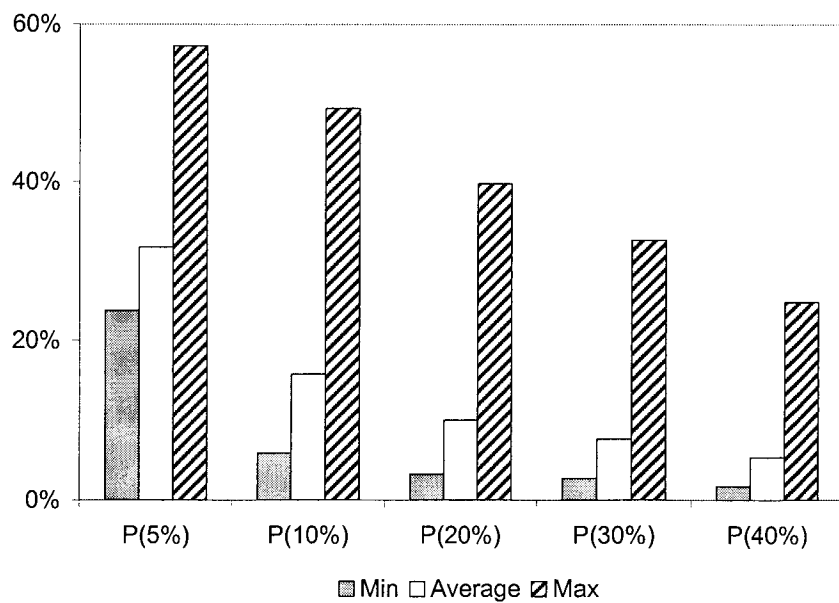
(a) t=0.989 ms
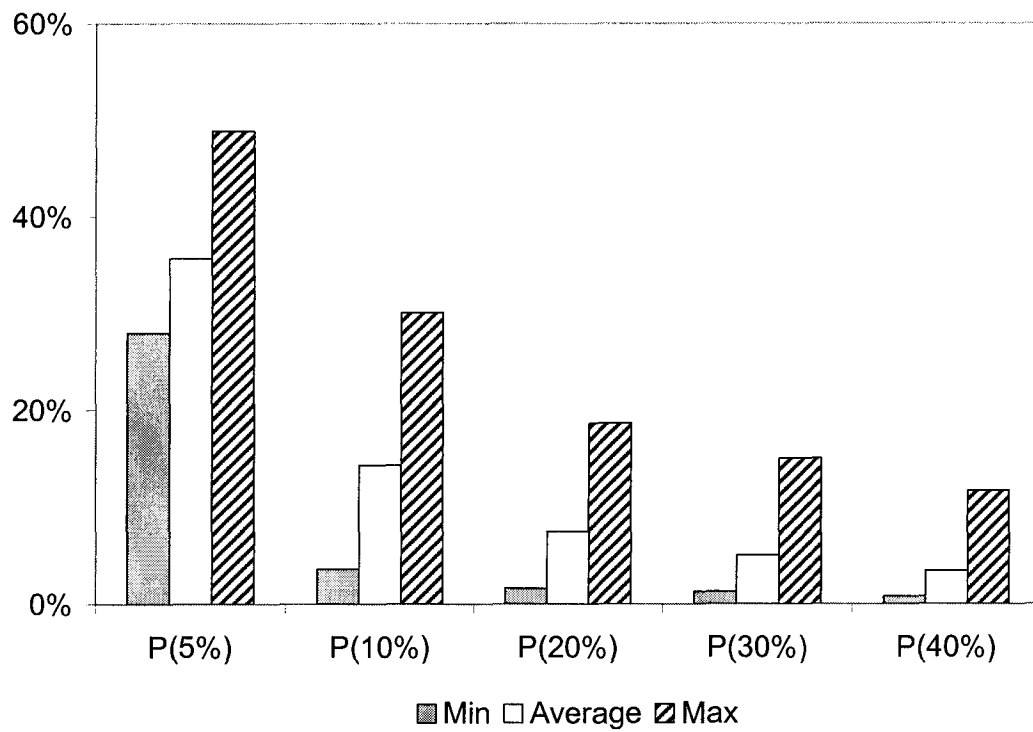
(b) t=1.189 ms
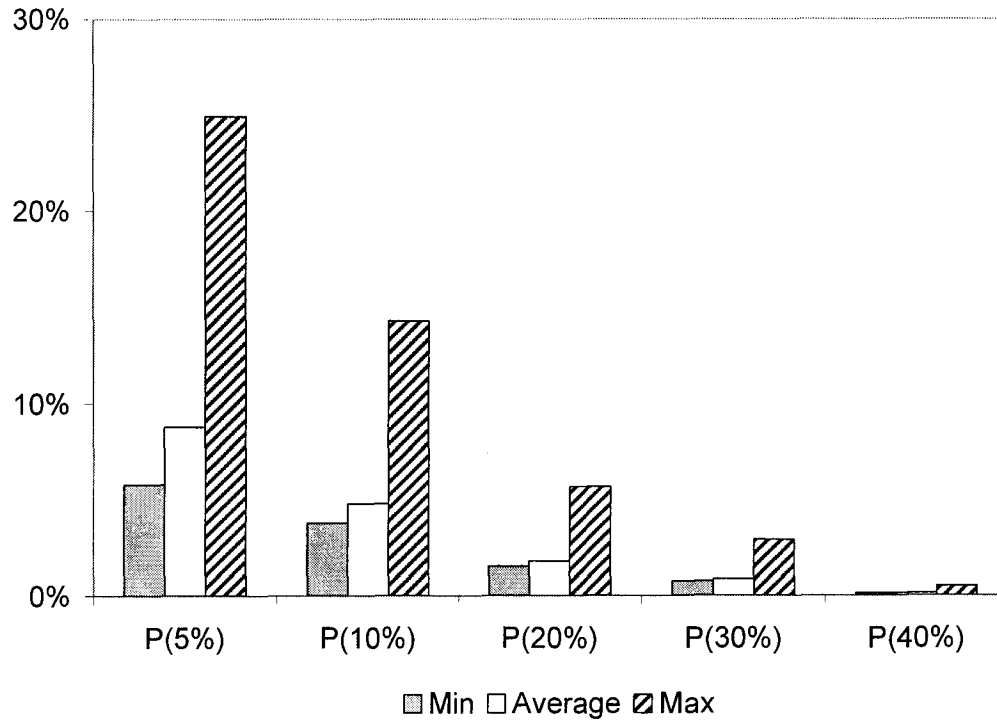
(c) t=1.389 ms

Figure 6.11 Minimum, average, and maximum P values for different threshold values

Effect of Sample Size

As shown in Figure 6.11, even for the most converged ensemble-averaged image at t=1.389 ms, removing a single image from the total 100 images can result in a $P(5\%)_{max}$ as high as 24.92%. To investigate whether removing outliers can lead to a more converged result, 5 images, corresponding to the images with the top 5 highest $P(5\%)$ values, are removed from the total 100 images. An ensemble-averaged image is then obtained for the remaining 95 images. Another ensemble-averaged image is obtained by removing the top 10 such images from the total 100 images. These two ensemble-averaged images are then evaluated following the same procedure as described at the beginning of this section.

Figure 6.12 shows the ensemble-averaged OH-PLIF images with different sample sizes. Here no obvious difference is observed with the outliers removed.
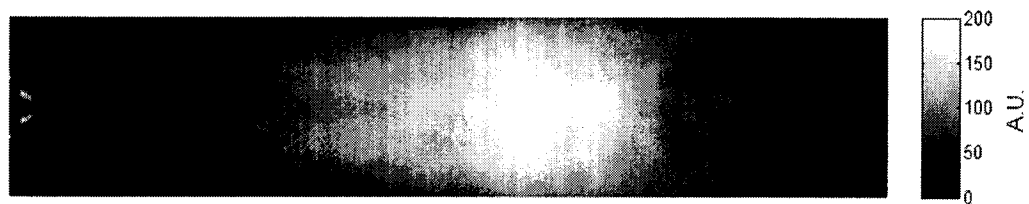
(a) Sample size: 100 images
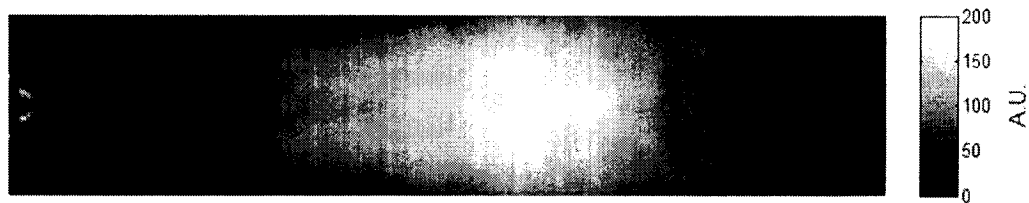
(b) Sample size: 95 images
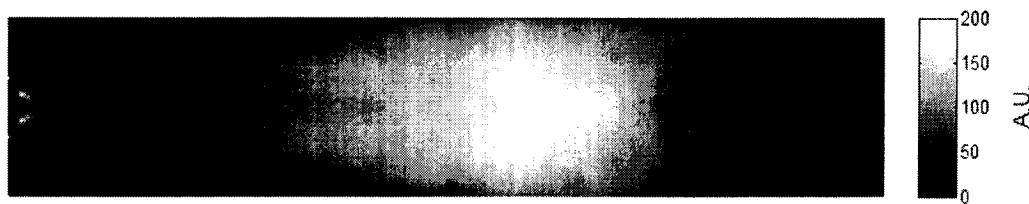
(c) Sample size: 90 images

Figure 6.12 Ensemble-averaged OH-PLIF images with different sample sizes (t=1.389 ms)

Figure 6.13 shows the minimum, average, and maximum absolute changes in I_{avg} for different sample sizes. Greater absolute changes in I_{avg} are observed when the sample size is reduced, even though those removed are outliers. Figure 6.14 compares the minimum, average, and maximum P values for different threshold values with different sample sizes. The removal of 5 and 10 outliers does lead to smaller $P(5\%)_{max}$, $P(10\%)_{max}$, and $P(20\%)_{max}$. But other than that, all the other P values increase with decreasing sample size. Results in Figures 6.13 and 6.14 both suggest that increasing the number of repeat experiments is an effective and robust way to achieve a more converged result.
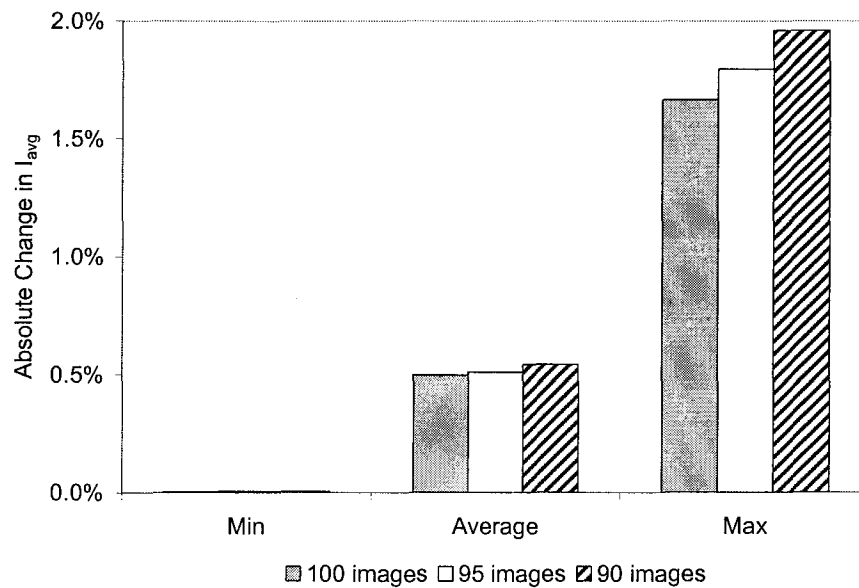
Figure 6.13 The effect of sample size on the absolute change in I_{avg} (t=1.389 ms)
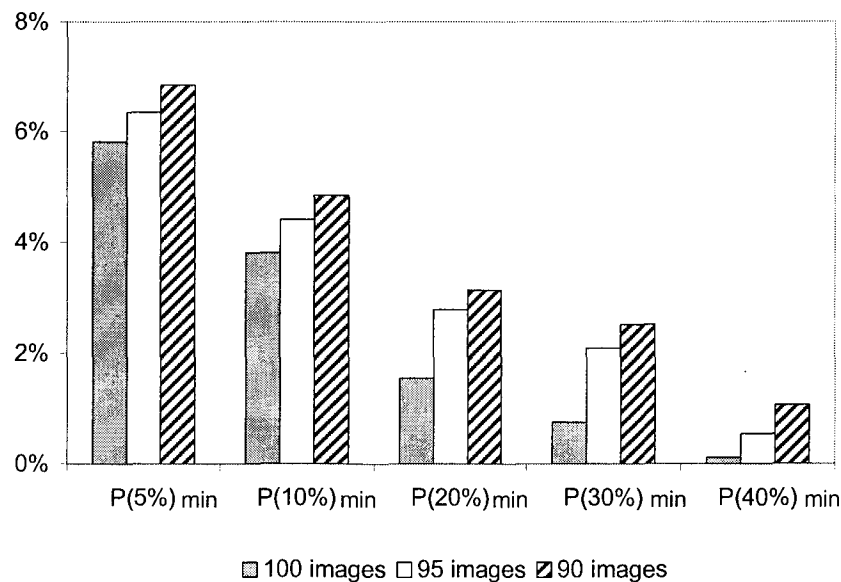
(a) Minimum P values for different threshold values
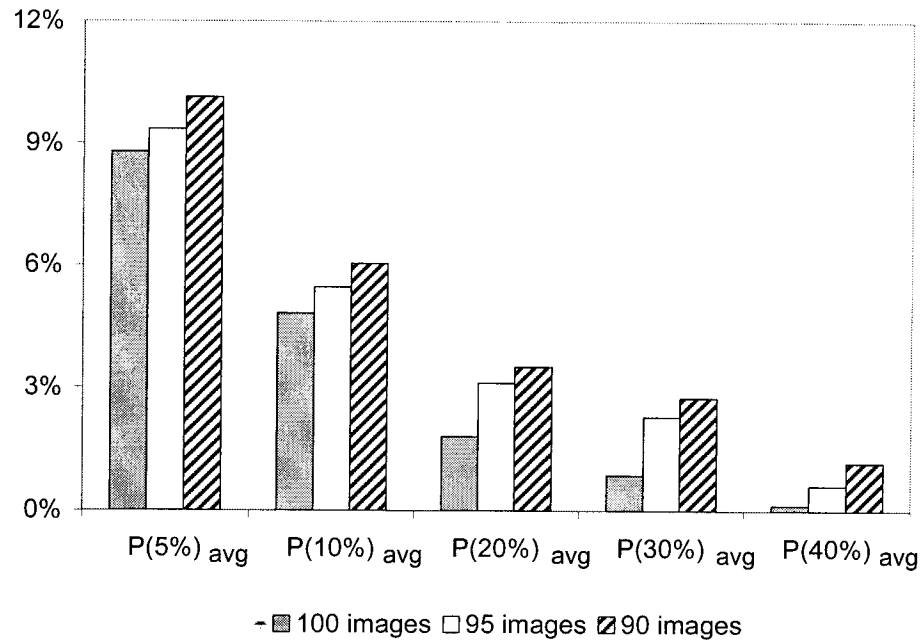
(b) Average P values for different threshold values
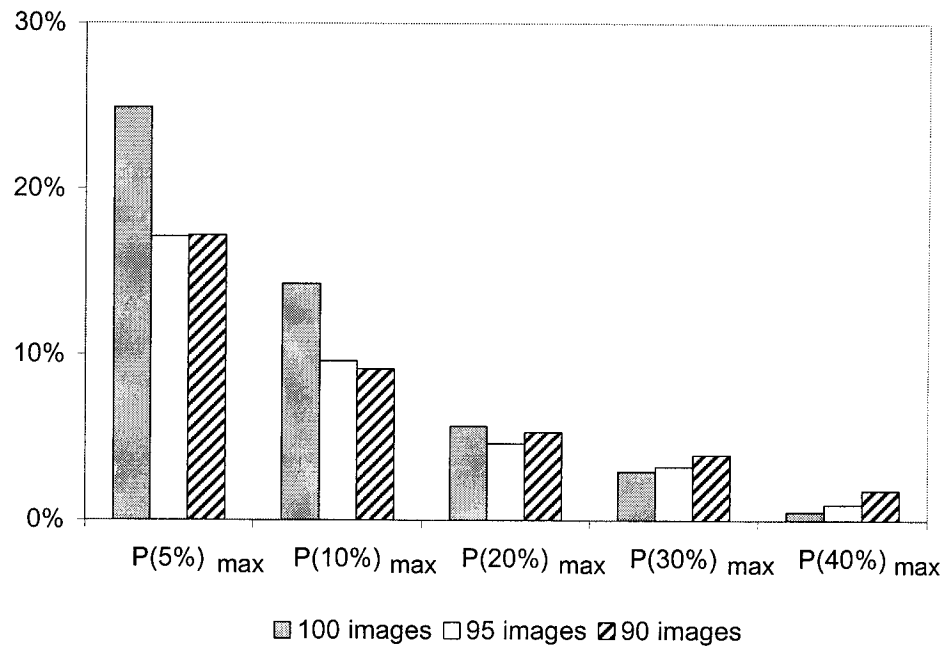
(c) Maximum P values for different threshold values

Figure 6.14 The effect of sample size on the P values (t=1.389 ms)

Effect of Ignition Delay

The ignition delay times measured by the Phantom camera for the 100 OH-PLIF experiments at t=1.389 ms are summarized in Table 6.2. For comparison, the sample statistics for the methane ignition delays reported in Chapter 3 are also included. It is interesting to note that increasing the number of repeat experiments does not reduce the variability. Slight increases in both standard deviation and COV are observed.

Table 6.2 Variability in ignition delay for methane

	Number of experiments	Min (ms)	Max (ms)	Mean (ms)	Std Dev (ms)	COV
OH-PLIF	100	0.489	1.188	0.778	0.150	19%
Chapter 3	20	0.465	0.901	0.736	0.113	15%

With regard to the effect of ignition delay on the convergence of the ensemble-averaged image, the 100 experiments are assigned into 3 bins based on the statistical distribution, as shown in Figure 6.15. Experiments with ignition delays within one standard deviation of the average are assigned to Bin 2. Experiments with ignition delays less or greater than one standard deviation from the average are assigned to Bin 1 and Bin 3, respectively.
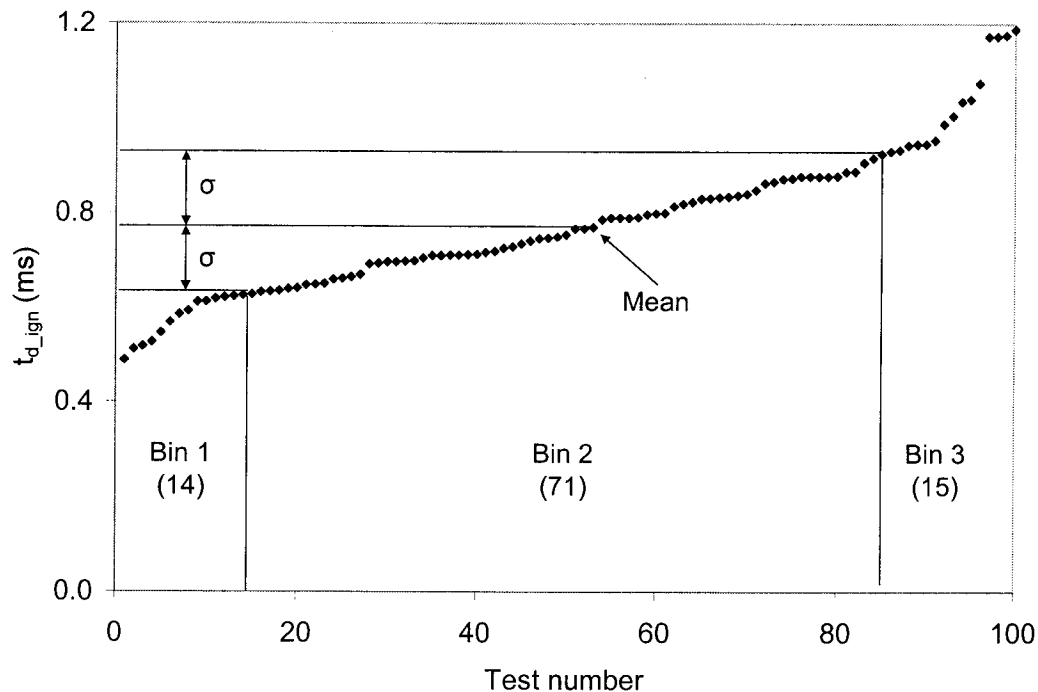
Figure 6.15 Assignment of OH-PLIF images into different bins based on statistical distribution

After sorting the ignition delay from low to high, a significant decrease in both standard deviation and COV is achieved for all the 3 bins, as shown in Table 6.3, as would be expected from the reduced spread in the individual distributions

Table 6.3 Variability in ignition delay for different bins (t=1.389 ms)

	Number of experiments	Min (ms)	Max (ms)	Mean (ms)	Std Dev (ms)	COV
Bin 1&2&3	100	0.489	1.188	0.778	0.150	19%
Bin 1	14	0.489	0.626	0.576	0.048	8%
Bin 2	71	0.628	0.925	0.764	0.084	11%
Bin 3	15	0.930	1.188	1.034	0.099	10%

One ensemble-averaged OH-PLIF image is obtained for each bin, as shown in Figure 6.16. Not surprisingly, the ensemble-averaged image from Bin 2 is most similar to that from Bin 1&2&3. The reaction zone in the ensemble-averaged image from Bin 3 (long ignition delays) is the smallest, since the flame has not been fully-developed when the images were taken. It is also interesting to note that the ensemble-averaged image from Bin 3 is similar to the ensemble-averaged image at t=0.989 ms in Figure 6.8, both of which are based on images taken relatively close to the start of ignition.

The convergence of these ensemble-averaged images in Figure 6.16 are evaluated following the same procedure as described at the beginning of §6.3.3. Figure 6.17 shows the absolute change in I_{avg} for different bins. Figure 6.18 compares the minimum, average, and maximum P values for different threshold values with different bins. In general the results in these two figures agree with each other. The ensemble-averaged image from Bin 2 is the most converged among the 3 bins, both due to a larger sample size and the removal of images with high ignition delay variability. But the image is still not as converged as that from Bin 1&2&3. Even though Bin 1 and 3 have similar sample size and COV, the result from Bin 1 is more converged than that from Bin 3. From these results, it can be inferred that both larger sample size and shorter ignition delay are favorable for a more converged result.
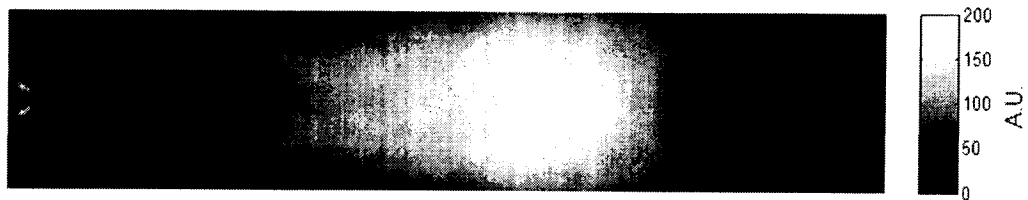
(a) Bin 1&2&3
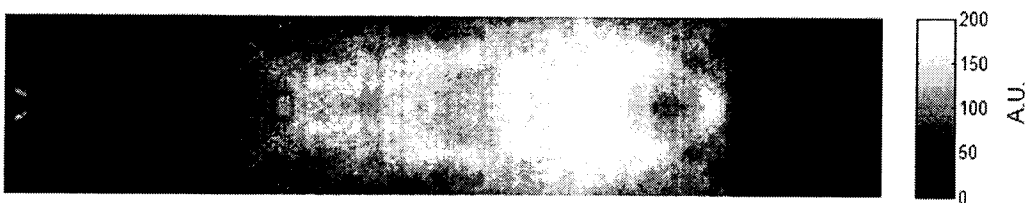
(b) Bin 1
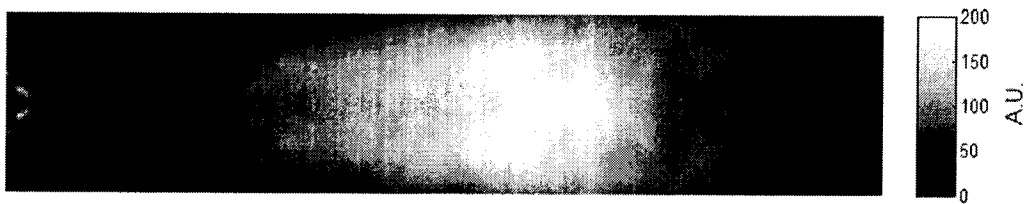
(c) Bin2
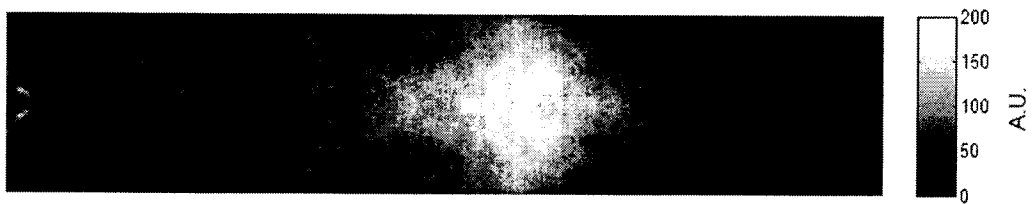
(d) Bin 3

Figure 6.16 Ensemble-averaged OH-PLIF images for different bins (t=1.389 ms)
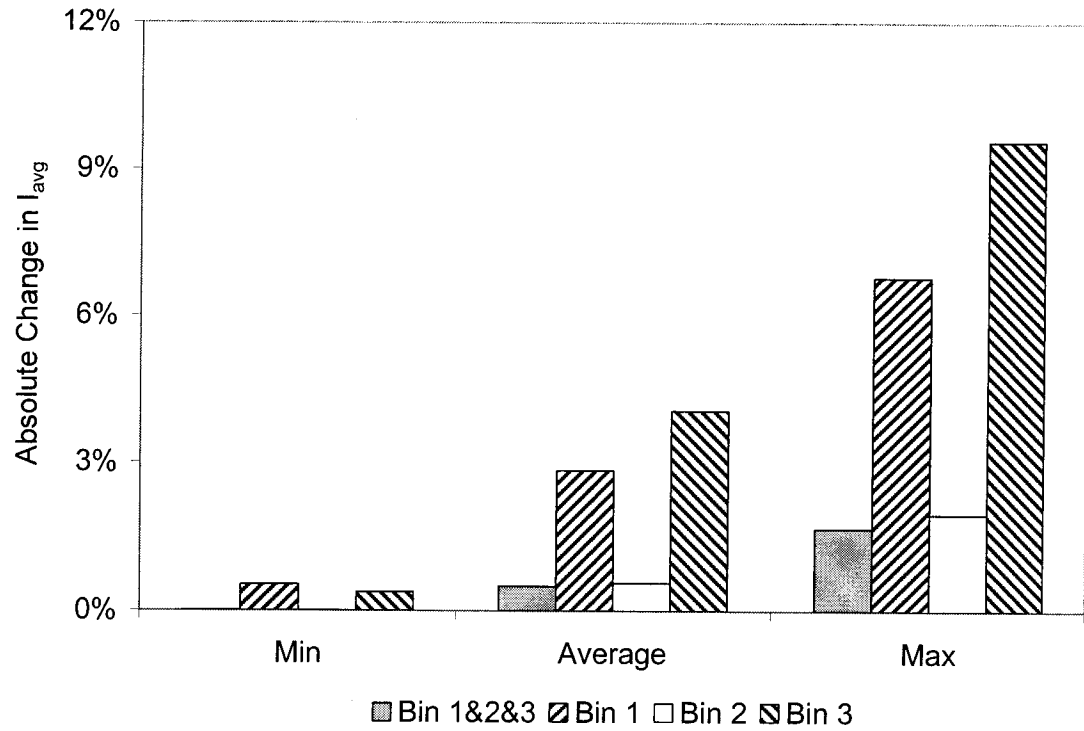
Figure 6.17 Absolute change in the average pixel intensity for different bins (t=1.389 ms)
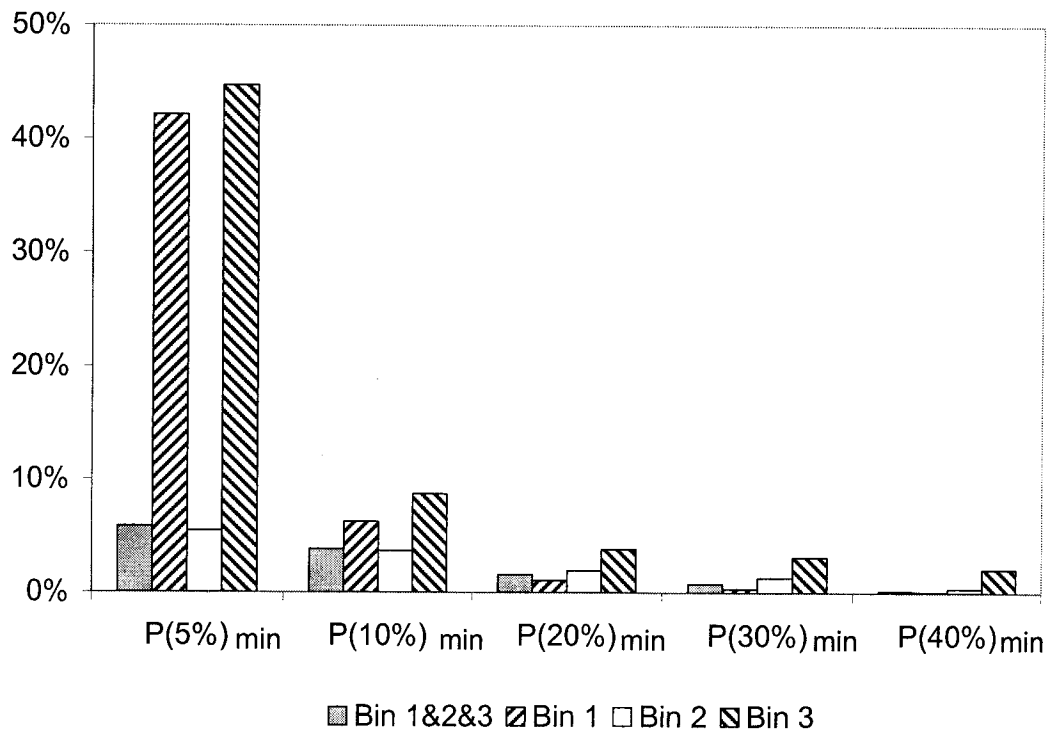
(a) Minimum P values for different threshold values
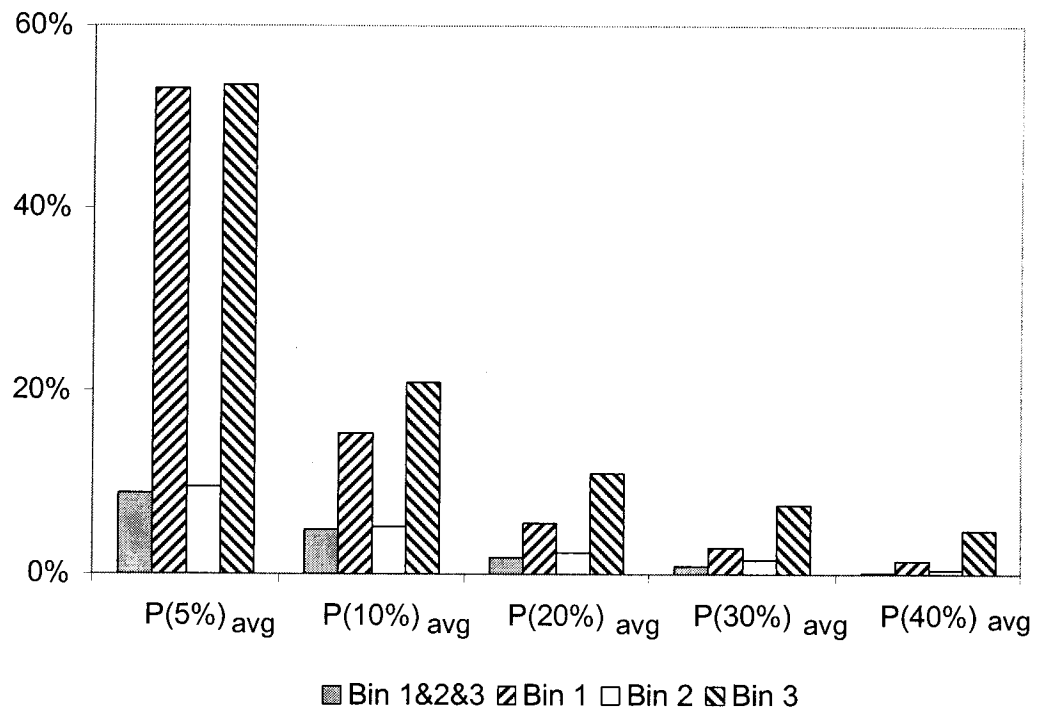
(b) Average P values for different threshold values
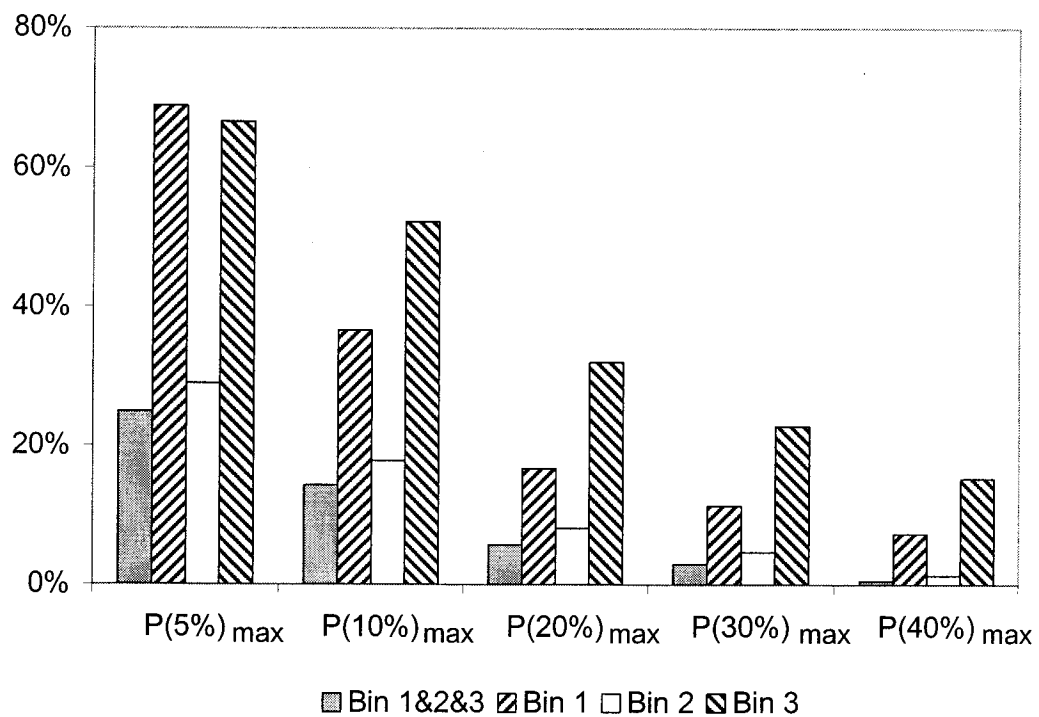
(c) Maximum P values for different threshold values

Figure 6.18 The effect of ignition delay on the absolute change in pixel intensity for each pixel over the flame region (t=1.389 ms)

6.4 Conclusions

PLIF was applied in a shock tube to visualize the OH distribution in turbulent igniting methane jets under engine-relevant conditions. Based on the single-shot OH-PLIF images, OH presence probability images and ensemble-averaged OH-PLIF images were obtained. The effects of sample size and ignition delay on the convergence of the ensemble-averaged OH-PLIF images were examined by means of average pixel intensity variation and pixel-by-pixel intensity variation. The main conclusions of this chapter can be summarized as follows:

1. The OH distributions from repeat experiments conducted under nominally identical operating conditions are markedly different. The single-shot OH images reflect the stochastic nature of the turbulent mixing and autoignition processes that, in turn, leads to significant variations in the ignition delay time and ignition kernel location as has been discussed in earlier chapters of this work.

2. Ensemble averaging of the single-shot OH images produces an image of the mean OH field that differs substantially in appearance from any single realization of the OH field. The ensemble-averaged images resemble the shape of a developing turbulent jet.

3. OH presence probability images show that the run-to-run variability in the OH field is mostly around the boundary of the jet. The variability in the OH distribution gets progressively smaller towards the core of the jet.

4. The results indicate that increasing the number of repeat experiments is the most effective way to produce a more converged ensemble-averaged OH-PLIF image.

Chapter 7
CSE-TGLDM Combustion Model Validation

7.1 Introduction

The combustion process of a transient turbulent natural gas jet is a subject under intense study. Thanks to progress in the study of the chemical kinetics that are important to natural gas combustion at elevated pressures and reduced temperatures, the combustion chemistry for natural gas under engine relevant conditions is now better understood. However, the implementation of detailed chemistry in a multi-dimensional simulation of a turbulent reactive natural gas jet remains a challenging task. In particular, two fundamental problems have to be addressed in order to simulate turbulent combustion using detailed chemistry. First, for any computational fluid dynamic models that do not resolve all of the turbulence scales, a turbulent combustion model is required to account for the effects of turbulent fluctuations on the chemical reaction rates. Second, the combustion system described by detailed chemistry is usually very stiff: the chemical time scales associated with different reaction scalars vary drastically. To solve such a stiff system directly in most practical turbulent reactive flow simulations is still beyond the reach with the existing computational power. Thus methods to reduce the CPU time required for computing the reaction rates from detailed chemistry must be used.

A combustion model was proposed by Huang *et al.* [120] to provide solutions to the above two problems. That model incorporates the Conditional Source-term Estimation (CSE) [115] and Trajectory Generated Low-Dimensional Manifold (TGLDM) [126] methods, which can provide a closure for the chemical source term at the level of the first moment with a relatively low computational cost. The model has been successfully applied to predict the autoignition delay time, ignition kernel location, and NOx emissions of non-premixed methane jets under engine relevant conditions, and the results have been validated using experimental data obtained from a high-pressure shock tube facility as well as data reported in literature.

In this chapter, the CSE-TGLDM combustion model is applied to predict the OH radical distribution in a combusting non-premixed methane jet. The simulation results are then compared to the results of the author's OH-PLIF experiments presented in Chapter 6.

7.2 Combustion Model Formulation

7.2.1 CFD Model Formulation

For the experimental conditions described in Chapter 6, the jet is choked at the nozzle exit. The flow field in the region close to the nozzle exit has a high Mach number and thus must be treated as being fully compressible. The Reynolds averaged transport equations for mass, momentum and energy in the cylindrical coordinates with an axisymmetric configuration are:

- Continuity

$$\frac{\partial \widetilde{\rho}}{\partial t} + \frac{1}{r}\frac{\partial}{\partial r}(\overline{\rho}r\widetilde{u}_r) + \frac{\partial}{\partial z}(\overline{\rho}\widetilde{u}_z) = 0 \tag{7.1}$$

- Momentum

$$\overline{\rho}\left(\frac{\partial \widetilde{u}_r}{\partial t} + \widetilde{u}_r\frac{\partial \widetilde{u}_r}{\partial r} + \widetilde{u}_z\frac{\partial \widetilde{u}_r}{\partial z}\right) = -\frac{\partial \widetilde{\rho}}{\partial r} + \left(\frac{1}{r}\frac{\partial}{\partial r}(r\tau_{rr}) + \frac{\partial \tau_{rz}}{\partial z}\right) \tag{7.2}$$

$$\overline{\rho}\left(\frac{\partial \widetilde{u}_z}{\partial t} + \widetilde{u}_r\frac{\partial \widetilde{u}_z}{\partial r} + \widetilde{u}_z\frac{\partial \widetilde{u}_z}{\partial z}\right) = -\frac{\partial \widetilde{\rho}}{\partial z} + \left(\frac{1}{r}\frac{\partial}{\partial z}(r\tau_{rz}) + \frac{\partial \tau_{zz}}{\partial z}\right) \tag{7.3}$$

where τ designates the stress tensor whose components are given by:

$$\tau_{rr} = \mu_t\left[2\frac{\partial \widetilde{u}_r}{\partial z} - \frac{2}{3}(\nabla \cdot v)\right] \tag{7.4}$$

$$\tau_{zz} = \mu_t\left[2\frac{\partial \widetilde{u}_z}{\partial z} - \frac{2}{3}(\nabla \cdot v)\right] \tag{7.5}$$

$$\tau_{zr} = \tau_{rz} = \mu_t\left[2\frac{\partial \widetilde{u}_z}{\partial r} + \frac{\partial \widetilde{u}_r}{\partial z}\right] \tag{7.6}$$

- Energy

$$\overline{\rho}C_p\left(\frac{\partial \widetilde{T}}{\partial t} + \widetilde{u}_r\frac{\partial \widetilde{T}}{\partial r} + \widetilde{u}_z\frac{\partial \widetilde{T}}{\partial z}\right) - \left(\frac{\partial p}{\partial t} + \widetilde{u}_r\frac{\partial \widetilde{p}}{\partial r} + \widetilde{u}_z\frac{\partial \widetilde{p}}{\partial z}\right) = \lambda\left[\frac{1}{r}\frac{\partial}{\partial r}\left(r\frac{\partial \widetilde{T}}{\partial r}\right) + \frac{\partial^2 \widetilde{T}}{\partial z^2}\right] \tag{7.7}$$

$$+\mu_t\left\{2\left[\left(\frac{\partial \widetilde{u}_r}{\partial r}\right)^2 + \left(\frac{\widetilde{u}_r}{r}\right)^2 + \left(\frac{\partial \widetilde{u}_z}{\partial z}\right)^2\right] + \left(\frac{\partial \widetilde{u}_r}{\partial z} + \frac{\partial \widetilde{u}_z}{\partial r}\right)^2 - \frac{2}{3}\left(\frac{1}{r}\frac{\partial}{\partial r}(r\widetilde{u}_r) + \frac{\partial \widetilde{u}_z}{\partial z}\right)^2\right\} + \overline{\dot{\omega}}$$

Body force and radiation effects have been neglected in these equations. All the chemical species are assumed to diffuse at the same rate and the Lewis number is assumed to be unity. The turbulent viscosity μ_t is calculated using the standard $k-\varepsilon$ model [195]

$$\mu_t = \bar{\rho} C_u \frac{\tilde{k}^2}{\tilde{\varepsilon}} \tag{7.8}$$

where $\tilde{k}$ is the Favre averaged turbulent kinetic energy; $\tilde{\varepsilon}$ is the Favre averaged dissipation rate of turbulent kinetic energy; the value of coefficient C_u is 0.09, as suggested in the work of Warnatz et al. [124].

7.2.2 Combustion Model Formulation

In the CSE method, a probability density function for mixture fraction is constructed from its local mean and variance. The closure for transport equations for the mean and variance of mixture fraction is achieved by employing a gradient transport hypothesis:

- Mean mixture fraction

$$\bar{\rho}\left(\frac{\partial \langle Z \rangle}{\partial t} + \tilde{u}_r \frac{\partial \langle Z \rangle}{\partial r} + \tilde{u}_z \frac{\partial \langle Z \rangle}{\partial z} \right) = \frac{1}{r}\frac{\partial}{\partial r}\left(\frac{\mu}{Sc} \frac{\partial \langle Z \rangle}{\partial r} \right) + \frac{\partial}{\partial z}\left(\frac{\mu}{Sc} \frac{\partial \langle Z \rangle}{\partial z} \right) \tag{7.9}$$

- Variance of mixture fraction

$$\bar{\rho}\left(\frac{\partial \langle Z''^2 \rangle}{\partial t} + \tilde{u}_r \frac{\partial \langle Z''^2 \rangle}{\partial r} + \tilde{u}_z \frac{\partial \langle Z''^2 \rangle}{\partial z} \right) = \frac{1}{r}\frac{\partial}{\partial r}\left(\frac{\mu}{Sc} \frac{\partial \langle Z''^2 \rangle}{\partial r} \right) \tag{7.10}$$

$$+ \frac{\partial}{\partial z}\left(\frac{\mu}{Sc} \frac{\partial \langle Z''^2 \rangle}{\partial z} \right) + \frac{2\mu}{Sc}\left(\frac{1}{r}\frac{\partial \langle Z \rangle}{\partial r} + \frac{\partial \langle Z \rangle}{\partial z} \right)^2 - \bar{\rho} c_x \frac{\varepsilon}{k} \langle Z''^2 \rangle$$

In these two equations, Sc denotes the turbulent Schmidt number. In this study, a value of 0.9 is assigned to Sc, which is identical to that used by Hasse et al. [96]. A standard value of 2.0 is assigned to the coefficient c_x in the source term of the variance of mixture fraction [196]. To use the two-dimensional TGLDM for the chemical source term, transport equations for two progress variables (Y_{CO_2} and Y_{H_2O} in this work) need to be solved. The basic form of the transport equation for a reaction scalar Y_i is given by:

$$\bar{\rho}\left(\frac{\partial \tilde{Y}_i}{\partial t} + \tilde{u}_r \frac{\partial \tilde{Y}_i}{\partial r} + \tilde{u}_z \frac{\partial \tilde{Y}_i}{\partial z} \right) = \frac{1}{r}\frac{\partial}{\partial r}\left(\frac{\mu}{Sc} \frac{\partial \tilde{Y}_i}{\partial r} \right) + \frac{\partial}{\partial z}\left(\frac{\mu}{Sc} \frac{\partial \tilde{Y}_i}{\partial z} \right) + \bar{\dot{\omega}}_i \tag{7.11}$$

where $\bar{\dot{\omega}}_i$ is the mean rate of change of Y_i due to chemical reaction. A total of ten transport equations are solved in the simulation model using a Flux-Corrected Transport (FCT) algorithm [197] with a finite-volume representation. This algorithm is suitable for dealing with flow fields with large gradients which often cause significant numerical dispersion or dissipation in ordinary discretization schemes. The FCT scheme used in this work is nominally fourth-order accurate in space. A second-order Runge-Kutta time advance scheme is used for the temporal discretization. Since the equations for a fully compressible flow are solved, the coupling between the density and pressure fields is achieved directly through the energy equation in conjunction with the equation of state.

A schematic of the simulation is shown in Figure 7.1. The instantaneous Favre probability density function, $\widetilde{P(Z)} = \dfrac{\rho(Z)P(Z)}{\bar{\rho}}$, is presumed to take on the form of a β function, which is completely determined by the mean and variance of the mixture fraction. The transport equations for the instantaneous values of the mean and variance of mixture fraction are solved, as are those for the means of the two progress variables, $\widetilde{Y_{CO_2}}$ and $\widetilde{Y_{H_2O}}$. The CSE module takes the PDF, $\widetilde{Y_{CO_2}}$ and $\widetilde{Y_{H_2O}}$ and solves for the conditional average of $\langle Y_{CO_2} \mid \eta \rangle$ and $\langle Y_{H_2O} \mid \eta \rangle$ using $\tilde{Y}_i = \int_0^1 \widetilde{P(Z)} \langle Y(Z) \rangle dZ$. The TGLDM module takes $\langle Y_{CO_2} \mid \eta \rangle$ and $\langle Y_{H_2O} \mid \eta \rangle$ as the input and performs an interior point search and interpolation to find the corresponding species mass fractions and reaction rates on the manifold. The conditional mass fractions of reaction scalar $\langle Y_i \mid \eta \rangle$ is reassembled using the PDF in the CSE module to get the unconditional mean, which is fed back to the CFD code to close the conservation equation.

The computational domain, which is half of the axisymmetric plane cutting through the centerline of the shock tube, was discretized using a 110 x 440 (radial x axial) structured grid. Figure 7.2 shows the computational grid used in the simulation. Since the grid is too fine, only every other 10 grids are shown in the figure. The nozzle exit was resolved using six grid points along the radial direction. A relatively fine mesh has been used close to the exit of the nozzle to resolve the sharp gradient locally. For the transient velocity profile at the nozzle exit of the injector, a polytropic expansion from the stagnation pressure was used. The polytropic coefficient was obtained by matching the steady state mass flow rate with the experimentally measured value.
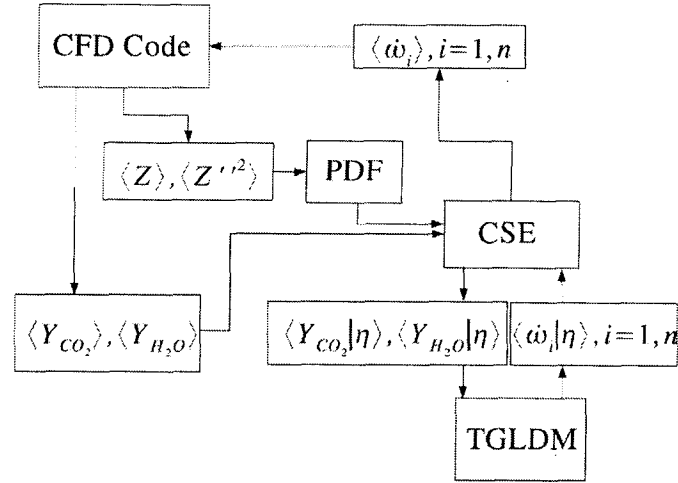
Figure 7.1 Structure of CSE-TGLDM method in the simulation
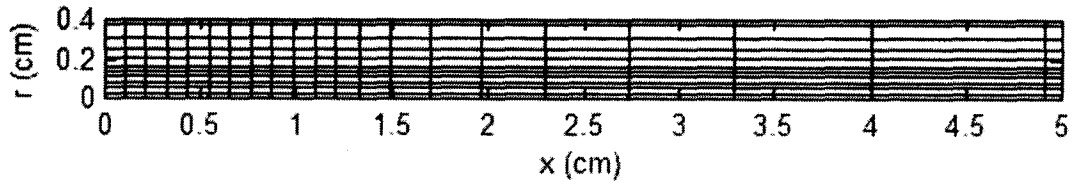
Figure 7.2 Computational grid in the simulation

7.3 Results and Discussion

Figure 7.3 shows profiles of OH mass fraction at different stages of combustion as predicted by the simulation. For comparison, ensemble-averaged OH-PLIF images from Chapter 6 are shown in Figure 7.4. It is immediately obvious that the OH distribution shown in the ensemble-averaged images (Figure 7.4) is totally different from that shown in the simulation results (Figure 7.3). The flame occupies a much larger area in the ensemble-averaged images, and resembles the shape of a developing turbulent jet. In contrast, the simulation results show a clearly defined diffusion flame, a thin layer of reaction zone surrounding the jet, and the flame being lifted-off near the nozzle.

On further consideration, the discrepancy between the simulated and the ensemble-averaged experimentally-measured OH distribution is not surprising. The ignition process is highly sensitive to the history of scalar dissipation [119]. In a given realization of the flow field in the present study, there will only be a relatively small volume of fluid that will be flammable, and an even smaller volume would be likely to undergo autoignition on relatively short time-scales. Within the extremely small volume of ignitable fluid, there will therefore only be a limited representation of the (essentially infinite) conceivable variations of scalar dissipation history.
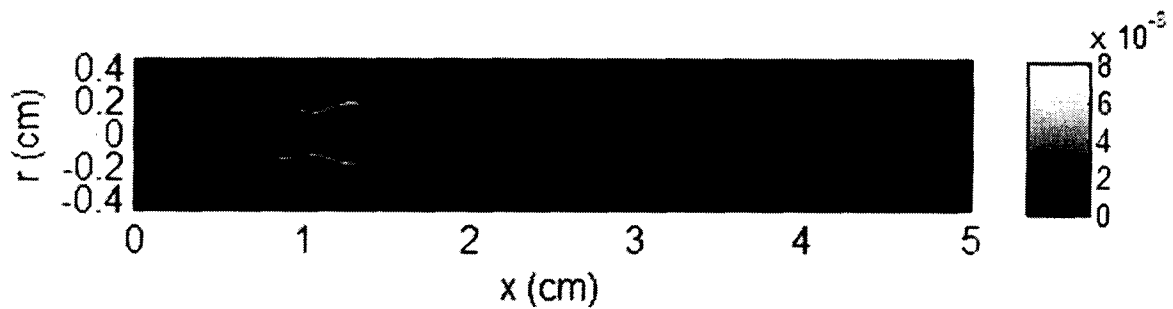
(a) Shortly after the ignition (t=0.1882 ms)
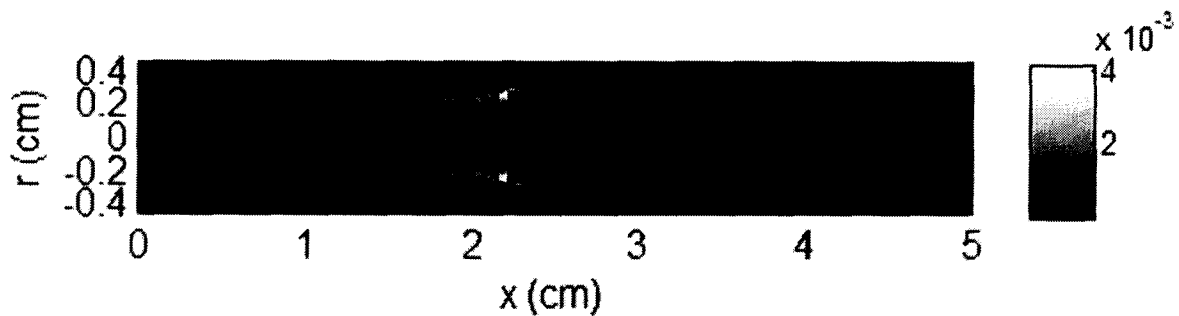
(b) Before the injection stops (t=0.979 ms)
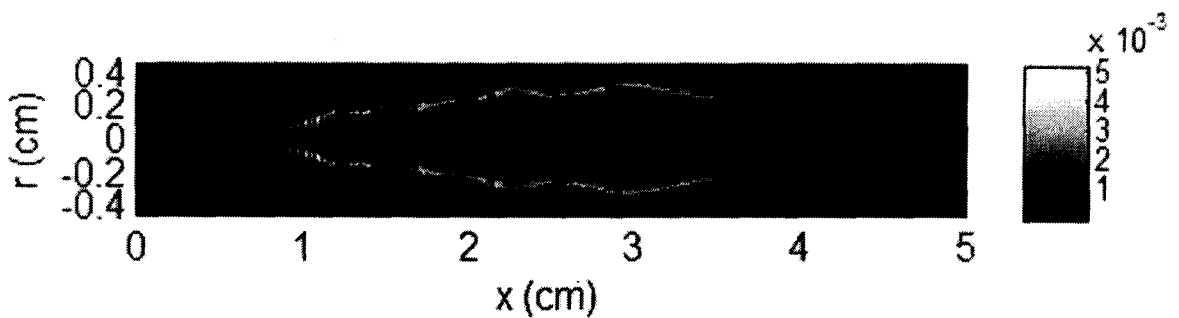
(c) After the injection stops (t=1.185 ms)
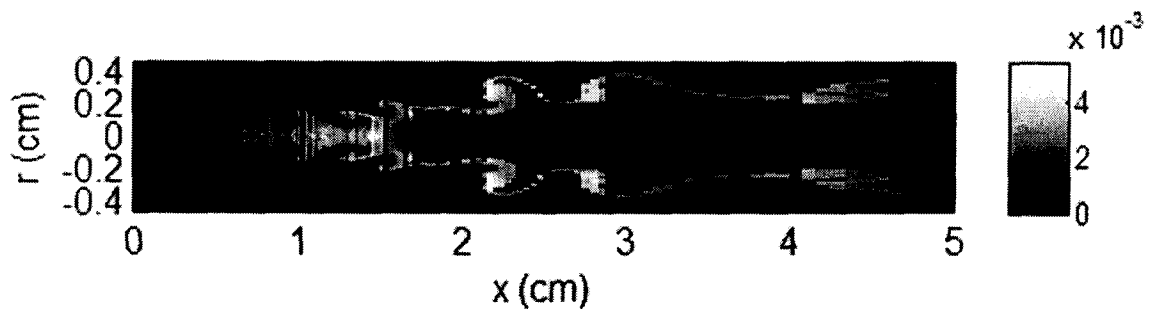
(d) After the injection stops (t=1.389 ms)

Figure 7.3 Profiles of OH mass fraction at different stages of combustion
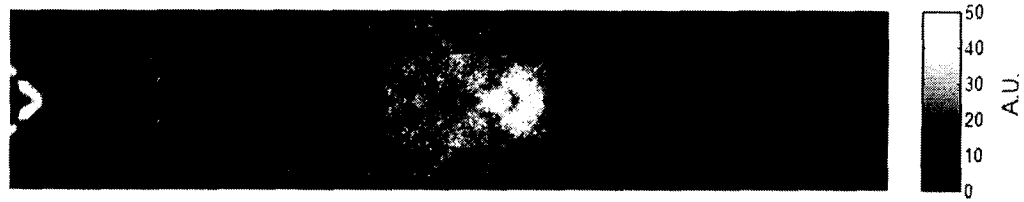
(a) t=0.989 ms
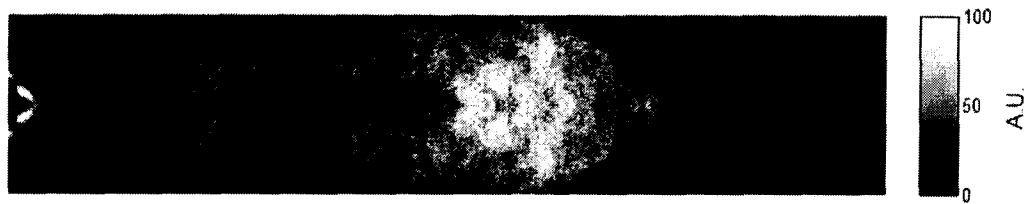
(b) t=1.189 ms
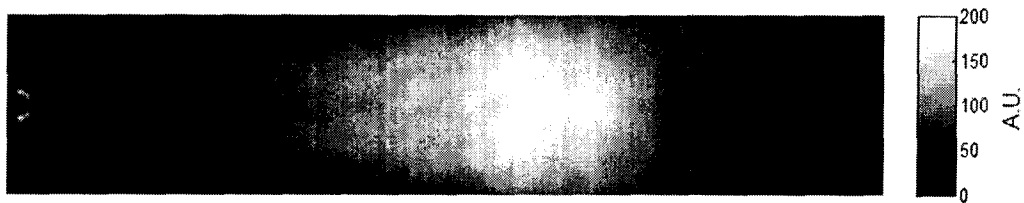
(c) t=1.389 ms

Figure 7.4 Ensemble-averaged OH-PLIF images at different stages of combustion

Furthermore, the chemical reactions participating in the autoignition process involve chemical species that have an extremely low concentration; indeed, in the initial field, most radical species have such a low concentration that there is a high likelihood that there are no molecules of these radicals present. If one assumes that there is only one molecule of a certain radical present, the ignition delay can be orders of magnitude shorter depending on the volume of the enclosure in which the ignition is taking place. With very low radical concentrations, it is likely inappropriate to treat the reacting flow with a continuum-based method. Using stochastic methods, it is found that, when the volume of fluid undergoing ignition is very small (as could well be the case for a non-premixed jet), variations in the ignition delay time can become very large [198].

The intrinsic shot-to-shot variations in turbulent mixing and shot-to-shot variations in the chemical reaction paths described above would suggest that there should be inherent variations in the ignition delay time from one realization to another. These variations are clearly visible in the experimental results presented in the previous chapter (Figures 6.5, 6.6, and 6.7). Each experiment is viewed as a separate realization. Ideally, a well designed simulation should be able to reproduce the mean of these realizations in some sense.

Herein lies a serious problem: the Reynolds averaged paradigm is particularly ill-suited to represent the true physics of a first-passage time problem [199]. In the present study, the simulation does not truly reproduce what one would expect the Reynolds averaged field from the experiments to look like, i.e., the ensemble-averaged images shown in Figure 7.4. In the simulations, ignition occurs at a particular location first and this appears as a very rapid rise in temperature at that particular location after an easily identifiable time. In the experiments, as is evidenced by the results presented in Chapters 3 and 5, ignition happens over a wide range of times and over a wide range of distances downstream from the nozzle. The Reynolds averaged field one would expect from averaging many experiments together would then likely see a fairly gradual rise in temperature over a broad area of the flow.

To illustrate this point, Figure 7.5 shows several realizations of the error function with a Gaussian-distributed random offset that has a mean of 0.5. The error function is chosen because it has a similar character to the temperature in a homogeneous autoignition problem. Also shown in the figure is the mean of 200 of these functions. Any one realization shows a very sharp rise with exactly the same profile – the only difference between two realizations is the point at which the sharp rise occurs. Meanwhile, when many realizations are averaged together, the average shows a much slower rise with x. A similar behaviour for the autoigniting jet is expected with the added complication that there would be smoothing both in time and in space. Instead, the Reynolds averaged simulation predicts a rapid rise in temperature is at a single location in space, which has the same character as one would expect from a single realization of the autoigniting jet.
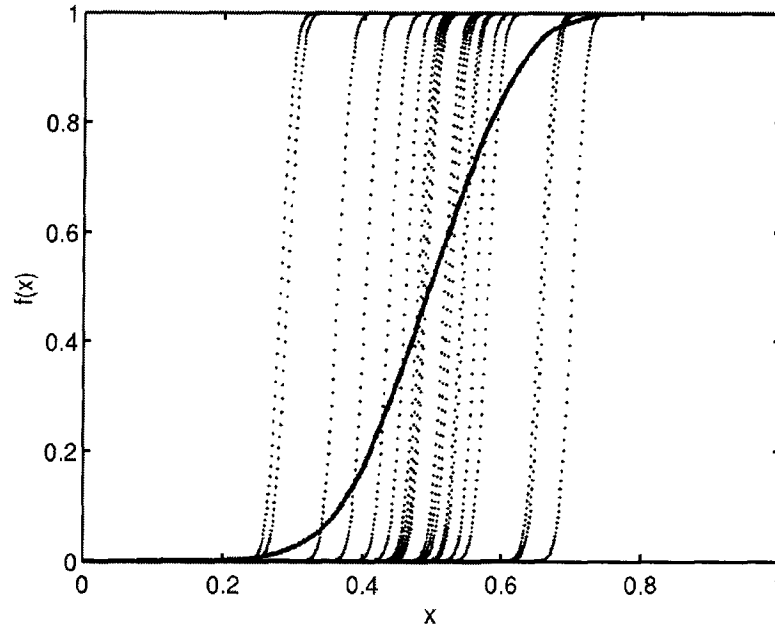
Figure 7.5 Illustration of fluctuations. Dashed curves: f(x) = erf(x − a) where a is Gaussian distributed random variable; solid curve: f(x) is mean over 200 realizations of a

7.4 Conclusions

A combustion model, which incorporated the Conditional Source-term Estimation (CSE) method for the closure of the chemical source term and the Trajectory Generated Low-Dimensional Manifold (TGLDM) method for the reduction of detailed chemistry, was applied to predict the OH distribution in a combusting non-premixed methane jet. The simulation fails to predict the OH distribution as indicated by the ensemble-averaged OH-PLIF images, since the model cannot account for fluctuations in either turbulence or chemistry. Instead, the simulation results show some features present in certain single-shot OH-PLIF images, such as a well-defined diffusion flame, a reaction zone surrounding the jet, flame being lifted from the nozzle. The failure of the model to predict even the general form of the ensemble-averaged OH field from the experiments demonstrates a significant weakness in the Reynolds averaged method. To accurately predict the combustion process of a transient turbulent natural gas jet, it maybe necessary to resort to using far more computationally expensive methods. For example, it is possible that LES could account for the fluctuations. However, the experimental results indicate that one would need to run the LES at least 100 times to get a converged average and LES would be significantly more computationally expensive than the RANS method used here. There is a clear need for further research to address this issue.

Chapter 8
Conclusions and Future Work

The objective of this research was to improve understanding of the direct-injection compression-ignition gaseous fuel combustion process under engine-relevant conditions. This objective has been addressed in 2 phases using two parallel strategies: experiments and simulation. The experiments made use of UBC's optically-accessible shock tube facility, which can provide flexible and reproducible conditions not achievable in an engine. The simulations, incorporating state-of-the-art numerical methods and combustion sub-models, were used to help achieve a better understanding of the experimental results. In Phase 1, the focus was on global measurements that are ultimately important in engine development. The influence of key operating parameters, including pre-combustion temperature, injection duration, and injection pressure, as well as fuel composition, on autoignition and NOx emissions was investigated. The autoignition delay was also predicted by simulating a counter-flow diffusion flame under similar conditions to the experiments with FlameMaster. In Phase 2, OH-PLIF was used to provide insight on the location and nature of the reaction zones of igniting turbulent methane jets. The experiments were complemented by a simulation of the autoignition and combustion process of a non-premixed methane jet using a CSE-TGLDM combustion model.

Autoignition of methane and methane/ethane under diesel conditions have been studied before. However no previous studies have been carried out to investigate the autoignition of high pressure non-premixed methane/nitrogen and methane/hydrogen jets under engine-relevant conditions. High speed video imaging was used to determine both ignition delay and ignition location; thus, providing valuable insight into the non-premixed autoignition and combustion process. OH-PLIF was used to study the location and nature of the reaction zones of the autoigniting jets. The author is unaware of any similar application of OH-LIF to turbulent igniting methane jets in a shock tube under engine-relevant conditions. Similarly, no previous studies have been found within the literature that investigate the convergence issue raised from applying single-shot laser imaging techniques to the measurement of non-premixed turbulent combustion phenomena. The significance of the OH-PLIF experiments in the present study is that it not only shows the existence of fluctuations in the non-premixed turbulent combustion process, but also reveals the inherent defect of RANS-based numerical models.

This chapter offers a general overview of the salient findings of the research and aims to provide an interpretation of these results in the context of improved understanding of the autoignition and emissions formation process. Summary plots which combine results presented in previous chapters are presented where they augment the discussion.

8.1 Summary of Results, and Conclusions

Gaseous Fuel Composition

The composition of the gaseous fuel has a substantial impact on the combustion process and emissions, as summarized in Figure 8.1. Experimentally, the addition of 10% ethane or 20% hydrogen to the methane fuel was found to reduce the mean ignition delay, while the addition of 20% nitrogen resulted in an increase in the mean ignition delay. However, the stochastic nature of the injection and autoignition processes result in significant scatter in the experimental data and therefore a low level of confidence in the above result. Adding credence to the experimental results are the results of the FlameMaster simulation shown in Figure 8.2. The predictions not only show the same trends as the experiments but provide insight to the mechanisms by which these trends might occur. FlameMaster simulation suggests that ethane or hydrogen addition accelerates methane oxidation by providing more reactive radicals. With nitrogen dilution, the predictions suggest that ignition delay increases simply because of an increase in the thermal mass, and that nitrogen is not involved in reactions generating reactive radicals. The strong agreement between the experimental and numerical results, Figures 8.1 (upper left) and 8.2 respectively, suggest that a greater level of confidence may be applied to the observed trend than is indicated by statistics alone. The combined use of experimental and numerical techniques to elucidate details of the autoignition and combustion processes is believed to be a particular strength in the present work.

With respect to the effects of fuel additives on the spatial location of the ignition kernel as shown in the upper right and lower left bar charts in Figure 8.1, with the addition of either ethane or nitrogen the ignition kernel moves further downstream both relative to the injector tip and relative to the jet length. The addition of hydrogen does not show significant influence on the ignition kernel location. Some similar trends are observed for all the four fuels however. Ignition kernels are generally not found in two regions: (1) the near injector orifice region, characterized by high probabilities of relatively rich mixture, short residence times, and high turbulent strain field; (2) the jet tip region, characterized by a

starting spherical vortex structure.

NOx emissions increase significantly with ethane addition, and decrease significantly with nitrogen or hydrogen addition. Thermodynamic calculations indicate that the changes are due to changes in adiabatic flame temperature of the base fuel with the addition of additional components.

The effects of fuel composition on variability in ignition delay, ignition kernel location, and NOx emissions are summarized in Figure 8.3. With ethane or hydrogen addition, the variability in ignition delay was found to increase slightly. Diluting the fuel with nitrogen was also found to cause higher variability in the ignition delay albeit to a greater degree. With ethane addition, the variability in ignition kernel location is almost unchanged. The addition of nitrogen or hydrogen results in higher variability in ignition kernel location. With ethane or hydrogen addition, a substantial decrease in NOx emissions variability is observed, suggesting the stability of the combustion process is improved. Nitrogen addition introduces more variability in NOx emissions, suggesting the combustion process becomes less stable.
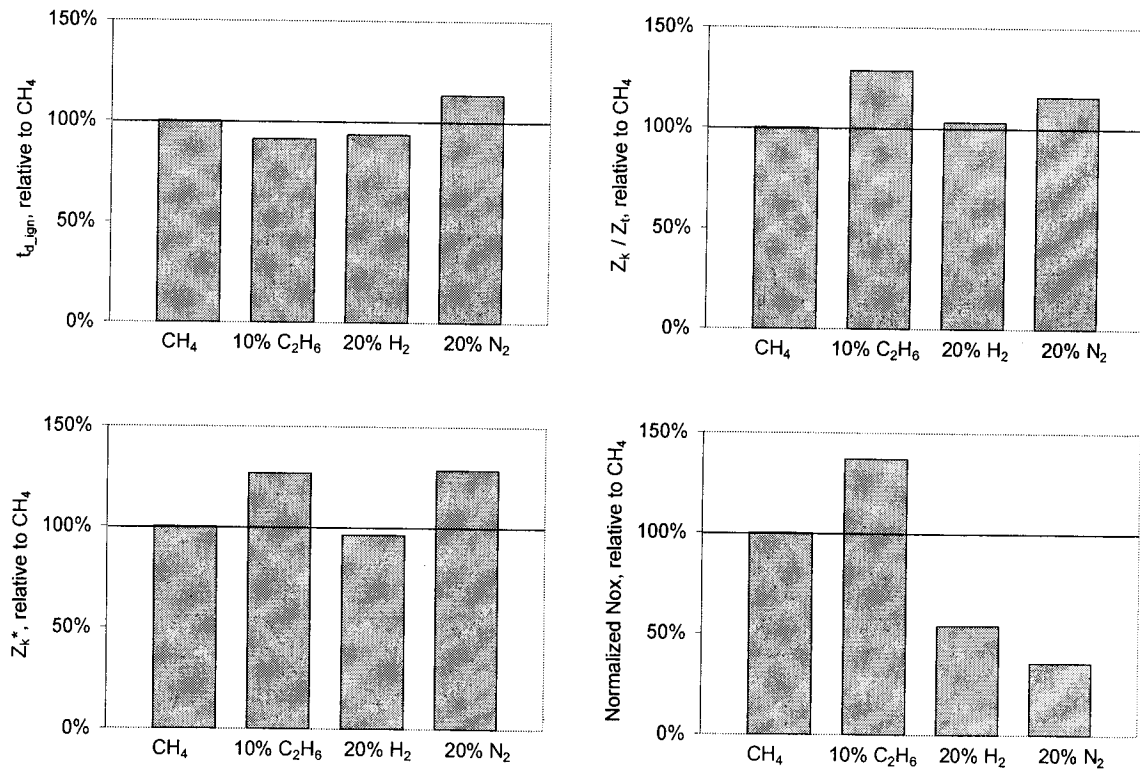
Figure 8.1 Summary of effects of fuel composition on t_{d_ign}, Z_k^*, Z_k/Z_t, and NOx emissions (P_o=30 bar, T_o=1300 K, P_i=120 bar, t_i=1.0 ms, experimental measurements)
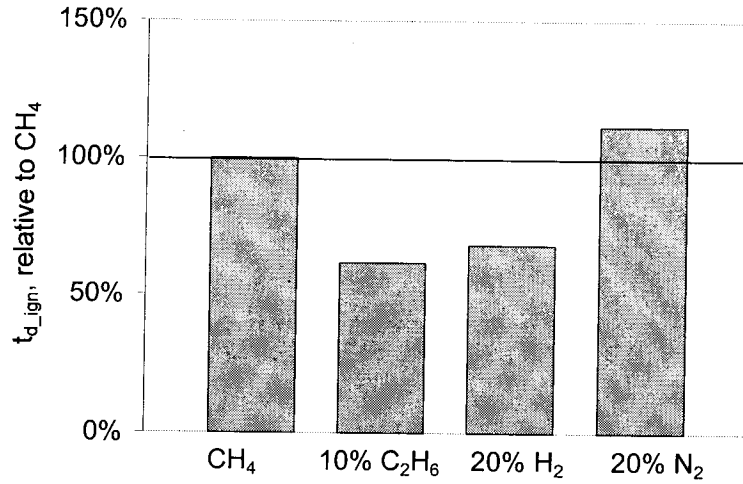
Figure 8.2 Summary of effects of fuel composition on t_{d_ign} simulated by FlameMaster

(T_f=300 K, T_o=1300 K, P=30 bar, χ=1)
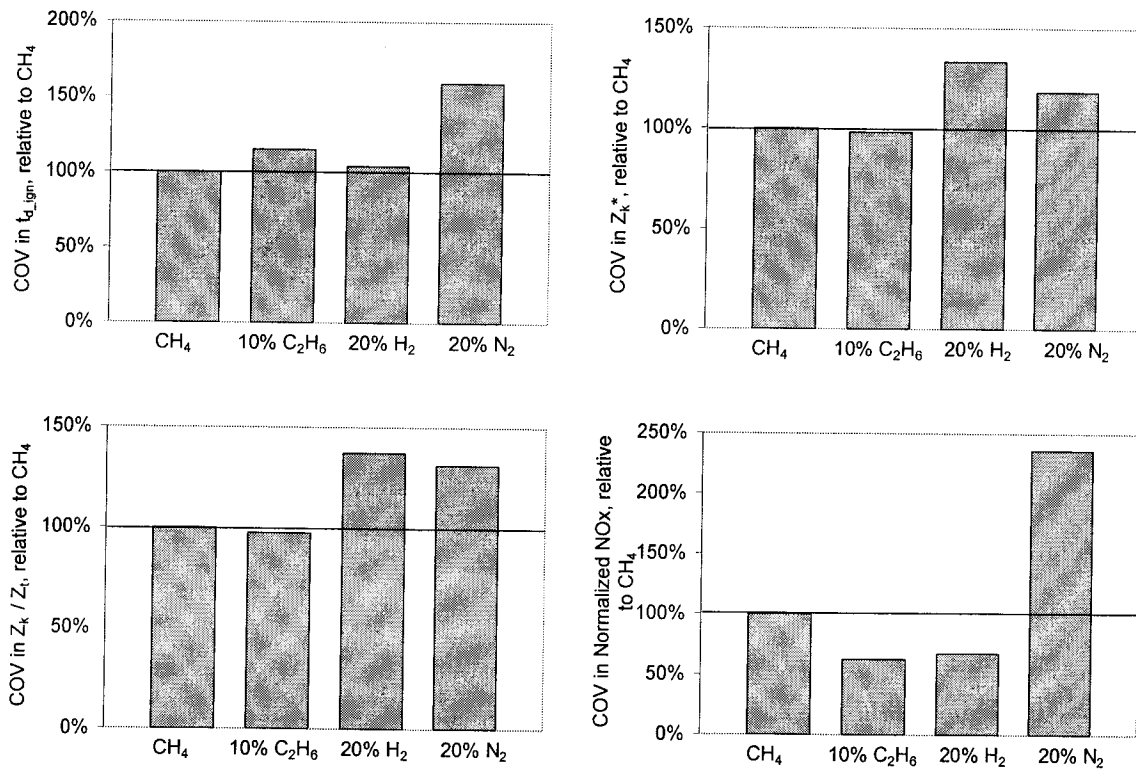
Figure 8.3 Summary of effects of fuel composition on run-to-run variability

(P_o=30 bar, T_o=1300 K, P_i=120 bar, t_i=1.0 ms)

Pre-Combustion Temperature

Pre-combustion temperature was found to have significant effects on the autoignition process and NOx emissions. Increasing pre-combustion temperature was seen to reduce the ignition delay significantly and increase NOx emissions significantly. With increasing pre-combustion temperature, the ignition kernel moves closer to the injector tip, although its location relative to the jet length is unchanged. The trend between the ignition delay and the pre-combustion temperature simulated by FlameMaster agreed closely with that from the experimental results.

Injection Pressure

A modest increase in injection pressure reduces the ignition delay for all fuels. As discussed in Chapters 3 and 5, increasing the injection pressure ratio will yield a higher Reynolds number and thereby improve mixing between fuel and oxidant. However, when the injection pressure is increased excessively, the ignition delay increases due to the heat released in the combustion process being dissipated too rapidly. These trends are seen experimentally, but are not predicted by FlameMaster under the conditions simulated. Also with increasing injection pressure ratio, the ignition kernel moves further downstream both relative to the injector tip and relative to the jet length. NOx emissions increase with increasing injection pressure ratio; this is thought due to the enhancement in fuel-air mixing (and thus heat transfer) associated with higher injection pressure which promotes the formation of thermal NOx.

Injection Duration

Injection duration showed only limited effect on ignition delay and ignition kernel location in the present study. One possible reason for this lack of sensitivity to injection duration is that the actual injection event was always longer than the commanded injection duration (often significantly so) due to the geometric properties of the fuel injector. With the likely adoption of multiple (short) injection pulses per cycle in direct injected engines, further studies in this area may be warranted.

OH Radical Distribution

Single-shot OH-PLIF imaging well illustrated the stochastic nature of the autoignition process of non-premixed methane jets. The OH distributions from repeat experiments conducted under nominally identical operating conditions were seen to differ

substantially (Figures 6.5, 6.6, and 6.7 refer). The shot-to-shot variations in OH distribution were attributed to the inherent variations in the ignition delay time and ignition kernel location, which are caused by shot-to-shot variations in turbulent mixing and shot-to-shot variations in the chemical reaction paths. Because of the randomness in the location, size, and shape of the OH field in each single-shot image, the flame was seen to occupy a much larger volume in the ensemble-averaged images than in any single realization of the OH field. As was discussed in Chapter 6, the ensemble averaging process, effectively, smoothes the data collected from the single-shot combustion images in both the spatial and temporal domains.

The convergence of the ensemble-averaged OH-PLIF images was examined by means of average pixel intensity variation and pixel-by-pixel intensity variation. The results indicated that increasing the number of repeat experiments was the most effective way to improve the convergence. Ensemble images constructed from 100 single-shot realizations of the autoigniting jet were found to be acceptably converged.

CSE-TGLDM Combustion Model Validation

A CSE-TGLDM combustion model was applied to predict the profiles of OH mass fraction of a combusting non-premixed methane jet under the same conditions as in the experiments. The simulation failed to predict even the general shape of the OH distribution as indicated by the ensemble-averaged OH-PLIF images. Instead, the simulation results showed some features present in certain single-shot OH-PLIF images, such as a well-defined diffusion flame, a reaction zone surrounding the jet, flame being lifted from the nozzle. In many ways, this is perhaps the most significant result of the present work as it effectively demonstrates a substantial defect in the RANS based methods that are commonly used in the modelling of a turbulent combusting jet. The results of this work therefore strongly support the view that alternatives to the existing RANS models are necessary for this and other similar applications.

8.2 Future Work

The work presented in this study provides insight into the combustion process of direct-injection, compression-ignition gaseous jets. In general, fuel availability and system restrictions resulted in the testing being carried out over a limited range of operating conditions. Further experimental studies are necessary to improve our understanding of the ignition and emissions characteristics of natural gas with different compositions under high-pressure and intermediate-temperature conditions.

Results from current study show significant run-to-run variability in the autoignition process and NOx emissions. Besides the random nature of the developing turbulent jet, influence from the initial temperature field may also play a role. Knowledge of the spatial distribution of temperature in the test section would be valuable and could be obtained from techniques such as two-line fluorescence thermometry [200], monochromatic fluorescence thermometry [201], etc. It would also be of interest to repeat some experiments from the present study in a different shock tube configuration to investigate whether the high run-to-run variability is still present.

The effect of the injection duration is not well studied in the present study. A larger gas hole or multi-hole is the obvious solution, but might not be feasible for the current setup considering the limited size of the optical window and the shock tube cross section. Ideally the whole developing turbulent jet should be observed through the optical window, and the interaction between the jet and the inner wall of the shock tube should be avoided. Conducting experiments in a combustion bomb may be a solution. With precisely controlled actual injection duration, not only single-pulse, but also multi-pulse injection can be studied with the new injector.

The measured NOx emissions at longer injection durations are problematic in the present study due to the relatively short, finite run-time of the present setup. To achieve a longer shock tube run-time, the driver section of the shock tube should be extended. Besides the cumulative NOx emissions measured in the present study, knowledge of the spatial distribution of NO in the flame is also valuable not only for studying the emissions formation process but for validating numerical models. Similar to OH, NO distribution in the flame can also be obtained by applying PLIF measurement [202].

In the present study, OH-PLIF measurement was only conducted at three fixed timings relatively long after the start of injection. Numerical simulations have predicted the evolution of OH mass fraction in the igniting turbulent methane jet. Thus it is of interest to extend the OH-PLIF measurement to earlier stages of combustion in the next step. More

repeat experiments will be needed to achieve a converged result, considering the laser might have been fired before the ignition actually occurs. This problem can be alleviated to some degree by using a dichroic beam splitter to separate the fluorescence signal into two parts, each recorded by an ICCD camera. This setup will allow two OH-PLIF images to be taken at different stages of combustion in a single shock tube experiment.

Fuel distribution is another important parameter in studying turbulent reacting gaseous jets. The flame-front equivalence ratio measurement can be integrated into the current OH-PLIF setup by using the simultaneous PLIF from 3-pentanone added to the fuel to measure the fuel concentration, and from OH radicals to track the flame-front position [203]. Knowledge of this, together with the spatial distribution of temperature, OH, NO, and, potentially, other radicals in the flame, would allow us to develop a more comprehensive understanding of the nature of transient reacting gaseous jets, and would be valuable for validating numerical models as well.

Since the CSE-TGLDM combustion model cannot account for fluctuations in either turbulence or chemistry, it fails to predict the run-to-run variations in OH distribution in the present study. The obvious cure for the problem is to use a simulation that can account for fluctuations. In terms of the fluctuations due to turbulence, a Large Eddy Simulation (LES) would be well suited to the task. This type of simulation would be significantly more computationally expensive than the RANS calculations performed in this work, since the field would now have to be simulated with a 3-dimensional grid. Furthermore, an ensemble of these simulations with enough realizations would be needed to provide meaningful statistics. That would make the computational cost to obtain a prediction for each temperature/pressure condition orders of magnitude higher than the simple RANS calculation – likely too high a cost to be of use given current computing technology.

Accounting for the effects of the fluctuations due to chemistry would likely require a stochastic method such as the Stochastic Particle Method [198], which has never been used to simulate a reacting flow with a complex flow field – let alone a turbulent one. Here, the computational cost per realization would likely be extremely high, and again one would need many realizations to obtain meaningful statistics. Altogether, accounting for the fluctuations in the turbulent autoignition problem appears to be very challenging. However, it is a problem that will likely have to be tackled, since the ignition delay time is an important factor in engines and other engineering applications. An accurate prediction of the ignition of a turbulent jet would offer important data to engine designers.

References

[1] Pischinger, S, The future of vehicle propulsion – combustion engines and alternatives, Topics in Catalysis, 30/31 (2004) 5-16.

[2] S. Soylu, Examination of combustion characteristics and phasing strategies of a natural gas HCCI engine, Energy Conservation and Management 46 (2005) 101-119.

[3] A. Ishida, A. Nishimura, M. Uranishi, R. Kihara, A. Nakamura, P. Newman, The development of the ecos-ddf natural gas engine for medium-duty trucks: exhaust emission reduction against base diesel engine, JSAE Review 22 (2001) 237-243.

[4] P. Ouellette, High-pressure direct injection of natural gas in diesel engines, Proceeding of NGV 2000: NGV-transportation for the new century, Seventh International Conference and Exhibition on Natural Gas Vehicles, International Association For Natural Gas Vehicles, Inc., Yokohama, Japan (2000) 235-241.

[5] G. McTaggart-Cowan, S. Rogak, P. Hill, W. Bushe, S. Munshi, Effects of operating condition on particulate matter and nitrogen oxides emissions from a heavy-duty direct injection natural gas engine using cooled exhaust gas recirculation, International Journal of Engine Research 5 (2004) 499-511.

[6] G. McTaggart-Cowan, W. Bushe, P. Hill, S. Munshi, The application of exhaust gas recirculation to a heavy duty direct injection of natural gas engine, International Journal of Engine Research 5 (2004) 175-191.

[7] G. McTaggart-Cowan, W. Bushe, S. Rogak, P. Hill, S. Munshi, The effects of varying EGR test conditions on a direct injection of natural gas heavy-duty engine with high EGR levels, SAE technical paper, No. 2004-01-2955. SAE Transactions, Journal of Engines 113 (2004) 1500-1509.

[8] G. McTaggart-Cowan, W. Bushe, P. Hill, S. A. Munshi, Supercharged single cylinder heavy duty engine for high pressure direct injection of natural gas, International Journal of Engine Research 4 (2004) 315-329.

[9] G. McTaggart-Cowan, W. Bushe, S. Rogak, P. Hill, S. Munshi, Injection parameter effects on a direct injected, pilot ignited, heavy duty natural gas engine with EGR, SAE technical paper 2003-01-3089. SAE Transactions, Journal of Fuels and Lubricants 112 (2003) 2103-2109.

[10] Dumitrescu, S., Hill, P. G., Li, G., and Ouellette, P., Effects of injection changes on efficiency and emissions of diesel engine fuelled by direct injection of natural gas, SAE technical paper, No. 2000-01-1805.

[11] Harrington, J., Munshi, S, Nedelcu, C., Ouellette, P., Thompson, J., Whitfield, S., Direct injection of natural gas in a heavy-duty diesel engine, SAE technical paper, No. 2002-01-1630.

[12] Douville, B., Ouellette, P., Touchette, A. and Ursu, B., Performance and emissions of a two-stroke engine fuelled using high-pressure direct injection of natural gas, SAE technical paper, No. 981160.

[13] Hong, S., Assanis, D., and Wooldridge, M., Multi-dimensional modelling of NO and soot emissions with detailed chemistry and mixing in a direct injection natural gas engine, SAE technical paper, No. 2002-01-1112.

[14] Ouellette, P., Mtui, P., and Hill P.G., Numerical simulations of directly injected natural gas and pilot diesel fuel in a two-stroke compression ignition engine, SAE technical paper, No. 981400.

[15] Li, G., Ouellette, P., Dumitrescu, S., and Hill, P.G., Optimization study of pilot-ignited natural gas direct-injection in diesel engines, SAE technical paper, No. 1999-01-3556.

[16] Annual energy outlook 2006 with projections to 2030, Energy Information Administration Report DOE/EIA-0383 (2006), http://www.eia.doe/gov/oiaf/aeo.

[17] Horning, D.C., A study of the high-temperature autoignition and thermal decomposition of hydrocarbons, PhD Thesis, Department of Mechanical Engineering, Stanford University, 2001.

[18] A.G. Gaydon, I.R. Hurle, The shock tube in high temperature chemical physics, Chapman and Hall Ltd. 1963.

[19] Gardiner W. C., Jr., "Shock Waves", Proc. 18th Int. Symp. Shock Waves, pp. 49-60, New York: Springer-Verlag

[20] Tsang W., Lifshitz, A., Shock tube techniques in chemical kinetics, Annu. Rev. Phys. Chem., 41 (1990) 559-99.

[21] Bowman, C. T., An experimental and analytical investigation of the high-temperature oxidation mechanisms of hydrocarbon fuels, Combustion Science and Technology 2 (1970) 161-172.

[22] Huang, J., Experimental shock tube study of ignition promotion for methane under engine relevant conditions, Master Thesis, Department of Mechanical Engineering, University of British Columbia, 2000.

[23] D.J. Seery, C. T. Bowman, An experimental and analytical study of methane oxidation behind shock wave, Combustion and Flame 14 (1970) 37-47.

[24] A. Lifshitz, k. Scheller, A. Burcat, G.B. Skinner, Shock-tube investigation of ignition in methane-oxygen-argon mixtures, Combustion and Flame 16 (1971) 311-321.

[25] T. Tsuboi, H.G. Wagner, Homogeneous thermal oxidation of methane in reflected shock waves, Proceedings of the Combustion Institute 15 (1974) 883.

[26] A.K. Cheng, R.K. and Oppenheim, Autoignition in methane-hydrogen mixtures,

Combustion and Flame 58 (1984) 125-139.

[27] A. Grillo, M. W. Slack, Shock tube study of ignition delay times in methane-oxygen-nitrogen-argon mixtures, Combustion and Flame 27 (1976) 377-381.

[28] E.L. Petersen, D.F. Davidson, R.K. Hanson, Kinetics modelling of shock-induced ignition in low-dilution CH_4/O_2 mixtures at high pressures and intermediate temperatures, Combustion and Flame 117 (1999) 272-290.

[29] J. Huang, P.G. Hill, W.K. Bushe, S.R. Munshi, Shock-tube study of methane ignition under engine-relevant conditions: experiments and modelling, Combustion and Flame 136 (2004) 25-42.

[30] E. Petersen, D. Davidson, R. Rohrig, M. and Hanson, High pressure shock-tube measurements of ignition times in stoichiometric $H_2/O_2/Ar$ mixtures, In 20th Symp. Int. Shock Waves (1996) 941-946.

[31] Sullivan, G.D., Huang J., Wang, T.X., Bushe, W.K., Rogak, S.N., Emissions variability in gaseous fuel direct injection compression ignition combustion, SAE technical paper, No. 2005-01-0917.

[32] Sullivan, G.D., Huang J., Bushe, W.K., Rogak, S.N., Autoignition of transient turbulent gaseous fuel jets at high pressure, SAE technical paper, No. 2006-01-3432.

[33] R.M.R. Higgin, A. Williams, A shock-tube investigation of the ignition of lean methane and n-butane mixtures with oxygen, Sixteenth Symposium (Int.) on Combustion. The Combustion Institute, Pittsburgh (1968) 579.

[34] M. Frenklach, D.E. Bornside, Shock-ignition in methane/propane mixture, Combustion and Flame 56 (1984) 1-27.

[35] S.C. Li, F.A. Williams, NOx formation in two-stage methane/air flames, Combustion and Flame 118 (1999) 399-414.

[36] K. Hughes, T. Turnyi, A. Clague, P.M.J., Development and testing of a comprehensive chemical mechanism for the oxidation of methane, International Journal of Chemical Kinetics 33 (2001) 513-538.

[37] T.B. Hunter, H. Wang, L.T.A., F.M., The oxidation of methane at elevated pressure: experiments and modelling, Combustion and Flame 87 (1991) 365-370.

[38] M. Frenklach, H. Wang, M. Goldenberg, G.P. Smith, D.M. Golden, B.C. T., R.K. Hanson, W. C. Gardiner, V. Lissianski, GRI-MECH: an optimized detailed chemical reaction mechanism for methane combustion, Report No. GRI-95/0058.

[39] C.T. Bowman, R.K. Hanson, D.F. Davidson, W.C. J. Gardiner, V. Lissianski, G.P. Smith, D.M. Golden, F. M., M. Goldenberg, GRI-MECH 2.11, http://www.me.berkeley.edu/grimech.

[40] G.P. Smith, D.M. Golden, M. Frenklach, N.W. Moriarty, B. Eiteneer, M. Goldenberg, C.

T. Bowman, R.K. Hanson, S.S. Song, W.C. Gardiner, V.V. Lissianski, Z. Qin, Gri-mech3.0, http://www.me.berkeley.edu/grimech.

[41] L.J. Spadaccini, M.B. Colket III, Ignition delay characteristics of methane fuels, Progress in Energy and Combustion Science 20 (1994) 431-460.

[42] E. Ranzi, A. Sogaro, P. Gaffuri, C. Pennati, C. K.Westbrook, W. J. Pitz, A new comprehensive reaction mechanism for combustion of hydrocarbon fuels, Combustion and Flame 99 (1994) 201-211.

[43] R.W. Crossley, E.A. Dorko, K. Scheller, A. Burcat, The effect of higher alkanes on the ignition of methane-oxygen-argon mixtures in shock waves, Combustion and Flame 19 (1972) 373-378.

[44] D.C. Bull, J.E. Elsworth, G. Hooper, Susceptibility of methane/ethane mixtures to gaseous detonation in air, Combustion and Flame 34 (1979) 327-330.

[45] C.S. Eubank, M. J. Rabinowitz, W. C. J. Gardiner, R. E. Zellner, Shock initiated ignition of natural gas-air mixtures, Eighteenth Symposium (Int.) on Combustion. The Combustion Institute, Pittsburgh (1981) 1767.

[46] R. Zellner, K. J. Niemitz, J. Warnatz, W.C.J. Gardiner, C.S. Eubank, J. M. Simmif, Prog. in Astro and Aero 88 (1981) 252.

[47] J.R. Griffiths, D. Coopersthwaite, C.H. Philips, C.K. Westbrook, Auto-ignition temperature of binary mixtures of alkane in a closed vessel: Comparisons between experimental measurements and numerical predictions, 23rd Symposium (Int.) on Combustion (1990) 1745.

[48] Huang, J., Bushe, W.K., Experimental and kinetic study of autoignition in methane/ethane/air and methane/propane/air mixtures under engine-relevant conditions, Combustion and Flame 144 (2006) 74-88.

[49] Fraser, R.A., Siebers, D.L., Edwards, C.F., Autoignition of methane and natural gas in a simulated diesel environment, SAE technical paper, No. 910227.

[50] Naber, J.D., Siebers, D.L., Julio, S.S. Westbrook C.K., Effects of natural gas composition on ignition delay under diesel conditions, Combustion and Flame 99 (1994) 192-200.

[51] Naber, J.D., Siebers, D.L., Caton, J. A., Westbrook, C. K., Dijulio, S. S., Natural gas autoignition under diesel conditions: experiments and chemical kinetic modelling, SAE technical paper, No. 942034.

[52] C.K. Westbrook, W.J. Pitz, Effects of propane on ignition of methane-ethane-air mixtures, Combustion Science and Technology 33 (1983) 315-319.

[53] C.K. Westbrook, An analytical study of the shock tube ignition of methane and ethane, Combustion Science and Technology 20 (1979) 5.

[54] Cheng, A.K., Oppenheim, R.K. Autoignition in methane-hydrogen mixtures, Combustion and Flame 58 (1984) 125-139.

[55] Huang, J., Bushe, W.K., Hill, P.G., Munshi, S.R., Experimental and kinetic study of shock initiated ignition in homogeneous methane/hydrogen/air mixtures at engine-relevant conditions, International Journal of Chemical Kinetics 38 (2006) 221-233.

[56] C.G. Fotache, G. Dreutz, T, C.K. Law, Ignition of hydrogen enriched methane by heated air, Combustion and Flame 110 (1997) 429-440.

[57] Naber J.D., Siebers, D.L., Hydrogen combustion under diesel engine conditions, International Journal of Hydrogen Energy 23 (1998) 363-371.

[58] Mastorakos, E., Baritaud, T. A., Poinsot, T. J., Numerical simulations of autoignition in turbulent mixing flows, Combustion and Flame 109 (1997) 198-223.

[59] Hilbert, R., Thévenin, D., Autoignition of turbulent nonpremixed fames investigated using direct numerical simulation, Combustion and Flame 128 (2002) 22-37.

[60] Im, H. G., Chen, J. H., Law, C. K., Ignition of hydrogen-air mixing layer in turbulent flows, Twenty-Seventh Symposium (International) on Combustion, The Combustion Institute, Pittsburgh, (1998) 1047-1056.

[61] Kim, S. H., Huh, K. Y., Fraser, R. A., Numerical prediction of the autoignition delay in a diesel-like environment by the condition moment closure model, SAE technical paper, No. 2000-01-0200.

[62] Kim, S.K., Yu, Y., Ahn, J., Kim, Y.M., Numerical investigation of the autoignition of turbulent gaseous jets in a high-pressure environment using the multiple-RIF model, Fuel, 83 (2004) 375–386.

[63] Hill, P.G., and Ouellette, P., Transient turbulent gaseous fuel jets for diesel engines, journal of fluids engineering 121 (1999) 93-101.

[64] Turner, J. S., The starting plume in neutral surroundings, Journal of Fluid Mechanics, 13 (1962) 356-368.

[65] Ricou, F.P., and Spalding, D.B., Measurements of entrainment by axisymmetrical turbulent Jets, Journal of Fluid Mechanics 11 (1961) 2132-2140.

[66] Santoro, V., A. Linan, and A. Gomez, Propagation of edge flames in counter-flow mixing layers: experiments and theory, Proceedings of the Combustion Institute 28 (2000) 2039-2046.

[67] Glassman, I. Combustion (2nd Ed.). San Diego, CA: Academic Press, Inc., 1987.

[68] Amantini, G., J. Frank, M. Smooke, and A. Gomez, Computational and experimental study of standing methane edge flames in the two-dimensional axisymmetric counter-flow

geometry, Combustion and Flame 147 (2006) 133-149.

[69] Plessing, T., P. Terhoeven, and N. Peters. An experimental and numerical study of a laminar triple flame, Combustion and Flame 115 (1998) 335-353.

[70] Heywood, J.B, Internal Combustion Engine Fundamental. McGraw-Hill, New York. 1988.

[71] Warnatz, J., U. Maas, and R.W. Dibble, Combustion. Physical and Chemical Fundamentals, Modelling and Simulation, Experiments, Pollutant Formation. 2nd Ed. Springer-Verlag, Berlin, 1999.

[72] Nishioka, M., Y. Kondoh and T. Takeno, Behaviour of key reactions on NO formation in methane-air flames, 26th international symposium on combustion, The Combustion Institute (1996) 2139-2145.

[73] Easley, W.L. and A.M. Mellor, NO decomposition in diesel engines. SAE technical paper, No. 1999-01-3546.

[74] Ahmad, T. and S.L. Plee, Application of flame temperature correlations to emissions from a direct-injection diesel engine, SAE technical paper, No. 831374.

[75] Hanson, Ronald K., Planar laser-induced fluorescence imaging, Journal of Quantitative Spectroscopy & Radiative Transfer 40 (1988) 343-362.

[76] Laurendeau, Normand M., Goldsmith, J.E.M.,Comparison of hydroxyl concentration profiles using five laser-induced fluorescence methods in a lean subatmospheric-pressure hydrogen/oxygen/argon flame, Combustion Science and Technology 63 (1989) 139-152.

[77] Eckbreth, Alan C, Laser Diagnostics for Combustion Temperature and Species, 2nd Edition. (1996), 596.

[78] Piepmeier, E.H, Theory of laser saturated atomic resonance fluorescence. Spectrochimica Acta, Part B: Atomic Spectroscopy 27(1972) 431-443.

[79] Fairchild, Paul W., Smith, Gregory P., Crosley, David R, Collisional quenching of $A_2 \Sigma +$ hydroxyl at elevated temperatures, Journal of Chemical Physics 79 (1983) 1795-1807.

[80] Kohse-Hoeinghaus, Katharina, Laser techniques for the quantitative detection of reactive intermediates in combustion systems, Progress in Energy and Combustion Science 20 (1994) 203-279.

[81] Barlow, R. S.; Dibble, R. W.; Chen, J. Y.; Lucht, R. P., Effect of Damkoehler number on super-equilibrium hydroxyl radical concentration in turbulent nonpremixed jet flames, Combustion and Flame 82 (1990) 235-251.

[82] Dyer, Mark J.; Crosley, David R., Two-dimensional imaging of hydroxyl radical laser-induced fluorescence in a flame, Optics Letters 7 (1982) 382-384.

[83] S.B. Pope, PDF methods for turbulent reactive flow, Progress in Energy and Combustion Science 11 (1985) 119-192.

[84] A.R. Masri, S.B. Pope, PDF calculations of piloted turbulent nonpremixed flames of methane, Combustion and Flame 81 (1990) 13-29.

[85] A. T. Norris, S.B. Pope, Modelling of extinction in turbulent diffusion flames by the velocity-dissipation-composition PDF method, Combustion and Flame 100 (1996) 211-220.

[86] V. Saxena, S.B. Pope, PDF calculation of major and minor species in a turbulent piloted jet flame, Twenty-Seventh Symposium (Int.) on Combustion, the Combustion Institute (1998) 1081-1086.

[87] Peters, N., Laminar diffusion flamelet models in non-premixed turbulent combustion, Progress in Energy and Combustion Science 10 (1982) 369-399.

[88] C.K. Law, Steady-state diffusion flame structure with Lewis number variation, Combustion Science and Technology 29 (1982) 129-145.

[89] W.P. Jones, W.J.H, Calculation methods for reacting turbulent flows: A review, Combustion and Flame 48 (1982) 1-26.

[90] T. Saitoh, O.Y., Unsteady behavior of diffusion flames and premixed flames for counter flow geometry, Combustion Science and Technology 12 (1976) 135.

[91] F. MauB, D. Keller, N. Peters, A Lagrangian simulation of flamelet extinction and re-ignition in turbulent jet diffusion flames, Twenty-third symposium (Int.) on combustion, the combustion institute (1990) 693-698.

[92] N. Peters, Turbulent combustion, Cambridge University Press, Cambridge, 2000.

[93] P.J. Coelho, N. Peters, Unsteady modelling of a piloted methane/air jet flame based on the Eulerian particle flamelet model, Combustion and Flame 124 (2001) 444-465.

[94] H. Barths, C. Antoni, N. Peters, Three-dimensional simulation of pollutant formation in a DI diesel engine using multiple interactive flamelets, SAE technical paper, No. 982459.

[95] C.A. Hergart, H. Barths, N. Peters, Modelling the combustion in a small-bore diesel engine using a method based on representative interactive flamelets, SAE technical paper, No. 1999-01-3550.

[96] C. Hasse, H. Barths, P.N., Modelling the effect of split injections in diesel engines using representative interactive flamelets, SAE technical paper, No.1999-01-3547.

[97] H. Barths, C. Hasse, P.N., Computational fluid dynamics modelling of non-premixed combustion in direct injection diesel engines, International Journal of Engine Research 1 (2000) 249-267.

[98] S. Rao, C.J. Rutland, A flamelet time scale model for nonpremixed combustion

including chemical kinetic effects, Combustion and Flame 133 (2003) 189-191.

[99] N. Swaminathan, Flamelet regime in non-premixed combustion, Combustion and Flame 129 (2002) 217-219.

[100] A.Y. Klimenko, Multicomponent diffusion of various admixtures in turbulent flow, Fluid Dynamics 25 (1990) 327-334.

[101] R.W. Bilger, Conditional moment methods for turbulent reacting flow using Crocco variable conditions, Report TN F-99, Department of Mechanical Engineering, University of Sydney.

[102] R. Lee, J. H. Whitelaw, T.S. Wung (Eds.), Aerothermodynamics in combustion, Springer, Berlin, 1991.

[103] A.Y. Klimenko, R.W. Bilger, Conditional moment closure for turbulent combustion, Progress in Energy and Combustion Science 25 (1999) 595-687.

[104] Bilger, R.W., Conditional Moment Closure for turbulent reacting flow, Phys Fluids A 5 (1993) 436-444.

[105] N. Smith, R. Bilger, C. Carter, A comparison of CMC and PDF modelling predictions with experimental nitric oxide LIF/RAMAN measurements in a turbulent H_2 jet flame, Combustion Science and Technology 105 (1995) 357-375.

[106] M. Roomina, R. Bilger, Conditional moment closure modelling of turbulent methanol jet flames, Combustion Theory and Modelling 3 (1999) 689-708.

[107] M. Roomina, R.W. Bilger, Conditional moment closure (CMC) prediction of a turbulent methane-air jet flames, Combustion and Flame 125 (2001) 1176-1195.

[108] M. Fairweather, R.M. Woolley, First-order conditional moment closure modelling of turbulent, non-premixed methane flames, Combustion and Flame 138 (2004) 3-19.

[109] C. Devaud, K.N.C. Bray, Assessment of the applicability of conditional moment closure to a lifted turbulent flame: first order model, Combustion and Flame 132 (2003) 102-114.

[110] S. Kim, K. Y. Huh, L. Tao, Application of the elliptic conditional moment closure model to a two-dimensional nonpremixed methanol bluff-body flame, Combustion and Flame 120 (2000) 75-90.

[111] S. Kim, K.Y. Huh, Use of the conditional moment closure model to predict no formation in a turbulent ch4/h-2 flame over a bluff-body, Combustion and Flame 130 (2002) 94-111.

[112] A. Kronenburg, R. Bilger, J. Kent, Modelling soot formation in turbulent methane-air jet diffusion flames, Combustion and Flame 121 (2000) 24-40.

[113] D. Bradley, D. Emerson, P. Gaskell, Mathematical modelling of turbulent non-premixed piloted-jet flames with local extinction, Proceedings of the Combustion Institute 29 (2002) 2155-2162.

[114] E. Mastorakos, R. Bilger, Second-order conditional moment closure for the autoignition of turbulent flows, Physics of Fluids 10 (1998) 1246-1248.

[115] W. Bushe, H. Steiner, Conditional moment closure for large eddy simulation of nonpremixed turbulent reacting flows, Physics of Fluids 11 (1999) 1896-1906.

[116] H. Steiner, W.K. Bushe, Large eddy simulation of a turbulent reacting jet with conditional source-term estimation, Physics of Fluids 13 (2001) 754-769.

[117] W. Bushe, H. Steiner, Laminar flamelet decomposition for conditional source-term estimation, Physics of Fluids 15 (2003) 1564-1575.

[118] C. Blair, Implementation of conditional source term estimation for prediction of methane ignition, Master Thesis, Department of Mechanical Engineering, University of British Columbia, 2003.

[119] R. Grout, W.K. Bushe, C. Blair, Predicting the ignition delay of turbulent methane jets using Conditional Source-term Estimation, Combustion Theory and Modelling 11 (2007).

[120] J. Huang, W. K. Bushe, Simulation of transient turbulent methane jet ignition and combustion under engine-relevant conditions using conditional source-term estimation with detailed chemistry, Combustion Theory and Modelling 11 (2007).

[121] S.H. Starner, R.W. Bilger, K.M. Lyons, J.H. Frank, M.B. Long, Conserved scalar measurements in turbulent-diffusion flames by a Raman and Rayleigh Ribbon Imaging method, Combustion and Flame 99 (1994) 347-354.

[122] Y. Chen, M.S. Mansour, Measurements of scalar dissipation in turbulent hydrogen diffusion flames and some implications on combustion modelling, Combustion Science and Technology 126 (1997) 291-313.

[123] K. K. Kuo, Principles of combustion, John Wiley and Son, New York, 2005.

[124] J. Warnatz, U. Maas, W. Dibble, R, Combustion, 2nd Edition, Springer-Verlag, New York, 1999.

[125] U. Maas, S.B. Pope, Simplifying chemical kinetics: Intrinsic low dimensional manifolds in composition space, Combustion and Flame 88 (1992) 239-264.

[126] S.B. Pope, U. Maas, Simplifying chemical kinetics: trajectory-generated low-dimensional manifolds, FDA 93-11.

[127] Renka, R.J., Algorithm 751: Tripack: A constrained two-dimensional delaunay triangulation package. ACM Transactions of Mathematical Software 22 (1996) 1–8.

[128] Richards, G.A., M.M. McMillian, R.S. Gemmen, W.A. Rogers and S.R. Cully, Issues for low-emission, fuel-flexible power systems, Progress in Energy and Combustion Science 27 (2001) 141-169.

[129] A. Turbiez, A. ElBakali, J.F. Pauwels, A. Rida, P. Meunier, Experimental study of a low pressure stoichiometric premixed methane, methane/ethane, methane/ethane/propane and synthetic natural gas flames, Fuel 83 (2004) 933-941.

[130] J. Hiltner, R. Agama, F. Mauss, B. Johansson, M. Christensen, Homogeneous charge compression ignition operation with natural gas: Fuel composition implications, Journal of Engineering for Gas Turbine and Power-Transaction of ASME 125 (2003) 837-844.

[131] D. Flowers, S. Aceves, C.K. Westbrook, J.R. Smith, D.R., Detailed chemical kinetic simulation of natural gas HCCI combustion: Gas composition effects and investigation of control strategies, Journal of Engineering for Gas Turbine and Power-Transaction of ASME 123 (2001) 433-439.

[132] M. Mbarawa, E.W. Mureithi, Modelling the effects of natural gas composition on dual-fuel combustion under constant-volume conditions, Journal of the Institute of Energy 76 (2003) 2-9.

[133] E.B. Khalil, G.A. Karim, A kinetic investigation of the role of changes in the composition of natural gas in engine applications, Journal of Engineering for Gas Turbine and Power-Transaction of ASME 124 (2002) 404-411.

[134] A. Burcat, K. Scheller, A. Lifshitz, Shock-tube investigation of comparative ignition delay times for C1-C5 alkanes, Combustion and Flame 16 (1971) 29-33.

[135] A. El Bakali, P. Dagaut, L. Pillier, P. Desgroux, J. F. Pauwels, A. Rida, P. Meunier, Experimental and modelling study of the oxidation of natural gas in a premixed flame, shock tube, and jet-stirred reactor, Combustion and Flame 137 (2004) 109-128.

[136] N. Lamoureux, C.E. Paillard, Natural gas ignition delay times behind reflected shock waves: Application to modelling and safety, Shock Waves 13 (2003) 57-68.

[137] Jorach, R., C. Enderle and R. Decker, Development of a low-NOx truck hydrogen engine with high specific power output, Int. J. Hydrogen Energy 22 (1997) 423-427.

[138] Kido, H., M. Nakahara, J. Hashimot and D. Barat, Turbulent burning velocities of two-component fuel mixtures of methane, propane, and hydrogen, JSME International Journal, Series B 45 (2002) 355-362.

[139] Gauducheau, J.L., B. Denet and G. Searby, A numerical study of lean CH_4/H_2/air premixed flames at high pressure, Combustion Science and Technology 137 (1998) 81-99.

[140] Larsen, J.F. and J.S. Wallace, Comparison of emissions and efficiency of a turbocharged lean-burn natural gas and hythane-fuelled engine, ASME Journal of Engineering for Gas Turbines and Power 119 (1997) 218-226.

[141] Schefer, R.W., Hydrogen enrichment for improved lean flame stability, International Journal of Hydrogen Energy 28 (2003) 1131-1141.

[142] Karbasi, M. and I. Wierzba, The effects of hydrogen addition on the stability limits of methane jet diffusion flames, International Journal of Hydrogen Energy 23 (1998) 123-129.

[143] Law, C.K. and O.C. Kwon, Effects of hydrocarbon substation on atmospheric hydrogen-air flame propagation, International Journal of Hydrogen Energy 29 (2004) 867-879.

[144] Naha, S. and S.K. Aggarwal, Fuel effects on NOx emissions in partially premixed flames, Combustion and Flame 139 (2004) 90-105.

[145] Rortveit, G.J., K. Zepter, O. Skreiberg, M. Fossum and J.E. Hustad, A comparison of low-NOx burners for combustion of methane and hydrogen Mixtures, Proceedings of the Combustion Institute 29 (2002) 1123-1129.

[146] Fotache, C.G., T.G. Kreutz, and C.K. Law, Ignition of hydrogen-enriched methane by heated air, Combustion and Flame 110 (1997) 429-440.

[147] Sorensen, H, The boston reformed fuel car – a low pollution gasoline fuel system for internal combustion engines, SAE technical paper, No. 729218.

[148] Houseman, J. and F.W. Hoehn, A two-charge engine concept: hydrogen enrichment, SAE technical paper, No. 741169.

[149] Swain, M.R., M.J. Yusuf, Z. Dulger and M.N. Swain, The effects of hydrogen addition on natural gas engine operation, SAE technical paper, No. 932775.

[150] Sierens, R. and E. Rosseel, Variable composition hydrogen/natural gas mixtures for increased engine efficiency and decreased emissions, ASME J. of Engineering for Gas Turbines and Power 122 (2000) 135-140.

[151] Munshi, S.R., C. Nedelcu, J. Harris, Hydrogen blended natural gas operation of a heavy duty turbocharged lean burn spark ignition engine, SAE technical paper, No. 2004-01-2956.

[152] Allenby, S., W-C. Chang, A. Megaritis and M.L. Wyszynski, Hydrogen enrichment: a way to maintain combustion stability in a natural gas fuelled engine with exhaust gas recirculation, the potential of fuel reforming, Proceedings of the Institution of Mechanical Engineers, Part D 215 (2001) 405-418.

[153] Collier, K., N. Mulligan, D. Shin and S. Brandon, Emission results from the new development of a dedicated hydrogen-enriched natural gas heavy duty engine, SAE technical paper, No. 2005-01-0235.

[154] Bauer, C.G. and T.W. Forest, Effect of hydrogen addition on the performance of methane-fuelled vehicles, Part I: effect on S.I. engine performance, International Journal of Hydrogen Energy 26 (2001) 55-70.

[155] Karim, G.A., I. Wierzba and Y. Al-Alousi, Methane-hydrogen mixtures as fuels, International Journal of Hydrogen Energy 21 (1996) 625-631.

[156] Akansu, S.O., Z. Dulger, N. Kahraman and T. Veziroglu, Internal combustion engines fuelled by natural gashydrogen mixtures, International Journal of Hydrogen Energy, 29 (2004) 1527-1539.

[157] Hill, P.G. and G.P. McTaggart-Cowan, Nitrogen oxide production in a diesel engine fuelled with natural gas, SAE Technical Paper, No. 2005-01-1727.

[158] Nellen, C. and K. Boulouchos., Natural gas engines for cogeneration: highest efficiency and near-zero emissions through turbocharging, EGR and 3-way catalytic converter. SAE technical paper, No. 2000-01-2825.

[159] Crookes, R.J., Comparitive bio-fuel performance in internal combustion engines. Biomass & Bioenergy 30 (2006) 461-468.

[160] Ladommatos, N., S. Abdelhalim, H. Zhao, The effects of exhaust gas recirculation on diesel combustion and emissions, International Journal of Engine Research 1 (2000) 107-126.

[161] Feese, J.J. and S.R. Turns, Nitric oxide emissions from laminar diffusion flames: effects of air-side versus fuel-side diluent addition, Combustion and Flame 113 (1998) 66-78.

[162] Fotache, C.G., T.G. Kreutz and C.K. Law, Ignition of counter-flowing methane versus heater air under reduced and elevated pressures. Combustion and Flame 108 (1997) 442-470.

[163] Gulder, O.L, Effects of oxygen on soot formation in methane, propane, and n-butane diffusion flames, Combustion and Flame 101 (1995) 302-310.

[164] Rubas, P.J., Paul, M. A., Martin, G.C., Coverdill, R.E., Lucht, R. P., Peters, J.E., DelVecchio, K. A., Methane jet penetration in a direct-injection natural gas engine, SAE technical paper, No. 980143.

[165] H. Pitsch, Flamemaster v3.1: a C++ computer program for 0D combustion and 1D laminar flame calculations, available from http://www.stanford.edu/hpitsch.

[166] Bi, H., Agrawal, A.K., Study of autoignition of natural gas in diesel environments using computational fluid dynamics with detailed chemical kinetics, Combustion and Flame 113 (1998) 289-302.

[167] Dyer, M.J. and Crosley, D.R., Fluorescence imaging for flame chemistry, Proceedings of the International Conference on Lasers '84, p. 211, K. Corcoran, D. Sullivan, and W. Stwalley, eds. (STS, McLean, Va., 1985).

[168] Allen, M.G. and Hanson, R.K., Digital imaging of species concentration fields in spray

flames, Twenty-First Symposium (Int.) on Combustion, The Combustion Institute, (1986) 1755-1762.

[169] Schefer, R.W., Namazian, M., and Kelley, J., CH, OH and CH_4 concentration measurements in a lifted turbulent-jet diffusion flame, Twenty-Third Symposium (Int.) on Combustion, The Combustion Institute, (1990) 669-676.

[170] Allen, M.G., Howe, R.D., and Hanson, R.K., digital imaging of reactions zones in hydrocarbon-air flames using planar laser-induced fluorescence of CH and C2, Optics Letters 11 (1986) 126-128.

[171] Paul, P.H. and Dec, J.E., Imaging of reaction zones in hydrocarbon-air flames using planar laser-induced fluorescence of CH, Optics Letters 19 (1994) 998-1000.

[172] Kychakoff, G., Howe, R.D., Hanson, R.K. and McDaniel, J. C., Quantitative visualization of combustion species in a plane, Applied Optics 21 (1982) 3225-3227.

[173] Sietzman, J.M., Üngüt, A., Paul, P.H., and Hanson, R.K., Imaging and characterization of oh structures in a turbulent nonpremixed flame, Twenty-Third Symposium (Int.) on Combustion, The Combustion Institute (1990) 637-644.

[174] Fenimore, C. P. and Jones, G. W., Oxidation of soot by hydroxyl radicals, J. Phys. Chem., 71 (1967) 593-597.

[175] Allen, M. G., McManus, K. R., and Sonnenfroh, D. M. and Paul, P. H., Planar laser-induced fluorescence imaging of oh and hydrocarbon fuel fragments in high-pressure spray-flame combustion, Applied Optics 34 (1995) 6287-6300.

[176] Puri, R., Santoro, R. J. and Smyth, K. C., The oxidation of soot and carbon in hydrocarbon diffusion flames, Combustion and Flame 97 (1994) 125-144.

[177] Espey, C., Dec, J.E., Litzinger, T.A. and Santavicca, D.A., Quantitative 2-D fuel vapour concentration imaging in a firing DI diesel engine using planar laser-induced Rayleigh scattering, SAE Transactions 103 (1994) 1145-1160.

[178] Lucht, R. P. Sweeney, D. W., and Laurendeau, N. M., laser-saturated fluorescence measurements of OH in atmospheric pressure $CH_4/O_2/N_2$ flames under sooting and non-sooting conditions, Combustion Science and Technology 42 (1985) 259-281.

[179] Felton, P.G., Mantzaras, J., Bornse, D.S., and Woodin, R.L., Initial two-dimensional laser-induced fluorescence measurements of OH radicals in an internal combustion engine, SAE technical paper, No. 881633.

[180] Suntz, R., Becker, H., Monkhouse, P., and Wolfrum, J., Two-dimensional visualization of the flame front in an internal combustion engine by laser-induced fluorescence of oh radicals, Applied Physics B 47 (1988) 287-293.

[181] Serpengüzel, Hahn, T.T. and Acker, W.P., Single-pulse planar laser-induced fluorescence imaging of hydroxyl radical in a spark ignition engine, SAE technical paper,

No. 932701.

[182] Tanaka, T. and Tabata M., Planar measurements of oh radicals in an SI engine based on laser induced fluorescence, SAE technical paper, No. 940477.

[183] Dec, J.E. and Coy, E.B., OH radical imaging in a di diesel engine and the structure of the early diffusion flame, SAE technical paper, No. 960831.

[184] Dec, J.E. and Kelly-Zion, P.L., The effects of injection timing and diluent addition on late-combustion soot burnout in a DI diesel engine based on simultaneous 2-D imaging of OH and soot, SAE technical paper, No. 2000-01-0238.

[185] Dec, J.E. and Tree, D.R., Diffusion-flame/wall interactions in a heavy-duty DI diesel engine, SAE technical paper, No. 2001-01-1295.

[186] Masculus, M. P.B., Effects of the in-cylinder environment on diffusion flame lift-off in a DI diesel engine, SAE technical paper, No. 2003-01-0074.

[187] Strand, T.E., Rothamer, D.A. and Ghandhi, J.B., Flame structure visualization of stratified combustion in a DISI engine via PLIF, SAE technical paper, No. 2001-01-3649.

[188] Kashdan, J. T., Cherel, J. and Thirouard, B., A study of combustion structure and implications on post-oxidation under homogeneous and stratified operation in a DISI engine, SAE technical paper, No. 2006-01-1262.

[189] Richter, M., Engström, J., Franke, A., Aldén, M., Hultqvist, A. and Johansson, B., The influence of charge inhomogeneity on the HCCI combustion process, SAE technical paper, No. 2000-01-2868.

[190] Kashdan, J. T., Docquier, N. and Bruneaux, G., Mixture preparation and combustion via LIEF and LIF of combustion radicals in a direct-injection, HCCI diesel engine, SAE technical paper, No. 2004-01-2945.

[191] Kashdan, J. T., Jean-François and Papagni, LIF imaging of autoignition and combustion in a direct injection diesel-fuelled HCCI engine, SAE technical paper, No. 2005-01-3739.

[192] Dec, J., Coy, E.B., OH radical imaging in a DI diesel engine and the structure of the early diffusion flame, SAE technical paper, No. 960831.

[193] Grimaldi, C.N., Postrioti, L., Stan, C., and Troger, R., Analysis method for the spray characteristics of a GDI system with high pressure modulation, SAE technical paper, No. 2000-01-1043.

[194] Hung, D.L.S., An imaging-based analysis tool for evaluating the macroscopic spray variations of a direct injection-gasoline injector, Proc. 15th ILASS-Americas, Madison, WI., 2002.

[195] B.E. Launder, D.B. Spalding, Mathematical model of turbulence, Academic Press,

1972.

[196] P.N., Laminar diffusion flamelet models in non-premixed turbulent combustion, Progress in Energy and Combustion Science 10 (1982) 369-399.

[197] B.J. P., D.L. Book, Flux-corrected transport I. SHAS-TA, a fluid transport algorithm that works, Journal of Computational Physics 11 (1973) 38-69.

[198] Frisque, A., Schnakenberg, J., Huang, J., and Bushe, W. K., Prediction of variations in the ignition delay time of methane/air with a stochastic particle model, Combustion Theory and Modelling 10 (2006) 241-256.

[199] Gardiner, C. W., Handbook of Stochastic Methods for Physics, Chemistry, and the Natural Sciences. Springer-Verlag, New York (1990) 136-142.

[200] Hua Zhao, Nicos Ladammatos, Engine Combustion Instrumentation and Diagnostics. Society of Automotive Engineers, Inc. Warrendale, Pa, 2001.

[201] A. Roller, A. Arnold, M. Decker, V. Sick, J. Wolfrum, W. Hentschel, K.-P. Schindler, Non-intrusive temperature measurements during the compression phase of a DI diesel engine, SAE technical paper, No. 952461.

[202] W.G. Bessler, C. Schulz, T. Lee, J.B. Jeffries, R.K. Hanson, Strategies for laser-induced fluorescence detection of nitric oxide in high-pressure flames: III. Comparison of A-X Strategies, Applied Optics 42-24 (2003) 4922-4936.

[203] D. A. Rothamer, J. B. Ghandhi, Determination of flame-front equivalence ratio during stratified combustion. SAE technical paper, No. 2003-01-0069.

Appendix A   Injector Characterization

To correctly interpret the shock tube experimental results, the injectors used in the experiments were characterized first. Parameters studied included injection delay and jet tip penetration. While injection delay is essential to help determine the ignition delay in the shock tube experiments, jet tip penetration can provide information about the location of the ignition kernel relative to the developing fuel jet.

A.1 Schlieren Imaging System

The impulsively started transient jet that develops during injection was investigated with a Schlieren imaging system. This apparatus (illustrated in Figure A.1) comprised of two 0.3048 m (12 in) diameter spherical mirrors each with a 2.4384 m (8 ft) focal length aligned to produce a parallel light beam between them. A 200 W mercury arc lamp was focused onto a 0.5 mm diameter pinhole to produce a point source of light and placed at the focal point of one of the concave mirrors, slightly off-axis to avoid interfering with any part of the parallel light beam. At the focal point of the other spherical mirror, also slightly off-axis, a circular aperture filtered the focused image, yielding a Schlieren image (rather than a shadowgraph) before projecting it onto the camera.

A circular aperture was used to filter the images, as opposed to a conventional Schlieren system using a knife edge, because the aperture allows resolving spatial density gradients in all planar directions rather than only visualizing those gradients that are perpendicular to the knife edge.

An optical pressure chamber was placed in the middle of these two spherical mirrors. The pressure chamber has four circular optical windows with a diameter of 108 mm (4.25 in). The injector was mounted horizontally at one side of the chamber. To increase the density difference, helium was used to pressurize the chamber and nitrogen was used as supply gas to the injector.

Images were captured with a Vision Research Phantom v7.1 CMOS-based camera equipped with a 50 mm F/1.2 Nikon lens. The camera was operated at a frame rate of 78,400 frames/second with an effective integration time of 2 µs per frame. The camera was operated with an aspect ratio of 112 pixels x 112 pixels. The injector and the camera were synchronization by triggering both with a National Instrument PCI-6602 timer/counter card and a LabView program.
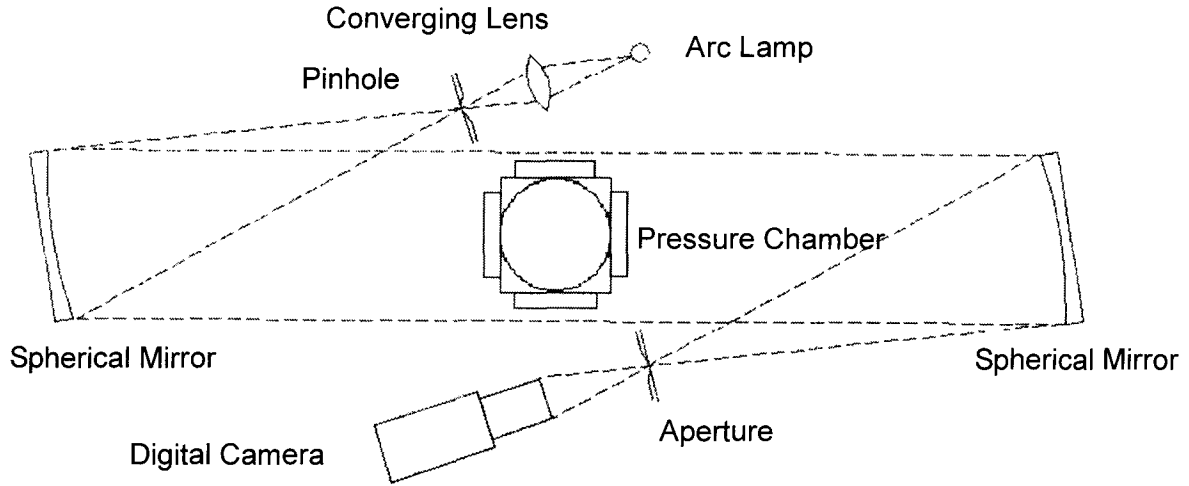
Figure A.1 Schlieren imaging system setup

A.2 Experimental Conditions

Table A.1 summarizes the experimental conditions and main parameters in these experiments. Repeat experiments were conducted for each operating condition for both the J43 and J43P2 injector.

Table A.1 Operating conditions for injector characterization experiments

P_o (bar)	P_i (bar)	t_i (ms)
30	60	1.0 – 2.5
30	90	1.0 – 2.5
30	120	1.0 – 2.5
30	150	1.0 – 2.5

A.3 Experimental Results

Figure A.2 shows selected spray-visualization images taken with Schlieren method from a sequence that spanned a complete injection event. The number below each image frame is the time after the injection trigger signal is issued to the driver. These images illustrate how the start of injection and jet length were relatively easily defined from the sequence of images as a consequence of the large density gradients between the nitrogen jet and surrounding still helium. Besides irregularities at the edge of the jet caused by turbulence fluctuation, which is expected, no obvious asymmetry along the centerline of the jet is observed.

0 ms   0.445 ms   1.082 ms   1.720 ms   2.357 ms

2.995 ms   3.632 ms   4.270 ms   4.907 ms   5.545 ms
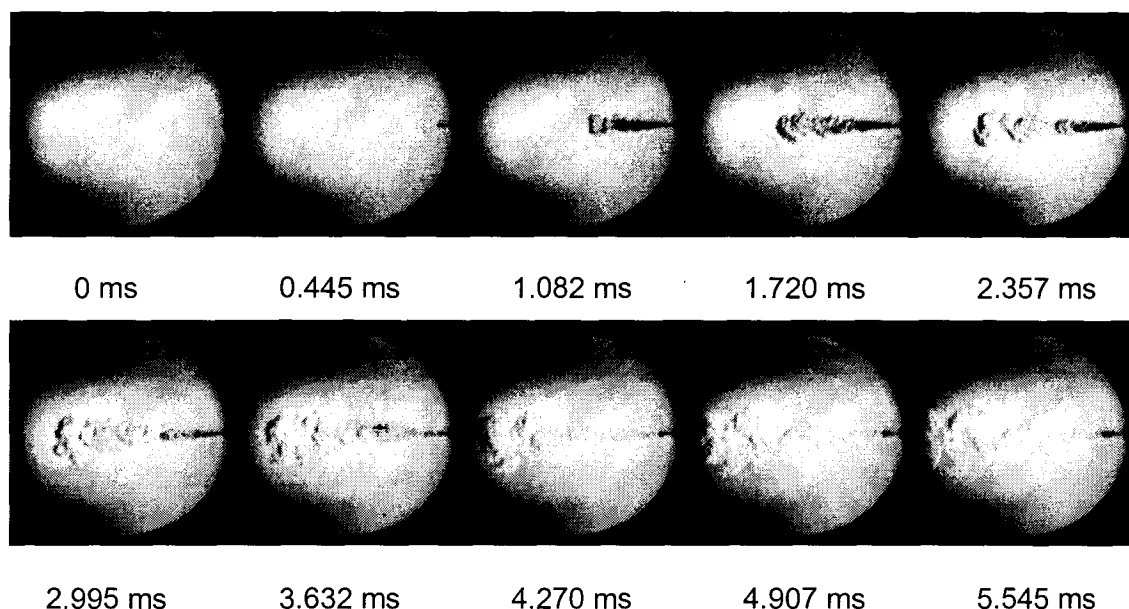
Figure A.2 Schlieren images of jet evolution in time

(J43 injector, T_a=300 K, T_o=300 K, P_i/P_o=4, t_i=1 ms)

A.3.1 Injection Delay

Detailed injection delay data for both injectors are available in Appendix C. The values in Table C.1 have been sorted from low to high. By applying Chauvenet's criterion, some dubious data points (shaded cells in the table) were picked up and eliminated. Table A.2 summarizes the injection delays for the final data for the J43 and J43P2 injector, respectively.

Table A.2 Summary of injection delays

(a) J43 injector

P_i/P_o	Min (ms)	Max (ms)	Mean (ms)	Std Dev (ms)	COV
2	0.361	0.401	0.374	0.008	2%
3	0.361	0.419	0.383	0.010	3%
4	0.370	0.457	0.397	0.027	7%
5	0.368	0.446	0.390	0.017	4%

(b) J43P2 injector

P_i/P_o	Min (ms)	Max (ms)	Mean (ms)	Std Dev (ms)	COV
2	0.288	0.304	0.297	0.004	1%
3	0.291	0.303	0.297	0.004	1%
4	0.304	0.319	0.311	0.004	1%
5	0.320	0.341	0.330	0.005	2%

A.3.2 Jet Tip Penetration

In Figures A.3 and A.4, the normalized jet length data following Equation 2.6 is plotted against the square root of time for J43 and J43P2 injector, respectively. A linear relation between normalized jet length and normalized time is clearly shown in these figures, which proves the scaling model.
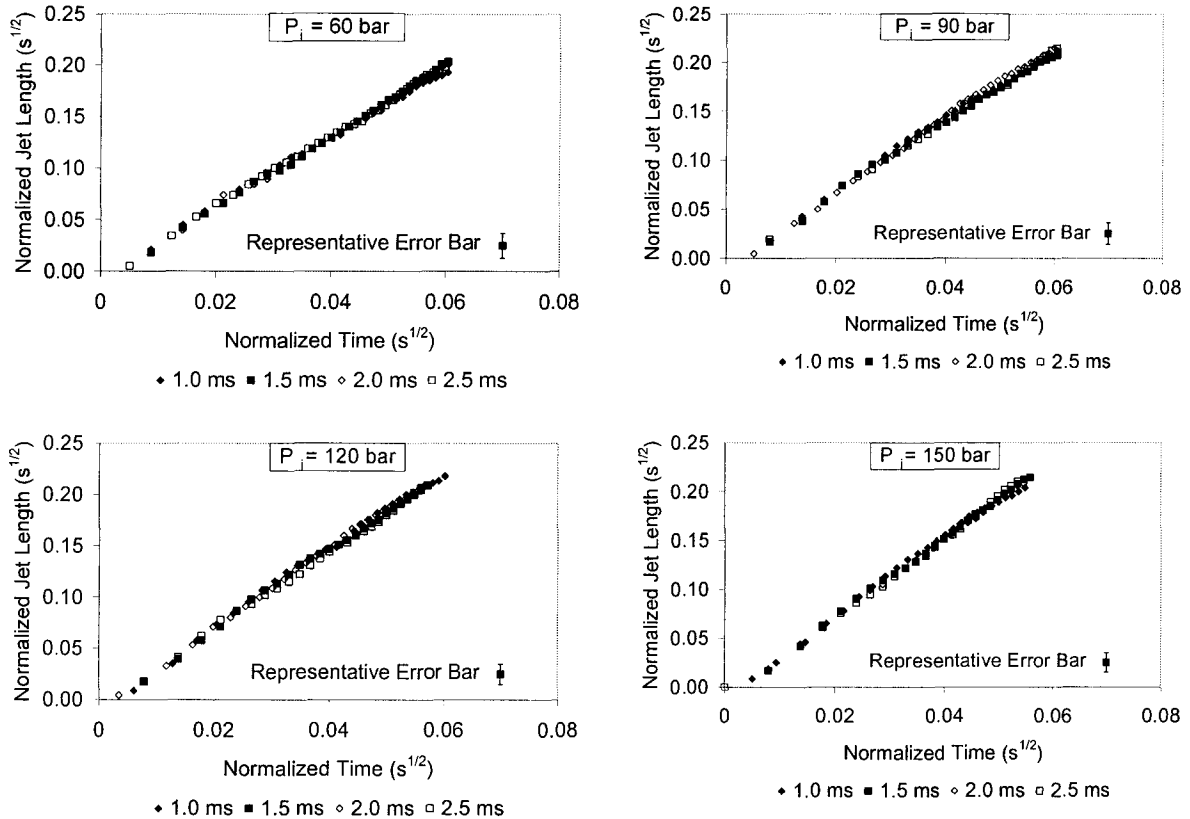
Figure A.3 Scaling model for J43 injector
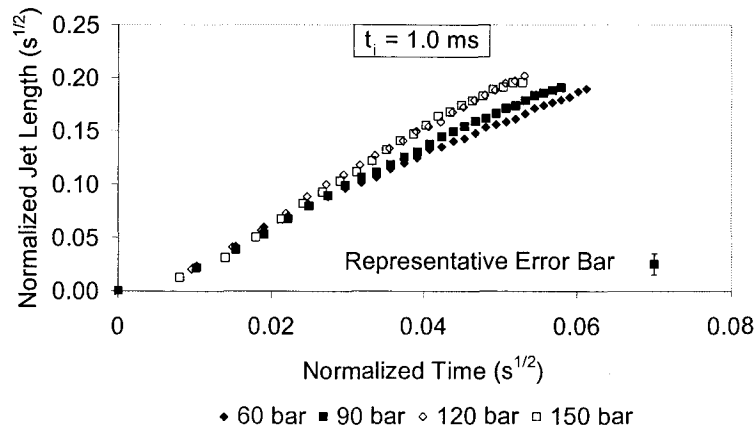
Figure A.4 Scaling model for J43P2 injector

Appendix B   Experimental Uncertainty Analysis

Experimental condition uncertainty in this study is summarized in Table B.1.

Table B.1 Experimental condition uncertainty

Pre-combustion Temperature	1-2%
Pre-combustion Pressure	3-4%
Atmospheric Temperature	1 K
Atmospheric Pressure	0.001 bar
Injection Pressure	1 bar
Injection Duration	0.01 ms

The ignition delay error was attributed to the uncertainty in injection delay and the time between CMOS camera frames (±0.014 ms for injection delay detection, ±0.032 ms for ignition detection respectively). Table B.2 shows the maximum possible deviation in the ignition delay for the J43 and J43P2 injector, respectively.

Table B.2 Ignition delay error for the J43 and J43P2 injector (ms)

P_i/P_o	J43		J43P2	
2	-0.059	+0.073	-0.055	+0.053
3	-0.068	+0.082	-0.052	+0.052
4	-0.073	+0.106	-0.053	+0.054
5	-0.068	+0.102	-0.056	+0.057

The technique used in this work to estimate the uncertainty in injection pressure ratio, jet length, normalized ignition kernel location and normalized NOx emissions is based on the calculated response, R, being a known function of a series of variables (x_i), each with a corresponding absolute uncertainty (w_i). Therefore, for an equation of the form $R = f(x_i)$, the total uncertainty W can be calculated based on:

$$W = \left[\sum_i \left(\left(\frac{\partial R}{\partial x_i} w_i \right)^2 \right) \right]^{1/2}$$

The formula can be used for any function where the underlying function and uncertainties are known.

An example of using this technique to calculate the uncertainty in injection pressure ratio is given below.

1. The formula used is identified:	$P_i / P_o = \dfrac{P_i}{P_o}$
2. The partial derivatives of the formula are calculated:	$\dfrac{\partial\left(\dfrac{P_i}{P_o}\right)}{\partial(P_i)} = \dfrac{1}{P_o} \; ; \; \dfrac{\partial\left(\dfrac{P_i}{P_o}\right)}{\partial(P_o)} = -\dfrac{P_i}{P_o^2}$
3. Identify the uncertainties:	$W_{P_i} = 1 \; bar$; $W_{P_o} = 4\%$
4. The net uncertainty is calculated:	$W_{P_i/P_o} = \sqrt{\left(\dfrac{1}{P_o}*W_{P_o}\right)^2 + \left(-\dfrac{P_i}{P_o^2}*W_{P_i}\right)^2}$

If the uncertainty calculated above still includes uncertainty terms in other measure values, the underlying uncertainties in each of these measure values can be obtained by repeating the same procedure, and then incorporated into the final experimental uncertainty.

Appendix C   Injection Delay Data

Table C.1 Injection delays for J43 and J43P2 injector (ms)

(a) J43 injector

$P_i/P_o = 2$	$P_i/P_o = 3$	$P_i/P_o = 4$	$P_i/P_o = 5$
0.361	0.361	0.370	0.368
0.364	0.373	0.370	0.372
0.365	0.373	0.373	0.373
0.366	0.374	0.374	0.376
0.366	0.375	0.375	0.376
0.367	0.375	0.376	0.378
0.368	0.376	0.378	0.378
0.369	0.377	0.378	0.379
0.369	0.377	0.378	0.379
0.370	0.378	0.378	0.381
0.370	0.380	0.379	0.381
0.370	0.380	0.380	0.381
0.371	0.380	0.381	0.381
0.371	0.380	0.381	0.382
0.372	0.380	0.383	0.382
0.373	0.380	0.384	0.384
0.373	0.380	0.385	0.385
0.373	0.381	0.385	0.385
0.373	0.381	0.386	0.386
0.373	0.381	0.387	0.387
0.374	0.381	0.388	0.387
0.374	0.381	0.388	0.388
0.375	0.382	0.388	0.388
0.375	0.383	0.389	0.389
0.375	0.383	0.391	0.390
0.375	0.383	0.391	0.391
0.376	0.385	0.392	0.392
0.376	0.387	0.392	0.392
0.376	0.387	0.396	0.393
0.376	0.387	0.400	0.394
0.377	0.387	0.400	0.396
0.377	0.387	0.411	0.396
0.379	0.388	0.436	0.401
0.379	0.389	0.438	0.402
0.386	0.389	0.439	0.403
0.389	0.401	0.451	0.403
0.390	0.412	0.452	0.432
0.401	0.419	0.454	0.438
0.426	0.440	0.456	0.446
0.442	0.444	0.457	0.481

Table C.1 Injection delays for J43 and J43P2 injector cont'd (ms)

(b) J43P2 injector

$P_i/P_o = 2$	$P_i/P_o = 3$	$P_i/P_o = 4$	$P_i/P_o = 5$
0.289	0.291	0.304	0.320
0.288	0.291	0.305	0.321
0.289	0.291	0.305	0.322
0.290	0.291	0.305	0.322
0.290	0.291	0.305	0.323
0.290	0.292	0.305	0.323
0.291	0.292	0.306	0.323
0.291	0.292	0.306	0.323
0.291	0.292	0.306	0.324
0.291	0.292	0.306	0.324
0.291	0.292	0.306	0.325
0.292	0.293	0.307	0.325
0.292	0.293	0.307	0.325
0.292	0.293	0.307	0.325
0.292	0.293	0.307	0.325
0.292	0.293	0.307	0.325
0.292	0.293	0.307	0.325
0.293	0.294	0.308	0.325
0.293	0.294	0.308	0.325
0.293	0.294	0.308	0.325
0.293	0.294	0.308	0.325
0.293	0.294	0.308	0.325
0.293	0.294	0.308	0.326
0.293	0.294	0.308	0.326
0.293	0.294	0.308	0.326
0.293	0.294	0.309	0.327
0.293	0.295	0.309	0.327
0.293	0.295	0.309	0.327
0.294	0.295	0.309	0.327
0.294	0.295	0.309	0.327
0.294	0.295	0.309	0.327
0.294	0.295	0.309	0.327
0.295	0.295	0.310	0.327
0.295	0.295	0.310	0.327
0.295	0.296	0.310	0.327
0.296	0.296	0.310	0.328
0.296	0.296	0.310	0.328
0.296	0.296	0.310	0.328
0.296	0.296	0.310	0.329
0.296	0.296	0.310	0.329

Table C.1 Injection delays for J43 and J43P2 injector cont'd (ms)

(b) J43P2 injector

$P_i/P_o = 2$	$P_i/P_o = 3$	$P_i/P_o = 4$	$P_i/P_o = 5$
0.297	0.297	0.310	0.329
0.297	0.297	0.311	0.329
0.297	0.297	0.311	0.329
0.297	0.297	0.311	0.330
0.297	0.298	0.311	0.330
0.297	0.298	0.311	0.330
0.298	0.298	0.311	0.330
0.298	0.298	0.312	0.330
0.299	0.298	0.312	0.331
0.299	0.298	0.312	0.331
0.299	0.298	0.312	0.332
0.299	0.298	0.312	0.332
0.300	0.298	0.312	0.332
0.300	0.298	0.313	0.332
0.300	0.299	0.313	0.333
0.300	0.299	0.313	0.333
0.300	0.299	0.313	0.333
0.300	0.299	0.313	0.334
0.301	0.299	0.314	0.334
0.301	0.300	0.314	0.334
0.301	0.300	0.314	0.334
0.301	0.300	0.314	0.334
0.301	0.301	0.314	0.334
0.301	0.301	0.314	0.334
0.301	0.301	0.314	0.334
0.301	0.301	0.315	0.335
0.301	0.301	0.315	0.335
0.301	0.302	0.315	0.335
0.302	0.302	0.315	0.336
0.302	0.302	0.315	0.336
0.302	0.302	0.316	0.336
0.302	0.302	0.316	0.337
0.302	0.302	0.316	0.337
0.302	0.302	0.316	0.337
0.303	0.302	0.317	0.337
0.303	0.303	0.317	0.338
0.303	0.303	0.318	0.338
0.303	0.303	0.318	0.339
0.303	0.303	0.318	0.339
0.304	0.303	0.319	0.341

Appendix D   Methane Experimental Data

Table D.1 Methane experimental data

File Name	P_o (bar)	T_o (K)	t_{d_ign} (ms)	Z_k (mm)	Z_t (mm)	NO (mg)	NO_2 (mg)	NOx/ Fuel
MCKP01	29.7	1293	0.612	16.4	32.5	0.002	0.082	4.75%
MCKP02	29.6	1291	0.624	18.4	32.8	0.002	0.090	5.21%
MCKP03	30.1	1302	0.837	21.2	38.3	0.001	0.102	5.86%
MCKP04	29.8	1295	0.465	11.0	28.0	0.003	0.095	5.58%
MCKP05	29.6	1291	0.695	17.2	34.8	0.002	0.102	5.88%
MCKP06	30.4	1309	0.644	18.4	33.3	0.001	0.072	4.16%
MCKP07	29.9	1298	0.647	10.8	33.4	0.002	0.097	5.61%
MCKP08	29.5	1289	0.658	19.4	33.8	0.002	0.078	4.52%
MCKP09	29.7	1293	0.647	13.0	33.4	0.002	0.084	4.87%
MCKP10	30.2	1305	0.644	20.4	33.3	0.001	0.065	3.74%
MCKP11	30.0	1299	0.644	17.0	33.3	0.004	0.081	4.86%
MCKP12	29.8	1296	0.860	9.8	38.9	0.004	0.075	4.46%
MCKP13	29.7	1294	0.885	29.6	39.5	0.003	0.078	4.63%
MCKP14	29.5	1289	0.837	21.4	38.4	0.002	0.039	2.35%
MCKP15	29.4	1286	0.778	23.0	36.9	0.002	0.082	4.80%
MCKP16	29.7	1293	0.734	15.8	35.8	0.002	0.084	4.92%
MCKP17	29.4	1286	0.686	15.4	34.5	0.002	0.056	3.26%
MCKP18	29.1	1280	0.764	22.2	36.6	0.002	0.080	4.71%
MCKP19	29.7	1293	0.810	16.8	37.7	0.004	0.045	2.77%
MCKP20	29.8	1296	0.837	19.0	38.3	0.002	0.068	3.98%
MCJP01	29.4	1286	1.093	12.8	37.2	0.002	0.026	4.62%
MCJP02	29.5	1288	0.809	14.0	31.7	0.003	0.022	4.13%
MCJP03	29.5	1288	1.185	15.6	38.8	0.003	0.018	3.29%
MCJP04	29.0	1277	0.734	10.4	30.2	0.002	0.021	3.82%
MCLP01	29.7	1294	0.891	18.0	36.9	0.005	0.051	4.62%
MCLP02	29.0	1278	0.919	19.0	37.6	0.004	0.043	3.84%
MCLP03	29.5	1289	0.613	10.8	30.3	0.003	0.062	5.34%
MCLP04	29.1	1279	0.887	21.0	36.9	0.003	0.074	6.32%
MCNP01	29.6	1291	0.864	19.4	41.3	0.007	0.158	6.99%
MCNP02	29.7	1292	0.714	26.8	37.3	0.007	0.159	7.06%
MCNP03	29.6	1290	0.946	23.4	43.3	0.007	0.152	6.74%
MCNP04	29.7	1292	0.520	16.2	31.5	0.005	0.157	6.86%

Table D.1 Methane experimental data cont'd

File Name	P_o (bar)	T_o (K)	t_{d_ign} (ms)	Z_k (mm)	Z_t (mm)	NO (mg)	NO_2 (mg)	NOx/ Fuel
MCKQ01	29.5	1288	0.956	21.6	41.2	0.005	0.106	4.50%
MCKQ02	28.1	1257	0.881	20.2	39.7	0.003	0.082	3.47%
MCKQ03	29.7	1293	0.919	30.4	40.3	0.005	0.154	6.44%
MCKQ04	29.5	1288	0.772	10.4	36.8	0.003	0.137	5.71%
MCKS01	29.6	1290	0.844	16.8	38.5	0.004	0.176	7.11%
MCKS02	29.9	1298	0.623	15.6	32.7	0.005	0.215	8.67%
MCKS03	30.0	1300	0.814	15.2	37.7	0.004	0.180	7.27%
MCKS04	29.5	1288	0.735	16.4	35.8	0.010	0.241	9.91%
MCKT01	29.4	1287	0.795	16.4	37.3	0.008	0.249	9.79%
MCKT02	29.4	1287	0.614	20.6	32.5	0.005	0.194	7.57%
MCKT03	29.3	1284	0.920	20.0	40.3	0.006	0.339	13.14%
MCKT04	29.7	1294	0.870	19.6	39.1	0.010	0.335	13.15%
MAKP01	29.2	1183	1.429	23.0	49.9	0.003	0.053	3.18%
MAKP03	29.6	1193	1.443	23.4	50.2	0.006	0.037	2.44%
MAKP05	29.8	1195	1.808	27.4	56.4	0.003	0.028	1.76%
MAKP06	29.0	1179	1.656	28.8	54.0	0.004	0.008	0.67%
MAKP07	29.1	1182	1.334	28.2	48.2	0.002	0.036	2.13%
MBKP06	29.3	1235	0.666	29.6	43.1	0.003	0.076	4.43%
MBKP07	29.5	1239	0.525	21.0	49.1	0.003	0.061	3.59%
MBKP08	29.6	1241	0.688	16.4	34.4	0.005	0.111	6.50%
MBKP09	29.5	1239	0.496	20.6	36.8	0.004	0.096	5.60%
MDKP08	29.4	1336	0.666	23.6	34.3	0.003	0.111	6.44%
MDKP09	29.2	1331	0.525	15.6	30.3	0.004	0.125	7.23%
MDKP10	29.4	1336	0.688	12.8	35.0	0.006	0.094	5.60%
MDKP11	29.7	1344	0.496	15.2	29.3	0.006	0.135	7.90%
MFKP06	29.4	1385	0.646	18.4	34.1	0.005	0.149	8.63%
MFKP07	29.2	1379	0.418	13.0	27.0	0.006	0.165	9.58%
MFKP08	29.5	1387	0.668	29.0	34.7	0.005	0.133	7.73%
MFKP09	29.6	1390	0.560	17.8	31.5	0.006	0.151	8.80%

Appendix E   Methane/Ethane Experimental Data

Table E.1 Methane/ethane experimental data

File Name	P_o (bar)	T_o (K)	t_{d_ign} (ms)	Z_k (mm)	Z_t (mm)	NO (mg)	NO_2 (mg)	NOx/ Fuel
MECKP01	29.9	1297	0.438	14.6	27.7	0.005	0.126	6.74%
MECKP02	30.0	1299	0.462	23.0	28.5	0.005	0.133	7.09%
MECKP03	29.5	1289	0.530	21.8	30.7	0.007	0.104	5.71%
MECKP04	29.6	1292	0.698	22.4	35.6	0.005	0.136	7.28%
MECKP05	30.0	1300	0.717	25.0	36.1	0.003	0.117	6.17%
MECKP06	29.9	1299	0.700	27.0	35.6	0.003	0.131	6.95%
MECKP07	29.7	1292	0.687	19.2	35.3	0.003	0.136	7.19%
MECKP08	29.9	1299	0.755	29.0	37.1	0.004	0.132	6.99%
MECKP09	29.7	1294	0.760	26.4	37.2	0.004	0.128	6.76%
MECKP10	29.7	1292	0.691	29.4	35.4	0.003	0.115	6.08%
MECKP11	29.7	1294	0.623	18.4	33.5	0.008	0.095	5.30%
MECKP12	29.6	1290	0.761	29.8	37.3	0.004	0.086	4.62%
MECKP13	29.6	1291	0.715	28.4	36.1	0.005	0.083	4.54%
MECKP14	29.8	1295	1.230	19.4	48.0	0.004	0.113	5.99%
MECKP15	29.6	1292	0.871	29.6	40.1	0.005	0.115	6.20%
MECKP16	29.5	1288	0.727	10.8	36.4	0.006	0.122	6.61%
MECKP17	29.8	1295	0.624	13.6	33.5	0.005	0.127	6.84%
MECKP18	30.0	1300	0.554	21.6	31.4	0.004	0.097	5.23%
MECKP19	30.1	1302	0.530	14.4	30.7	0.005	0.108	5.82%
MECKP20	30.0	1300	0.688	24.4	35.3	0.004	0.120	6.39%
MECJP04	29.5	1288	0.810	15.6	32.4	0.002	0.018	3.02%
MECJP05	29.5	1288	0.823	10.2	32.7	0.002	0.029	4.60%
MECJP06	29.6	1291	0.843	17.0	33.1	0.002	0.031	5.08%
MECJP07	29.8	1294	0.925	16.4	34.7	0.002	0.024	3.92%
MECLP01	29.2	1282	0.784	24.2	35.3	0.002	0.046	3.64%
MECLP02	29.6	1291	0.709	14.4	33.4	0.003	0.061	4.77%
MECLP03	29.9	1298	0.831	22.6	36.3	0.004	0.106	8.26%
MECLP04	29.8	1296	0.693	14.8	33.0	0.004	0.089	7.02%
MECLP05	30.0	1300	0.796	18.2	35.4	0.002	0.053	4.20%
MECNP01	30.0	1301	0.807	22.4	41.9	0.004	0.128	4.99%
MECNP02	30.0	1301	0.917	24.0	44.8	0.005	0.169	6.61%
MECNP03	29.6	1292	0.817	27.4	42.2	0.004	0.141	5.50%
MECNP04	29.5	1287	0.776	16.4	41.1	0.005	0.158	6.18%

Table E.1 Methane/ethane experimental data cont'd

File Name	P_o (bar)	T_o (K)	t_{d_ign} (ms)	Z_k (mm)	Z_t (mm)	NO (mg)	NO_2 (mg)	NOx/ Fuel
MECKQ01	29.9	1299	0.640	19.0	33.9	0.008	0.214	8.46%
MECKQ02	29.7	1292	0.750	16.6	36.9	0.008	0.140	5.65%
MECKQ03	29.6	1291	0.692	26.0	35.4	0.004	0.156	6.11%
MECKQ04	29.9	1299	0.797	23.6	38.2	0.005	0.199	7.78%
MECKS01	29.3	1284	0.437	16.8	27.7	0.018	0.209	6.43%
MECKS02	30.0	1299	1.111	11.8	45.4	0.012	0.203	6.08%
MECKS03	29.7	1294	0.771	18.4	37.5	0.010	0.176	5.24%
MECKS04	29.5	1289	0.890	25.0	40.5	0.008	0.170	5.05%
MECKT02	28.9	1276	1.008	21.0	43.4	0.007	0.277	7.54%
MECKT03	30.1	1302	0.416	16.8	26.9	0.009	0.248	6.82%
MECKT04	29.7	1293	0.652	15.0	34.3	0.015	0.227	6.44%
MECKT05	29.9	1298	0.837	17.6	39.2	0.019	0.233	6.69%
MEAKP01	29.6	1192	0.892	17.0	39.8	0.003	0.077	4.13%
MEAKP03	30.0	1200	1.096	21.2	44.2	0.002	0.052	2.82%
MEAKP04	30.0	1199	1.382	27.4	49.9	0.002	0.048	2.62%
MEAKP05	29.9	1198	1.003	18.4	42.2	0.002	0.062	3.31%
MEBKP01	29.9	1248	1.223	31.2	47.4	0.006	0.075	4.20%
MEBKP02	29.8	1246	0.933	29.8	41.1	0.007	0.059	3.44%
MEBKP03	29.6	1245	0.965	19.2	41.9	0.003	0.059	3.21%
MEBKP04	29.7	1244	1.001	21.6	42.6	0.003	0.065	3.54%
MEDKP01	29.9	1347	0.432	12.4	27.7	0.004	0.108	5.79%
MEDKP02	30.3	1357	0.397	14.4	26.4	0.005	0.128	6.86%
MEDKP03	30.0	1350	0.861	22.0	40.1	0.010	0.095	5.42%
MEDKP04	29.9	1348	0.647	13.2	34.4	0.006	0.114	6.14%
MEFKP01	30.0	1400	0.484	17.8	29.7	0.004	0.127	6.72%
MEFKP02	30.0	1400	0.496	17.2	30.1	0.005	0.144	7.69%
MEFKP03	29.8	1395	0.486	13.4	29.8	0.008	0.128	6.97%
MEFKP04	29.9	1398	0.705	20.0	36.4	0.006	0.154	8.24%

Appendix F   Methane/Hydrogen Experimental Data

Table F.1 Methane/hydrogen experimental data

File Name	P_o (bar)	T_o (K)	t_{d_ign} (ms)	Z_k (mm)	Z_t (mm)	NO (mg)	NO_2 (mg)	NOx/ Fuel
MHCKP01	30.2	1304	0.763	29.0	34.3	0.003	0.038	2.18%
MHCKP02	29.4	1285	0.662	16.8	31.6	0.004	0.036	2.08%
MHCKP03	29.8	1295	0.518	8.8	27.2	0.005	0.052	2.99%
MHCKP04	29.6	1292	0.471	12.4	25.6	0.002	0.045	2.49%
MHCKP05	29.6	1291	0.675	23.6	31.9	0.003	0.043	2.44%
MHCKP06	29.4	1287	0.717	15.8	33.1	0.003	0.043	2.42%
MHCKP07	29.1	1280	0.485	11.8	26.2	0.004	0.043	2.47%
MHCKP08	29.6	1291	0.724	17.0	33.3	0.002	0.044	2.46%
MHCKP09	29.4	1287	0.779	22.4	34.8	0.004	0.040	2.36%
MHCKP10	29.7	1293	0.717	22.4	33.1	0.004	0.044	2.53%
MHCKP11	29.7	1293	0.643	10.6	31.0	0.004	0.057	3.19%
MHCKP12	29.3	1285	0.765	14.4	34.5	0.003	0.032	1.85%
MHCKP13	29.4	1286	0.887	13.4	37.6	0.005	0.044	2.60%
MHCKP14	30.5	1311	0.710	14.0	32.8	0.002	0.044	2.40%
MHCKP15	29.8	1295	0.672	23.8	31.9	0.002	0.039	2.15%
MHCKP16	29.8	1295	0.672	23.4	31.9	0.001	0.042	2.26%
MHCKP17	29.4	1287	0.718	11.8	33.2	0.003	0.053	2.93%
MHCKP18	29.6	1290	0.732	12.8	33.5	0.002	0.055	3.03%
MHCKP19	30.0	1300	0.568	12.2	28.8	0.002	0.039	2.15%
MHCKP20	29.7	1292	0.861	26.4	36.9	0.004	0.037	2.17%
MHCJP01	30.2	1304	1.129	5.2	31.7	0.004	0.003	0.82%
MHCJP04	30.3	1307	1.066	7.8	30.8	0.002	0.005	0.77%
MHCJP05	29.4	1285	0.997	6.4	29.9	0.003	0.003	0.64%
MHCJP06	29.6	1292	0.735	5.8	25.6	0.003	0.009	1.28%
MHCLP01	29.3	1284	1.107	8.6	35.7	0.002	0.010	0.91%
MHCLP02	30.2	1304	0.883	18.8	31.6	0.003	0.008	0.79%
MHCLP03	29.7	1293	0.598	9.4	25.7	0.005	0.015	1.50%
MHCLP04	30.2	1305	1.132	7.0	36.0	0.004	0.010	1.06%
MHCNP01	29.6	1290	0.968	11.4	41.2	0.003	0.076	3.17%
MHCNP02	29.5	1288	0.721	14.2	34.4	0.004	0.073	3.08%
MHCNP03	30.3	1307	0.753	14.0	35.3	0.004	0.085	3.57%
MHCNP04	29.8	1296	0.715	15.6	34.2	0.006	0.092	3.94%

Table F.1 Methane/hydrogen experimental data cont'd

File Name	P_o (bar)	T_o (K)	t_{d_ign} (ms)	Z_k (mm)	Z_t (mm)	NO (mg)	NO_2 (mg)	NOx/ Fuel
MHAKP02	29.1	1181	0.828	11.6	47.0	0.000	0.008	1.46%
MHAKP03	29.5	1189	1.212	19.8	35.5	0.001	0.027	0.32%
MHAKP04	29.2	1184	0.978	27.4	44.1	0.001	0.005	1.46%
MHBKP01	30.1	1253	0.670	21.2	39.1	0.001	0.027	2.29%
MHBKP02	29.9	1248	1.176	17.0	31.5	0.002	0.042	1.83%
MHBKP03	30.1	1252	1.120	24.4	43.8	0.002	0.033	1.64%
MHBKP04	30.4	1258	0.983	18.4	42.5	0.001	0.031	2.14%
MHDKP01	30.1	1354	0.442	32.2	39.4	0.001	0.040	3.90%
MHDKP02	30.1	1354	0.661	19.4	24.9	0.002	0.071	3.47%
MHDKP04	30.1	1351	0.774	12.2	31.8	0.003	0.063	3.60%
MHDKP05	30.2	1355	0.594	10.0	34.9	0.007	0.061	3.76%
MHFKP01	30.4	1410	0.604	14.6	29.8	0.004	0.067	4.87%
MHFKP02	30.1	1402	0.419	20.2	30.4	0.003	0.090	5.11%
MHFKP03	30.1	1402	0.578	15.0	24.2	0.005	0.092	4.31%

Appendix G   Methane/Nitrogen Experimental Data

Table G.1 Methane/nitrogen experimental data

File Name	P_o (bar)	T_o (K)	t_{d_ign} (ms)	Z_k (mm)	Z_t (mm)	NO (mg)	NO_2 (mg)	NOx/ Methane
MN2CKP01	29.9	1299	0.910	31.6	41.5	0.001	0.019	1.24%
MN2CKP02	30.2	1304	0.743	19.4	37.2	0.002	0.029	2.00%
MN2CKP03	29.9	1297	0.863	21.4	40.2	0.003	0.039	2.71%
MN2CKP04	30.4	1310	0.548	16.8	31.5	0.002	0.035	2.36%
MN2CKP05	30.0	1300	1.172	28.8	47.3	0.002	0.008	0.60%
MN2CKP06	30.2	1304	0.971	18.4	42.8	0.002	0.013	0.90%
MN2CKP08	29.7	1294	1.134	38.4	46.5	0.003	0.004	0.44%
MN2CKP09	30.0	1301	0.453	25.6	28.5	0.002	0.026	1.77%
MN2CKP10	30.0	1301	0.754	9.6	37.4	0.003	0.037	2.56%
MN2CKP11	30.0	1300	0.671	25.8	35.2	0.002	0.010	0.80%
MN2CKP12	30.4	1309	0.633	15.4	34.1	0.001	0.026	1.74%
MN2CKP13	30.3	1306	0.653	25.8	34.7	0.003	0.038	2.57%
MN2CKP14	30.3	1307	0.673	16.4	35.2	0.003	0.028	1.95%
MN2CKP15	30.4	1309	1.127	28.6	46.2	0.001	0.008	0.59%
MN2CKP16	30.3	1306	0.869	28.8	40.3	0.002	0.024	1.69%
MN2CKP17	30.3	1307	0.909	25.4	41.3	0.001	0.006	0.45%
MN2CKP19	30.0	1301	0.788	21.2	38.4	0.003	0.019	1.40%
MN2CKP20	30.2	1305	0.828	16.4	39.3	0.003	0.046	3.09%
MN2CKP21	30.2	1305	0.801	27.4	38.7	0.001	0.031	2.03%
MN2CKP22	30.0	1299	1.152	13.2	46.9	0.002	0.024	1.65%
MN2CJP02	30.5	1312	1.691	11.0	42.3	0.001	0.005	0.92%
MN2CJP03	30.0	1300	1.246	20.4	36.3	0.002	0.006	1.42%
MN2CJP04	30.0	1299	0.876	14.8	30.3	0.001	0.013	2.42%
MN2CLP01	29.9	1297	1.240	21.4	43.9	0.002	0.005	0.83%
MN2CLP02	30.1	1301	0.682	17.8	32.5	0.001	0.015	1.79%
MN2CLP03	30.0	1299	0.806	10.4	35.3	0.001	0.018	2.13%
MN2CLP05	30.3	1306	0.593	12.8	30.2	0.001	0.022	2.53%
MN2CNP01	30.3	1306	0.664	19.2	38.2	0.002	0.049	2.52%
MN2CNP02	30.4	1310	1.251	33.0	53.5	0.002	0.050	2.58%
MN2CNP03	29.8	1294	0.991	14.6	47.3	0.003	0.054	2.78%
MN2CNP05	30.2	1304	0.788	31.4	41.8	0.003	0.056	2.94%

Table G.1 Methane/nitrogen experimental data cont'd

File Name	P_o (bar)	T_o (K)	t_{d_ign} (ms)	Z_k (mm)	Z_t (mm)	NO (mg)	NO_2 (mg)	NOx/ Methane
MN2CKQ01	30.0	1301	0.788	17.2	38.4	0.001	0.011	0.57%
MN2CKQ02	30.0	1299	0.758	30.4	37.6	0.001	0.011	0.59%
MN2CKQ03	30.4	1308	0.738	25.8	37.0	0.002	0.054	2.69%
MN2CKS01	29.7	1294	0.574	22.2	32.5	0.002	0.076	2.88%
MN2CKS03	30.1	1302	0.849	12.4	39.9	0.002	0.061	2.31%
MN2CKS04	30.3	1307	0.807	21.0	38.8	0.003	0.091	3.45%
MN2CKT02	30.3	1307	0.713	15.8	36.3	0.003	0.098	3.17%
MN2CKT03	30.1	1303	0.752	28.4	37.4	0.002	0.058	1.88%
MN2CKT04	30.1	1302	0.610	22.2	33.4	0.003	0.082	2.65%
MN2AKP01	30.0	1199	1.670	20.8	55.8	0.001	0.005	0.36%
MN2AKP02	29.7	1193	1.492	29.6	52.7	0.000	0.002	0.14%
MN2AKP03	29.7	1193	1.201	29.4	47.0	0.001	0.006	0.42%
MN2AKP04	30.1	1202	1.468	42.0	52.1	0.001	0.003	0.25%
MN2BKP01	29.9	1248	0.985	21.8	42.6	0.001	0.006	0.39%
MN2BKP02	29.8	1246	1.205	36.8	47.4	0.001	0.005	0.34%
MN2BKP06	30.0	1257	0.702	29.0	35.8	0.001	0.010	0.70%
MN2DKP03	30.2	1355	0.586	23.8	33.0	0.003	0.038	2.55%
MN2DKP04	30.4	1359	0.553	22.2	32.0	0.002	0.047	3.11%
MN2DKP05	30.2	1355	0.617	20.8	34.0	0.003	0.061	4.04%
MN2FKP01	30.4	1411	0.634	16.4	34.7	0.006	0.043	3.11%
MN2FKP02	30.4	1409	0.677	19.8	35.9	0.002	0.043	2.87%
MN2FKP04	30.2	1406	0.657	24.2	35.4	0.002	0.058	3.83%

Appendix H   OH-PLIF Experimental Data

Table H.1 OH-PLIF experimental data

File Name	Laser Timing (ms)	P_o (bar)	T_o (K)	$t_{d\ ign}$ (ms)	I_{laser} (mJ)
M17LIF01	1.389	29.8	1295	1.074	0.091
M17LIF02	1.389	30.5	1297	0.754	0.089
M17LIF03	1.389	30.5	1284	1.176	0.097
M17LIF04	1.389	29.8	1280	0.800	0.096
M17LIF05	1.389	30.4	1285	0.916	0.085
M17LIF06	1.389	30.4	1286	0.790	0.082
M17LIF07	1.389	30.1	1284	0.834	0.097
M17LIF09	1.389	29.3	1281	0.711	0.083
M17LIF10	1.389	29.2	1303	0.840	0.093
M17LIF11	1.389	30.1	1281	0.569	0.100
M17LIF12	1.389	30.1	1307	0.767	0.098
M17LIF13	1.389	29.7	1286	1.005	0.089
M17LIF14	1.389	29.4	1306	0.823	0.095
M17LIF15	1.389	29.7	1304	0.698	0.099
M17LIF16	1.389	30.5	1291	0.633	0.102
M17LIF17	1.389	29.3	1309	1.188	0.091
M17LIF18	1.389	30.2	1292	0.489	0.103
M17LIF20	1.389	30.0	1291	0.719	0.106
M17LIF21	1.389	29.8	1291	0.518	0.092
M17LIF22	1.389	29.2	1298	0.697	0.083
M17LIF23	1.389	30.3	1304	1.040	0.104
M17LIF24	1.389	29.2	1294	0.866	0.092
M17LIF25	1.389	29.1	1304	0.613	0.086
M17LIF27	1.389	29.8	1296	0.887	0.088
M17LIF28	1.389	29.7	1285	0.767	0.091
M17LIF29	1.389	30.3	1295	0.670	0.091
M17LIF30	1.389	29.9	1283	0.527	0.101
M17LIF31	1.389	29.9	1296	0.954	0.096
M17LIF32	1.389	29.4	1309	0.699	0.086
M17LIF33	1.389	29.1	1286	0.612	0.099
M17LIF34	1.389	29.1	1311	0.814	0.090
M17LIF35	1.389	30.4	1305	0.651	0.093
M17LIF36	1.389	30.1	1288	0.547	0.095
M17LIF37	1.389	29.3	1281	0.660	0.103
M17LIF38	1.389	29.4	1309	0.694	0.087
M17LIF39	1.389	29.8	1297	0.634	0.099
M17LIF40	1.389	29.4	1280	0.512	0.096
M17LIF41	1.389	29.5	1282	0.636	0.089
M17LIF42	1.389	30.2	1302	0.626	0.099
M17LIF43	1.389	29.5	1282	1.035	0.097

Table H.1 OH-PLIF experimental data cont'd

File Name	Laser Timing (ms)	P_o (bar)	T_o (K)	$t_{d\ ign}$ (ms)	I_{laser} (mJ)
M17LIF44	1.389	29.6	1294	0.819	0.103
M17LIF45	1.389	29.7	1280	0.943	0.101
M17LIF46	1.389	29.8	1283	0.837	0.103
M17LIF47	1.389	30.4	1303	0.735	0.106
M17LIF48	1.389	29.8	1293	0.786	0.106
M17LIF49	1.389	29.7	1280	0.830	0.104
M17LIF50	1.389	30.5	1293	0.750	0.082
M17LIF51	1.389	29.5	1301	0.848	0.086
M17LIF52	1.389	29.9	1287	0.946	0.095
M17LIF53	1.389	30.4	1282	0.878	0.090
M17LIF54	1.389	30.4	1289	0.746	0.095
M17LIF55	1.389	30.4	1282	0.770	0.108
M17LIF56	1.389	30.0	1294	0.705	0.082
M17LIF57	1.389	29.8	1295	0.888	0.087
M17LIF58	1.389	29.1	1311	0.790	0.096
M17LIF59	1.389	30.0	1280	0.642	0.103
M17LIF60	1.389	30.5	1281	0.741	0.091
M17LIF61	1.389	29.1	1298	1.173	0.101
M17LIF62	1.389	30.0	1282	0.873	0.084
M17LIF63	1.389	30.4	1310	0.791	0.090
M17LIF64	1.389	29.3	1280	0.790	0.093
M17LIF65	1.389	30.3	1311	0.697	0.104
M17LIF66	1.389	30.3	1297	0.622	0.082
M17LIF67	1.389	29.1	1310	0.662	0.090
M17LIF68	1.389	30.4	1309	1.173	0.098
M17LIF69	1.389	29.4	1295	0.619	0.105
M17LIF70	1.389	29.9	1283	0.945	0.082
M17LIF71	1.389	29.2	1286	0.710	0.099
M17LIF72	1.389	29.9	1292	0.640	0.083
M17LIF73	1.389	30.0	1300	0.624	0.092
M17LIF74	1.389	29.3	1285	0.711	0.091
M17LIF75	1.389	29.3	1299	0.877	0.103
M17LIF76	1.389	29.3	1291	0.713	0.105
M17LIF77	1.389	29.9	1283	0.593	0.082
M17LIF78	1.389	30.0	1291	0.717	0.105
M17LIF79	1.389	30.3	1311	0.628	0.106
M17LIF80	1.389	30.3	1297	0.665	0.087
M17LIF81	1.389	29.7	1281	0.726	0.096
M17LIF82	1.389	30.3	1294	0.933	0.095
M17LIF83	1.389	29.8	1309	0.877	0.105

Table H.1 OH-PLIF experimental data cont'd

File Name	Laser Timing (ms)	P_o (bar)	T_o (K)	$t_{d\ ign}$ (ms)	I_{laser} (mJ)
M17LIF84	1.389	29.9	1281	0.692	0.106
M17LIF85	1.389	29.7	1287	0.729	0.086
M17LIF86	1.389	29.7	1303	0.872	0.092
M17LIF87	1.389	30.4	1290	0.930	0.100
M17LIF88	1.389	30.2	1310	0.586	0.092
M17LIF89	1.389	30.1	1301	0.863	0.090
M17LIF90	1.389	30.2	1292	0.648	0.102
M17LIF91	1.389	29.3	1308	0.710	0.084
M17LIF92	1.389	30.1	1299	0.877	0.092
M17LIF93	1.389	30.2	1300	0.712	0.086
M17LIF94	1.389	29.3	1304	0.747	0.101
M17LIF95	1.389	29.2	1289	0.925	0.094
M17LIF96	1.389	29.9	1310	0.797	0.096
M17LIF97	1.389	29.4	1296	0.907	0.107
M17LIF98	1.389	29.4	1306	0.988	0.094
M17LIF99	1.389	29.2	1305	0.831	0.105
M17LIF100	1.389	29.9	1303	0.877	0.100
M17LIF101	1.389	29.7	1280	0.799	0.103
M17LIF102	1.389	30.5	1296	0.649	0.103
M17LIF103	1.389	29.6	1311	0.833	0.096
M15LIF01	1.189	30.3	1305	0.623	0.101
M15LIF02	1.189	29.6	1281	0.587	0.097
M15LIF03	1.189	30.3	1293	0.838	0.083
M15LIF04	1.189	29.9	1288	0.588	0.099
M15LIF05	1.189	30.2	1281	0.698	0.089
M15LIF06	1.189	29.5	1288	0.659	0.081
M15LIF08	1.189	30.2	1314	1.033	0.086
M15LIF09	1.189	30.1	1312	0.514	0.101
M15LIF10	1.189	29.1	1304	0.638	0.093
M15LIF11	1.189	29.7	1296	0.727	0.085
M15LIF12	1.189	30.2	1308	0.698	0.089
M15LIF13	1.189	29.3	1312	1.021	0.105
M15LIF14	1.189	30.2	1302	0.613	0.099
M15LIF15	1.189	29.4	1307	0.601	0.089
M15LIF16	1.189	30.3	1290	0.778	0.095
M15LIF17	1.189	29.9	1301	0.806	0.096
M15LIF18	1.189	29.2	1292	0.769	0.091
M15LIF19	1.189	30.3	1301	0.727	0.102
M15LIF20	1.189	29.6	1279	0.804	0.094
M15LIF21	1.189	29.5	1305	0.556	0.099

Table H.1 OH-PLIF experimental data cont'd

File Name	Laser Timing (ms)	P_o (bar)	T_o (K)	$t_{d\ ign}$ (ms)	I_{laser} (mJ)
M13LIF02	0.989	30.1	1283	0.635	0.088
M13LIF03	0.989	29.1	1282	0.809	0.092
M13LIF04	0.989	29.2	1296	0.680	0.102
M13LIF05	0.989	29.4	1296	0.674	0.092
M13LIF06	0.989	29.0	1284	0.759	0.098
M13LIF07	0.989	29.1	1314	0.832	0.086
M13LIF08	0.989	29.5	1288	0.794	0.103
M13LIF09	0.989	29.7	1306	0.808	0.099
M13LIF10	0.989	29.6	1289	0.777	0.084
M13LIF11	0.989	29.8	1284	0.697	0.093
M13LIF12	0.989	30.6	1313	0.586	0.102
M13LIF13	0.989	29.4	1283	0.746	0.095
M13LIF14	0.989	29.5	1289	0.708	0.099
M13LIF15	0.989	30.3	1283	0.659	0.089
M13LIF16	0.989	30.4	1282	0.584	0.088
M13LIF17	0.989	29.6	1302	0.739	0.103
M13LIF19	0.989	29.8	1287	0.863	0.085
M13LIF20	0.989	29.5	1295	0.751	0.098
M13LIF21	0.989	29.0	1291	0.711	0.105
M13LIF22	0.989	30.2	1300	0.728	0.099